INFORMATION TO USERS

This manuscript has been reproduced from the microfilm master. UMI films the text directly from the original or copy submitted. Thus, some thesis and dissertation copies are in typewriter face, while others may be from any type of computer printer.

The quality of this reproduction is dependent upon the quality of the copy submitted. Broken or indistinct print, colored or poor quality illustrations and photographs, print bleedthrough, substandard margins, and improper alignment can adversely affect reproduction.

In the unlikely event that the author did not send UMI a complete manuscript and there are missing pages, these will be noted. Also, if unauthorized copyright material had to be removed, a note will indicate the deletion.

Oversize materials (e.g., maps, drawings, charts) are reproduced by sectioning the original, beginning at the upper left-hand corner and continuing from left to right in equal sections with small overlaps.

ProQuest Information and Learning
300 North Zeeb Road, Ann Arbor, MI 48106-1346 USA
800-521-0600



Downloaded from SHAREOK. Persistent Handle URL: https://hdl.handle.net/11244/569

UNIVERSITY OF OKLAHOMA

GRADUATE COLLEGE

THE IMPACT OF RADAR DATA ASSIMILATION ON THE CHORWON-YONCHON 1996 HEAVY RAINFALL EVENT

A Dissertation

SUBMITTED TO GRADUATE FACULTY

in partial fulfillment of the requirements for the

degree of

Doctor of Philosophy

By

Hee-Dong Yoo

Norman, Oklahoma

2003

UMI Number: 3082926



UMI Microform 3082926

Copyright 2003 by ProQuest Information and Learning Company.
All rights reserved. This microform edition is protected against unauthorized copying under Title 17, United States Code.

ProQuest Information and Learning Company
300 North Zeeb Road
P.O. Box 1346
Ann Arbor, MI 48106-1346

© Copyright by Hee-Dong Yoo 2003
All Rights Reserved

THE IMPACT OF RADAR DATA ASSIMILATION ON THE CHORWON-YONCHON 1996 HEAVY RAINFALL EVENT

A DISSERTATION APPROVED FOR
THE SCHOOL OF METEOROLOGY

BY

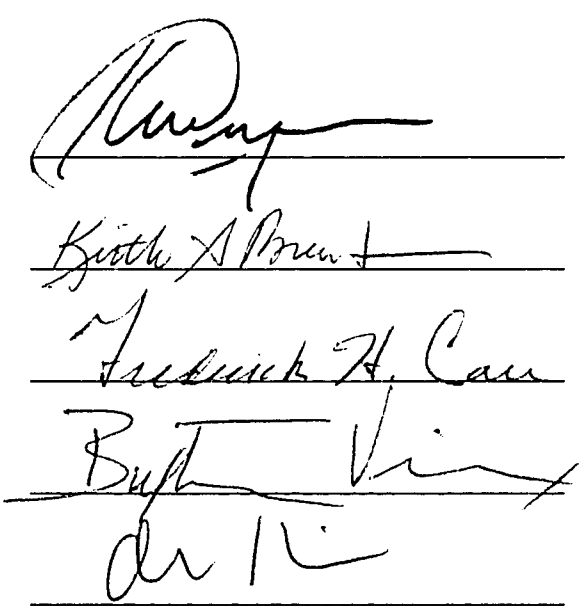

ACKNOWLEDGMENTS

Now is a time to give a period mark in my long journey. However, I know well that this is not an ending time, but a new starting time. There are a lot of great people who are acknowledged for their help during the time I have been here at the School of Meteorology (SoM) and Center for Analysis and Prediction of Storms (CAPS) of University of Oklahoma (OU).

I must first thank my advisor, Dr. Kelvin Droegemeier. He was always willing to give me his special teaching and direction to improve my weaknesses. All the while he did not hesitate to give me his cerebration when I was up, and he encouraged me when I was down. I have no words to express my deepest thanks to him, and I am very proud of being one of his students.

I am also grateful to Dr. Keith Brewster, one of my doctoral committee, for his continued help to complete my research. He always welcomed to my unexpected visits and erratic questions. I would not hesitate to call him my second advisor. Thanks also go to my other committee members, Drs. Fred Carr, Alan Shapiro, and Baxter Vieux. I have no doubt that I can make a more qualified dissertation owing to their detailed comments and discussions for my research. Furthermore, I'd like to give another thank to Dr. Shapiro for his sincere effort regarding the co-project between Korea Meteorological Administration (KMA)/Meteorological Research Institute (METRI). Dr. Baxter Vieux, his wife Mrs. Jean Vieux, and Mr. Eddie Koehler of Vieux and Associates Inc. They are acknowledged for their work to estimate rainfall from NEXRAD data. I can make good progress for the quantitative verification in my research owing to their support. I am also grateful to Dr. Yoshi Sasaki for his concern and neat comments about my research. I thank Dr. Stephen Bloom of NASA/Goddard Space Flight Center for his sincere explanations about my questions via private communication.

I also wish to give my gratitude to all CAPS members, Drs. Ming Xue, Dan Webber, and other scientists and staffs, and my school friends of SoM, Bill Martin, Ernani Nascimento, Paul Nutter, and so on, for their help and encouragement. Particular thanks go to Ed Alderman and Dan Dawson who were willing to give me their favor for the reviewing of my write-up. I am also very thankful to Brand George, Scott Hill, and Courtney Garrison for their effort to maintain CrayJ90. During the time my family stayed in Norman, we met wonderful American people, Tony and Joe Henning and McGee's family who always gave their hands whenever our family needed any help.

I extend my special thanks to Drs. Hi-Ku Cho, my Master's thesis advisor, and Seong-Man Lee of Yonsei University. Their continued concern and special care can always make me comfortable and give me enough encouragement to overcome many obstacles. Thanks are also due to Drs. Tae-Young Lee of Yonsei University and Dong-Kyoo Lee of Seoul National University. They were willing to give their concern and opinions to my advisor and myself when we were deciding on the track of my research topic. I also extend my sincere thanks to Dr. Seon Ki Park of Ewha Woman's University, for his help and good advice for my life here. I always keep his favor in my mind.

Fortunately, I could start my study here at the SoM, which has the best meteorological study and research program in the world, owing to the consideration of the Korean government and KMA via the Korean Government's Long Term Fellowship.

I am deeply grateful to Dr. Kyung-Sup Shin of KMA. He strongly recommended that I should start my study at SoM of OU. He gave me a great mission for my research topic regarding radar data assimilation to expect a significant contribution to KMA NWP works in the future. Many thanks go to the Director of NWP division of KMA, Joo-Young Cho, for her consideration and offering the data what I wanted. I'd like also extend my thanks to the members of KMA/METRI who offered me extensive data from Korea, Dr. Won-Tae Kwon, Nam Ouk-Kim, Dong-Il Lee, Young-Hwa Kim, and Jeong-Whan Lee. I am especially thankful to Dr. Hyo-Sang Chung, Director General of METRI and Dr. Chun-Ho Cho, Director of Forecasting Research Lab. of METRI. Owing to their help, a co-project between METRI and CAPS was conducted, which led to the continuing of my research here.

I gratefully acknowledge my friends in Korea and the US. I could get brand new energy from their encouragement. I want to give my special thanks to Mr. Dong Won Kim. Owing to his kind mind and gentle attitude, I can refresh my mind and can reduce a stress obtained from my research work. I also appreciate Mr. Ki-Young Kim, a former Director of KMA. He has always given me good advice and encouragement as a senior of my life. I will not hesitate to give my sincere thanks to Mr. Gi-Beom Jin and his wife Jae-Hee Kim. Although we don't have a relationship by blood, he and she are giving me and my family sincere care and constant consideration.

I am giving my deepest love and thanks to my younger brother Eui-Dong and his family, his wife, my lovely Min-Hyuk and Yon-Jin in Florida and to my youngest brother, Kyoung-Dong and his family, his wife, my lovely Man-Ji and Ja-Min in Tokyo. Although they live far from me, their consideration, encouragement, and love for me and my family allowed me to get where I am today. Now I want to express my thanks wholeheartedly to my wife and my kids, Tae-Hyuk and Chang-Hyuk. I know very well that I owe my achievement to my wife's assistance in no small measure. Most of all, I would finally like to express my deepest thanks from the bottom of my heart to my great parents. They have given me and our whole family endless love. I can only stand up here because of their endless love and devotion. I dedicate this tiny fruit to my great parents.

This research was supported by Korea Government Long Term Fellowship and by CAPS at OU under the grant of the co-projects between KMA/METRI and CAPS, and under the grant of ATM99-81130 from the National Science Foundation and a supplement grant thorough the NSF from Federal Aviation Administration.

TABLES OF CONTENTS

ACKNOWLEDGEMENT.....iv
TABLE OF CONTENTS..... vi
LIST OF TABLES.....ix
LIST OF FIGURES..... x
ABSTRACT..... xvii

Chapter 1 Introduction and Motivation..... 1

Chapter 2. Literature Review.....7
2.1 Basic Concepts and a Brief History of Data Assimilation..... 7
2.2 Data Assimilation Methods..... 11
2.2.1 OI (Optimum Interpolation) Analysis..... 11
2.2.2 Insertion Methods..... 14
2.2.2.1 Intermittent Data Assimilation 14
2.2.2.2 Continuous Data Assimilation (Newtonian Relaxation or Nudging)16
2.2.3 Advanced Data Assimilation..... 19
2.2.3.1 3D-VAR..... 23
2.2.3.2 4D-VAR..... 27
2.2.3.3 Kalman Filteri..... 28
2.3 Previous Studies of Heavy Rainfall Forecasting..... 30
2.3.1 Conceptual Models and Observation-Based Physical Analysis..... 30
2.3.2 Studies Based on Numerical simulation Midels..... 34

Chapter 3 The Chorwon-Yonchon Heavy Rainfall Event..... 40
3.1 Synoptic-Scale Aspects..... 40
3.2 Sub-Synoptic Scale Aspects..... 54
3.2.1 Q-vector Analysis..... 61
3.2.2 Radar Images..... 65

Chapter 4 Numercal Model and Experiment Design..... 71

4.1 The Numerical Model: Advanced Regional Prediction System (ARPS) 71
4.2 ARPS Data Assimilation System (ADAS) 75
4.2.1 ADAS Cloud Analysis 71
4.2.2 Diabatic and Moisture Initialization/Adjustment.....79
4.2.3 Correlation Ranges Used for the Observations in ADAS..... 80
4.3 Domain Setup and Computer Resources..... 82
4.4 NEXRAD (WSR-88D) Radar Data..... 85
4.5 Experiment Design.....87
4.6 The Data Assimilation Procedure: Incremental Analysis Updating (IAU) 92
4.6.1 The Scheme and Linear Analysis of IAU..... 92
4.6.2 Difference between IAU and Nudging..... 98
4.6.3 IAU in ADAS..... 101
4.7 ARPS Parameters for Radar Data Assimilation..... 102

Chapter 5 Results of 27-km and 9-km Resolution Experiments..... 107
5.1 Overview of the 27-km Grid Spacing Experiments.....107
5.1.1 Difference Between the Two First Guess Fields..... 108
5.1.2 21-hour Total Rainfall Forecast from the 27-km Grid Spacing Experiments 108
5.1.3 Synoptic Comparison.....111
5.2 Overview of the 9-km Grid Spacing Experiments.....112
5.2.1 Results Using the Old First Guess Field.....112
5.2.2 Results Using the New First Guess Field..... 115
5.2.3 Grid-Scale Precipitation and Parameterized Convection Precipitation 118

Chapter 6 3-km Resolution Experiments..... 121
6.1 Methodology of the 3-km Resolution Experiments.....121
6.1.1 Assessing the Relative Value of Reflectivity and Radial Velocity.....121
6.1.2 Assessing Different Data Assimilation Strategies.....122
6.2 Results of 3-km Resolution Experiments..... 127
6.2.1 Use of Different Background Fields to Initialize the Outermost Grid..... 127
6.2.2 Relative Impact of Reflectivity and Radial Velocity..... 131
6.2.3 Experiments with and without Radar Data..... 136
6.2.4 The Results Using Different Data Assimilation Strategies.....144

Chapter 7 Quantitative Verification of 3-km Grid Spacing Experiments..... 155
7.1 Methodology.....155
7.1.1 Bias Score..... 155
7.1.2 Threat Score.....157
7.1.3 Equitable Threat Score.....158
7.1.4 Mean Absolute Error.....159
7.1.5 Root Mean Square Error.....159
7.2 Quantitative Precipitation Estimation from WSR-88D Level II Data.....160
7.2.1 The Limitations of Observed Surface Rain Gauge Data..... 160
7.2.2 Estimation of Surface Accumulated Precipitation From WSR-88D Level II Data..... 162
7.2.3 Validation of Estimation of Surface Accumulated Precipitation from RV 1.0. 167
7.2.4 Radar Beam Blockage..... 173
7.3 Quantitative Verification of 3 km Grid Spacing Forecast..... 174
7.3.1 Impact of Radar Data Assimilation.....174
7.3.2 Use of Different Data Assimilation Strategies..... 186
7.4 Analysis of IAU for Experiment 03RAR_1h_rap..... 196
7.4.1 Forecasted and Observed Radar Reflectivity..... 197
7.4.2 Analysis Error 198
7.4.3 Origin of Erroneous Coastal Convection 210
7.5 Structure and Effect of Increments on Experiment 03RAR_1h_rap..... 216
7.6 Summary.....238

Chapter 8 Summary, Conclusions, and Future Work..... 242
8.1 Summary..... 242
8.2 Concluding Remarks and Future Work..... 247

APPENDIX A Using the ARPS WSR-88D Data Remapper..... 249
A.1 Introduction..... 249
A.2 Main Files and Link to Library..... 250
A.3 Building the Executable..... 250
A.4 Running the Program..... 252
A.5 Reading and Plotting the Output..... 255

REFERENCES..... 256

LIST OF TABLES

TABLE 1.1 Summary of natural disaster damage by cause in Korea (annual average) (From NDPCH, 2001). 5
TABLE 1.2 The damage conditions of the ten major floods by heavy rainfall until 2000 in Korea. (From NDPCH, 2001). 5

TABLE 2.1 Summary of the relationship nudging strength and damping (From Hoke and Anthes 1976). 20

TABLE 4.1 The correlation ranges associated with observations for ADAS with 3 km dx in the case of radar data assimilation.The configuration of domain and grid. 81
TABLE 4.2 The configuration of domain and grid. 83
TABLE 4.3 WSR-88D specification summary (from Kim 2000 and NCDC Radar Data Inventory's home page). 86
TABLE 4.4 Summary of All Experiments. 88
TABLE 4.5 Selected ARPS parameters for 3-km horizontal resolution. 104
TABLE 4.6 Selected ARPS parameters for 27-km horizontal resolution. 105
TABLE 4.7 Selected ARPS parameters for 9-km horizontal resolution. 106

TABLE 6.1 Predicted and observed maximum rainfall and the distances between the locations of maximum forecasted and observed rainfall position for the experiments with or without radar data. 138
TABLE 6.2 Predicted and observed maximum rainfall and the distances between the locations of maximum forecasted and observed rainfall position for different data assimilation strategies, especially for 03RAR_initrad, 03RAR_1t, and 03RAR_1h_rap experiments. 153
TABLE 6.3 Predicted and observed maximum rainfall and the distances between the locations of maximum forecasted and observed rainfall position for the experiments of different length of data assimilation window. 153

TABLE 7.1 Contingency 2 x 2 table for calculating Bias, Threat, and Equitable Threat scores. 156
TABLE 7.2 The statistics of parameters for radar data calibration used in the present study and used in the study of Wilson and Brandes (1979). 164
TABLE 7.3 Instatbility indices for each experiment and observation at Osan, 0000 UTC July 27. 183
Table 7.4 AWS and official observation stations used in the analysis error. A and S stand for AWS station and official surface station, respectively. 201

LIST OF FIGURES

FIG. 2.1 Pointwise selection as a strategy of OI data selection, where x1 and x2 are analysis points (From Bouttier and Courtier 2001)..... 15
FIG. 2.2 An example of the process of intermittent data assimilation (From Carr 2000) 21
FIG. 2.3 Schematic representation of Newtonian relaxation data assimilation via analysis-nudging technique (From Seaman 1990). 22
FIG. 2.4 A schematic representation of the variational cost function minimization (from Bouttier and Courtier 2001)..... 26
FIG. 2.5 An example of 4D-VAR assimilation in a numerical forecasting system (From Bouttier and Courtier 2001). 29
FIG. 2.6 The schematic diagram of conveyer belts. WCB and CCB stand for warm conveyer belt and cold conveyer belt. And, shaed area depicts the precipitation region (From online lecture note of University of East Anglia 2002)..... 33

FIG. 3.1 Surface weather charts at (a)0000UTC July 26, (b)1200UTC July 26, (c)0000UTC July 27, and (d)1200UTC July 27. 41
FIG. 3.2 850hPa weather charts at (a)0000UTC July 26, (b)1200UTC July 26, (c)0000UTC July 27, and (d)1200UTC July 27. 45
FIG. 3.3 500hPa weather charts at (a)0000UTC July 26, (b)1200UTC July 26, (c) 0000UTC July 27, and (d)1200UTC July 27. 47
FIG. 3.4 850hPa streamline and isotach at (a) 0000UTC July 26, (b) 1200UTC July 26, (c) 0000UTC July 27, and (d) 1200UTC July 27. 50
FIG. 3.5 Same as in Fig. 3.5 but for 200hPa. 52
FIG. 3.6 GMS-5 IR images at (a) 0000UTC July 26, (b) 0600UTC, (c) 1200UTC, (d) 1800UTC, (e) 0000UTC July 27, (f) 0600UTC, (g) 1200UTC, and (h) 1800UTC. 55
FIG. 3.7 Schematic of the relationship between the tropical cirrus cloud shield and the axis of dilation (confluence) (From Bluestein, 1993). 59
FIG. 3.8 Observed hourly rainfall (mm) recorded from 06 UTC July 26 to 03 UTC July 27 (a) and observed accumulated rainfall recorded from 16 UTC July 26 to 03 UTC July 27 (b) at Chorwon..... 60
FIG. 3.9 850hPa Q-Vector divergence at (a) 0000UTC July 26, (b) 1200UTC, (c) 0000UTC July 27, and (d) 1200UTC (kPa/m^{2}s, positive value means divergence). 63
FIG. 3.10 WSR-88D reflectivity (at the lowest elevation angle) obtained from the RKSG radar at (a) 1500UTC July 26, (b) 1600UTC, (c) 1700UTC, (d) 1800UTC, (e) 1900UTC, (f) 2000UTC, (g) 2100UTC, (h) 2200UTC, (i) 2300UTC, (j) 0000UTC July 27, (k) 0100UTC (l) 0200UTC, and (m) 0300UTC. 68

FIG. 4.1 Algorithm for the treatment of radar data in ADAS. 74
FIG. 4.2 Schematic diagram of the ADAS cloud analysis used in this study (shaded area indicates the ADAS cloud analysis scheme). 76

FIG. 4.3 Schematic diagram of the ADAS volumetric cloud fraction analysis used in this study (modified from Zhang 1999). 77
FIG. 4.4 Schematic diagram of the ADAS cloud water (q_c and q_i) content analysis used in this study (modified from Zhang 1999). 77
FIG. 4.5. The analysis and prediction domains and the terrain for the 27-km grid. .83
FIG. 4.6 Terrain used in (a) 9-km and (b) 3-km horizontal resolutions experiments, respectively. The filled circle and the filled retangle indicate the positions of Yonchon and Chorwon, respectively. 84
FIG. 4.7 Experiment design for control 27-km and 9-km resolution forecasts. 90
FIG. 4.8 Experiment design for 3-km resolution forecasts. 91
FIG. 4.9 The schematic of IAU technique. 93
FIG. 4.10 IAU response function for (a) ? = |R|, the amplitude of the response functions for three values of the growth-decay rate, s = 0 (neutral case, solid line), 1/s = 12 h (dashed line) and 1/s = 6 h (dotted line), (b) the phase ? of the response function R, for four cases, s = 0 (heavy solid line), 1/s = ±6 h (light solid line for growth, dashed line for decay), and 1/s = 12 h (dotted line) (From Bloom et al., 1996). 99

FIG. 5.1 Comparison of the surface wind field from observations at 06UTC July 26 with (a) the old first guess field (RDAPS 18-hour forecast initialized at 12UTC July 25) and (b) the new first guess field (RDAPS 6-hour forecast initialized at 00UTC July 26). Red and black arrows represent observed surface wind and the winds obtained from each first guess filed, respectively. 109
FIG. 5.2 Total predicted rainfall (mm) for 21 hours valid 03UTC July 27 for outer grid (a) for using old first guess field and (b) for using new first guess field. ... 110
FIG. 5.3 Forecasted 850 hPa height, temperature, wind field, and reflectivity at 0000 UTC July 27 for (a) 27R and (b) 27R_n. 113
FIG. 5.4 12-hour accumulated rainfall for (a) 09RNR, (b) 09RYR, and (c) 09RAR forecasts. ('C': Chorwon position, 'Y': Yonchon position, 'm': observed maximum position). 116
FIG. 5.5 12-hour accumulated rainfall for (a) 09RNR_n, (b) 09RYR_n, (c) 09RAR_n forecasts. ('C': Chorwon position, 'Y': Yonchon position, 'm': observed maximum position) 117
FIG. 5.6 12-hour accumulated rainfall for (a) grid-scale precipitation, (b) cumulus convection precipitation, and (c) grid-scale plus cumulus convection precipitation on 09RYR experiment. 120

FIG. 6.1 Experiment design for different data assimilation strategies; (a) 03RAR, (b) 03RAR_initrad, (c) 03RAR_1t, and (d) 03RAR_1h_rap. Each thick arrow indicates the radar data assimilation and the numbers in parentheses mean the data time. For example, AWS(1500) and radar(1551-1556) mean AWS data at 1500 UTC and one volume scan radar data for 5 minutes from 1551 UTC to 1556 UTC, respectively. 124
FIG. 6.2 Same as Fig. 6.1 but for (a) 03RAR_cent10, (b) 03RAR_cent5, and (c) 03RAR_cent20. 126

FIG. 6.3 Observed accumulated rainfall estimated from NEXRAD Level II data (a) 6 hour accumulated rainfall for 1500-2100 UTC and (b) 12 hour accumulated rainfall, 15-03UTC. Star, asterisk, filled triangle, and filled circle mean the positions of Pyoungtaek radar, Chowon, Yonchon, and observed maximum rainfall, respectively. 128
FIG. 6.4 Predicted accumulated rainfall for 12 hr valid at 0300 UTC July 27 for (a) 03RNR, (a') 03RNR_n, (b) 03RAR, and (b') 03RAR_n experiments. Left panels are the results using old first guess field and right panels are the results using new first guess field. 'c', 'y', and 'm' mean the positions of Chrowon, Yonchon, and the position of observed maximum rainfall, respectively. 129
FIG. 6.5 Predicted accumulated rainfall for 12 hr valid at 0300 UTC July 27 for (a) 03RYR, (a') 03RYR_ref, (b) 03ROR, and (b') 03ROR_ref experiments. Left panels are the results using both reflectivity and radial velocity and right panels are the results using reflectivity alone. 'c', 'y', and 'm' mean the positions of Chrowon, Yonchon, and the position of observed maximum rainfall, respectively. 133
FIG. 6.6 Predicted accumulated rainfall for 6 hr valid at 2100 UTC July 26 for (a) 03RNR, (b) 03RYR, (c) 03ROR, and (d) 03RAR experiments. 'c', 'y', and 'm' mean the positions of Chrowon, Yonchon, and the position of observed maximum rainfall, respectively. 134
FIG. 6.7 Predicted accumulated rainfall for 12 hr valid at 0300 UTC July 27 for (a) 03RNR, (b) 03RYR, (c) 03ROR, and (d) 03RAR experiments. 'c', 'y', and 'm' mean the positions of Chrowon, Yonchon, and the position of observed maximum rainfall, respectively. 135
FIG. 6.8 Time evolution of observed and predicted accumulated maximum rainfall from 1600 UTC (1 hour) July 26 to 0300 UTC (12 hour) July 27 for observation (dashed line with filled rectangles), 03RNR (dotted line with filled circles), 03RYR (solid line with open circle), and 03RAR (solid line with filled triangles) experiments. 138
FIG. 6.9 Observed and predicted radar reflectivity at 1900 UTC July 26 (4-hr forecast, 1 hour after finishing data assimilation for 03RAR experiment). (a) is observed horizontal reflectivity at lowest elevation angle (0.48°), (b) and (c) are the predicted horizontal reflectivity at 1.1 km height from sea level for 03RNR and 03RAR experiments, respectively. 139
FIG. 6.10 The reflectivity difference between forecasted and observed reflectivity (forecast – observation) for 03RNR (upper panels, a, d, and g), 03RYR (middle panels, b, e, and h), and 03RAR (lower panels, c, f, and i) experiments at 2100 UTC (left panels of first page, a, b, and c), 0000 UTC (right panels of first page, d, e, and f), and 0300 UTC (g, h, and i in second page). Red and blue color means over predicted and under predicted reflectivity, respectively. 140
FIG. 6.11 Predicted accumulated rainfall for 6 hr valid at 2100 UTC July 26 for (a) 03RAR, (b) 03RAR_initrad, (c) 03RAR_1t, (d) 03RAR-1h_rap, (e) assi_cent5, (f) assi_cent10, and (g) assi_cent20 experiments. 'c', 'y', and 'm' mean the positions of Chrowon, Yonchon, and the position of observed maximum rainfall, respectively. 145

FIG. 6.12 Predicted accumulated rainfall for 12 hr valid at 0300 UTC July 27 for (a) 03RAR, (b) 03RAR_initrad, (c) 03RAR_1t, (d) 03RAR-1h_rap, (e) assi_cent5, (f) assi_cent10, and (g) assi_cent20 experiments. 'c', 'y', and 'm' mean the positions of Chrowon, Yonchon, and the position of observed maximum rainfall, respectively. 147
FIG. 6.13 The reflectivity difference between forecasted and observed reflectivity (forecast – observation) for 03RAR (left panels, a, b, and c) and 03RAR_1h_rap (right panels, d, e, and f)) experiments at 2100 UTC (upper panels, a and d), 0000 UTC (middle panels, b and e), and 0300 UTC (lower panels, c and f). Red and blue colors mean over predicted and under predicted reflectivity, respectively. 154
FIG. 7.1 Observed accumulated rainfall for 12-hr from 1500 UTC July 26 to 0300 UTC July 27 made by the data of surface rain gauge at official statios and AWS of KMA. 161
FIG. 7.2 An example of the relationship between rainfall rate and radar reflectivity (from Short et al. 1990). 164
FIG. 7.3 Domain and grid of 3-km horizontal resolution and NEXRAD range. Each small rectangular means the grid with 3 km x 3km, while large rectangular including each small rectangular displays the domain of the experiment on 3 km horizontal resolution. Small circle and star indicate Chorwon position and NEXRAD position in Pyungtaek, respectively. 168
FIG. 7.4 Gauge-measured hourly rainfall at a weather station versus NEXRAD-estimated hourly rainfall at a grid which includes the station point from 1000 UTC July 26 to 0900UTC July 27 in (a) Chorwon, (b) Chunchon, (c) Seoul, and (d) Kangwha (G/R value means the ratio of gauge measured total rainfall to NEXRAD estimated total rainfall for this time period). 169
FIG. 7.5 Schematic for blockage problem (a) radar and topography and (b) the result of blockage problem. 171
FIG. 7.6 Verification domain (large rectangular) and erroneous area which is removed for the verification (small rectangular in the center of verification domain). 172
FIG. 7.7 Bias scores for accumulated rainfall forecast; (a) 3-hr accumulated rainfall from 1800 UTC to 2100 UTC July 26, (b) 6-hr accumulated from 1800 UTC July 26 to 0000 UTC July 27, and (c) 9-hr accumulated rainfall from 1800 UTC July 26 to 0300 UTC July 27. Thick dashed line with asterisk, solid line with filled triangle, solid line with filled diamond, and solid line with filled rectangular indicate 03RAR, 03RYR, 03RYR_ref, and 03RNR, respectively. And, the ts in x-axis stands for threshold. Namely, ts2.5 means the threshold with 2.5 mm. 177
FIG. 7.8 Same as in Fig. 7.6 except for threat scores (TS). 179
FIG. 7.9 Same as in Fig. 7.6 except for equitable threat score (ETS). 181
FIG. 7.10 Time evolution of domain maximum updraft from 1500 UTC July 26 to 0300 UTC July 27 (12 hours) for 03RNR (dashed line with opened diamond), 03RYR (solid line with filled diamond), and 03RAR (thick solid line with opened rectangular). 185

FIG. 7.11 Bias scores for accumulated rainfall forecast; (a) 3-hr accumulated rainfall from 1800 UTC to 2100 UTC July 26, (b) 6-hr accumulated from 1800 UTC July 26 to 0000 UTC July 27, and (c) 9-hr accumulated rainfall from 1800 UTC July 26 to 0300 UTC July 27. Thick dashed line with asterisk, solid line with filled rectangular, thick solid line with filled circle, dashed line with filled triangle, dashed line with filled diamond, solid line with opened diamond, and solid line with filled diamond indicate 03RAR, 03RAR_1t, 03RAR_1h_rap, 03RAR_initrad, 03RAR_cent10, 03RAR_cent5, and 03RAR_cent20 and 03RNR, respectively. And, the ts in x-axis stands for threshold. Namely, ts2.5 means the threshold with 2.5 mm. 189
FIG. 7.12 Same as in Fig. 7.11 except for threat scores (TS)..... 191
FIG. 7.13 Same as in Fig. 7.11 except for equitable threat scores (ETS)..... 193
FIG. 7.14 Mean Absolute Error from the forecasted and observed radar reflectivity for 03RAR_1h_rap (heavy solid line with filled circle), 03RAR (dashed line with filled rectangular), 03RYR (solid line with filled triangle), and 03RNR (dashed line with opened circle). U1600 means 1600 UTC and others are same as this. 195
FIG. 7.15 The reflectivity difference between forecast and observation (forecast minus observation) for 03RAR_1h_rap experiment at before IAU (left panels) and after IAU (right panels). 199
FIG. 7.16 Forecasted reflectivity from 03RAR_1h_rap versus observed reflectivity at (a) before 2nd IAU, 1730 UTC and (b) after 2nd IAU, 1740 UTC July 26..... 200
FIG. 7.17 Time evolution of the correlation between forecasted reflectivity by 03RAR_1h_rap and observed reflectivity. 202
FIG. 7.18 Temperature analysis error at (a) the first IAU period (1710 UTC and 1720 UTC), (b) the second IAU period (1730 to 1740 UTC), and (c) the third IAU period (1750 to 1800). 203
FIG. 7.19 Same as in Fig. 7.18 except for u-v vector. 205
FIG. 7.20 The domains for analysis (The filled circle indicates Osan position). 208
FIG. 7.21 Observations (red arrows and red characters) at 1800 UTC and ADAS analysis at 1700 UTC. 523 and 526 indicate the number of AWS stations and S stands for the official surface station (a:wind, b:air temperature). 209
FIG. 7.22 Surface horizontal reflectivity and surface wind vector at 1500 UTC July 26 (a) and 1700 UTC (b) simulated from 03RAR_1h_rap experiment..... 212
FIG. 7.23 Skew-T plot of sounding over a land position (a) and a sea position (b) near coastal are (Fig. 7.19 displays the exact land position and the sea position). 213
FIG. 7.24 Skew-T plot of sounding at Osan (the filled circle in Fig. 7.20) for observation and 03RAR_1h_rap (b). 214
FIG. 7.25 Schematic illustration of examination of analysis increments for 03RAR_1h_rap. 217
FIG. 7.26 The increments of the potential temperature between the analysis and the background (analysis –background) at 1710 UTC (a) and the difference of the potential temperature between the forecast at 1720 UTC and the forecast at 1710 UTC (b). The box in (b) will be used for zooming work. 219

FIG. 7.27 The increments of the potential temperature between the analysis and the background (analysis –background) at 1730 UTC (a) and the difference of the potential temperature between the forecast at 1740 UTC and the background at 1730 UTC (b). 220
FIG. 7.28 The increments of the qc between the analysis and the background (analysis – background) at 1710 UTC (a) and the difference of the qc between the forecast at 1720 UTC and the background at 1710 UTC (b). The box in (b) will be used for zooming work. 222
FIG. 7.29 The increments of the qc between the analysis and the background (analysis – background) at 1730 UTC (a) and the difference of the qc between the forecast at 1740 UTC and the background at 1730 UTC (b). 223
FIG. 7.30 The increments of the qr between the analysis and the background (analysis – background) at 1710 UTC (a) and the difference of the qr between the forecast at 1720 UTC and the background at 1710 UTC (b). The box in (b) will be used for zooming work. 224
FIG. 7.31 The increments of the qr between the analysis and the background (analysis – background) at 1730 UTC (a) and the difference of the qr between the forecast at 1740 UTC and the background at 1730 UTC (b). 225
FIG. 7.32 The increments of the w between the analysis and the background (analysis – background) at 1710 UTC (a) and the difference of the w between the forecast at 1720 UTC and the background at 1710 UTC (b). The box in (b) will be used for zooming work. 226
FIG. 7.33 The increments of the w between the analysis and the background (analysis – background) at 1730 UTC (a) and the difference of the w between the forecast at 1740 UTC and the background at 1730 UTC (b). 227
FIG. 7.34 The increments of the u between the analysis and the background (analysis – background) at 1710 UTC (a) and the difference of the u between the forecast at 1720 UTC and the background at 1710 UTC (b). The box in (b) will be used for zooming work. 228
FIG. 7.35 The increments of the u between the analysis and the background (analysis – background) at 1730 UTC (a) and the difference of the u between the forecast at 1740 UTC and the background at 1730 UTC (b). 229
FIG. 7.36 The difference of (a) w, (b) qr, (c) pt, (d) qc, and (e) u between the forecast at 1720 UTC and the background at 1710 UTC. 230
FIG. 7.37 Time evolution of the domain maximum qr and w in the 03RAR_1h_rap. Each data assimilation period indicates the periods of 130 min. (1710 UTC) to 140 min. (1720 UTC), 150 min. (1730 UTC) to 160 min. (1740 UTC), and 170 min. (1750 UTC) to 180 min., (1800 UTC) indicate the first, second, and third data assimilation period, respectively. Two different units of Y axis are used in this figure: 'g/kg' for qr and 'm/s' for w. 233
FIG. 7.38 (a) The ratio of 'the range value (max. minus min.) of the difference between forecast after IAU and the background before IAU (DR)' to 'the range value (max. minus min.) of the increment between analysis and background(IR)' for each variable. (b) The ratio of 'the range value (max. minus min.) of the difference between the forecast after IAU and the background before IAU for 2nd

and 3rd IAU periods' to 'the range value (max. minus min.) of the difference between the forecast after IAU and the background before IAU for 1st IAU period'. 237

ABSTRACT

One of the most effective tools for observing the atmosphere at fine scales is the Doppler radar. In recent years, considerable research has been directed toward using radar data as a component of numerical prediction model initialization, especially at the meso- and storm-scales. In Korea, where locally heavy rainfall events cause tremendous damage and loss of life each year, radar data could be expected to have a significant positive impact on numerical forecast quality. The first step toward testing this hypothesis has been undertaken in the present study, the purpose of which is to assess the impact of WSR-88D radar data assimilation in the numerical forecast of a deadly heavy rainfall event in Korea.

We use the CAPS Advanced Regional Prediction System (ARPS), in combination with WSR-88D Level II data gathered by the US Air Force radar in Pyoungtaek, Korea, to generate a series of multi-resolution forecasts. One-way grid nesting is employed, with a horizontal resolution of 27-km for the coarse outer grid, 9-km for the middle grid, and 3-km for the inner fine grid. Incremental analysis updating (IAU) is employed to assimilate radar reflectivity and velocity data on the finest resolution grid, with variations made to the length of the assimilation window, the number of assimilation cycles, the time of model initialization, and various model parameters such as boundary condition update times.

A total of twenty six forecasts, two at 27-km, six at 9-km, and eighteen at 3-km resolution, were conducted. Quantitative verification is made against available observations, including accumulated rainfall estimates from the WSR-88D calibrated against surface gauge observations using software from Vieux and Associates, Inc. Our results suggest that radar data assimilation leads to significant improvements in forecast quality as measure by threat, equitable threat, and other quantitative and qualitative measures, though position errors in the maximum observed precipitation persist. It was clear that *an experiment using three data inserts within a one-hour period, as compared to three inserts over a three hour period, produced the most skillful forecast.* IAU is shown to be a viable mechanism for radar data assimilation, particularly in its ability to remove incorrectly-forecasted convection. We found that *the positive impact of radar data for this particular event, using a grid spacing of 3 km, is approximately 3 to 4 hours process presented a limitation as forecast time increased.* The structure and physical impact of the increments were examined for the rapid data assimilation case as well. The potential temperature, water substance, and vertical motion were incorporated well into the model forecast when employing radar data assimilation using IAU. This also led to a positive feedback mechanism in the convective system.

Chapter 1
Introduction and Motivation

Heavy rainfall forecasting has long been one of the most scientifically challenging and societally important problems for meteorologists owing to the fact that associated flooding can produce significant human suffering and economic loss. For this reason, considerable attention has been given to this topic (e.g., Droegemeier et al. 2000). Indeed, during the past two decades in particular, numerous numerical simulation and observational studies have attempted to better understand the mechanisms associated with heavy rainfall as a means for improving its numerical prediction (references and a more detailed discussion are provided in Chapter 2).

It has long been recognized that the success of numerical weather prediction depends upon adequate representation of relevant physical processes, the use of suitable numerical solution techniques, and the quality of model initial and boundary conditions (e.g., Charney et al. 1969; Anthes 1977; Gal-Chen 1978; Fox-Rabinovitz 1996; Rogers et al. 2000). With regard to the latter, Aonashi (1993), among others, showed that a poor initial condition can lead to large spin-up error, i.e., even though precipitation may be present at the initial time, the model prediction may not produce precipitation for several hours. This, as well as position error, is especially critical for precipitation prediction. In order to improve the initial condition of numerical models, considerable attention has been given to improving data assimilation techniques, to using new sources of remotely sensed data such as satellite data (e.g. Krishnamutri et al. 1991; Puri and Davidson 1992; Kasahara et al. 1994), radar data (e.g., Wang and Warner 1988; Takano and Segami

1993; Crook 1994; Rogers et al. 2000), and profiler data (e.g. Crook and Sun 2002), and to using increasingly fine grid spacings – even down to the scale of individual convective elements (e.g., Birchfield 1960; Hemler et al. 1991; Belair et al. 1994; Warner and Hsu 2000).

In this regard, one of the most powerful tools for remotely sensing the atmosphere at fine scales is the Doppler radar. For example, the WSR-88D (NEXRAD) radar network (Next Generation Weather Surveillance Radar-1988 Doppler; e.g., Klazura and Imy 1993) was intended initially to improve severe weather warnings. However, it soon was recognized that radial wind and hydrometeor reflectivity data had the potential to greatly improve the prediction of mesoscale and stormscale weather (e.g., Lilly 1990; Droegemeier 1997). [We use the term stormscale to indicate flows that are highly non-hydrostatic and occur on temporal scales of one to a few hours. It may be viewed as synonymous with the meso-γ scale.]

Since the study of Brewster et al. (1995) for making real-time forecasts with a simple, direct use of radial velocity data, the Center for the Analysis and Prediction of Storms (CAPS) at the University of Oklahoma has had many ongoing efforts for using NEXRAD data in stormscale numerical forecasting. For example, techniques for retrieving all three components of wind given time series observations of radial velocity and reflectivity have been developed by CAPS scientists (Shapiro et al. 1995; Zhang and Gal-Chen 1996; Gao et al., 2001) and applied to actual storm cases (e.g., Weygandt et al., 2002a,b). A new 3-D variational single-Doppler velocity retrieval (SDVR) method using reflectivity and anelastic mass continuity equations as weak constraints also has been developed (Gao et al. 1999).

The encouraging results obtained by CAPS and others (Sun 1994; Sun and Crook 1994, 1997, 2001) are particularly important in light of the intense weather systems that occur frequently in southeast Asia. It is well known, for example, that heavy rainfall is the most hazardous and costly event among all kinds of weather disasters over the Korean Peninsula (National Disaster Prevention and Countermeasures Headquarters (NDPCH) 1999). Compared to other natural disasters, as shown in Table 1.1, the loss of life and property damage associated with heavy rainfall average 46% and 59%, respectively, each year, even though the frequency of heavy rainfall is only 35%. On average, annual heavy rainfall event causes about 343 million U.S. dollars in property damage and the loss of 213 lives. According to the Korea Meteorological Administration (KMA), a heavy rainfall event is defined as an observed rainfall amount greater than 100 mm for a single day at a given location, or greater than 150 mm for two consecutive days for at least one surface station. Table 1.2 shows the damage associated with ten recent major floods due only to heavy rainfall, excluding typhoons, in Korea.

Heavy rainfall occurs frequently over the Korean Peninsula during the summer season, especially in association with the Changma (East Asian summer monsoon). Lee et al. (1998) showed that three synoptic patterns typically are responsible for this yearly event. The first is associated with mesoscale convective systems (MCS) influenced by upper level troughs along the Changma front from late June through late July. Another is related to MCSs associated with an unstable air mass within the North Pacific subtropical high from middle August through early September, after the Changma season, and the third is associated with the influence of typhoons.

In light of the fact that Korea suffers significant loss from flooding nearly every year, considerable effort has been devoted to studying heavy rainfall forecasting, especially via numerical simulation. Whereas many studies have been performed successfully (e.g., Lee and Wee 1997), it is difficult to produce operational heavy rainfall forecasts because the size and lifetime of the most intense convective elements within MCSs, i.e., elements that produce extremely heavy rainfall locally, are relatively small and short-lived. Additionally, the complex topography in Korea makes heavy rainfall prediction an even greater challenge. An accurate hydrological forecasting as well as improved a meteorological forecasting should be considered in attempting to reduce severe damage caused by heavy rainfall, including the use of radar-based precipitation estimates. However, it is clear that a sophisticated stormscale numerical model, run at high resolution (1-2 km) with as much detail as possible in the initial conditions, likely will be needed to successfully predict heavy rainfall in Korea, and thus hopefully reduce the current loss of life and property.

Despite the importance of radar data for use in warning and numerical simulations, there remains to date no effort to include analyzed radar data in the data assimilation cycle of operational numerical weather prediction models in Korea. There are a number of reasons for this, including various limitations in the quality of KMA radar data and the lack of suitable data assimilation techniques. The first step in bringing Korean radar data into a numerical model for heavy rainfall forecasting has been undertaken within this study. The purpose is to assess the impact of NEXRAD data in the numerical forecast of a highly convective, localized heavy rainfall event in Korea, and to evaluate for small scale flows a relatively new data assimilation technique –

Table 1.1 Summary of natural disaster damage by cause in Korea (annual average) (From NDPCH, 2001).

	Heavy Rain	Typhoon	Others
Frequency (%)	35	32	32
Death and Missing (person)	213 (46 %)	125 (27 %)	79 (17 %)
Property Loss (million US $)	343 (59 %)	163 (28 %)	76 (13 %)

Table 1.2 The damage conditions of the ten major floods by heavy rainfall until 2000 in Korea. (From NDPCH, 2001).

Case	Date	Property loss (million US $)	Death & missing (person)	Max rainfall amount for a day (mm/day)	Major damaged area
1	July 31 – August 18, 1998	959	324	407.5 in Boeun	Whole nation
2	September 9 - 12, 1990	562	179	330.8 in Daegwan-ryoung	Central area
3	July 21 - 23, 1987	386	167	517.6 in Buyo	Central area
4	**July 26 - 28, 1996**	**383**	**29**	**268.0 in Cheolwon**	**Central area**
5	July 25 - 27, 1989	331	178	335.6 in Kwangju	Southern area
6	August 31 – September 4, 1984	192	189	314.2 in Sokcho	Central area
7	July 21 – 23, 1980	187	180	302.6 in Boeun	Central area
8	August 19 - 20, 1972	171	301	313.6 in Suwon	Central area
9	July 18 -20, 1925	151	517		Central area
10	August 19 – 20, 1991	116	70	308.5 in Chunchon	Central area

increment analysis updating - that originally was developed for large-scale flows. Stated more formally, we hypothesize that the assimilation of WSR-88D data into a high-resolution model will improve the prediction of a localized heavy rainfall event.

A 3-D atmospheric model, the Advanced Regional Prediction System (ARPS), in combination with NEXRAD Level II data gathered by the US Air Force Base in Pyoungtaek, Korea, is applied to the Chorwon-Yonchon heavy rainfall event (case 4 in Table 1.2). Details of data assimilation methods, including a brief history of data assimilation research and theory, and brief review of the previous studies of heavy rainfall events in Korea, are presented in Chapter 2. Chapter 3 provides a more detailed description of the Chorwon-Yonchon heavy rainfall event, while Chapter 4 details the numerical model and experiment design. The results of 27-km and 9-km resolution experiments are presented in Chapter 5, while Chapter 6 presents the results of 3-km resolution experiments, including qualitative verification against radar and other available data. Chapter 7 introduces the quantitative verification for the results of 3-km resolution experiments. Finally, Chapter 8 summarizes the results of this study and proposes future work.

Chapter 2
Literature Review

2.1 Basic Concepts and a Brief History of Data Assimilation

Numerical weather prediction (NWP) may be regarded as an initial-boundary value problem, the unique solution to which depends upon accurate specification of initial and boundary conditions as well as factors such as model grid spacing and appropriate representations of dynamical and physical processes (e.g., Harms et al.1992; Holton 1992; Rogers et al. 2000). An important component of NWP is data assimilation, or the process by which observations are combined with previous forecasts and other information to yield a unified, consistent description of the atmosphere, for use as a model initial condition.

Charney et al. (1969) put forth the basic concept of data assimilation by showing that satellite observations of the mass field could, through use of geostrophic or balance approximation, be used to infer the wind field and thus provide a complete set of initial conditions for a simple forecast model. This merging of objective analysis of new observational data simultaneously with the integration of a NWP model typically is regarded as four-dimensional data assimilation (FDDA) (e.g., Morel 1981). Even though two-dimensional (e.g., Rutherford 1973) and three- dimensional (e.g., Flattery 1970) frameworks in space can be used for data assimilation, FDDA is most often regarded as including the time dimension, usually in a sequential manner.

In general, it has been recognized that data assimilation has two, three, or four components. Holton (1992) classified data assimilation into two components, namely, objective analysis and data initialization. A three-component framework includes analysis, initialization, and the associated forecast (e.g. Bengtsson 1975; 1985; National Research Council 1991). Daley (1991) argued for a more detailed classification that includes quality control (e.g. Gandin 1988, Lorenc and Hammon 1988), objective analysis, initialization (e.g. Bourke and McGregor 1983; Lynch 1985; Satomura 1988), and the short forecast needed to prepare the background field for the next cycle (though not the entire forecast itself). Harms et al. (1992) also included quality control, objective analysis, and initialization as the parts of data assimilation.

Data assimilation in NWP has grown considerably since its inception some 30 years ago, and according to Daley (1997), the start of atmospheric data assimilation resulted from the development of subjective analysis procedures for producing hand-drawn weather maps. Although there exist generally two frameworks for data assimilation (e.g., Ide et al. 1997; Talagrand 1997; Sun 2002) -- sequential (e.g. Cohn 1997; Ghil 1997) and variational (e.g., Derber 1989; Courtier 1997; Le Dimet et al. 1997), another classification is suggested by historical evolution. If we regard subjective analysis as the first attempt at atmospheric data assimilation, then the evolution of data assimilation research can be traced from subjective analysis to advanced methods.

The first attempt at objective data assimilation was objective analysis (e.g. Cressman 1959; Gandin 1963; Barnes 1964; Eddy 1967; Kruger 1969; Daley 1991) and optimum interpolation (OI), the latter of which is a statistical approach that minimizes analysis error variance and provides the estimated values of atmospheric states

statistically by a weighted least squares fit to observations and a background field (e.g. Gandin 1963; Rutherford 1973; McPherson et al. 1979; Lorenc 1981; Daley 1991; Parrish and Derber 1992). An important aspect of OI is its use of linear multivariate relations between different meteorological variables, or a so-called multivariate algorithm (e.g. Rutherford 1973; Bergman 1979; Lorenc 1981; National Research Council, 1991). Even though OI has contributed significantly to the development of operational NWP, it sometimes suffers from considerable error owing to the use of only linear relations among model variables.

For example, model variables that are related via non-linear processes, such as satellite radiances and temperature, should be transformed to linearly-related variables before OI processing (e.g. Durand 1985; National Research Council, 1991; Chao and Chang , 1992; Courtier 1997). During the period over which objective analysis and OI were being developed and applied, Sasaki introduced a number of variational techniques (e.g. Sasaki 1969; 1970; Sasaki and McGinley 1980) following the seminal paper of Sasaki (1958). We note that his prominent studies of variational methods form the basis of today's advanced data assimilation methods such as 3D-VAR and 4D-VAR.

The next approach to data assimilation, which involves a time component, was data insertion. Research involving this strategy, which can be divided into intermittent data assimilation and continuous data assimilation, started in the mid-1970s (e.g., Bourke et al. 1985). Intermittent data assimilation is the analysis-forecast technique involving periodic re-analysis (Harms et al. 1992). It has been used by many operational meteorological centers, such as the European Centre for Medium Range Weather Forecasts (ECMWF, e.g. Bengtsson et al. 1982), the National Meteorological Center

(NMC, e.g. Kistler and Parrish 1982), the Japan Meteorological Agency (JMA, e.g. Kanamitusu et al. 1983), and the Australia National Meteorological Research Center (ANMRC, e.g. Bourke et al. 1982).

The process of continuous data assimilation by gradual insertion, commonly referred to dynamic relaxation or nudging, is one in which "the observed data are repeatedly inserted at each time step of the forward integration, using the relaxation technique for injection of data (Hoke and Anthes 1976)" (e.g. Lorenc 1976; Lyne et al. 1982). The Geophysical Fluid Dynamics Laboratory (GFDL, Stern and Ploshay 1983) and United Kingdom Meteorological Office (UKMO, Bell 1983) used this scheme as the basis for data assimilation (Bourke et al. 1985). It is important to note, as reported by Bourke et al. (1985), that continuous data assimilation is usually multivariate when all dynamic variables are analyzed simultaneously.

More recently, data assimilation approaches involving variational methods or optimal control theory have been developed and are being used operationally (e.g., Anderson et al. 1998). They can, from a basic point of view, be divided into three genre (Schlatter et al. 1998): three-dimensional variational methods (3D-VAR), four-dimensional variational methods (4D-VAR), and Kalman Filtering (KF). Both KF and 3D-VAR/4D-VAR seek to minimize, over a given time interval, the distance in phase space between a system trajectory, constrained by model dynamics, and existing data (Ghil and Malanotte-Rizzoli, 1991). Since Sasaki (1969) showed that data assimilation can easily incorporate dynamical constraints via the use of variational approaches, numerous applications of this concept have taken place, including the pioneering study by Lewis (1972), in which the thermal wind and hydrostatic equations were used as

constraints. This study led to numerous others, including work by Derber (1985) in the context of the so-called adjoint method (Harms et al. 1992).

Historically, Kalman filtering has seen somewhat less use since the early studies by Kalman (1960), Kalman and Bucy (1961), Jones (1965), Petersen (1973), Ghil et al. (1979), and Bucy and Joseph (1987), though is becoming more popular as computing capabilities increase. A more detailed and scientific description of 3D-VAR, 4D-VAR, and Kalman Filtering, along with nudging, will be presented in the next section.

The study of data assimilation began with simple, somewhat idealized simulations and then progressed to the use of more physically complete models with real data (e.g., Kasahara 1972; McPherson 1975). With regard to data, assimilation research has developed from using conventional synoptic data to various sources of remotely sensed data such as satellite data (e.g., Krishnamutri et al. 1991; Puri and Davidson 1992; Kasahara et al. 1994) and radar data in mesoscale models (e.g., Wang and Warner 1988; Takano and Segami 1993; Aonashi 1993).

2.2 Data Assimilation Methods

2.2.1 OI (Optimum Interpolation) Analysis

Optimum (or Optimal) Interpolation (OI) is a minimum variance analysis method that seeks to minimize the mean square error between the analyses and observations using the statistical covariance of observation errors and errors in the background field (also known as the 'first guess') (Bourke et al. 1985; Daley 1991). OI has a fundamental hypothesis that only a few observations for each model variable are important to be

determined the analysis increments (Bouttier and Courtier 2001). Bourke et al. (1985) listed four factors which must be considered in OI:

(1) the spatial distribution of observations related to each other and to grid points;

(2) the characteristics of the error associated with different observing systems;

(3) through the first guess field and the forecast error covariance function, the available information obtained from earlier data, and;

(4) the quasi-geostrophic and hydrostatic relations among variables.

The mathematical concept of OI can be expressed via the following interpolation equations, which are presented by Bouttier and Courtier (2001) and Schlatter et al. (1998).

Let

$$\mathbf{x}_a = \mathbf{x}_b + \mathbf{K}(\mathbf{y}_o - \mathbf{H}(\mathbf{x}_b)), \tag{2.1}$$

$$\mathbf{K} = \mathbf{B}\mathbf{H}^T(\mathbf{H}\mathbf{B}\mathbf{H}^T + \mathbf{R})^{-1}, \tag{2.2}$$

where

$\mathbf{x}_a$ is the best (optimal) analysis vector

$\mathbf{x}_b$ is the background vector (first guess)

$\mathbf{K}$ is the weight matrix of the analysis

$\mathbf{y}_o$ is the observation vector

$\mathbf{H}$ is an observation operator (forward operator: this operator transforms the backround into the form of the observations)

$\mathbf{B}$ is the covariance matrix of the background errors

$\mathbf{R}$ is the covariance matrix of the observation errors

Note that $(\ )^T$ and $(\ )^{-1}$ represent the transpose and inverse of a matrix or vector, respectively. The OI seeks to obtain an algebraic simplification of the computation of the weight matrix **K** in Eq. 2.1 and 2.2. In OI, as shown in Eq. 2.1 and 2.2, the analysis increments ($\mathbf{x}_a$-$\mathbf{x}_b$) are equal to **K** times the background departure ($\mathbf{y}_o$-$\mathbf{H}(\mathbf{x}_b)$). To obtain **K** (Bouttier and Courtier 2001), we need

(1) the covariance of the background errors between the model variable **x** and the model state interpolated at the observation points ($\mathbf{BH}^T$),

(2) the sub-matrices of the background and observation error covariance formed by the restrictions of $\mathbf{HBH}^T$ and the covariance matrix of the observation errors, **R**, to the selected observations,

(3) to invert the positive definite matrix formed by the restriction of ($\mathbf{HBH}^T$+**R**) to the selected observations, and

(4) to multiply $(\mathbf{HBH}^T+\mathbf{R})^{-1}$ by $\mathbf{BH}^T$.

Bouttier and Courtier (2001) presented a detailed explanation regarding the roles of the background error covariance **B** and the selection of observations in OI. According to their review, OI should have the covariance matrix of the background error **B** as a model that can be applied to pairs of model and observed variables and the pairs of observed variables. They also noted that **B** usually depends upon the scheme used for the empirical autocorrelation function, e.g., Gaussian or Besssel, along with any assumed balances, such as hydrostatic balance. For the selection of observations in OI, they note that all observations having a significant weight (a significant background error covariance $\mathbf{BH}^T$) should be selected. However, only the observations near the model grid points can be selected since the background error covariances are presumed to be small

over large distances. In light of computational costs, this limited selection of observations at each time can be economical.

Fig. 2.1 depicts a common example of data selection in OI. This strategy, or so-called 'pointwise selection', assumes that each analysis point (x_1, x_2) strongly depends on the observations located in a small nearby vicinity. Thus, the analysis field can be intermittent, not continuous, in space since the observations used for the analysis at two neighboring points, x1 and x2, are usually different.

Though OI is relatively simple and economical, it has the drawback that numerous errors can occur in the analysis fields since different sets of observations are used in different parts of the model state. Further, it is very hard to see consistency between small and large scales of the analysis (Lorenc 1981; Bouttier and Courtier 2001).

2.2.2 Insertion Methods

2.2.2.1 Intermittent Data Assimilation

One of the most valuable yet simple data assimilation techniques developed in the mid 1980s is the so-called intermittent strategy, which is one general category, along with continuous assimilation, in the general context of insertion assimilation methods. In intermittent assimilation, all observational data within a time interval (window) are used at a single time to correct the forecast made from the previous analysis (Bengtsson 1975; Bourke et al. 1985; Ghil and Malanotte-Rizzoli 1991). According to Bourke et al. (1985), "the intermittent method of assimilation ignores the asynoptic error associated

with grouping the data into time block of forecasting period and relies entirely on the prediction model capability to coordinate the data in the time domain."

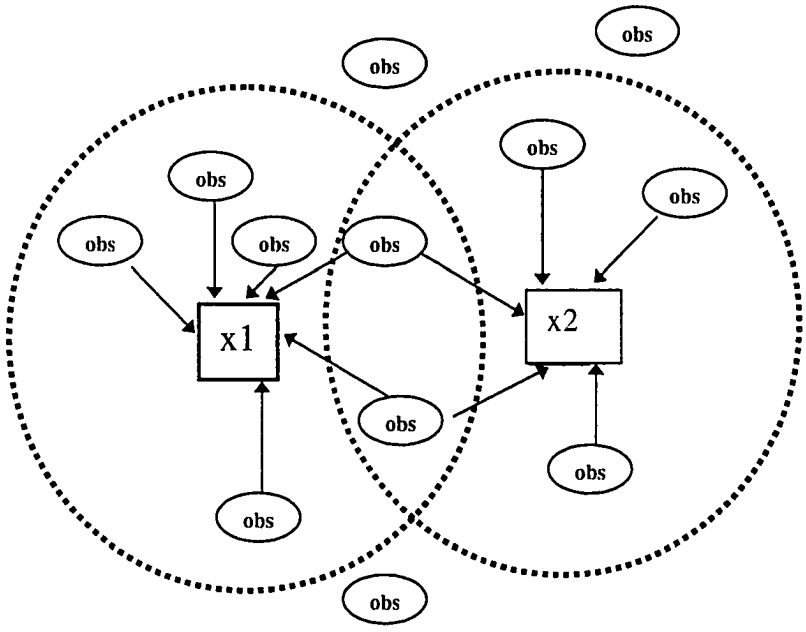

Fig. 2.1 Pointwise selection as a strategy of OI data selection, where x1 and x2 are analysis points (From Bouttier and Courtier 2001).

Fig. 2.2 shows an example of intermittent data assimilation. Operational forecasts typically are started at main observational (synoptic) times, 00UTC and 12UTC. Each 3-hr analysis is made from new observations, which provide corrections to the background forecasts. This process leads to a relatively smooth transition from one forecast to another, and also introduces less noise owing to the changes to the model values imposed by the analysis (Carr 2000). The forecast should be updated new data at each analysis time, and then combined and blended with them (Ghil and Malanotte-Rizzoli 1991). As shown in Fig. 2.2 and mentioned by Carr (2000), the 3-hr error for the background field at 12UTC, obtained from the analysis at 09UTC, should be less than the error associated with a 12-hr forecast from the 00UTC analysis

2.2.2.2 Continuous Data Assimilation (Newtonian Relaxation or Nudging)

One of the simplest and most widely used techniques of continuous data assimilation is Newtonian relaxation, or more simply "nudging", which is a method of dynamic relaxation (e.g. Haltiner and Williams 1980; Bao and Errico 1997; Kalnay 1998). Since Kistler (1974) first applied nudging in his M.S. thesis, many researchers have used this method as a data assimilation tool in the U.S. (e.g. Hoke and Anthes 1976; Ramamurthy and Carr 1987, 1988; Wang and Warner 1988; Wang 2001), in Europe (e.g. Davies and Turner 1977; Lorenc et al. 1991), in Japan (e.g. Kanamitusu et al. 1983), and in Australia (Bourke et al., 1982).

In nudging, model variables from one or more of the prognostic equations are nudged gradually toward observations, or a gridded analysis, via forcing terms that are added to the equations and calculated at each time step during model integration (Haltiner

and Williams 1980; Schlatter 1988; Seaman 1990). Thus, the main objectives of nudging are to harmonize data and model and to minimize the noise generated by gravity waves.

Haltiner and Williams (1980) summarize briefly the process of nudging in three steps. The first step involves specifying the initial condition during a pre-forecast period T at time t_0-T, where t_0 is the starting time of the new forecast. The second step involves performing the pre-forecast or assimilation integration from (t_0 – T) to t_0 by including extra terms in the model equations to force the variables during the preforecast toward the observations. In the last step, the actual forecast is generated from the initial time, t_0, after dropping the forcing or nudging terms.

To illustrate the specifics of the nudging method, let α be any prognostic variable of the model, with its governing equation written as (largely following the descriptions of Haltiner and Williams 1980; Schlatter 1988)

$$\frac{\partial \alpha}{\partial t} = F + G(\alpha,t)\varepsilon(\alpha^0 - \alpha), \tag{2.3}$$

where the term on the left hand side of this equation represents the local tendency, F is the model forcing, and the final term on the right hand side of the equation is the nudging term. $G(\alpha,t)$ is a non-negative nudging coefficient, ε is the analysis weight factor with a value ≤ 1, and α^0 is the best estimated grid point value from observations. Schlatter (1988) notes that the nudging term depends upon time since it forces the model every time step. He also explains that the nudging term should be large enough to affect the model solution, though not so large that it overwhelms other terms in the equations. Considering the horizontal equation of motion, for example, the nudging term may be larger than the vertical advection term, as large as the horizontal advection term, and smaller than pressure gradient term or Coriolis terms.

To better understand the nudging process (largely following the descriptions of Haltiner and Williams 1980), equation 2.3 can be simplified under the assumption that F is zero, G is constant, and ε is unity. This yields

$$\frac{\partial \alpha}{\partial t} = G(\alpha^0 - \alpha), or$$
$$\alpha = \alpha_0 e^{-Gt} + Ge^{-Gt}\int_0 e^{Gt}\alpha^0 dt \quad , \tag{2.4}$$

where α_0 is the value of α at t = 0, the beginning of the pre-forecast period. In order to obtain a more simplified solution to equation 2.4, first assume that α^0 is a constant toward which α is nudged. Then, the solution of equation 2.4 is

$$\alpha = \alpha^0 + (\alpha_0 - \alpha^0)e^{-Gt} \tag{2.5}$$

Note that α approaches exponentially the grid value, α^0, obtained from observation as time evolves. If we now assume that the observations vary linearly with time, i.e. $\alpha^0=\alpha_0{}^0+at$, then the solution becomes

$$\alpha = \alpha^0 + (\alpha_0 - \alpha_0^0)e^{-Gt} - (a/G)(1-e^{-Gt}) \tag{2.6}$$

The second term on the right hand side means that the existing initial error difference is damped to zero as time passes. However, the last term is damped to (-a/G), not to zero. In other words, α can at most approach α^0, the observationally-determined value, only to within the constant a/G, the ratio of the change rate of α^0 with time to the nudging coefficient.

Hoke and Anthes (1976) studied the relationship between the nudging coefficient and the damping of waves. They did not impose geostrophic balance and considered that all of the variables were unknown. They obtained interesting results for strong (G = 10^{-3} sec^{-1}) and moderate (G = 10^{-4} sec^{-1}) nudging coefficients for either winds or geopotential

using a typical midlatitude value of Coriolis force and a horizontal length of 10^3 m, corresponding to an internal gravity wave mode. Stationary and oscillating waves of both long wave or short wavelengths were taken into account, and winds were divided into rotational and divergent components. Table 2.1 shows the summary of their results.

Seaman (1990) depicted, in schematic form, the nudging technique (Fig. 2.3). As shown in this figure, pre-calculated analyses are interpolated in time and applied at each time step during integration period, say from 0000UTC to 12000UTC, for the assimilating model. The pre-calculated analyses are also prepared over a limited area, with asynoptic observed data between the complete analyses at 0000UTC and 1200UTC.

Although nudging lacks a solid theoretical foundation compared to advanced methods of data assimilation, it continues to be used and has a number of advantages (Schlatter 1988):

(1) relatively economical

(2) balance can be maintained in the model

(3) asynoptic data (e.g., radar data) as well as synoptic data can be incorporated at the appropriate time

(4) it is easy to accommodate physical processes in the model.

2.2.3 Advanced Data Assimilation

As mentioned in section 2.1, more advanced techniques exist for data assimilation. A three –dimensional variational (3D-VAR) method is not technically an assimilation process in itself. However, we are now introducing the 3D-VAR method as a more advanced technique for the data assimilation since the dynamic constraints in 3D-VAR can make the analysis more compatible with a specific model or scale of motion

and the 3D-VAR method has been largely used as an important tool of data assimilation techniques. Following Schlatter et al. (1998), Bouttier and Courtier (2001), and Sun (2002), we mainly describe the basic aspects of three-dimensional variational (3D-VAR) assimilation since other advanced methods, such as four dimensional variational (4D-VAR) assimilation and Kalman Filtering (KF), can be considered extensions of 3D-VAR.

Table 2.1 Summary of the relationship between nudging strength and damping (From Hoke and Anthes 1976)

		Stationary wave		Oscillating wave	
		long	short	long	short
Strong Nudging ($G=10^{-3}$ sec^{-1})	total wind	*poor damping*	damped well	damped well	damped well
	rotational wind	damped well	damped well	*poor damping*	*poor damping*
	geopoten-tial	damped well	*poor damping*	*poor damping*	damped well
Moderate Nudging ($G=10^{-4}$ sec^{-1})	total wind	*poor damping*	damped well	damped well	damped well
	rotational wind	*poor damping*	damped well	damped well	damped well
	geopoten-tial	damped well	*poor damping*	*poor damping*	damped well

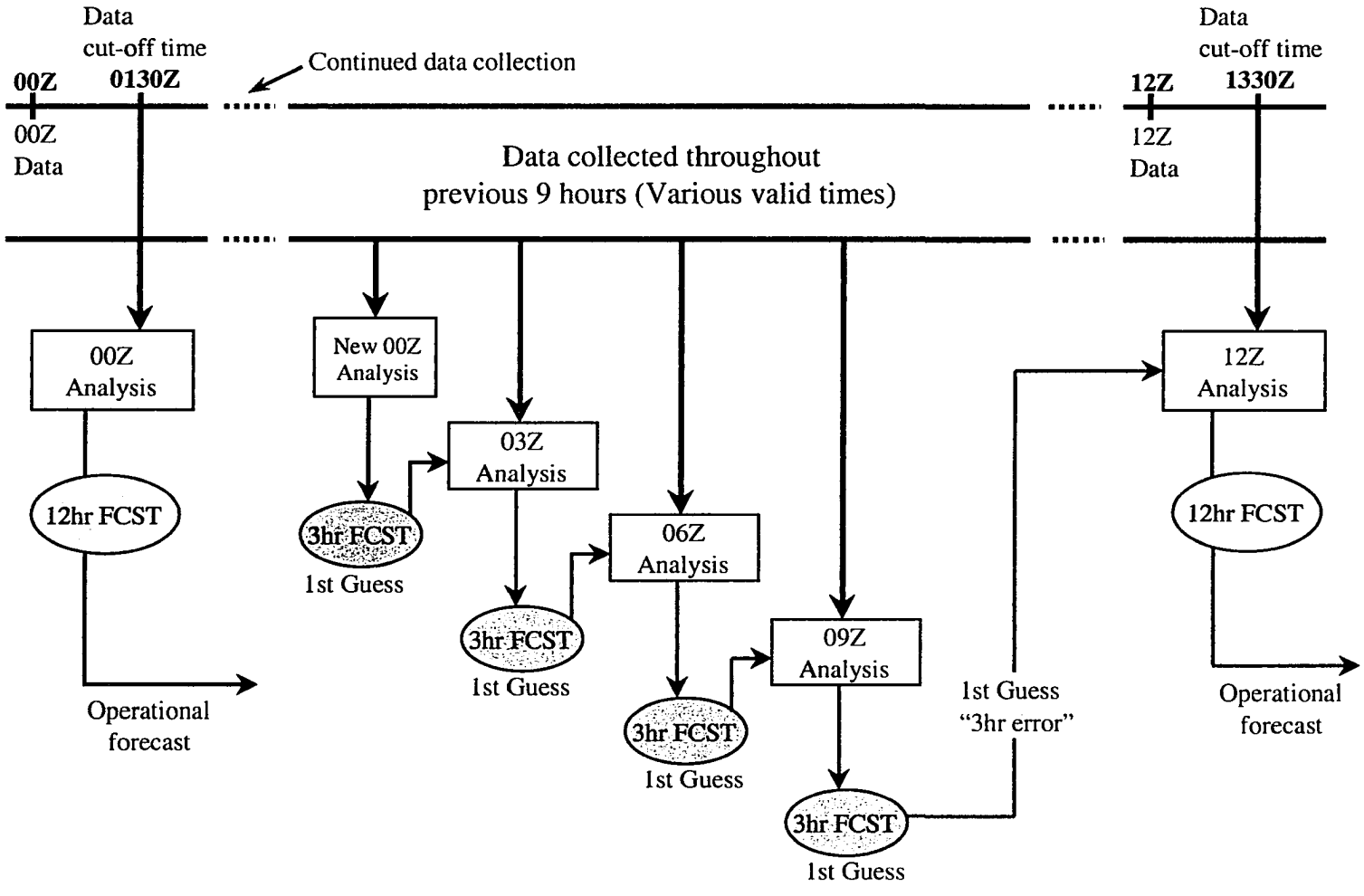

Fig. 2.2 An example of the process of intermittent data assimilation (From Carr 2000)

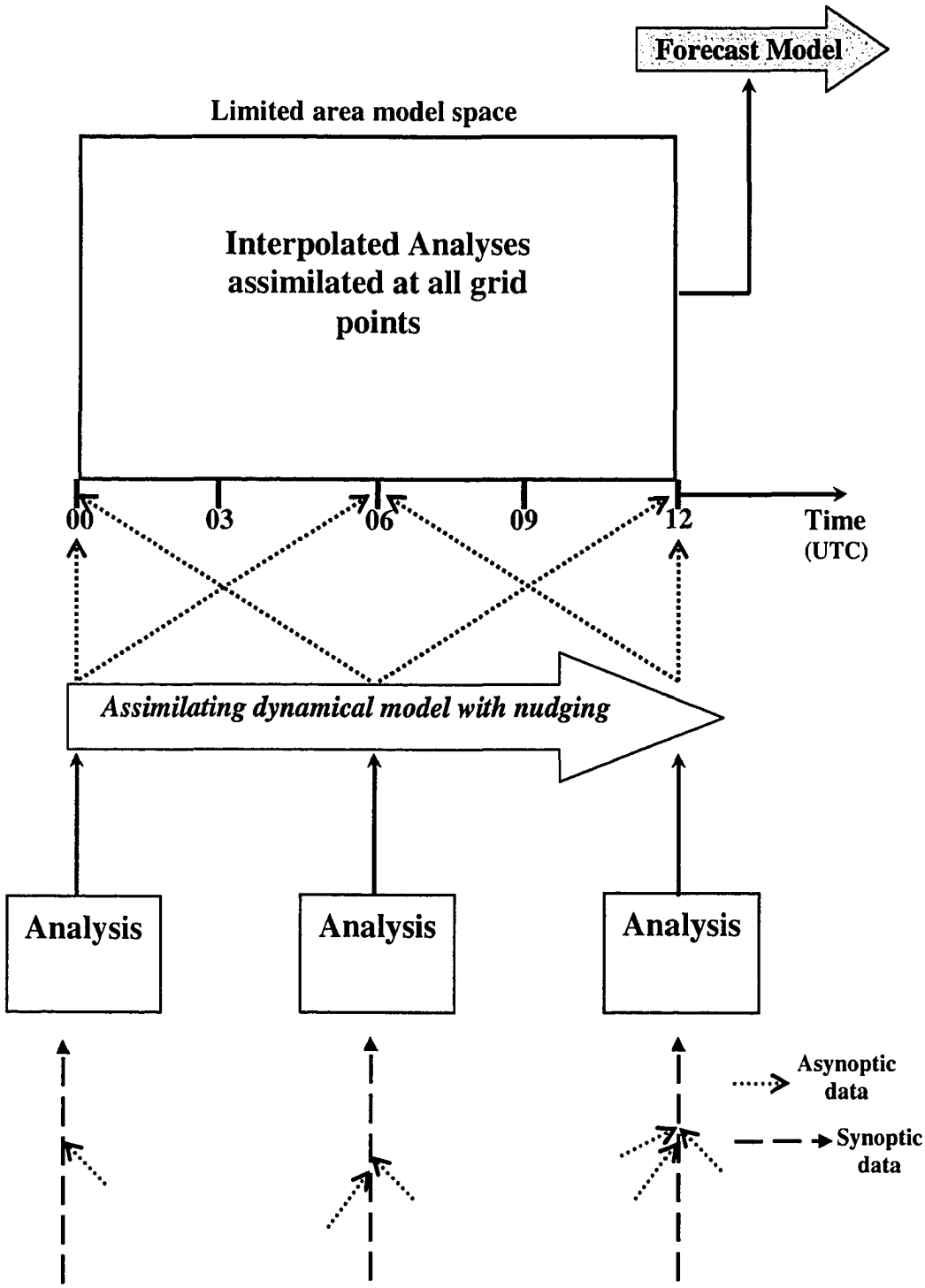

Fig. 2.3 Schematic representation of Newtonian relaxation data assimilation via analysis-nudging technique (From Seaman 1990)

2.2.3.1 3D-VAR

3D-VAR has been used in storm-scale data assimilation (e.g., Gao et al. 1999a 1999b) and also applied to the large scale atmosphere (e.g., Andersson et al. 1998). It is especially popular at many operational weather centers even though emphasis for the future is on 4D-VAR and KF. Several assumptions are made in applying 3D-VAR; 1) unbiased analysis and observations, 2) normally distributed errors, and 3) no correlation between the errors in the observations and the errors in the forecast and the dynamical constraints. With these assumptions, which are not always valid, the key attribute of 3D-VAR is to avoid calculating the analysis weight matrix **K** directly via minimizing a cost function **J**. This cost function is a measure of the total distance of the analysis from the prior information whose sources are weighted by the inverses of their associated error covariances (Schlatter et al. 1998; Bouttier and Courtier 2001). The cost function can be defined as

$$\mathbf{J}(\mathbf{x}) = 1/2\ \{(\mathbf{x}-\mathbf{x}_b)^T\mathbf{B}^{-1}(\mathbf{x}-\mathbf{x}_b) + (\mathbf{y}_o-\mathbf{H}(\mathbf{x}))^T\mathbf{R}^{-1}(\mathbf{y}_o-\mathbf{H}(\mathbf{x})) + \mathbf{C}(\mathbf{x})^T\mathbf{D}^{-1}\mathbf{C}(\mathbf{x})\}, \qquad (2.7)$$

where **x** is the analysis vector, **C** is a set of constraints, **D** is the error covarinace associated with the constraints, and other notation is same as in Eq. 2.1 and 2.2 of section 2.2.1. Equation 2.7 also may be written as

$$\mathbf{J} = \mathbf{J}_b + \mathbf{J}_o + \mathbf{J}_c, \qquad (2.8)$$

where $\mathbf{J}_b$, $\mathbf{J}_o$, and $\mathbf{J}_c$ are referred to as the background term, the observation term, and the constraint term, respectively. Following Schlatter et al. (1998), these terms are explained in detail below.

a. The background term

The background term is a measure of the fit between the analysis and the background. The background error covariances **B** can be regarded as the associated error statistics for the optimal estimation. Thus, if a significant change occurs in the background state, the error covariances **B** have to be modified to reflect the associated changes in statistical properties. Note that the quality of the analysis strongly depends on the weighting implied by the background error covariance **B**. However, the use of background error covarinace **B** cannot be a good approximation in mesoscale situations whose states usually change rapidly (Schlatter et al. 1998).

b. The observation term

The observation term represents a measure of the fit between the analysis and the observations. The observation operator (forward operator) **H** propagates the model variables to the observed variables, like the relationship between u, v, w and the radial velocity v_r obtained from radar observations (Sun 2002). The relative weighting of observations in reference to other observations, the background, and the constraints is determined by the covariance matrix of the observation errors (including representativeness errors) **R**. The representativeness error is a significant component of this matrix. In general, **R** is defined empirically and assumed to be diagonal, even though this assumption is invalid when correlated errors are present.

c. The constraint term

This constraint term represents a measure of the fit to constraints, which can consist of dynamical constraints, physical constraints, or the constraints imposed by

statistical relationships among variables. Similar to the covariance matrix of observation error **R,** the error covariance matrix associated with the constraints **D** determines the relative weighting of a specific constraint with respect to the other constraints and with the respect to the background and the observations.

3D-VAR is the iterative attempt to minimize the cost function **J** in Eq. 2.7 by using nonlinear minimization. The minimization algorithms require the computation of the gradient of **J**, which is given by

$$\nabla \mathbf{J}(\mathbf{x}) = \mathbf{B}^{-1}(\mathbf{x}-\mathbf{x}_b) - \mathbf{H}^T\mathbf{R}^{-1}(\mathbf{y}_o-\mathbf{H}(\mathbf{x})) + \mathbf{C}^T\mathbf{D}^{-1}\mathbf{C}(\mathbf{x}) \qquad (2.9)$$

The minimization process ceases when the norm of this gradient $\|\nabla \mathbf{J}(\mathbf{x})\|$ decreases by a predefined amount. Figure 2.4 depicts a schematic of the geometry of minimization. In this figure, the cost function is parabolic, and the minimum is located at the best analysis $\mathbf{x}_a$. The control variable, or analysis **x**, is moving to areas where the cost function is a minimum (Bouttier and Courtier 2001).

Courtier et al. (1998) discussed the merits and shortcomings of 3D-VAR and noted that it has two main advantages. One is its conceptual simplicity and the other is the ease of using complex observation operators, including even those which are weakly non-linear. However, 3D-VAR requires specific model design for obtaining the matrix of background errors **B** that can properly define background covariances for all pairs of model variables.

Overall, 3D-VAR can be summarized as having the following three properties; (1) iteratively minimizing the cost function defined at a single time, (2) the numerical model is not used in the analysis, and (3) the covariance matrix of the background errors B is modeled using simple functions and does not vary with time.

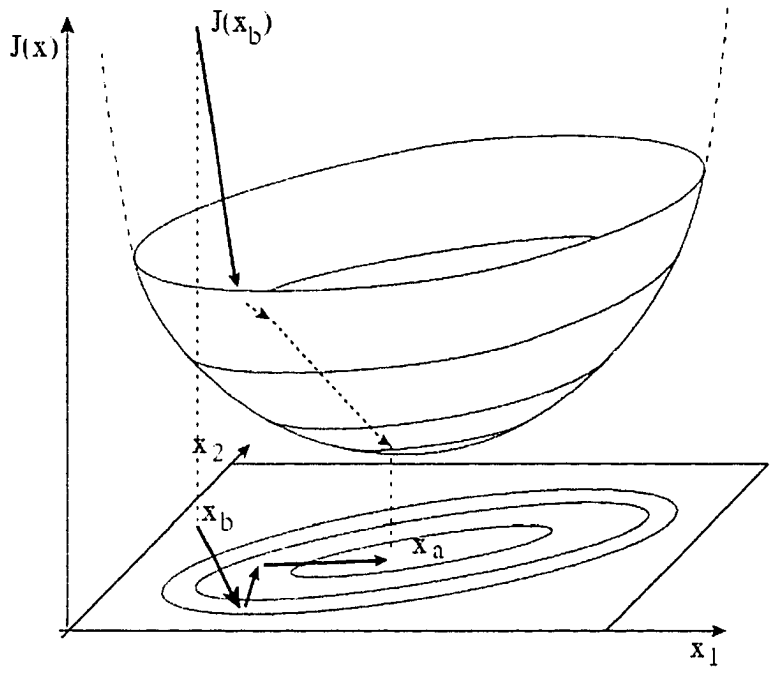

Fig. 2.4 A schematic representation of the variational cost function minimization (From Bouttier and Courtier 2001).

2.2.3.2 4D-VAR

4D-VAR can be regarded as an extension or generalization of 3D-VAR. In it, observations are distributed within a time window (t_i or $0 \le i \le n$) and the analysis is performed over the same time interval. Thus, similar to the cost function in 3D-VAR, that in 4D-VAR is given by

$$\mathbf{J}(\mathbf{x}) = (\mathbf{x} - \mathbf{x}_b)^T \mathbf{B}^{-1} (\mathbf{x} - \mathbf{x}_b) + \sum_{i=0}^{n} (\mathbf{y}_i - \mathbf{H}(\mathbf{x}_i))^T \mathbf{R}^{-1} (\mathbf{y}_i - \mathbf{H}(\mathbf{x}_i)) + \mathbf{J}_c , \qquad (2.10)$$

where the subscript i means the i-th time step. Figure 2.5 shows an example of 4D-VAR, in which the assimilation of the most recent observations is performed at every time interval within the assimilation window, using a segment of the previous forecasts as a background. This performance repeats updating the initial model trajectory to get subsequent forecast (Bouttier and Courtier 2001).

According to Weygandt et al. (2002a), the advantages of 4D-VAR are use of the full model equations as constraints, simultaneous use of all observations in their original form, the possibility of retrieving unobserved fields, and ease of finding optimal values for model parameters. They also pointed out four difficulties of 4D-VAR. First, it is difficult to obtain a unique solution owing to the strong nonlinearity of the problem. Second, the construction of accurate tangent linear and adjoint models is made difficult by the many nondifferentiable switches (on and off) found in moist physical parameterizations (Xu 1996). Third, the use of full-model equations as a strong constraint leads to the neglect of model errors. The final difficulty is the high cost of computation for minimizing the cost function. Compared to 3D-VAR, overall, 4D-VAR has the following characteristics; (1) the cost function in 4D-VAR is defined for a

specific time window, (2) the numerical model is used as a strong constraint in the analysis to link the model states at different times, (3) and 4D-VAR can work under the assumption that the forecast model used in the assimilation is perfect.

2.2.3.3 Kalman Filtering

Kalman Filtering (KF) is a key tool of estimation theory and has become increasingly popular in recent years as many scientists (e.g. Todling and Cohn 1994; Houtekamer and Mitchell 1998; Anderson 2001) have applied it to meteorological problems based on the general theory of Kalman (1960) and Jazwinski (1970).

The analysis equations used in KF are same as those in least-squares analysis method, except for differences in notation. The background error covariance **B**, the analysis error covariance **A**, and the background state $\mathbf{x}_b$ in least square analysis theorem are respectively replaced by $\mathbf{P}_f$, $\mathbf{P}_a$, and $\mathbf{x}_f$ in the analysis equations of KF to show that the background is now a forecast (Talagrand 1997; Bouttier and Courtier 2001). Schlatter et al. (1998) summarized the characters of KF as follows:

> "The background error covariance B is estimated by using the model equations to extrapolate forward in time the analysis error covariance while including a model error covariance term. The major differences from 4D-VAR are that the model is assumed to be imperfect, and, since the algorithm is sequential, theoretically the analysis interval can extend arbitrarily far back in time. These differences should give KF an advantage over variational approaches in meteorological data assimilation. However, application of the complete KF in this context is very difficult because of the huge

computational demand for prediction of the covariance matrix, inadequately defined forecast error covariances, and nonlinear effects of the dynamics and physics in the assimilation system. It is very possible that eventually the computationally feasible analysis technique will be a hybrid of the 4D-VAR and KF techniques. The extrapolation of error covariance forward in time in KF is extremely important. If no data are incorporated, the prediction of the error covariance is a measure of model forecast skill. Likewise, with the inclusion of the data, the error covarinace provides a measure of the amplitude and structure of the expected error in the analysis and can be used in initializing ensemble predictions."

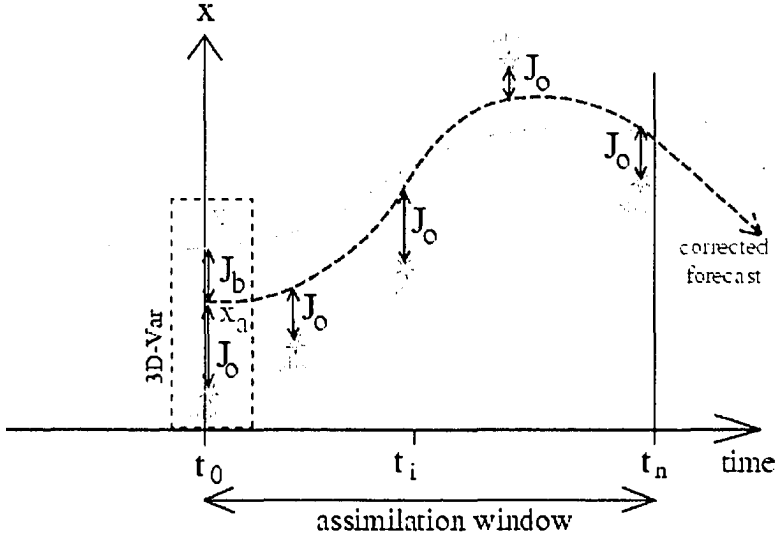

Fig. 2.5 An example of 4D-VAR assimilation in a numerical forecasting system (From Bouttier and Courtier 2001).

2.3. Previous Studies of Heavy Rainfall Forecasting

During the past 20 years, numerous studies have been conducted in an effort to improve the forecasting of heavy precipitation, principally because of the significant human suffering and economic loss associated with such events (as discussed in Chapter 1). The methodologies used can be divided into two principal categories: the development and application of conceptual models using observational data, and the use of numerical simulation models applied to both real and idealized settings. Although in recent years the latter has become the preferred or dominant strategy, we feel it is useful to treat the two separate methodologies separately in the context of discussing previous research.

2.3.1. Conceptual Models and Observation-Based Physical Analysis

The development of conceptual models, based upon detailed physical analyses of observed events, is a traditional and very effective methodology for improving our understanding of heavy rainfall events and thus their prediction. The basic strategy involves identifying common synoptic and mesoscale features and understanding their origin and morphology. Maddox et al. (1979) developed four classifications for heavy rainfall triggers based upon to climatological differences in events: synoptic event, meso-high event, frontal event, and western event. This conceptual model includes various meteorological features and parameters such as surface and upper-air patterns, mid-level wind patterns, thunderstorm outflow boundary dynamics, surface dew point structure, and so on – all of which are very useful for understanding the synoptic and smaller scale conditions associated with heavy rainfall events.

To forecast heavy rainfall with this conceptual model, forecasters can use the following important facts: (1) an advanced short wave trough at mid-levels often helps to trigger and focus thunderstorm activity; (2) the storm area is often located very near the large scale ridge in troposphere and occurs in normally benign surface pressure patterns; and (3) many intense rainfall systems occur during nighttime.

Maddox (1980) also developed a conceptual model related to mesoscale convective complexes (MCCs). According to his study, many heavy rainfall events are directly caused by intensive MCCs. After he classified MCCs by size, initiation, and duration, he found that MCCs exhibit two significant features in the context of heavy rainfall forecasting. The first is that MCCs often produce considerable heavy rainfall, the moisture fluxes from which can be processed by other mesoscale systems; and second, most warm season rainfall in the U.S. can be explained by MCCs.

Other conceptual models have focused on jet streaks (e.g. Ucellini and Kocin 1987). Ucellini and Kocin (1987) showed that wide spread areas of excessive precipitation often are located between two jet streaks, in the left-front quadrant of the exit region of the southern jet and in the right –rear quadrant of the northern jet. Although this conceptual model is not without problems, it is useful for determining the position of potentially heavy rainfall or snowfall.

Another important conceptual model is the so-called conveyer belt, which provides an integrated view of linkages between the upper-air flow patterns and frontal movement and development (e.g. Kreitzberg and Brown 1970; Carlson 1980; Browning and Monk 1982; Browning 1986). The conveyor belt conceptualizes moving streams of air that are vertically thin but very wide, as shown schematically in Figure 2.6. The

warm conveyor belt (WCB) rises from SE to NE and produces cloudiness in the middle and upper layers of the atmosphere. It is located in front of the frontal cloud band, which is under the influence of an upper-level stream from behind. This juxtaposition leads to a high probability that the relative stream from behind will overrun the warm conveyor belt at upper levels, producing static instability and development of convective cells (Browning, 1986).

Along with the development of conceptual models, improved analysis technologies have led to the development of new composite charts for forecast heavy rainfall forecasting. Maddox (1979) developed a series of sophisticated gridded composites of meteorological fields by overlaying important features and parameters from the significant level analyses onto an appropriate basic chart. Owing to the results of his study, forecasters can more readily identify features associated with heavy rainfall that might otherwise be overlooked through the use of conventional synoptic charts. For example, warm air advection, which occurs in a region of conditional instability, can be easily identified using Maddox's methodology.

Another valuable tool in heavy rainfall forecasting is the meteorological satellite (e.g. Weiss and Smith 1987; Thial et al. 1993). Thiao et al. (1993) determined that heavy rainfall events have a strong linkage with water vapor plumes. He showed that water vapor satellite imagery is useful in identifying such plumes and their associated jets. Satellite data also can aid the interpretation not only of large-scale features but also synoptic and mesoscale systems, such as thunderstorm outflow boundaries.

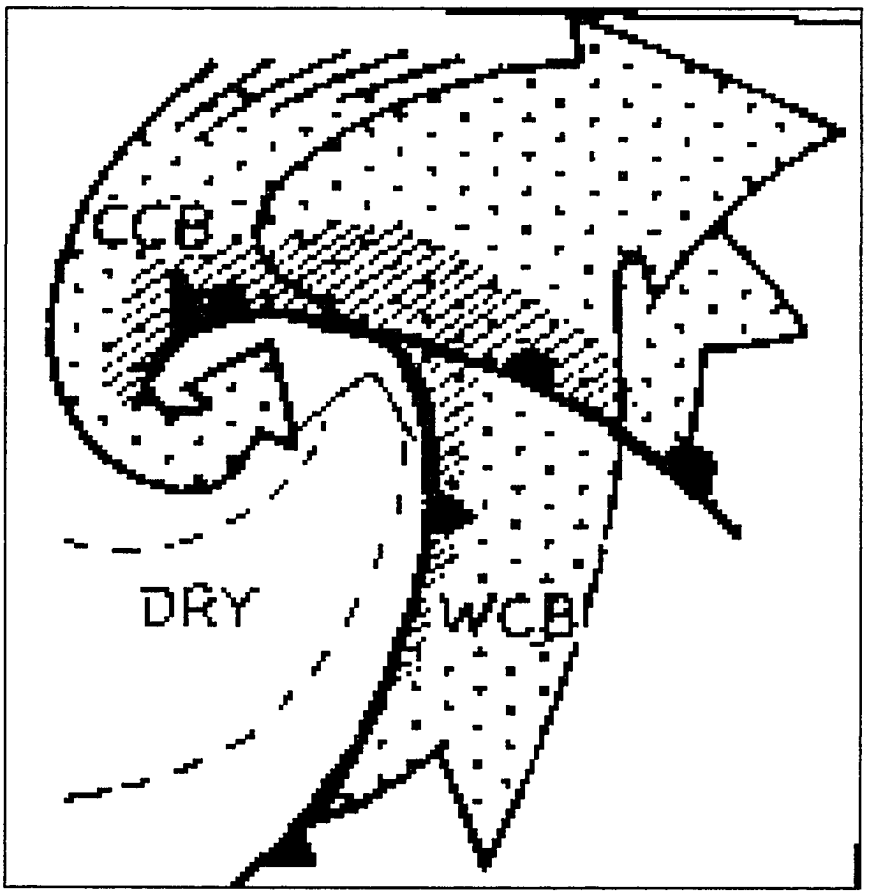

Fig. 2.6 The schematic diagram of conveyer belts. WCB and CCB stand for warm conveyer belt and cold conveyer belt. And, shaed area depicts the precipitation region (From online lecture note of University of East Anglia 2002).

Radar data also are utilized extensively for heavy rainfall forecasting, one of the most important advantages being that radar provides aerial estimates of rainfall, whereas surface gauges provide only spotty point observations (e.g. Manion and Klazura 1993; Klazura et al. 1999) and satellites often are blocked from viewing the region below cloud top. Small-scale heavy rainfall may occur between surface gauges, thus precluding detection without radar. Operationally, radar may be used simply to track individual storm cells and synoptic systems and alert forecasters to a developing heavy rainfall situation (e.g. Changnon and Vogel 1981). In addition, mesoscale convective systems (MCSs) also may be tracked with the data obtained from the WSR-88D (e.g. Houze et al. 1989; Hilgendorf and Johnson 1998).

Surface observations also are extremely useful to operational forecasters in heavy rainfall situations. Additionally, surface rain gauge networks provide ground truth for radar-based estimates and are used to verify flood forecasts and warnings (e.g. Brandes et al. 1999; Klazura et al. 1999). Fixed surface mesonets, along with mobile mesonets, also provide detailed information for heavy rainfall forecasting, including information related to the location of surface outflow boundaries, mesohighs and lows, and frontal boundaries (e.g. Brock et al. 1995; Straka et al. 1996).

2.3.2. Studies Based on Numerical Simulation Models

Arguably the most frequently used tool for understanding heavy rainfall is the numerical model. Despite the sophistication of numerical models and the power of computers on which they are run, accurate quantitative precipitation forecasts (QPFs) of heavy rainfall using either experimental numerical simulation or operational prediction

models continue to challenge the scientific community. According to Olson et al. (1995), who studied the impact of using numerical models to predict heavy rainfall, the 48-hour National Weather Service (NWS) QPFs have improved steadily since the introduction of the Limited-area Fine Mesh (LFM) model. However, the 24-hr QPFs have improved at a slower rate than 48-hour QPFs because models continue to be unable to capture sub-synoptic and mesoscale features. The Nested Grid Model (NGM) still provides excellent guidance for heavy rainfall forecasting since National Meteorological Center (NMC) began to operate it in 1985 (Hoke et al. 1989; Junker and Hoke 1990). The NGM rarely misses heavy rainfall events, though of course cannot capture the heavy amounts that tend to occur locally and cause the greatest loss of life and disruption of commerce.

Numerical models contain many deficiencies that inhibit their exclusive use (Junker and Hoke 1990; Dunn 1991), with the amplitude error for heavy rainfall forecasting being more serious in case of small scale events because of inadequate model resolution. To overcome this limitation, many of the problems associated with large-scale models – such as coarse terrain and physics parameterizations -- are being addressed by new non-hydrostatic mesoscale and storm-scale models which can explicitly resolve most small-scale features.

Continued improvements in computer power have paved the way for continued improvements in the physics and resolution of meso- and storm-scale models, especially in the context of heavy rainfall forecasting. Zhang and Fritsch (1986) performed a numerical simulation of the meso-β scale structure associated with the 1977 Johnstown heavy rainfall event using a modified version of the Pennsylvania State University/National Center for Atmospheric Research (PSU/NCAR) mesoscale model

(PSU/NCAR numerical model originally developed by Anthes and Warner in 1978). The principal features of this model are as follows: (1) three-dimensional hydrostatic; (2) two way interactive nested-grid procedure with a 75 km coarse grid mesh (CGS) and 25 km fine grid mesh (FGM); (3) Anthes and Kuo convective parameterization (Anthes and Keyser 1979) for CGM and Fritsch and Chappell (1980) convective parameterization, along with convective adjustment, for the FGM.

Zhang and Fritsch demonstrated the possibility that the heavy rainfall event associated with the meso-β scale structure of a convective system could be forecasted with useful skill for periods up to 18 hours. Using the same numerical model, they also studied the relation between the warm core vortex and evolution of MCCs and MCSs, both of which are strongly related to producing heavy rainfall. The results of this study indicate that the model's ability to re-create the timing and location of resolvable-scale condensation is equally important as the convective parameterization in the successful prediction of mesoscale convective system evolution. These two studies by Zhang and Fritsch have served as valuable guidelines in the development of subsequent studies regarding mesoscale numerical simulation of heavy rainfall events.

Recently, another approach has been introduced for making heavy rainfall forecasts based upon numerical model output combined with the latest observations (e.g. Xia and Chen 1999) – the so-called model output dynamics (MOD). In MOD, any real time numerical model output is combined with the latest observed rainfall data (without using historical data) to produce heavy rainfall forecasts. Xia and Chen (1999) compared the MOD results with a dynamical prediction from the limited area forecast (LAF) model in China, which has coarse horizontal resolution (1.875° in both x and y). The results of

this study show significant improvements associated with MOD for heavy rainfall forecasting in the summer season, compared to the results obtained by the LAF model, even though MOD depends to a considerable extent on observational data coverage (MOD is worse in data poor regions) and cannot account for topographical influences (the importance of which is discussed below). Although MOD is not a numerical simulation method, it involves the use of numerical model output and may become a useful tool for heavy rainfall forecasts considering the positive results noted above.

It has long been recognized that orography can play a profound role in generating heavy precipitation (e.g. Mahrer and Pielke 1977; Benjamin and Carlson 1984; Bougeault and Lacarrere 1989; Romero et al. 1997). Chang and Yoshizaki (1991) conducted a numerical simulation study to examine if an MCS, which produced heavy rainfall over Okinawa (which has elongated mountains ranging in altitudes of 100 m to 500 m) during the Changma (East Asian monsoon) season, is related to orographic forcing. A two-dimensional compressible model developed by Yoshizaki and Ogura (1988) was employed for the simulation experiments, and warm rain processes for cloud physics in the model were used, along with grid stretching in both directions. By varying the terrain height in the model, they were able to study the response of the MCS. They found remarkable orographic effects as follows: (1) forced lifting on the upwind side of the mountain and the suppression of outflow spreading in the lee resulted in a steady configuration for the MCS; and (2) in the simulation with lower terrain heights, the MCS moved faster in the upwind direction when cold-air overflowed the mountain crest.

Another interesting numerical study regarding the effects of topography in heavy rainfall was conducted by Buzzi et al. (1998). As the part of Mesoscale Alpine

Programme (MAP; Binder et al. 1996), they simulated a severe heavy rainfall event that occurred in northwestern Italy from 3 to 6 November 1994. Ultimately, they sought to improve the capability of heavy rainfall forecasts in areas of complex orography (NW Italy is in the southwestern Alps region). In this area, according to Tibaldi et al. (1990), steep and complex topography, and the sea that acts the source of moisture and heat, usually affect the production of heavy rainfall. Buzzi et al. used a hydrostatic mesoscale model (BOLAM) with about 30 km horizontal resolution. To examine orographic effects, they varied the terrain height, and also turned on or off latent heat and surface sensible heat fluxes. The numerical simulations exhibited strong feedback mechanisms in the presence of considerable moisture having relatively high air temperature and steep orographic forcing. They also found that strong orographic ascent is associated with a prefrontal moist low-level jet. Romero et al. (1998) also performed mesoscale model simulation in the same region and found similar results. Overall, it is clear that orography can have a profound influence on the creation of heavy precipitation, and that the accurate representation of terrain in a model is critical for capturing this influence (as also noted in a recent study by Mass et al. 2002 for numerical experiments conducted over the Pacific Northwest of the United States).

Compared to the previous research described in this section regarding heavy rainfall simulations or predictions made using numerical models, the present study has several important and distinguishing features. First of all, we employ a non-hydrostatic framework with relatively fine grid spacing (3 km). Second, we utilize fine-scale radar data (as well as other observations) via a dynamic assimilation procedure in an effort to capture the small-scale structures responsible for producing locally heavy rainfall -- both

in terms of providing the correct structures to the model and eliminating those in the background field which are not correct. Third, we quantitatively evaluate the quality of these forecasts against both surface gauge observations and radar-based precipitation estimates. Finally, we have chosen a case for which orographic forcing is believed to be relatively weak, and thus for which fine-scale observations are expected to have a significant impact.

Chapter 3

The Chorwon-Yonchon Heavy Rainfall Event

A heavy rainfall event occurred over the middle part of the Korean peninsula (hereafter KP; we are careful to distinguish between the entire geographic region of Korea and only South Korea) from 26 to 28 July 1996. During this period, the total rainfall accumulation exceeded 650 mm in many regions, including the Chorwon-Yonchon area. According to the National Disaster Prevention and Countermeasures Headquarters (NDPCH 2001) in Korea, the associated storm claimed 29 lives, and property damage exceeded 380 million US dollars. A special report (KMA 1996) recounts that several mesoscale and synoptic features contributed to the flooding, including: the northwest boundary of a stationary North Pacific high (NP high) located in the central part of the KP; the boundary between two air masses having different characteristics (one is the Okhotsk mP, which was responsible for heavy rainfall in the central part of the KP, and the other is the North Pacific mT, which prevented rain from occurring in the southern part of the KP); a continuous strong moisture flux into the middle part of the KP; and the passage of two upper-air troughs over the KP.

3.1 Synoptic-Scale Aspects

Figure 3.1 shows surface weather charts in 12-hour intervals from 0000UTC on the 26th to 1200UTC on the 27th of July 1996. The NP high extended to the southern part

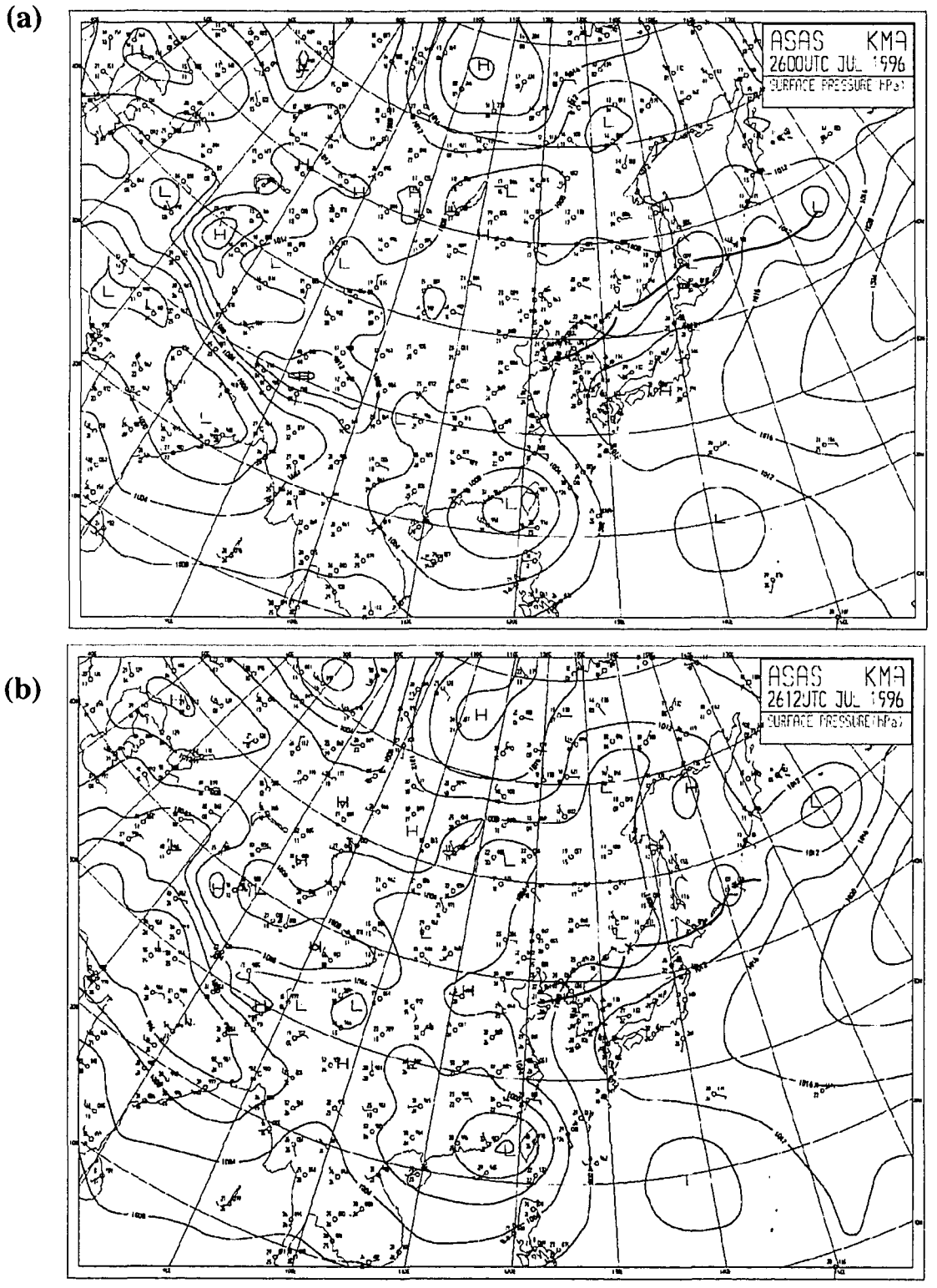

Fig. 3.1 Surface weather charts at (a) 0000UTC July 26, (b) 1200UTC July 26, (c) 0000UTC July 27, and (d) 1200UTC July 27.

(c)

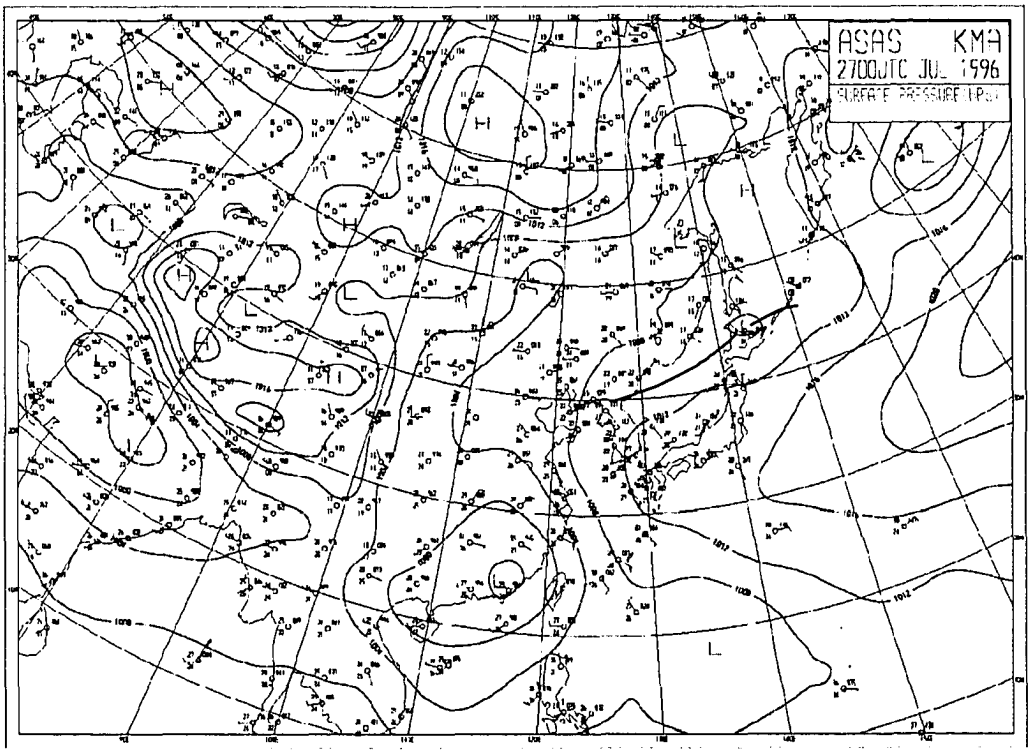

(d)

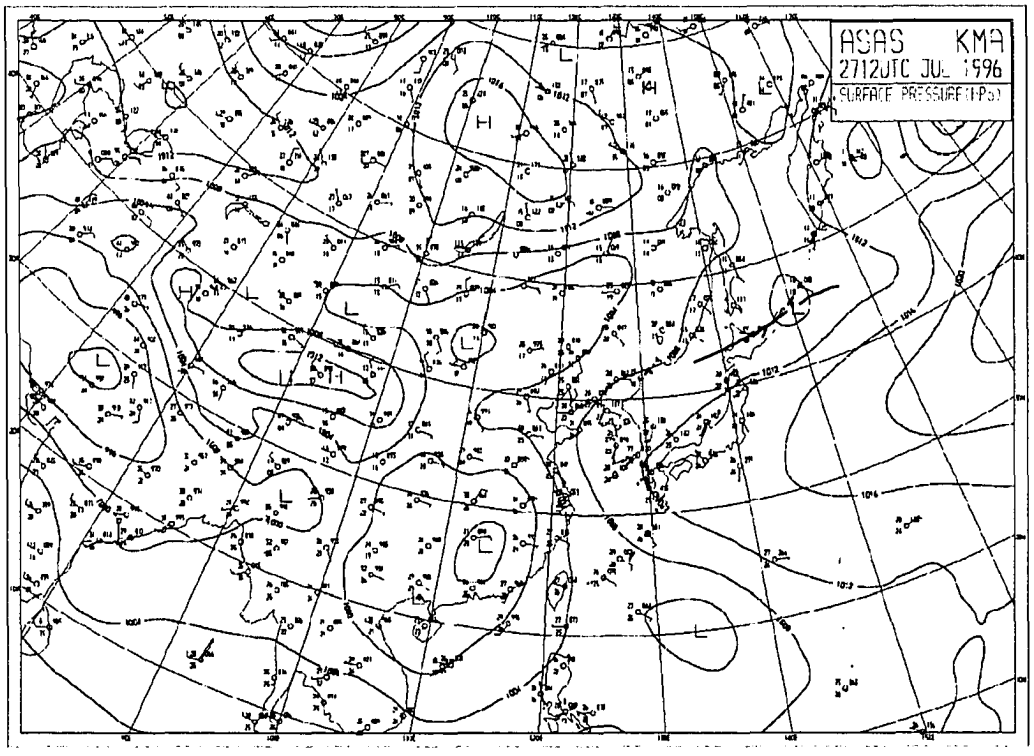

Fig. 3.1 (continued)

of the KP and a weak low was located northeast of the border between North Korea and Russia (Fig. 3.1 (a)). A cold front associated with the latter extended to the middle part of the KP and to near the Kuril Islands via Sakhalin Island at 0000UTC July 26 (Fig. 3.1 (a)). This arrangement produced significant moisture advection into the central part of the KP. Typhoon Gloria, located near Taiwan at 0000UTC and 1200UTC on July 26, also played an important role in the heavy rainfall event considered here by providing a strong moisture flux into south central Korea in conjunction with strong southwesterly winds. By 1200UTC on July 26, the weak low noted above had moved to the east (Fig. 3.1 (b)), and the cold front over the central part of the KP had moved slightly to the north and had changed its orientation from southwest-northeast to almost directly west-east. The southwesterly flow associated with Typhoon Gloria still provided a strong moisture flux into the middle part of the Korean peninsula at this time, even though the typhoon had weakened by virtue of moving inland over the southeast part of China.

At 0000UTC on July 27, the center of the low previously located northeast of the North Korea-Russia border was located over Hokkaido (Fig. 3.1(c)), and the cold front over the KP had moved slightly to the north compared to the previous position at 1200UTC on July 26. The NP high extended to the southern part of the KP, thereby accelerating the flow of moisture northward. This moisture resulted in heavy rainfall over the central part of the KP from 2000UTC on July 26 to 0300UTC on July 27. As shown in figure 3.1 (d), the KP was dominated by the influence of the NP high after the low and cold front moved to the east by 1200UTC on July 27.

Figures 3.2 and 3.2 depict the 850hPa and 500hPa weather charts, respectively, in the same format as in Fig. 3.1. At 850hPa, southwesterly flow was present over the

central part of the KP and high relative humidity was present over southeast China and the middle and northern regions of the KP. The northern region of China north of 40° was much drier. A strong thermal trough existed in the region of heavy rainfall in central Korea at 0000UTC and 1200UTC on July 26 (Fig. 3.2 (a) and (b)). In this region, the isotherms were nearly perpendicular to the wind direction, indicative of low-level warm air advection that aided in the production of heavy rain. At 0000UTC on July 27 (Fig. 3.2 (c)), a ridge was located over the Manchuria region. As it weakened by 1200UTC on July 27, the wind speed over northern Korea was reduced. The 500hPa weather charts (Fig. 3.3) show that southwesterly flow and northwesterly flow merged west of the KP, and this merged flow (now westerly) continued eastward over the rest of Korea. The 5880gpm height line, which indicates the boundary of the NP high at 500hPa, remained over the southern region of the KP during the entire time period.

Considering the 5820gpm (or 5850gpm) height line, a trough was developing over the middle and north part of the Korean peninsula at 0000UTC and 1200UTC on July 26 (Fig. 3.3 (a) and (b)). According to quasi-geostrophic theory, the maximum positive differential vertical vorticity advection would occur to the east of the trough axis, or the middle northwest region of the KP in this case. It is clear that the heavy rainfall region coincides well with this maximum, along with the region of strong geopotential height gradient (the central part of the KP between 5820gpm and 5880gpm in Fig. 3.3 (b)). The trough maintained its configuration through 0000UTC on July 27(Fig. 3.3 (c)). At 1200UTC on July 27 (Fig. 3.3 (d)), the trough had weakened and the geopotential height had increased over the middle and northern region (including the heavy rainfall region) of the KP. This weakening marked the initial demise of the heavy rainfall event.

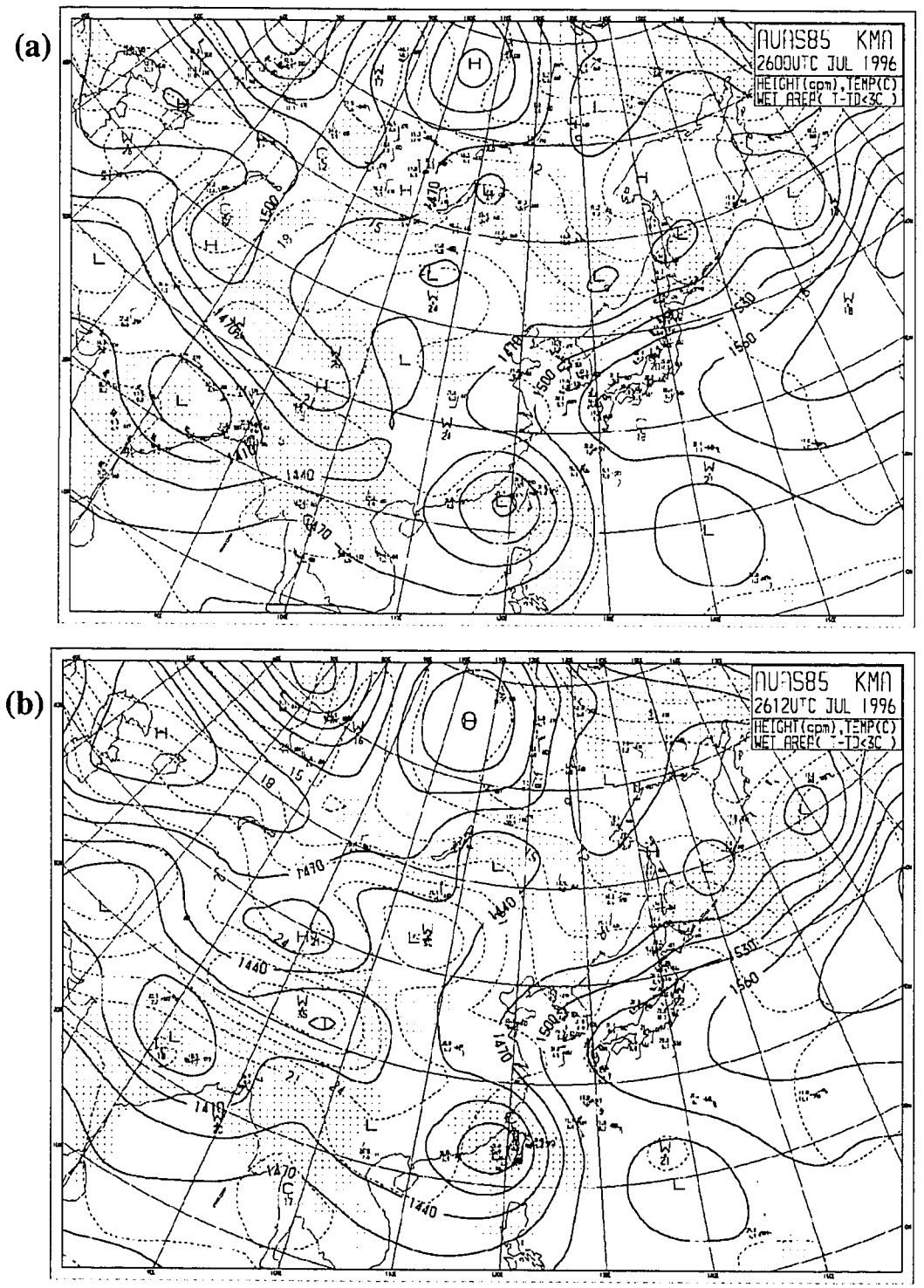

Fig. 3.2 850hPa weather charts at (a)0000UTC July 26, (b)1200UTC July 26, (c)0000UTC July 27, and (d)1200UTC July 27.

(c)

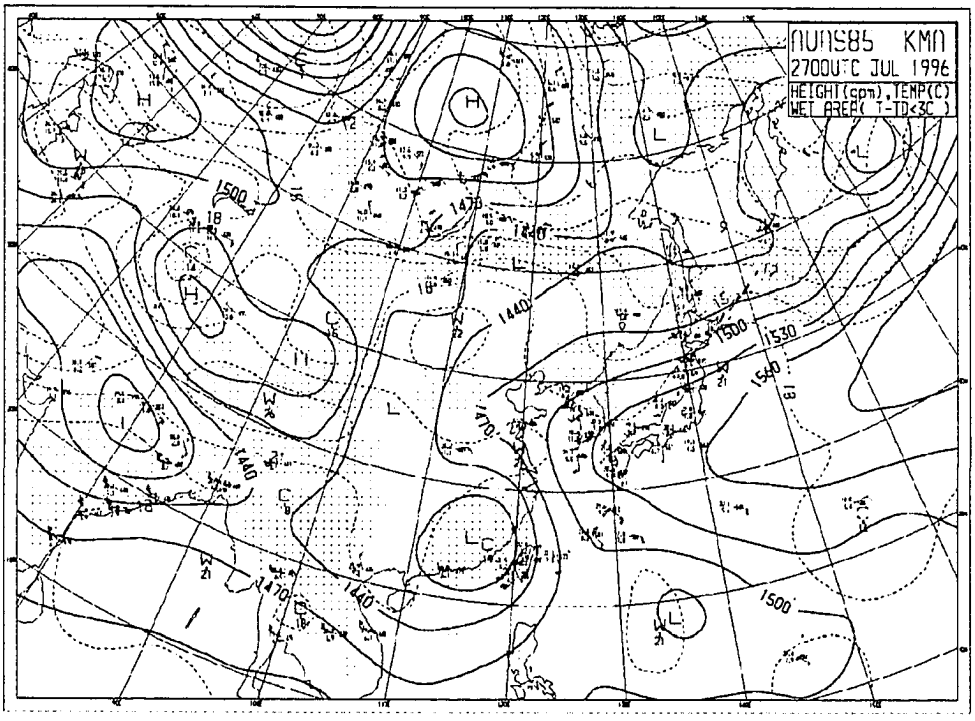

(d)

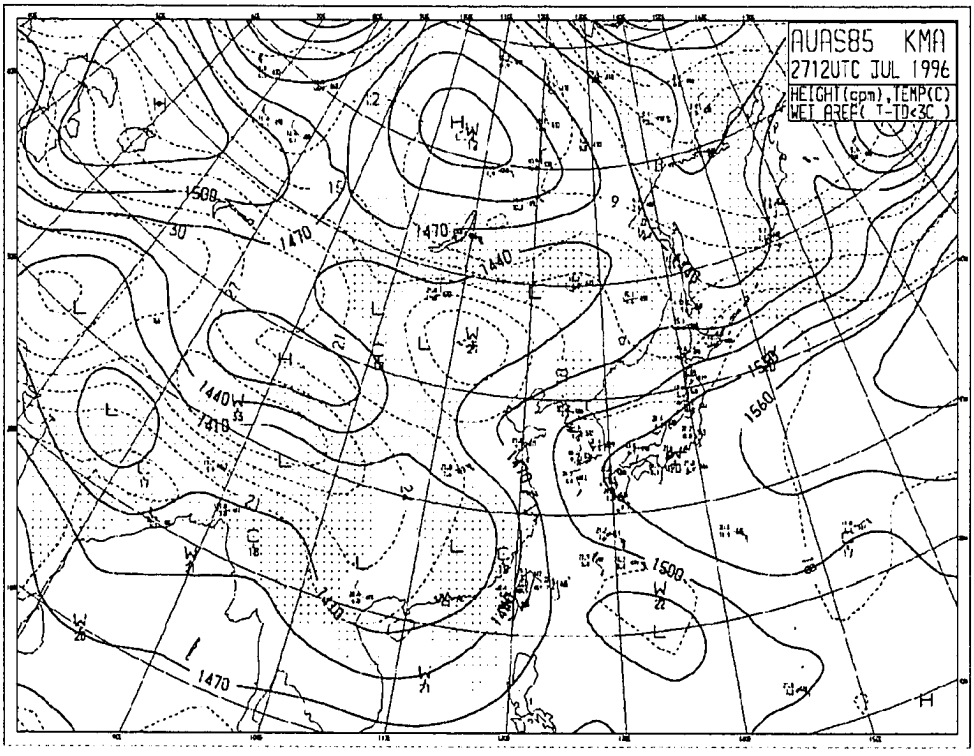

Fig. 3.2 (continued)

(a)

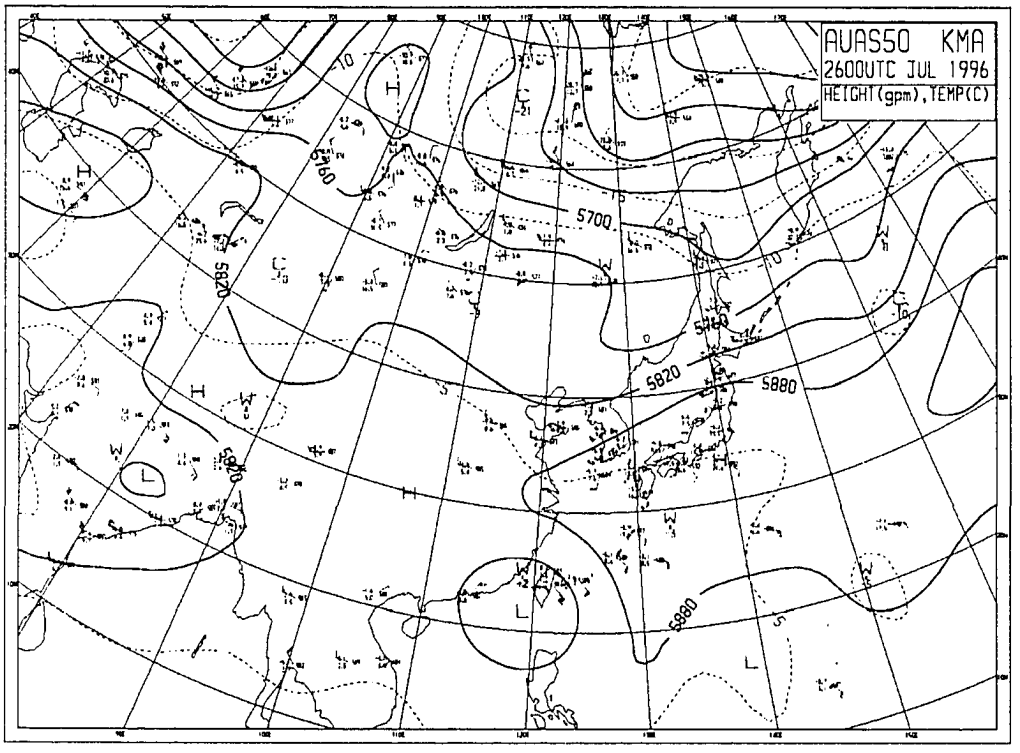

(b)

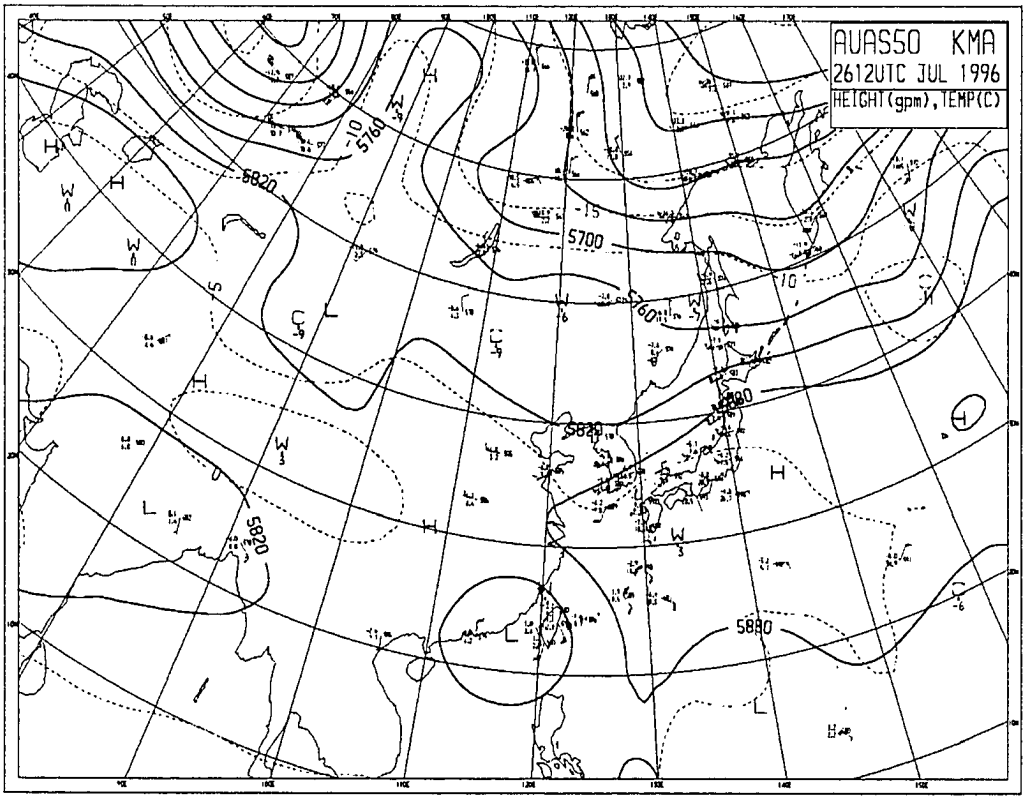

Fig. 3.3 500hPa weather charts at (a)0000UTC July 26, (b)1200UTC July 26, (c) 0000UTC July 27, and (d)1200UTC July 27.

(c)

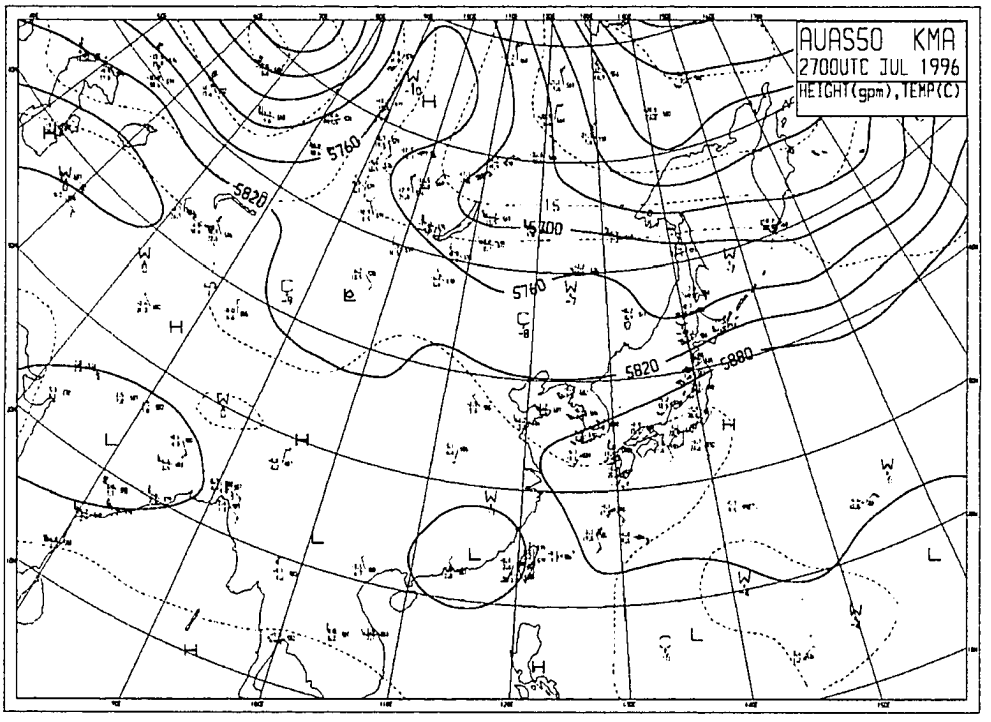

(d)

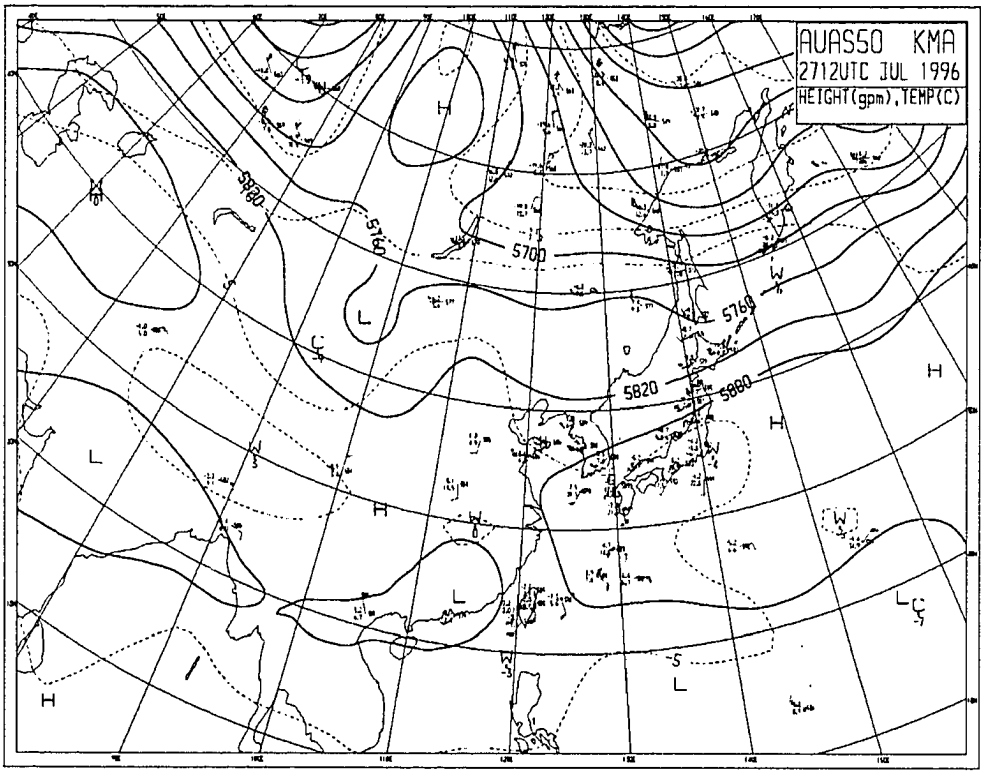

Fig. 3.3 (continued)

850hPa and 200hPa streamlines at 12-hour intervals are depicted in Figures 3.4 and 3.5, respectively. Two features clearly contributing to the heavy rainfall are a strong upper level jet (Fig. 3.5) that extends from the northern part of China to the central part of the KP via the Shantung peninsula, and a low level jet (Fig. 3.4), which induces strong moisture flux into the central part of the KP from the west region of the East China Sea at the same time. Many studies have been undertaken regarding the interaction of upper and low level jets and precipitation (e.g. Uccellini and Kocin 1987). According to the previous results, the jet streak is associated with the front and traveling cyclonic (baroclinic) systems. There usually exists an upper level trough (ridge) near the exit region of the southeastward (northeastward) upper jet streak. This leads to a region of convergence west of trough axis (in the southeast exit region of the jet streak) and a region of divergence east of the trough axis. As shown in Fig. 3.5, a strong upper level jet existed west of the Shantung peninsula, which led to divergence over the Yellow Sea that played an important role in the production of heavy rainfall in the central part of the KP. Although it is difficult to match quantitatively the precipitation region with the jet analysis, the upper level jet is well-placed with respect to the heavy rainfall region in a qualitative sense.

Figure 3.6 shows GMS-5 IR images at 6-hour intervals from 0000UTC on the 26th to 1800UTC on the 27th of July 1996. A long cloud band was present from the Mongolian region to the Kuril Islands in an east-west orientation from 0000UTC to 1800UTC on July 26 (Fig. 3.6 (a)-(d)), associated with high clouds over the Shantung peninsula and the northeast part of the KP (the arrows in Fig. 3.6 (a)-(d) indicate these high clouds). According to Bluestein (1993), a band of cirrus clouds typically occurs in

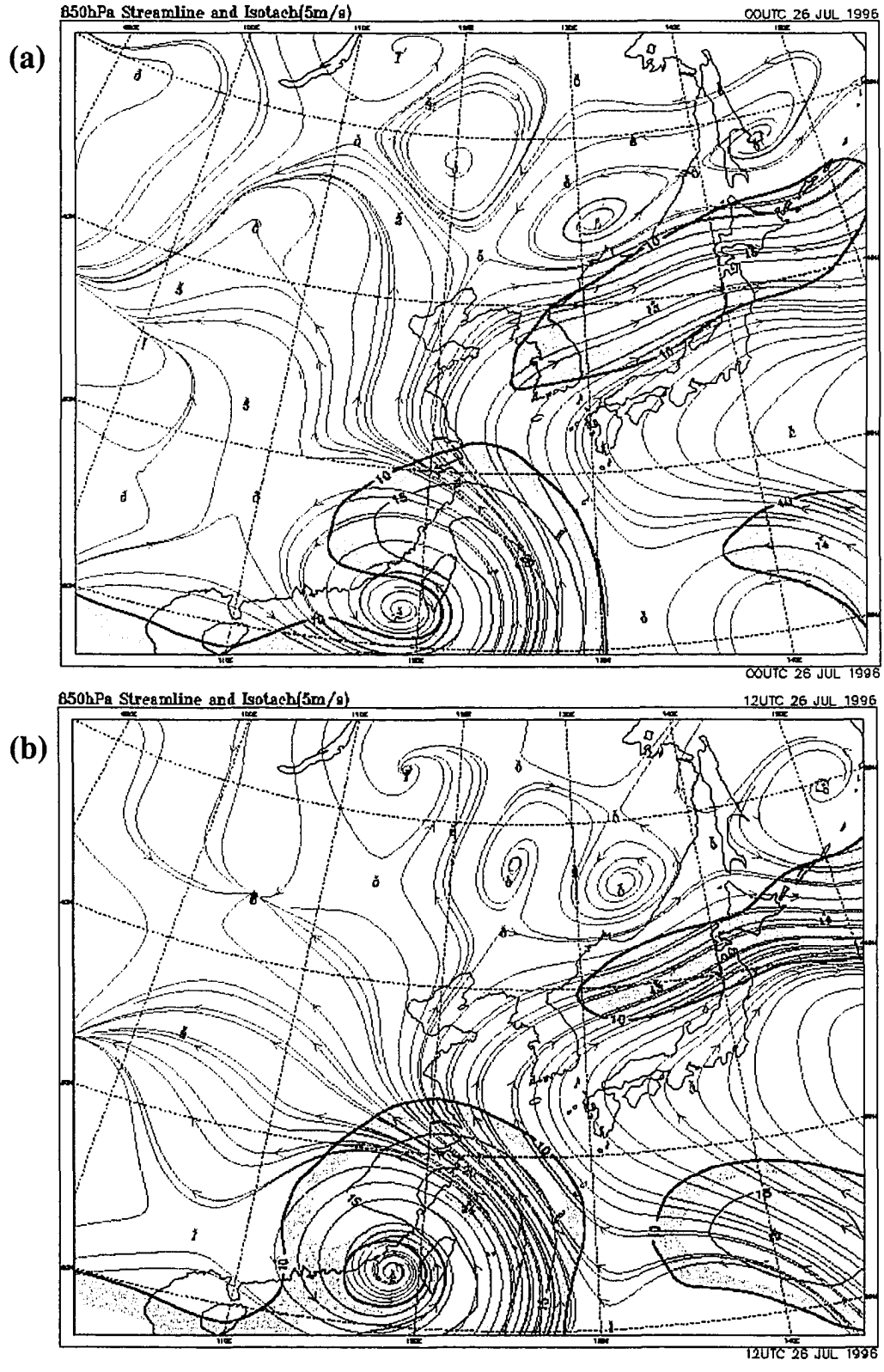

Fig. 3.4 850hPa streamline and isotach at (a) 0000UTC July 26, (b) 1200UTC July 26, (c) 0000UTC July 27, and (d) 1200UTC July 27.

(c)

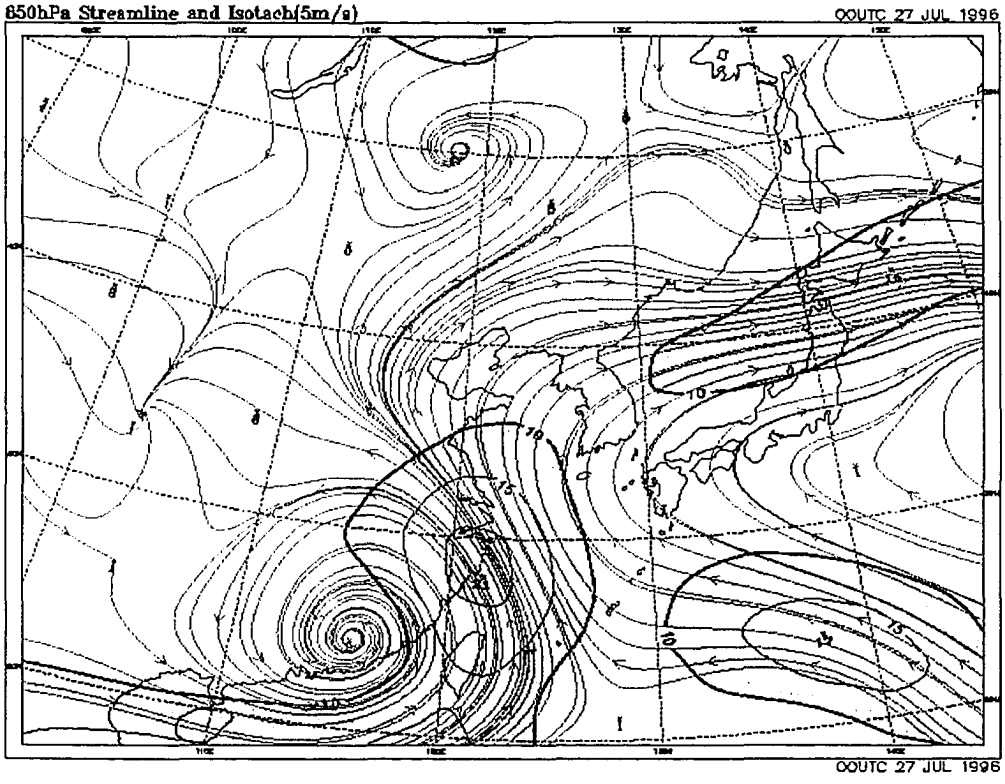

(d)

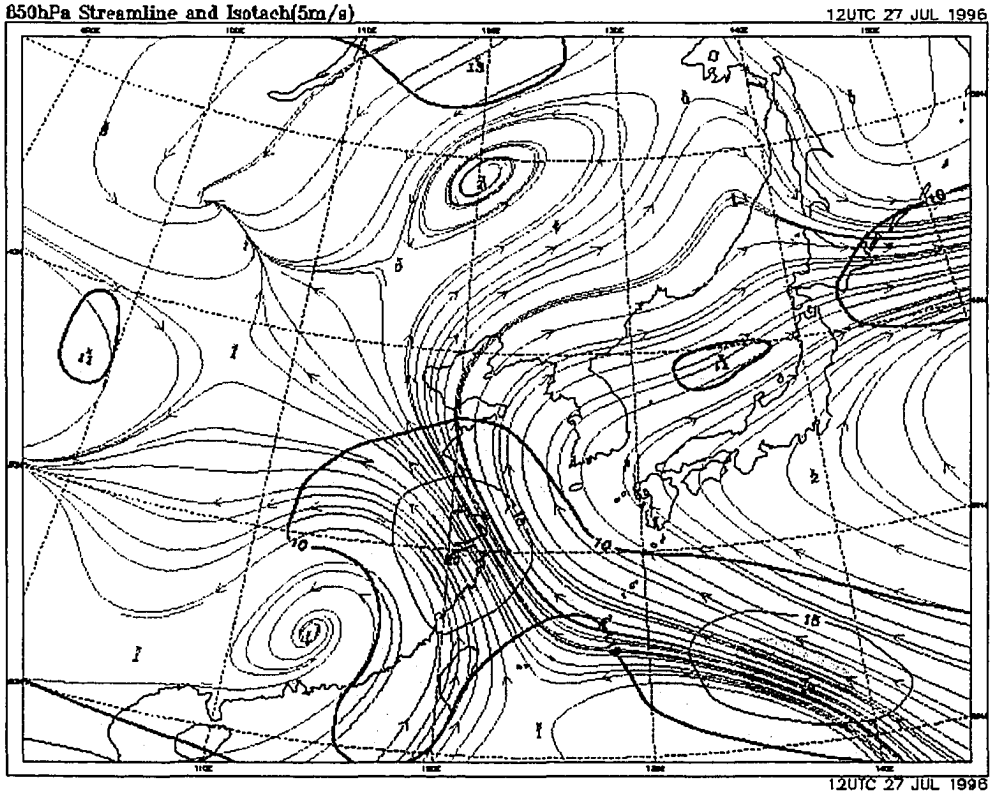

Fig. 3.4 (continued)

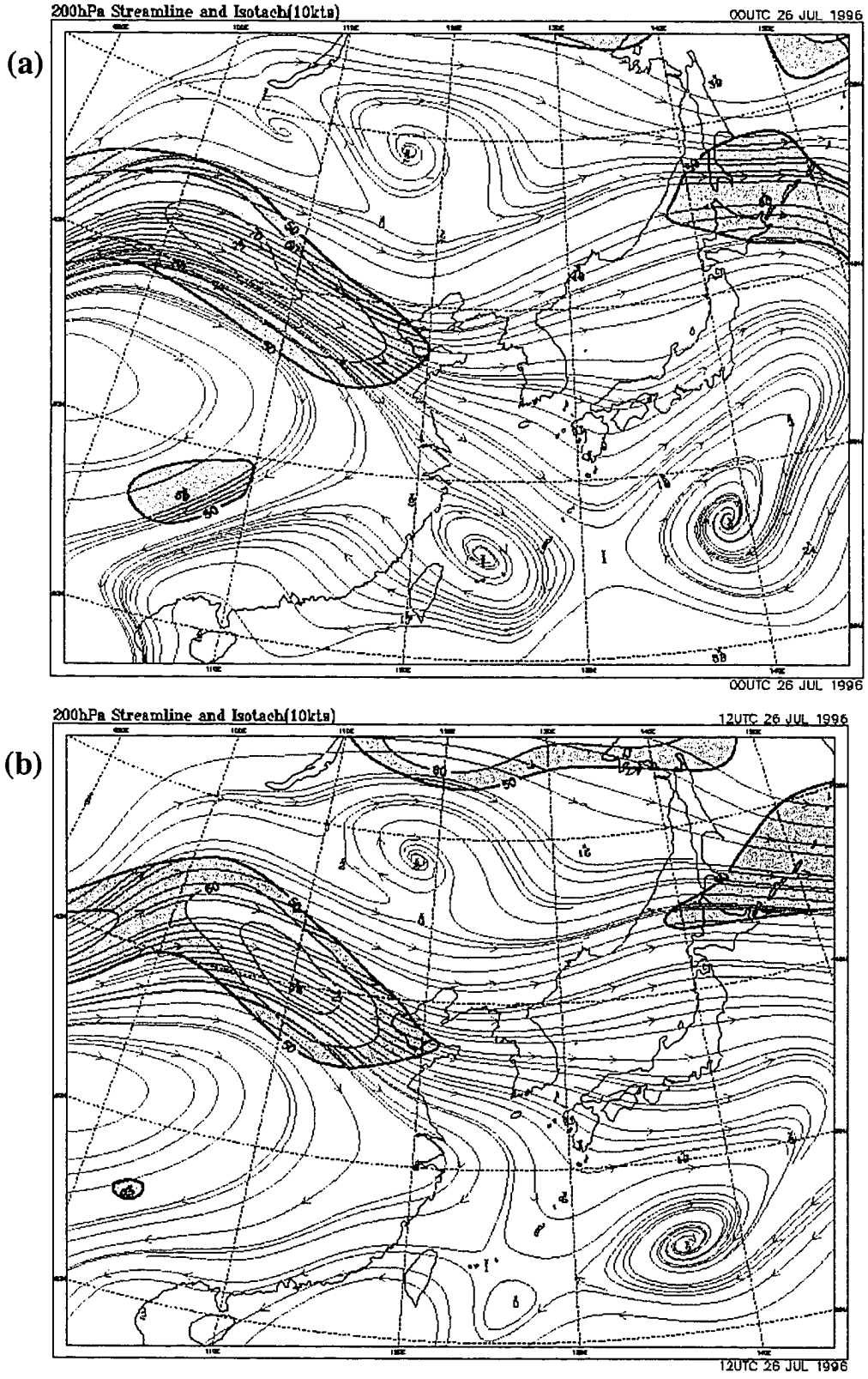

Fig. 3.5 Same as in Fig. 3.4 but for 200hPa.

(c)

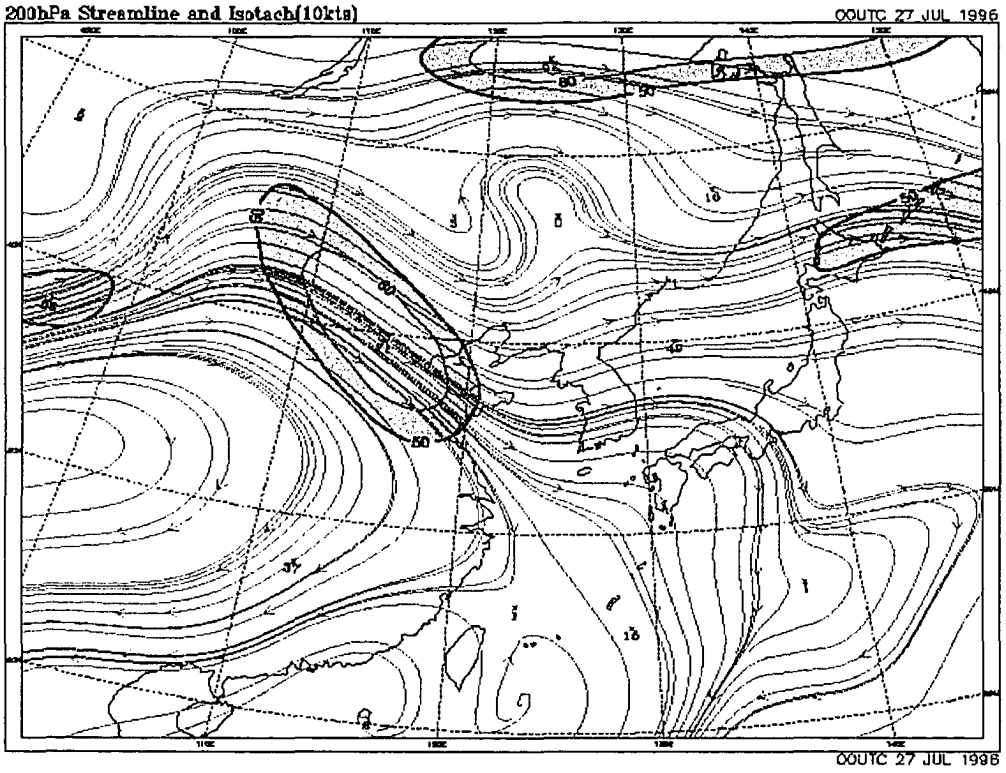

(d)

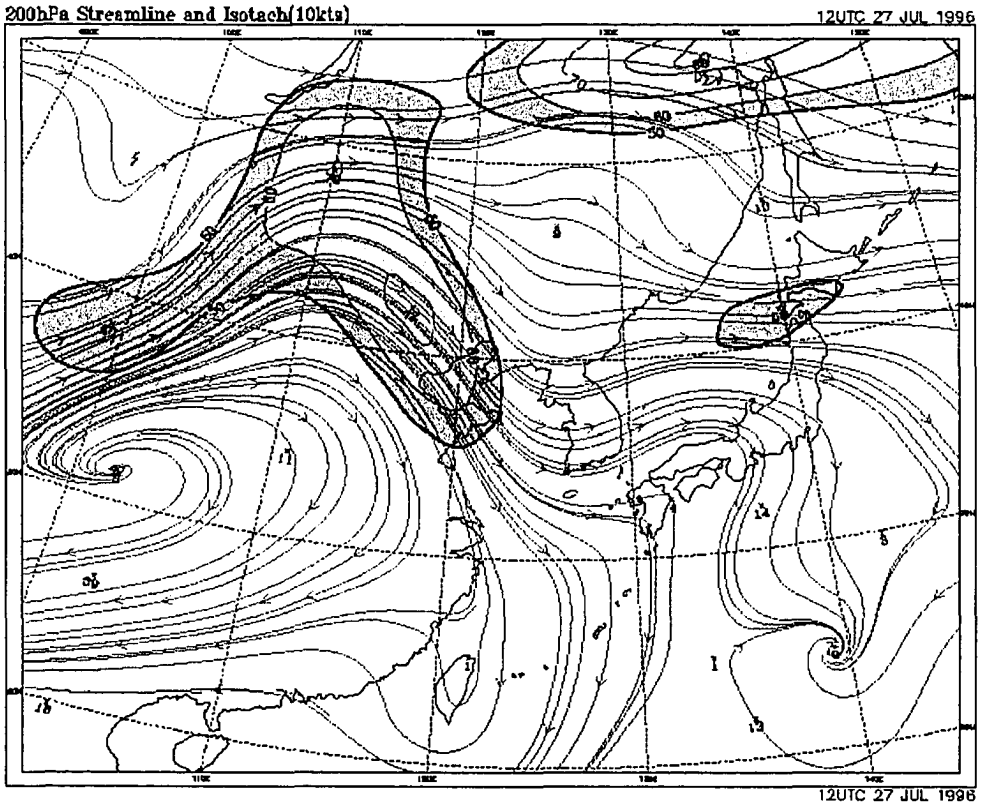

Fig. 3.5 (Continued).

association with the subtropical jet, and the cirrus is subsequently transported downstream by it. The position of this long cloud band, associated with high clouds, is very consistent with the position of the upper level jet. Bluestein (1993) also explained that "the sharp poleward edge of the cirrus owes its existence to deformation and a horizontal moisture gradient.". Such a configuration is depicted in Fig. 3.7. As shown in Fig. 3.6 (b), the dashed area indicates dry subsiding air from northwest and moist ascending air from southwest. This confluence region can produce severe storms, as occurred in the present case.

The orientation of cloud band located over the KP remained relatively constant during the entire time period. Within the long cloud band, several smaller cloud bands developed over the Mongolian region, the Gulf of Phohi, and the KP from 0000UTC on July 27 onward (the three arrows in Fig. 3.6 (e) indicate these cloud bands). Two cloud bands over the Gulf of Phohi and the KP started to move southward and were well developed by 0600UTC (the two arrows in Fig. 3.6 (f) indicate these two cloud bands). These cloud bands started to dissipate at 1800UTC (Fig. 3.6 (h)).

3.2 Sub-Synoptic Scale Aspects

The most severe local flooding occurred in the Chorwon (38.15N, 127.32E)-Yonchon (38.11N, 126.92E) region, and thus the storm is appropriately named the Chorwon-Yonchon heavy rainfall event. Figure 3.8 shows the time series of hourly rainfall (mm) and accumulated rainfall (mm) for the flood event at the Chorwon Meteorological Station, which was the only official weather station in the heavy rainfall region. It should be noted that the heavy rainfall was most concentrated over the

(a)

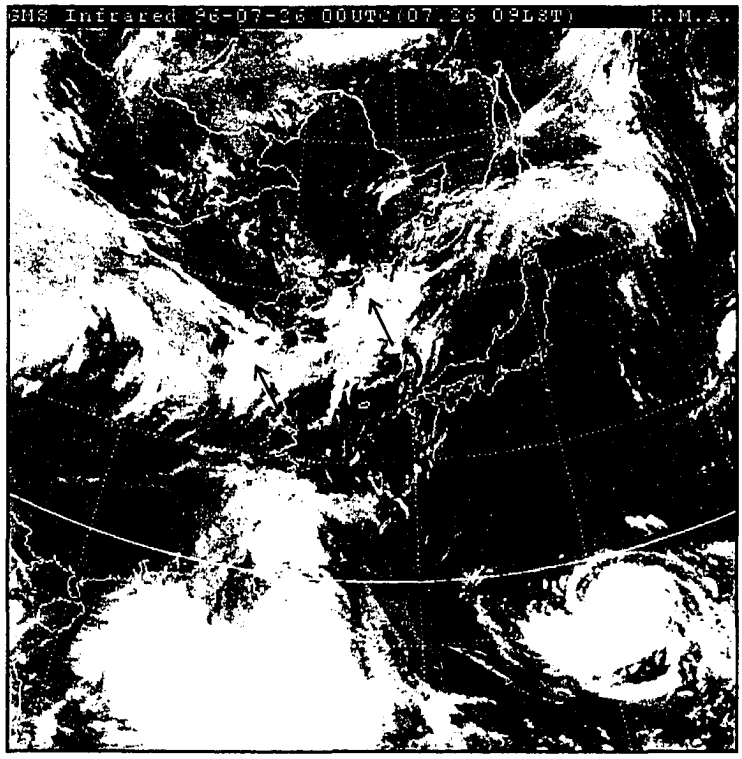

(b)

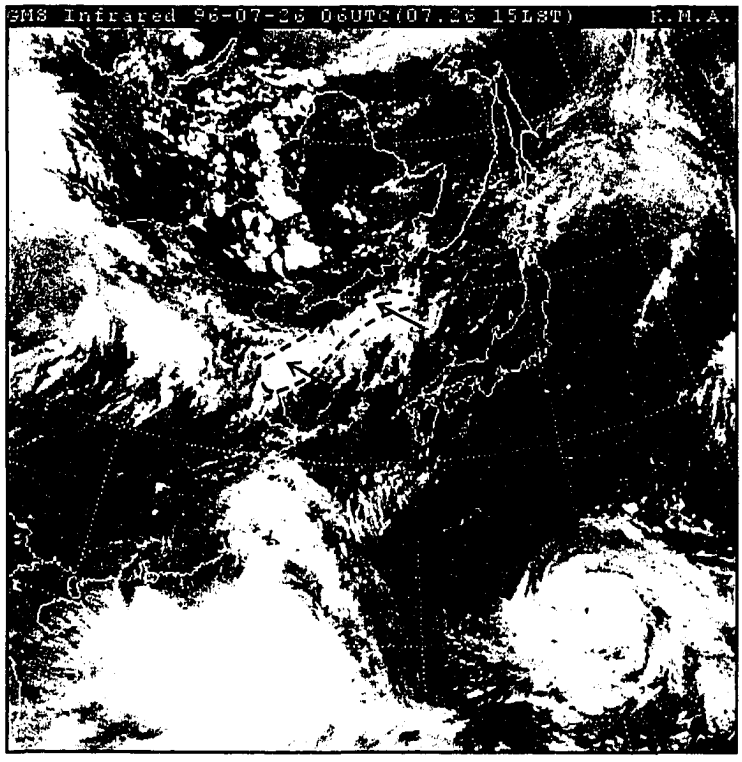

Fig. 3.6 GMS-5 IR images at (a) 0000UTC July 26, (b) 0600UTC, (c) 1200UTC, (d) 1800UTC, (e) 0000UTC July 27, (f) 0600UTC, (g) 1200UTC, and (h) 1800UTC.

(c)

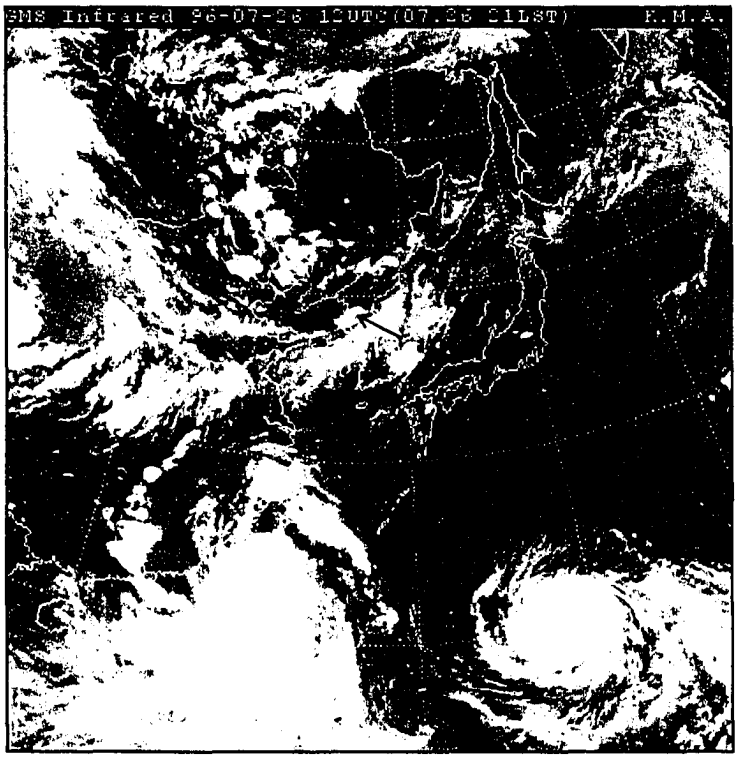

(d)

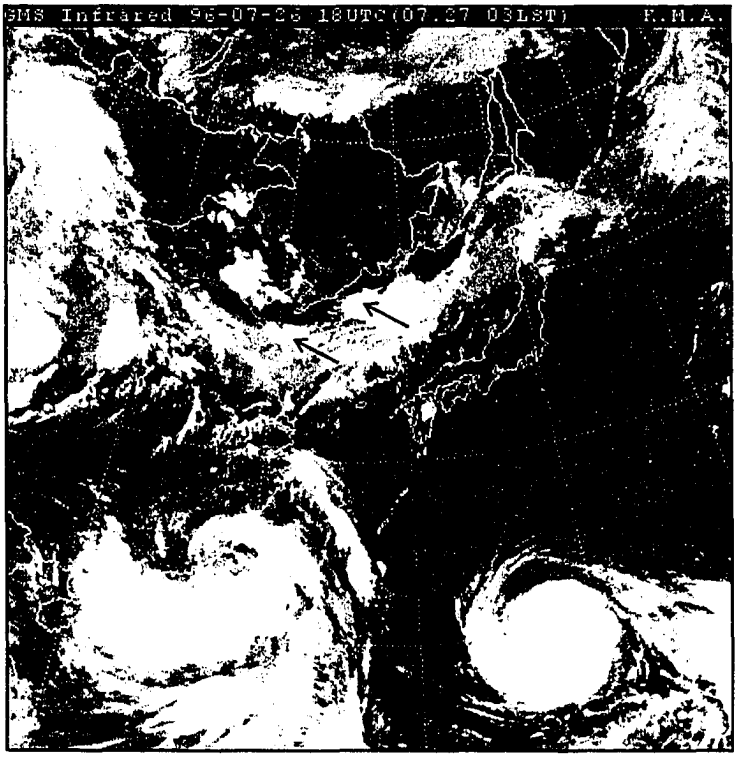

Fig. 3.6 (Continued).

(e)

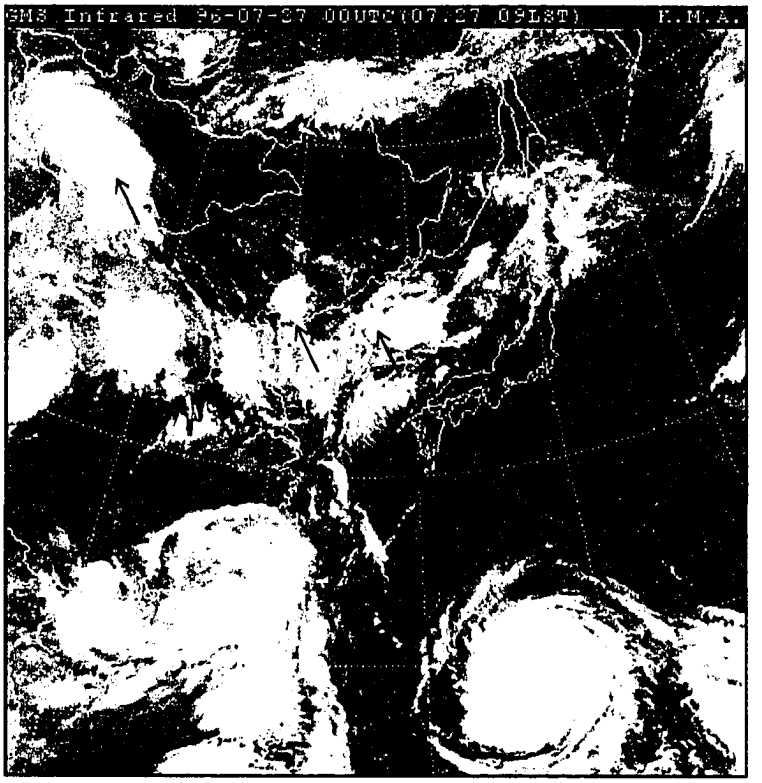

(f)

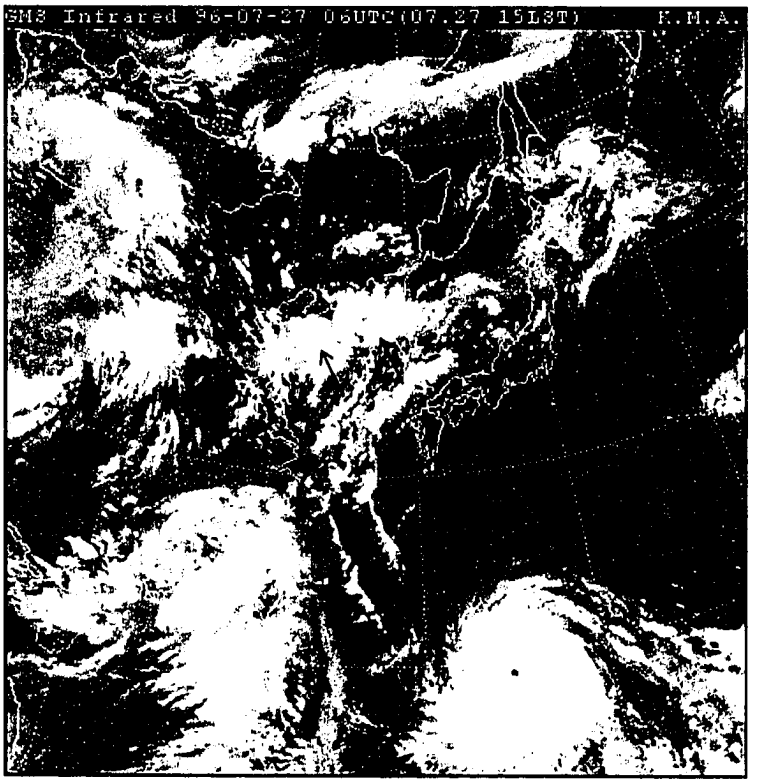

Fig. 3.6 (Continued).

(g)

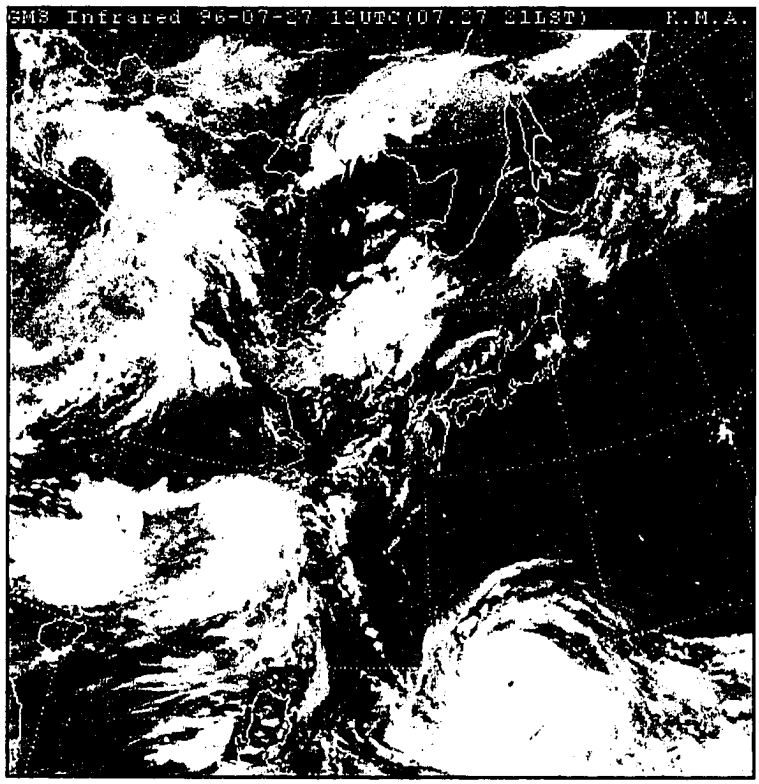

(h)

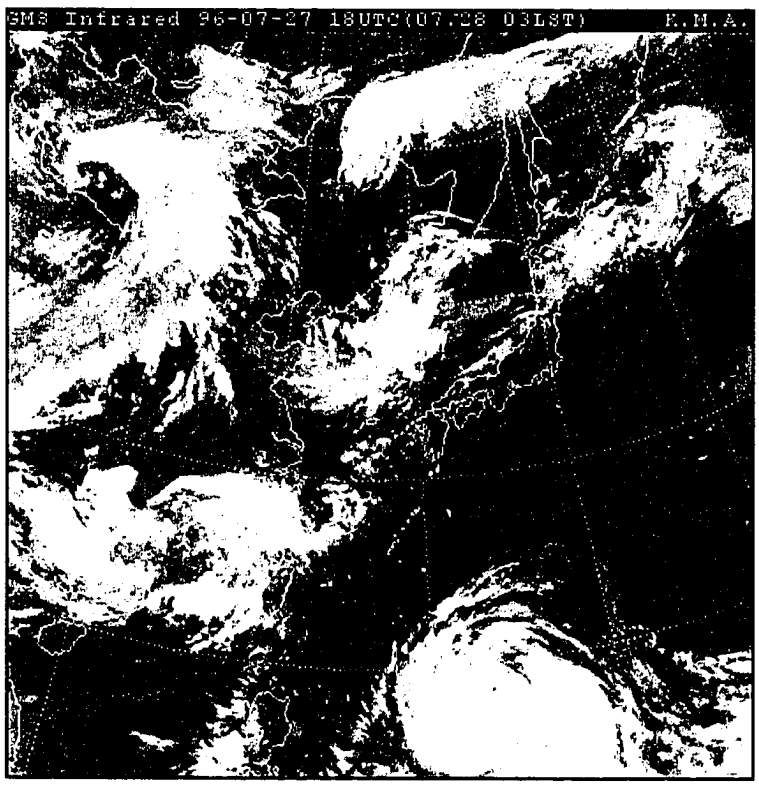

Fig. 3.6 (Continued).

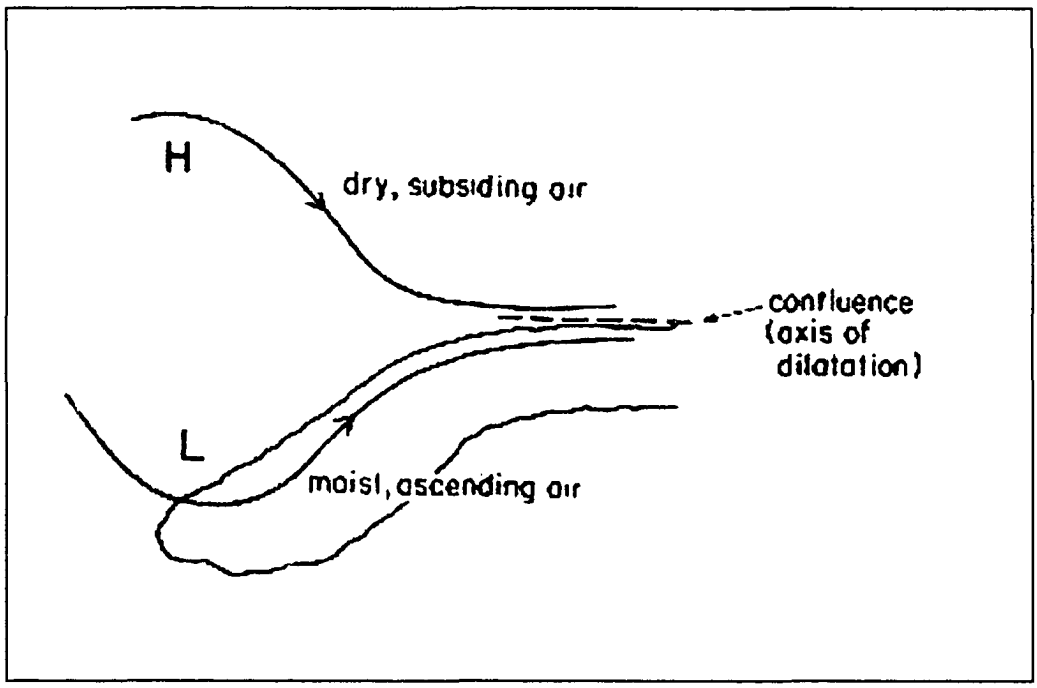

Fig. 3.7 Schematic of the relationship between the tropical cirrus cloud shield and the axis of dilation (confluence) (From Bluestein, 1993)

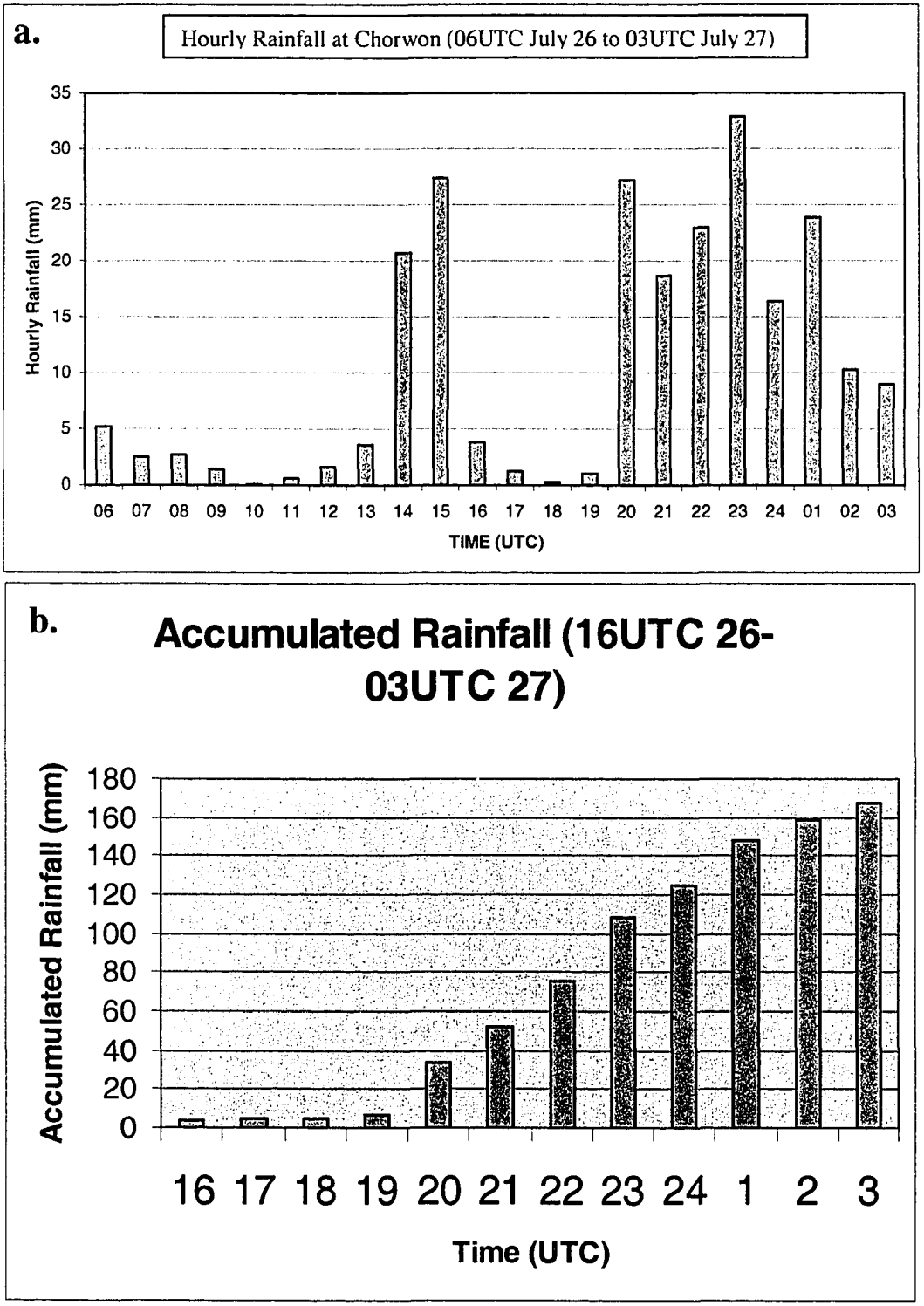

Fig. 3.8 Observed hourly rainfall (mm) recorded from 06 UTC July 26 to 03 UTC July 27 (a) and observed accumulated rainfall recorded from 16 UTC July 26 to 03 UTC July 27 (b) at Chorwon.

Chorwon region from 1900UTC on July 26 to 0100UTC on July 27. Future forecasting work in this study will be focused on this heavy rainfall time period. In this subsection, sub-synoptic scale analyses will be presented to denote this local heavy rainfall event by examining **Q**-vector divergence fields and observed radar reflectivity.

3.2.1 Q-vector Analysis

The omega equation, used to calculate vertical motion, can be rewritten in a proportionality form using the **Q**-vector: $\omega \propto \nabla \bullet \mathbf{Q}$, (See below for a discussion of the validity of this expression.) where ω is a vertical velocity (dp/dt). The **Q**-vector defined as

$$\mathbf{Q} = -\frac{R}{\sigma p}\begin{pmatrix} \frac{\partial \mathbf{v}_g}{\partial x} \bullet \nabla_p T \\ \frac{\partial \mathbf{v}_g}{\partial y} \bullet \nabla_p T \end{pmatrix}, \qquad (3.1)$$

where R is the gas constant for dry air (287.04 J kg^{-1} K^{-1}), σ is the static-stability parameter (m^2 s^{-2} kPa^{-2}), and $\mathbf{v}_g$ is the geostrophic wind vector. The proportionality form shows that **Q**-vector divergence is a good indicator of vertical motion. Namely, upward vertical motion (lifting) occurs in regions of **Q**-vector convergence, while downward motion (sinking) exists in regions of **Q**-vector divergence (Djuric, 1994). Although the analysis of **Q**-vector divergence is useful for determining vertical motion, other factors not considered in the **Q**-vector formulations preclude an exact correspondence between **Q**-vector divergence and ω. Although the quasi-geostrophic approximation enables us to isolate simple physical processes through the elimination of meteorologically insignificant wave motion, such as high frequency inertial gravity waves, the real

atmosphere is not exactly quasi-geostrophic so that a more accurate representation is needed for numerical weather prediction (Bluestein 1992). Thus, the **Q**-vector divergence field only approximates the real ω field and the **Q**-vector divergence (convergence) is not exactly correlated with sinking (rising) motion. In this section, **Q**-vector divergence (convergence) is used only for qualitative evaluation of wave-type structures to examine if the **Q**-vector divergence (convergence) can be roughly correlated with rainfall regions.

To estimate the vertical motion field in the heavy rainfall region, **Q**-vector divergence fields at 850hPa were examined from 0000UTC on July 26 to 1200UTC on July 27 at 12-hour intervals (Fig. 3.9). The region over the Yellow Sea and the KP, including the heavy rainfall region (central part of the KP) was dominated by **Q**-vector convergence at 0000UTC on July 27. This fact indicates that lifting of warm air at 850hPa occurred, underneath relatively cool air at higher levels, during this time period. This led to more unstable conditions that contributed to the production of heavy rain. Over the heavy rainfall region, the values of **Q**-vector convergence were approximately -6.0 x 10^{-16} kPa/m^{2}s at 0000UTC on July 26, -2.0 x 10^{-16} kPa/m^{2}s at 1200UTC on July 26, -5.0 x 10^{-16} kPa/m^{2}s at 0000UTC July 27, and almost zero at 1200UTC on July 27. Compared to these values, the rising motion over the heavy rainfall region decreased slightly by 1200UTC on July 26 (Fig. 3.9b) increased again by 0000UTC on July 27 (Fig. 3.9c), and finally almost disappeared at 1200UTC (Fig. 3.9d). At 000UTC on July 27 (Fig. 3.12c), in particular, the contours of **Q**-vector convergence over the Yellow Sea to the east of the KP tilted southwest to northeast. This shape can lead to frontogenesis over the central part of the KP, with **Q**-vectors pointing toward the region of warm air (not

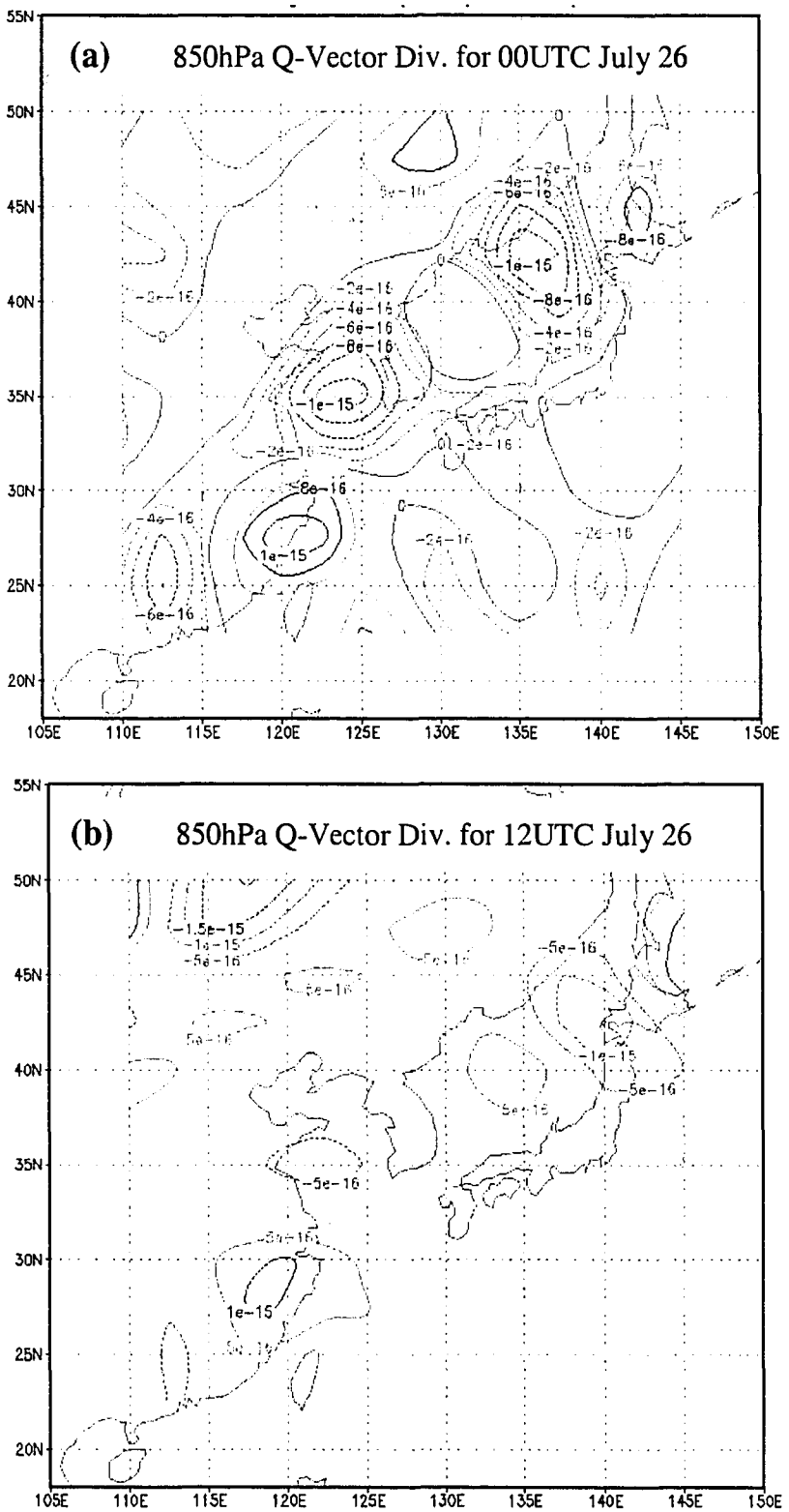

Fig. 3.9 850hPa Q-Vector divergence at (a) 0000UTC July 26, (b) 1200UTC, (c) 0000UTC July 27, and (d) 1200UTC (kPa/m^{2}s, positive value means divergence).

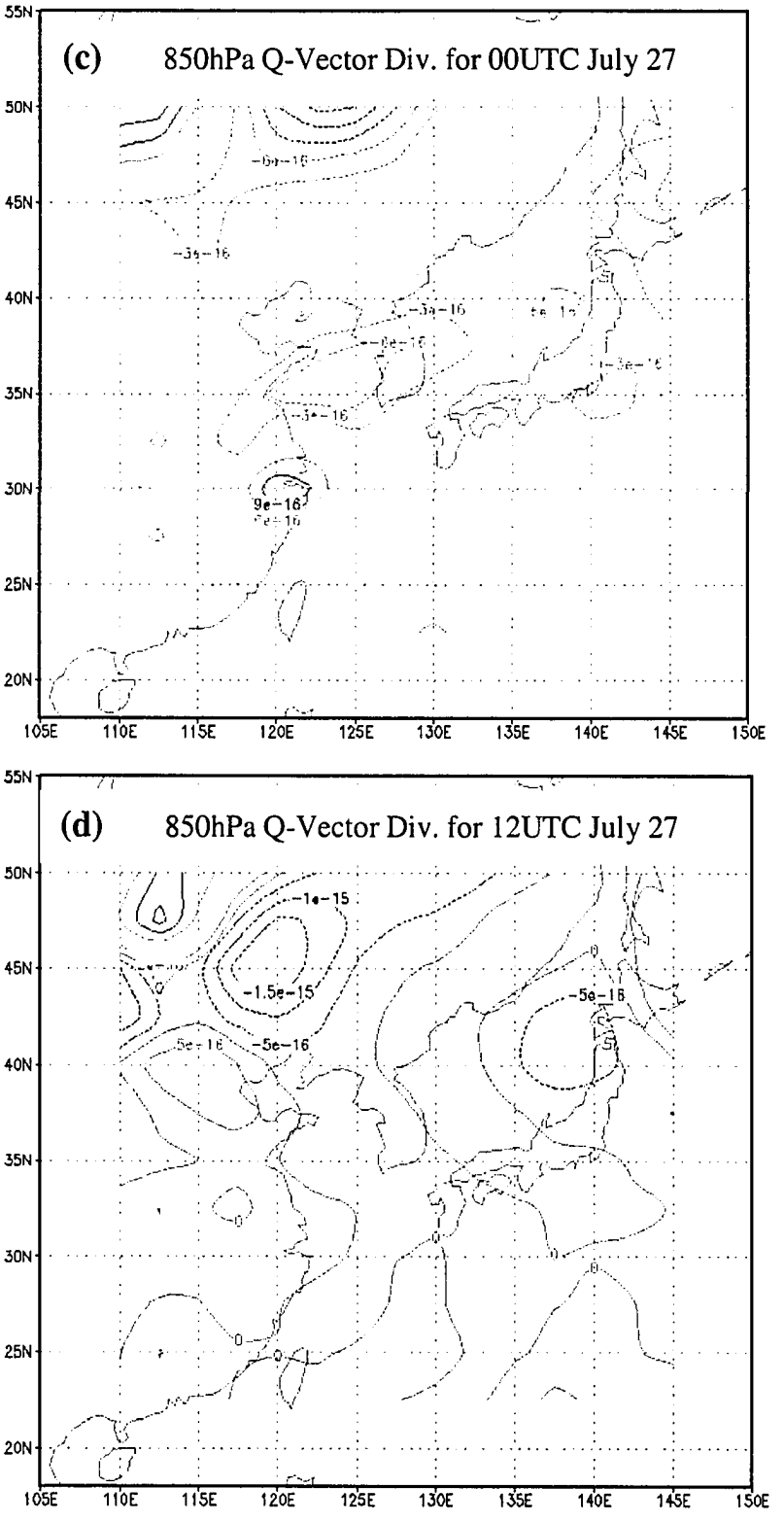

Fig. 3.9 (Continued).

shown here). As a result of the increased **Q**-vector convergence and frontogenesis at 0000UTC on July 27, the greatest rainfall over the central part of the KP could be expected just before and after 0000UTC on July 27. This expectation coincides with the observed hourly rainfall at Chorwon (Fig. 3.8a). Overall, we find that the Q-vector divergence field offers only an approximate indication of the region of heavy rainfall.

3.2.2 Radar Images

WSR-88D Doppler radar coverage radii are 460 km and 230 km for maximum reflectivity and Doppler velocity, respectively. Because the heavy rainfall region, including the Chorwon-Yonchon area, is within 150 km of the RKSG radar site (Pyoungtaek, Korea), it is reasonable to use radar data as a tool for sub-synoptic analysis.

Figure 3.10 shows the observed hourly radar reflectivity (horizontal reflectivity at the lowest elevation angle, 0.48°) from the RKSG WSR-88D radar from 1500UTC on July 26 to 0300UTC on July 27 (as shown in Fig. 3.8, the greatest hourly rainfall at Chorwon occurred during this time period). The filled circle and the filled rectangle on each figure indicate Chorwon and Yonchon, respectively.

Although clouds had continually moved over the Korean peninsula from the Yellow Sea, as shown in the satellite images (Fig. 3.6), it is difficult to find any strong convective clouds upstream of the KP, except at 0600UTC on July 27 (Fig. 3.6f). Instead, the strong storms developed after the clouds from the Yellow Sea had moved inland over the KP. This can be confirmed by the radar images, which show that higher values of reflectivity (exceeding 41 dBZ, with the colors of very light green, yellow and red) were found in the central and eastern part of the KP, but not in the west coastal

region during the entire time period. Considering only satellite images, giant convective clouds seemed to cover the central part of the KP. As shown in these radar images, however, convective activity occurred in a very small area and high-level cirrus and stratus clouds covered the other regions.

During the entire time period, reflectivity values less than 33 dBZ (with the colors of dark green and blue) covered the central part of the KP, with scattered strong echoes exceeding 41dBZ representing the strongest convection at that time. At 1900UTC on July 26 (Fig. 3.10e), the scattered strong echoes started to merge. At 2000UTC on July 26 (Fig. 3.10f), a large region of high reflectivity developed over the northern part of the Chorwon region and maintained its shape through 2200UTC on July 26 with a slight movement to the south. From 1900UTC on July 26 (Fig. 3.10e). high reflectivity (41 dBZ, with the color of very light green) was present over the Chorwon region, and the echo continued to evolve through 2200UTC on July 26 (41-45 dBZ at 2000UTC (Fig. 3.10f), 45-49 dBZ at 2100UTC (Fig. 3.10g), 49-53 dBZ at 2200UTC (Fig. 3.10h)). These developing echoes over the Chorwon region are consistent with the observed hourly rainfall at the Chorwon station (Fig. 3.8); 18.7 mm –2000UTC to 2100UTC, 23.0 mm –2100UTC to 2200UTC, and 32.9 mm –2200UTC to 2300UTC (the greatest hourly rainfall time). At 2300UTC on July 26 (Fig. 3.10(i)), the high reflectivity over the Chorwon region had almost disappeared and a new storm, which appeared first at 2200UTC (Fig. 3.10 (h)), developed very rapidly (exceeding 53 dbZ, with the color of light orange). This new storm had not changed its position by 0200UTC on July 27 (Fig. 3.10 (l)), and started to decay by 0300UTC on July 27 (Fig. 3.10 (m)).

Considering all of the radar images, the heavy rainfall event was highly local and strong storms developed locally and moved very little. Orographic effects can be inferred as one of reasons for this heavy behavior, as Chorwon is located at the west of Taeback Mountains.

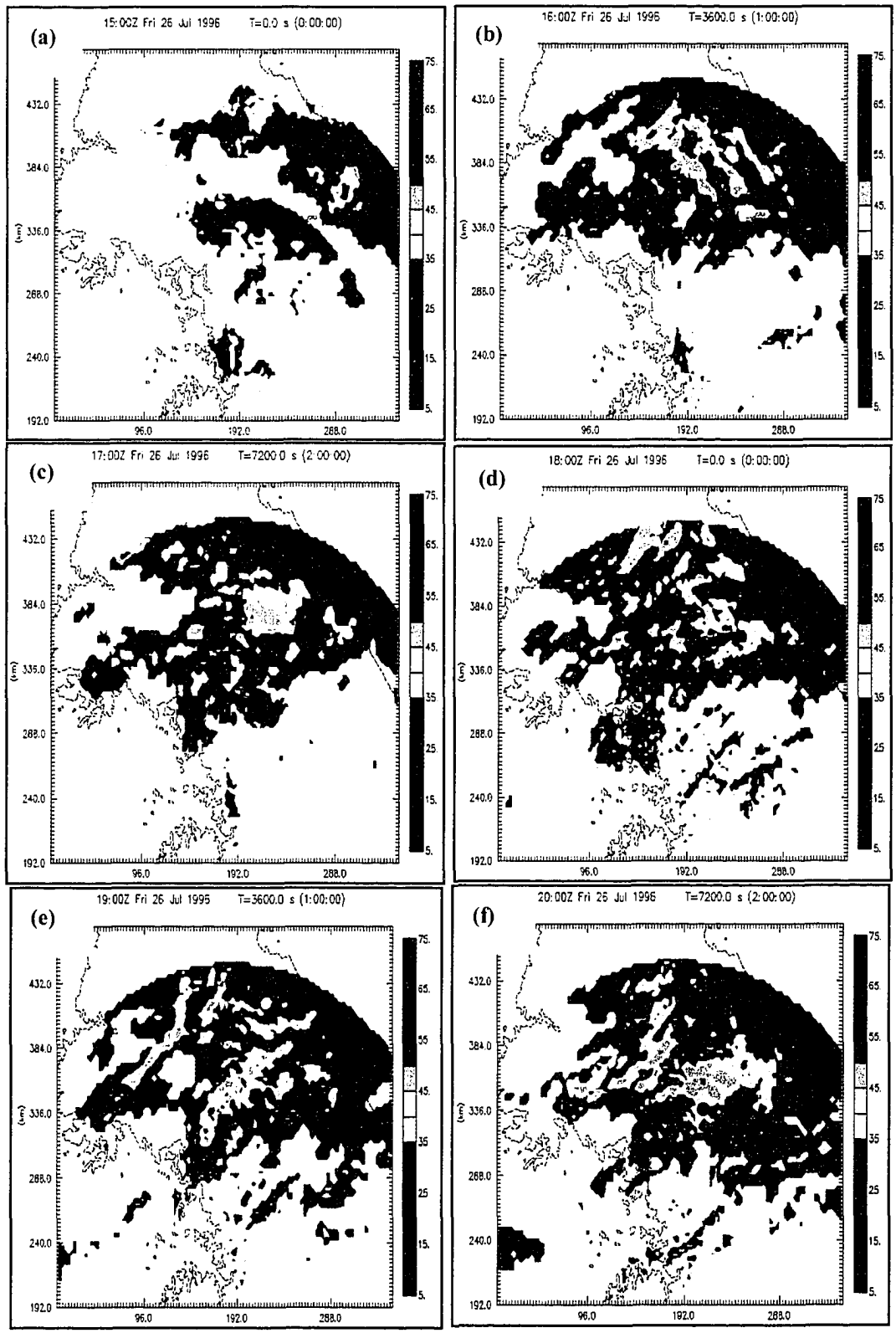

Fig. 3.10 WSR-88D reflectivity (at the lowest elevation angle) obtained from the RKSG radar at (a) 1500UTC July 26, (b) 1600UTC, (c) 1700UTC, (d) 1800UTC, (e) 1900UTC, (f) 2000UTC, (g) 2100UTC, (h) 2200UTC, (i) 2300UTC, (j) 0000UTC July 27, (k) 0100UTC (l) 0200UTC, and (m) 0300UTC.

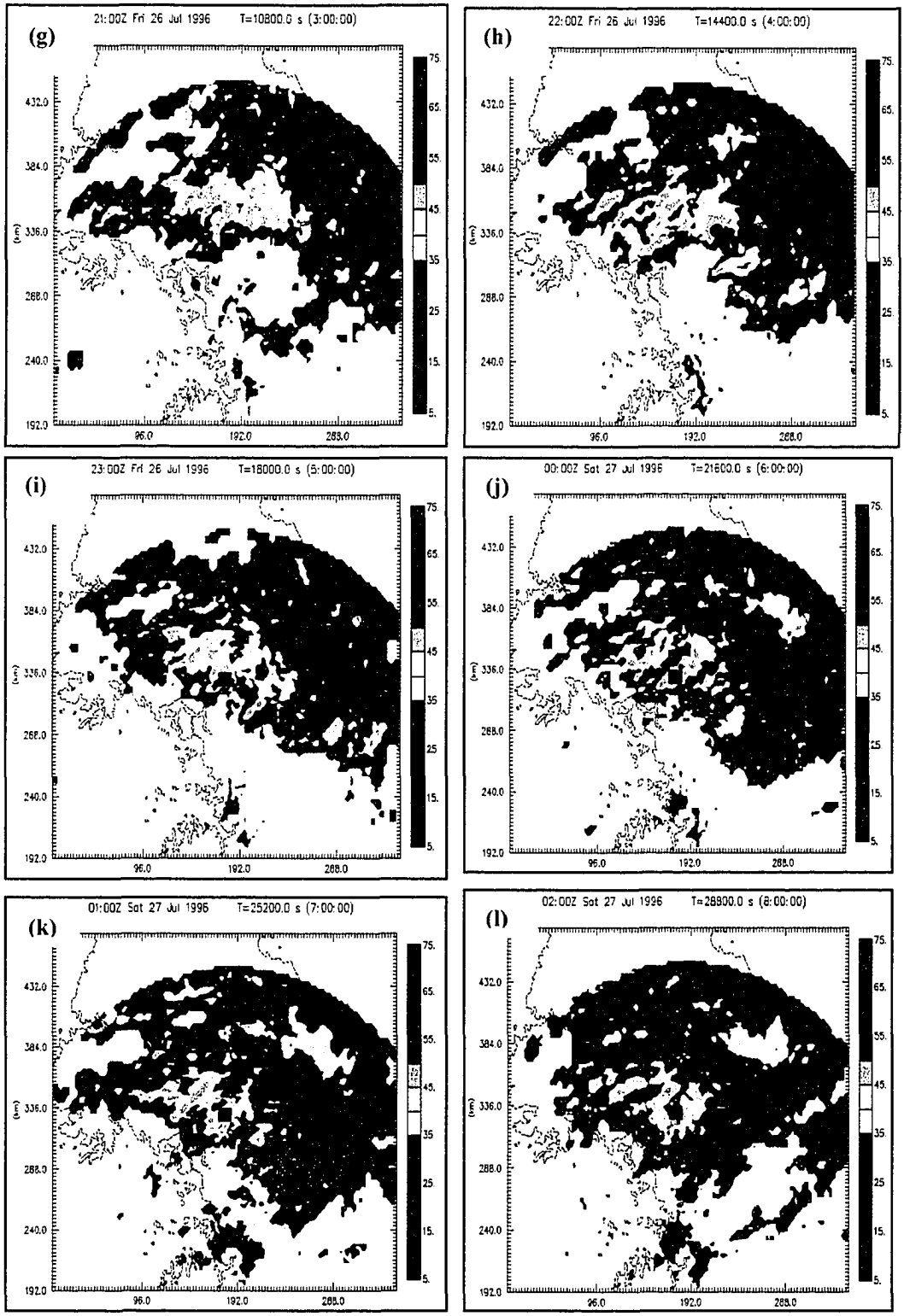

Fig. 3.10 (Continued)

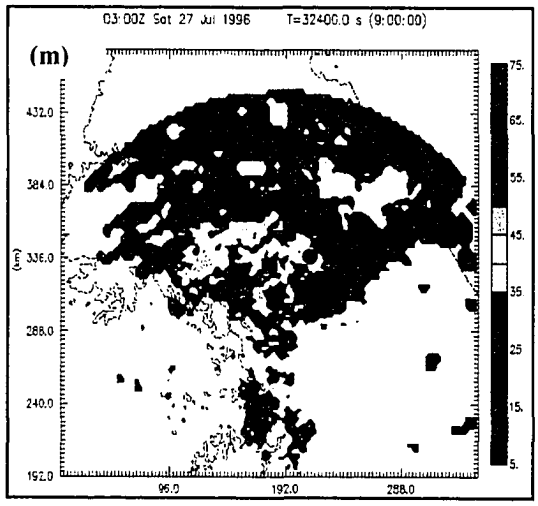

Fig. 3.10 (Continued)

Chapter 4

Numerical Model and Experiment Design

4.1 The Numerical Model: Advanced Regional Prediction System (ARPS)

The Advanced Regional Prediction System (ARPS), including the ARPS Data Assimilation System (ADAS), was developed at the Center for Analysis and Prediction of Storms (CAPS) at the University of Oklahoma. Xue et al. (2000, 2001) denote the features and advantages of the ARPS as follows:

> "The ARPS was designed from the beginning to serve as an effective tool for basic and applied research and as a system suitable for explicit prediction of convective storms as well as weather systems at other scales. The ARPS includes its own data ingest, quality control and objective analysis packages, a data assimilation system which includes single Doppler velocity and thermodynamic retrieval algorithms, the numerical prediction component, and a self-contained post-processing, diagnostic and verification package. The numerical prediction component of the ARPS is a three-dimensional, nonhydrostatic compressible model formulated in generalized terrain-following coordinates. The ARPS also includes state-of-the-art physics parameterization schemes that are important for explicit prediction of convective storms as well as the prediction of flows at larger scales."

The ARPS User's Guide Version 4.0 (Xue et al. 1995) provides a detailed description of the formulation, physics parameterizations, computational implementation,

and numerical solution methods for the ARPS. Significant improvements have been made to the ARPS system since the ARPS Version 4.0 was officially announced in the mid-90s. Xue et al. (2000; 2001) describe the more recent improvements for the ARPS system. Overall, the key features employed in the ARPS are as follows: (1) nonhydrostatic compressible dynamics, (2) comprehensive physics packages including cloud microphysics parameterization, cumulus parameterization, non-local PBL parameterization, and the inclusion of snow cover and refinement of the current land surface-vegetation model; and (3) a complete data ingest and analysis system capable of dealing with various observational data sources, including Doppler radar data and satellite data. The simulations described in this study were made using ARPS Version 4.5.1.

4.2 ARPS Data Assimilation System (ADAS)

A separate software package, the ARPS Data Assimilation System (ADAS), is used for initializing the ARPS. ADAS contains sophisticated data quality control procedures and is used to interpolate observed data onto the ARPS grid (Brewster, 1996) using a successive correction scheme (Bratseth 1986) applied to the grid relative winds (u and v), pressure, potential temperature and specific humidity. Other meteorological variables are analyzed using straightforward modification. Largely following Brewster (1999), this section describes briefly the cloud analysis scheme and associated treatment of radar data in ADAS – both of which are crucial elements of the present study.

Figure 4.1 depicts schematically the treatment of radar data in ADAS. In the first step, all raw radar data (here referring to the Level II or base radial velocity and reflectivity data received from the radar, without any further quality control) are remapped onto the ARPS grid and then averaged. NIDS or Level III data could be accommodated, though with a loss of accuracy owing to value quantization; thus, only Level II data are used in the present study. Next, the remapped data are read and precipitation terminal velocity is removed, after which the radial velocity data are converted to increments of u and v wind components. These u and v increments are created by subtracting the observed radial wind at each grid, v_{r_g}, from the dot product of the analysis wind and the radar azimuth angle, ϕ at the same point.

The equations used to impute the velocity correction assigned in a direction parallel to the azimuth angle are given by

$$u'_g(x,y,\phi) = \cos\phi[v_{r_{gh}} - (\sin\phi u(x,y) + \cos\phi v(x,y)], \tag{4.1}$$

$$v'_g(x,y,\phi) = \sin\phi[v_{r_{gh}} - (\sin\phi u(x,y) + \cos\phi v(x,y)], \tag{4.2}$$

where $v_{r_{gh}}$ is the horizontal wind in the radial direction determined from the observed v_{r_g}. For practical computation of remapping work in ADAS, the former is defined as the radial wind and the slope of ray path with respect to curved earth

$$v_{r_{gh}} = v_{r_g}(\frac{\partial s}{\partial r})^{-1}, \tag{4.3}$$

where s is the surface range (distance along the earth's surface), r is the slant range (distance along radar radial). $\frac{\partial s}{\partial r}$ is obtained from the local slope of radar beam using

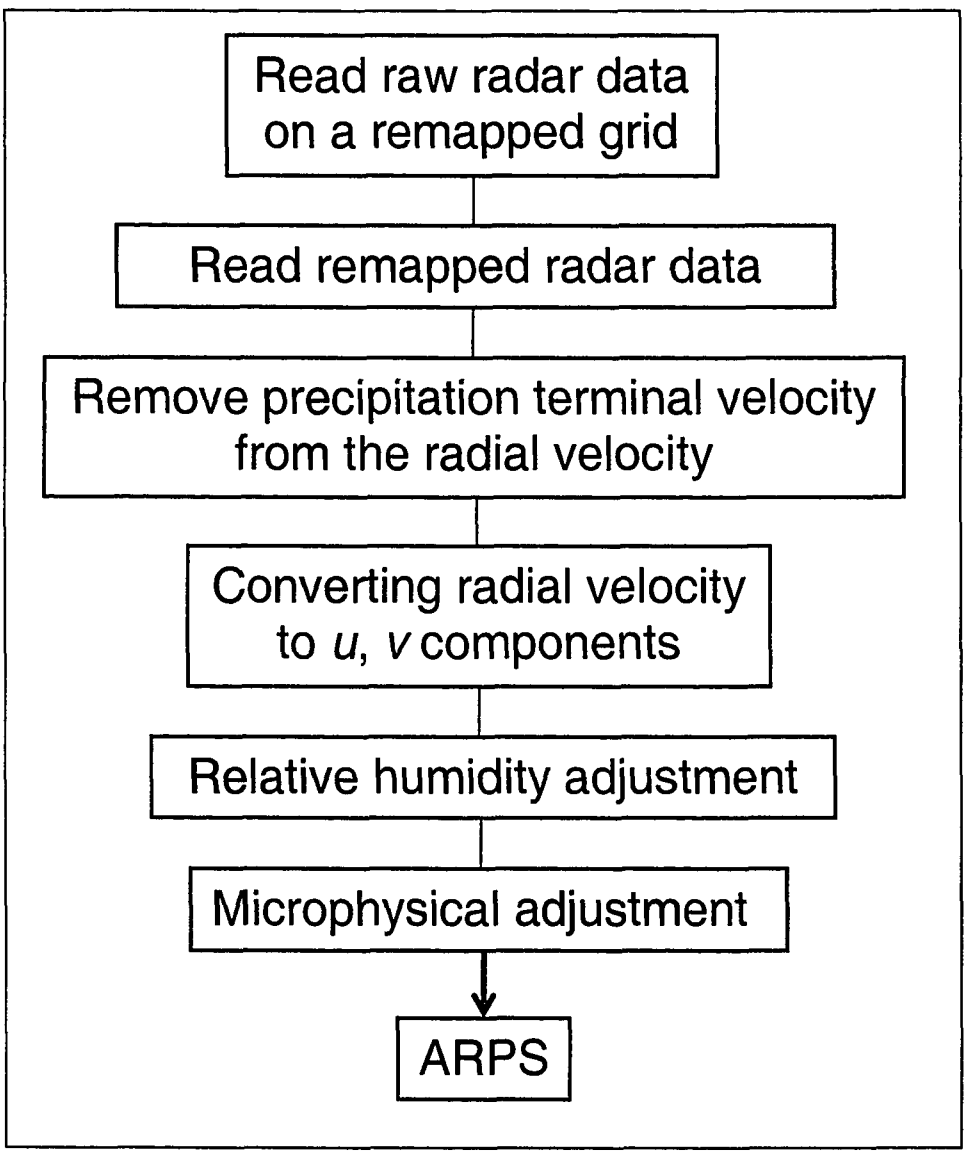

Fig. 4.1 Algorithm for the treatment of radar data in ADAS

$\left(\frac{\partial s}{\partial r}\right)^2 + \left(\frac{\partial h}{\partial r}\right)^2 = 1$, where h is the height of above the antenna height of the beam and $\frac{\partial h}{\partial r}$ is the local slope of the radar ray path with respect to the curved Earth, determined from the 4/3rds Earth approximation.

4.2.1 ADAS Cloud Analysis

ADAS contains a module for cloud analysis using cloud cover and height from surface observations, as well as radar and satellite data (Zhang et al., 1998; Zhang 1999). This module was derived and modified from the complex cloud analysis of the Local Analysis and Prediction System (LAPS, Albers et al., 1996). In the ADAS cloud analysis, users can select a variety of options to determine which observed variables from the cloud analysis contribute to the final output file (Brewster, 1999). Further, the results obtained from this ADAS analysis are used as the base for a moisture and diabatic initialization as well as the initialization of the ARPS condensate fields. The following description of the ADAS cloud analysis largely follows the Zhang (1999) study.

Figure 4.2 shows a schematic diagram of the ADAS cloud analysis used in this study. It consists of three parts; (1) 3-D cloud distribution analysis including VCF (Volumetric Cloud Fraction) analysis, (2) cloud water (q_c and q_i) content analysis, and (3) precipitation content analysis. In the ADAS 3-D cloud distribution analysis, the background VCF field is obtained from the ADAS relative humidity (RH) analysis. An empirical relationship is employed for this process (following Zhang, 1999).

$$VCF = \left(\frac{RH - RH_{th}}{1.0 - RH_{th}}\right)^b, \tag{4.4}$$

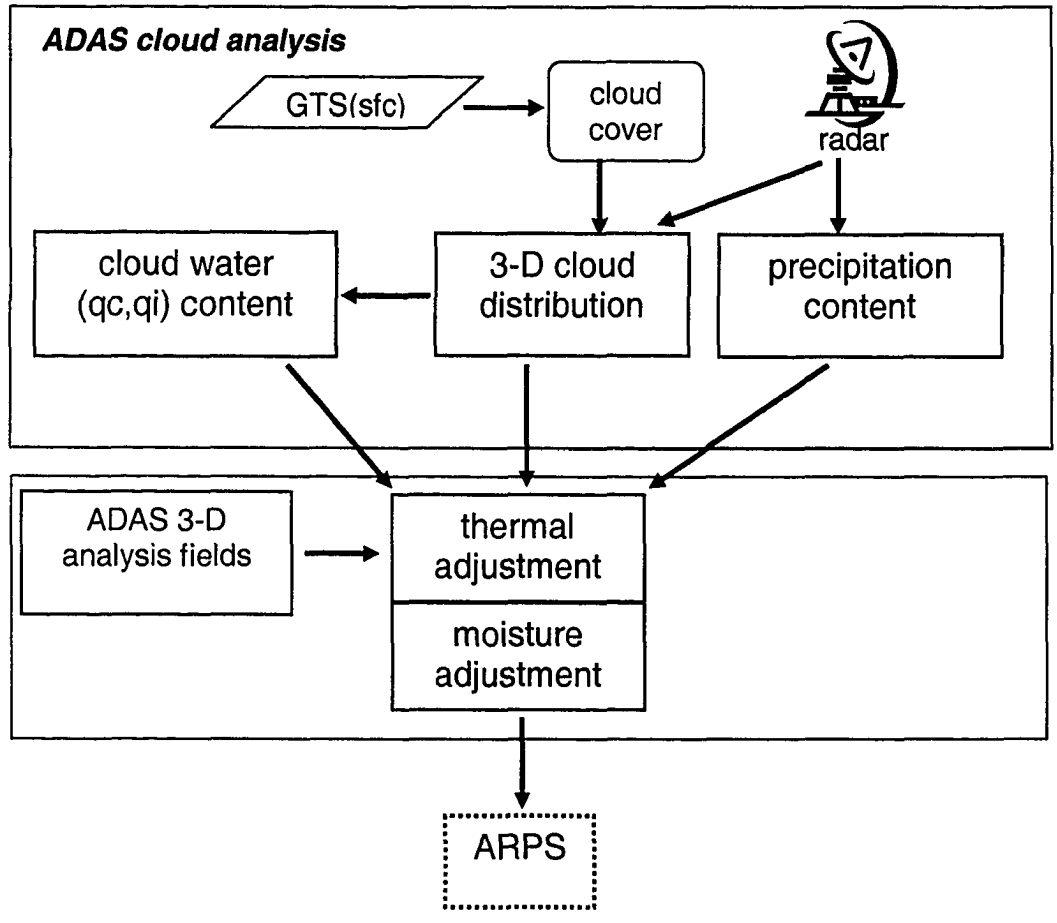

Fig. 4.2 Schematic diagram of the ADAS cloud analysis used in this study (shaded area indicates the ADAS cloud analysis scheme).

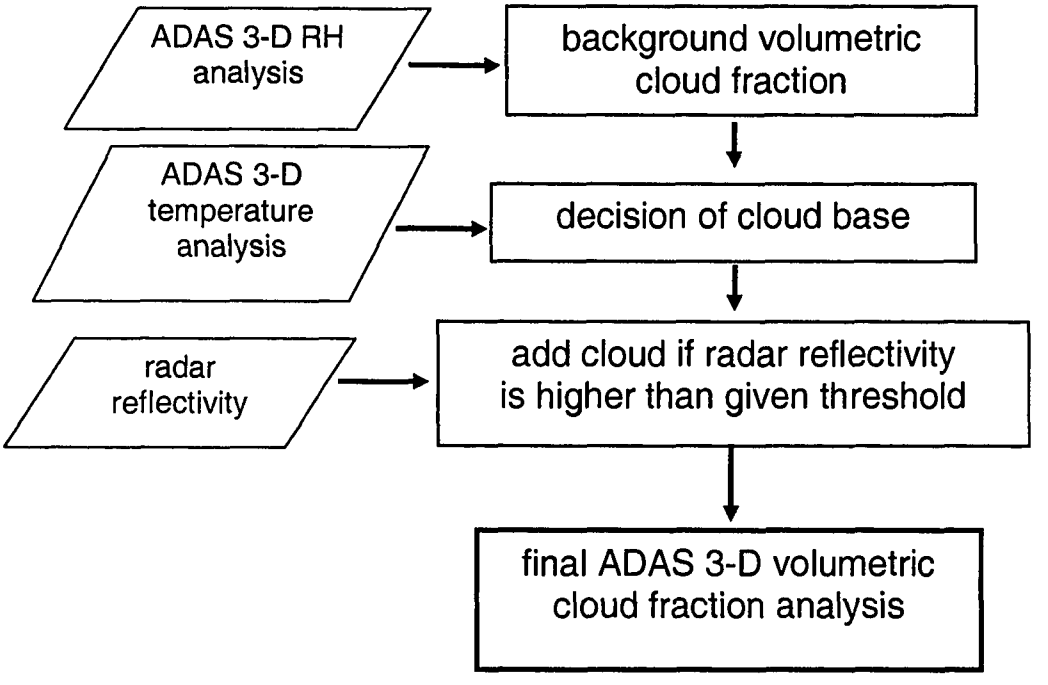

Fig. 4.3 Schematic diagram of the ADAS volumetric cloud fraction analysis used in this study (modified from Zhang 1999).

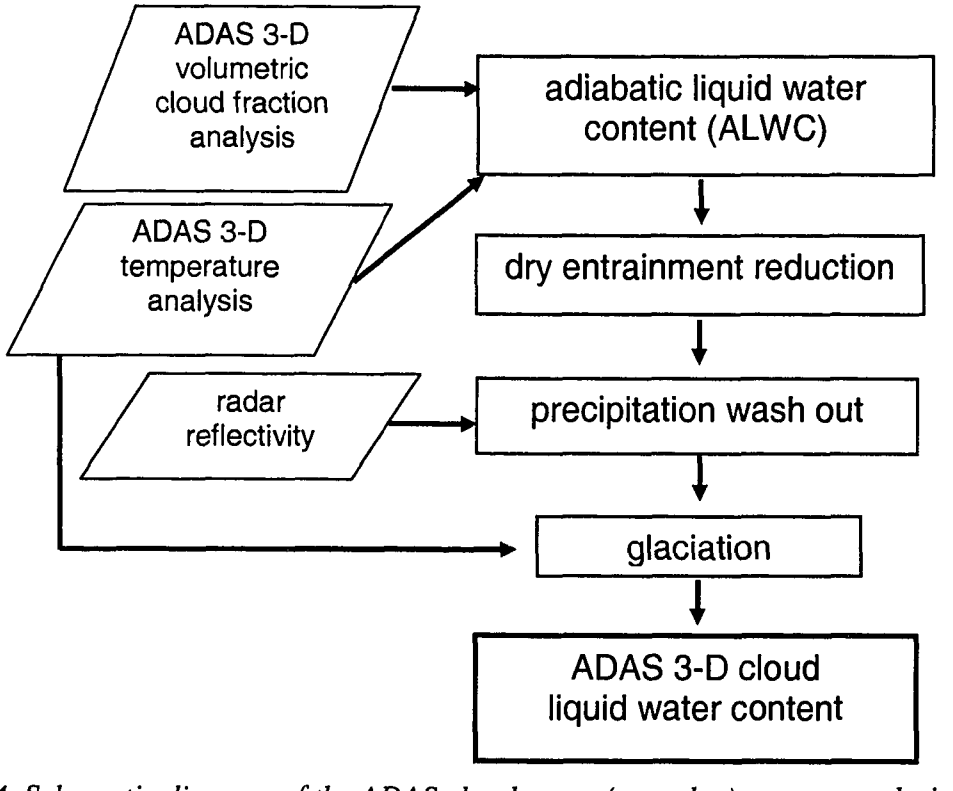

Fig. 4.4 Schematic diagram of the ADAS cloud water (q_c and q_i) content analysis used in this study (modified from Zhang 1999).

where RH is the relative humidity, RH_{th} is the threshold of RH, and b is an empirical constant set to 2 in the present study. Clouds with VCF = 1.0 are inserted in the radar echo region above the lowest cloud base if the reflectivity exceeds a threshold. In this study, cloud base is the lifting condensation level obtained from the ADAS temperature analysis because no sounding data are used. The radar threshold to insert radar reflectivity in this study is 25 dBZ for points below 2,000 m AGL and 20 dBZ for points above 2,000 m AGL. Figure 4.3 depicts the VCF analysis process.

In the second step of VCF analysis, cloud water (q_c and q_i) content (liquid and frozen) analysis is analyzed (Fig. 4.4). The cloud water (q_c and q_i) for the regions where the cloud fraction is over the given threshold are computed following Zhang's (1999) method which is based on Smith-Feddes model (Albers et al. 1996). The adiabatic liquid water content (ALWC) is introduced in this analysis defined as

$$ALWC_k = ALWC_{k-1} + q_{vs,k-1} - q_{vs,k}, \tag{4.5}$$

where k is the vertical grid index and q_{vs} is the saturation specific humidity. An assumption of moist ascent from cloud base to cloud top is employed to estimate the ALWC. When temperatures are warmer than -10°C, the ALWC is parameterized as all liquid water, while the ALWC is parameterized as all ice for temperatures colder than -30°C.

In the third component, or precipitation content analysis, the precipitate starts as snow and rain when the wet bulb temperature at the echo top is below 0°C and over 0°C, respectively. The precipitates are obtained from radar reflectivities directly. The following empirical relation is used for computing rain water (Kessler 1969)

$$Z = 1.73 \times 10^4 (\rho q_r)^{1.75}, \tag{4.6}$$

where Z is the reflectivity factor in mm^6/m^3, ρ is the air density in kg/m^3, and q_r is the rain water mixing ratio. Another empirical relation (Rogers and Yau 1989) for computing snow is defined as

$$Z = 3.8\times10^4(\rho q_s)^{2.2}, \tag{4.7}$$

where q_s is the snow mixing ratio.

4.2.2 Diabatic and Moisture Initialization/Adjustment

The role of diabatic initialization is to force vertical motion and associated divergence in a manner consistent with processes responsible for creating observed precipitation. The moisture initialization process seeks to provide sources for cloud condensation, and to maintain vertical circulations produced by diabatic initialization (Zhang 1999). In the present study, we use the Zhang (1999) diabatic and moisture initialization scheme. In it, a thermal adjustment is introduced to compensate the negative buoyancy produced by the cloud and precipitation analyses. Although the thermal adjustment can produce appropriate vertical circulations in the cloud and rain regions, these circulations cannot be maintained if continued condensation is not produced in a saturated updraft. Thus, the moisture adjustment process is also needed to retain consistent cloud condensation. The moisture adjustment used in this study imposes minimum RH values in the diagnosed cloudy region, after which the q_v field is adjusted following the Zhang's scheme.

The following buoyancy-preserving formulation is employed for the thermal and moisture adjustments:

$$\Delta\theta' = \bar{\theta}\left[\frac{(\Delta q_v' + \Delta q_w)}{(1+\bar{q}_v)} - \frac{\Delta q_v'}{(\varepsilon+\bar{q}_v)}\right], \tag{4.8}$$

where $\Delta\theta'$ is the temperature perturbation increment, $\Delta q_v'$ is the specific humidity perturbation increment, Δq_w is total water increment, and $\varepsilon = 0.622$. We also note in the present study that thermal adjustment is employed in advance of the moisture adjustment to ensure the pre-specified minimum RH in clouds.

An advanced latent heating adjustment in ADAS (not used in the present study) can also be employed owing to the relationship between the thermal field and latent heating by cloud condensation (Zhang 1999; Brewster 2002). The simple latent heating adjustment is defined as

$$\begin{aligned} \Delta\theta' &= \beta_\theta L_v(\Delta q_c + \Delta q_i)/(C_p\pi), \\ \pi &= (p/p_0)^{R_d/C_p} \end{aligned}, \tag{4.9}$$

where β_θ is a weighting factor between 0 and 1 that is applied to avoid excessive temperatures, L_v is the latent heat of vaporization for water, p is pressure, Δq_c is the cloud water increment and Δq_i is the cloud ice increment in kg/kg, C_p is the specific heat of air at constant pressure, p is pressure, p_0 is 1000 hPa, and R_d is the gas constant for dry air. This simple latent heating adjustment will be considered in the future work.

4.2.3 Correlation Ranges Used for the Observations in ADAS

In ADAS, it is important to use correlation range values in the horizontal and vertical dimensions consistent with the spacing of observations used. When the correlation range is smaller than the average spacing of the observations, coarse data can be omitted, preventing the generation of spurious bullseyes around isolated stations

(Brewster, 1998). Furthermore, the impact of any observation may be affected by the correlation ranges.

Table 4.1 shows correlation ranges and observations used in the 3 km radar data assimilation experiments. In this table, R and R_z indicate the horizontal vertical correlation range, respectively. The SYNOP data are used in only the first iteration with the 10 km horizontal range and 300 m vertical range. The AWS data are denser and thus are used in the second iteration. Radar data, which are the finest scale observations used, relatively confined, with 6 km horizontal range and up to 80 m in vertical range. Via iterations according to correlation ranges, the AWS and SYNOP data are damped quickly to produce small scale increments and thus these data will have the smaller impact than radar data in 3 km experiments.

Table 4.1 The correlation ranges associated with observations for ADAS with 3 km dx in the case of radar data assimilation.

Pass	R (km)	R_z (m)	AWS	SYNOP	SHIP	BUOY	Radar	U/A
1	10	300	yes	yes	yes	no	no	no
2	10	200	yes	no	no	no	no	no
3	6	100	no	no	no	no	yes	no
4	6	100	no	no	no	no	yes	no
5	6	80	no	no	no	no	yes	no

4.3 Domain Setup and Computer Resources

Three domains are applied using one-way grid nesting. The number of points in each domain are 99x103x37, 115x139x37, and 144x187x37 for 27-km, 9-km, and 3-km horizontal resolutions, respectively. Following conventional procedures to avoid vertical imbalances among the nested grids, we used same number of vertical levels and same vertical grid spacing (400 m) in all domains. However, we used smaller vertical minimum grid spacing (20 m) in 3 km domain than that in 27 km and 9 km domains (50 m) since the finer terrain is employed in 3 km domain. Table 4.2 presents the configurations of domain and grid, including the values of latitude and longitude for the center of domain at each horizontal resolution. Figures 4.5 and Figure 4.6a,b show the terrain used in this study for the 27-km, 9-km, and 3-km grids, respectively. As shown in Figure 4.6b, Chorwon is located approximately 250 m MSL and a mountain of altitude ~700 m height is positioned just to the east.

All simulations were performed on the Cray-J90 computer at the University of Oklahoma. However, the conversion of NEXRAD data to ADAS format was conducted on a Sun SPARC workstation.

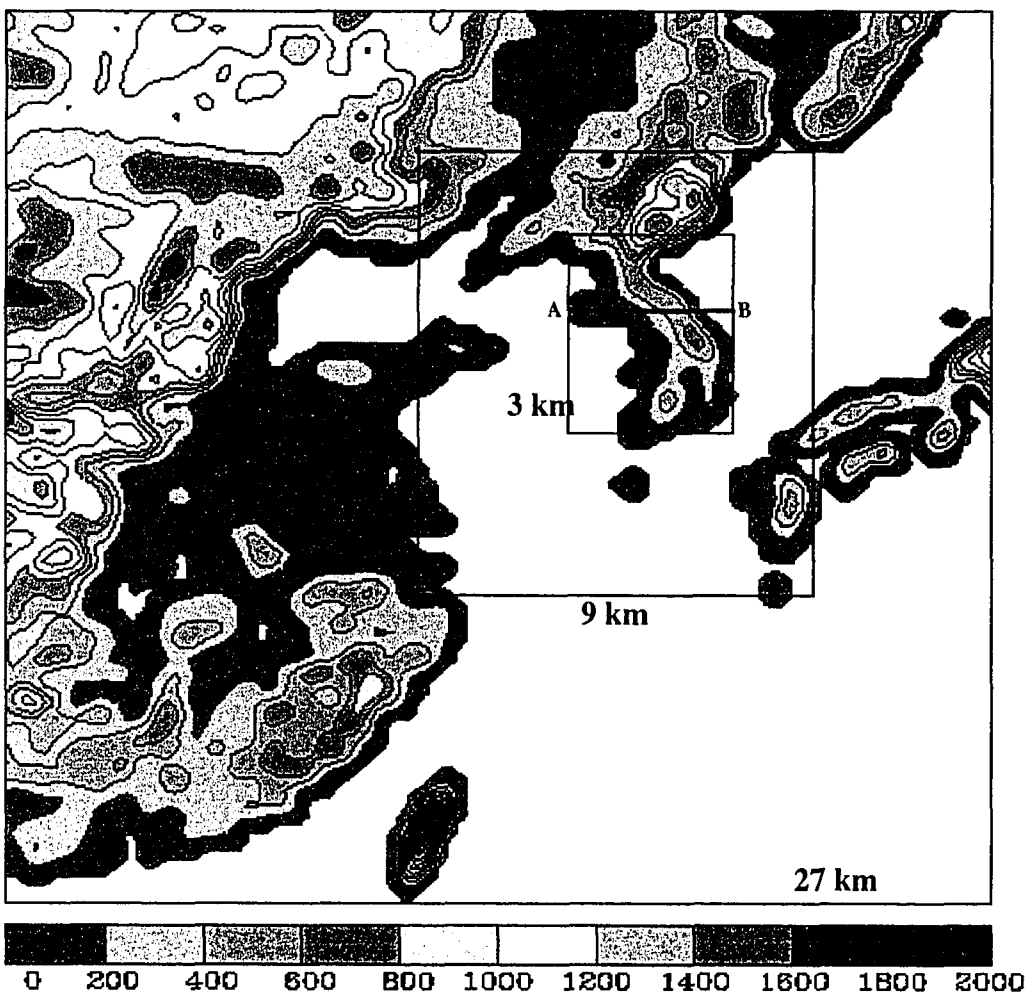

Fig. 4.5. The analysis and prediction domains and the terrain for the 27-km grid.

Table 4.2 The configurations of domain and grid.

Horizontal Resolution	Grid	Center of Domain
27 km	99 x 103 x 37	34.0N, 122.5N
9 km	115 x 139 x 37	36.0N, 126.0E
3 km	144 x 187 x 37	37.5N, 127.3E

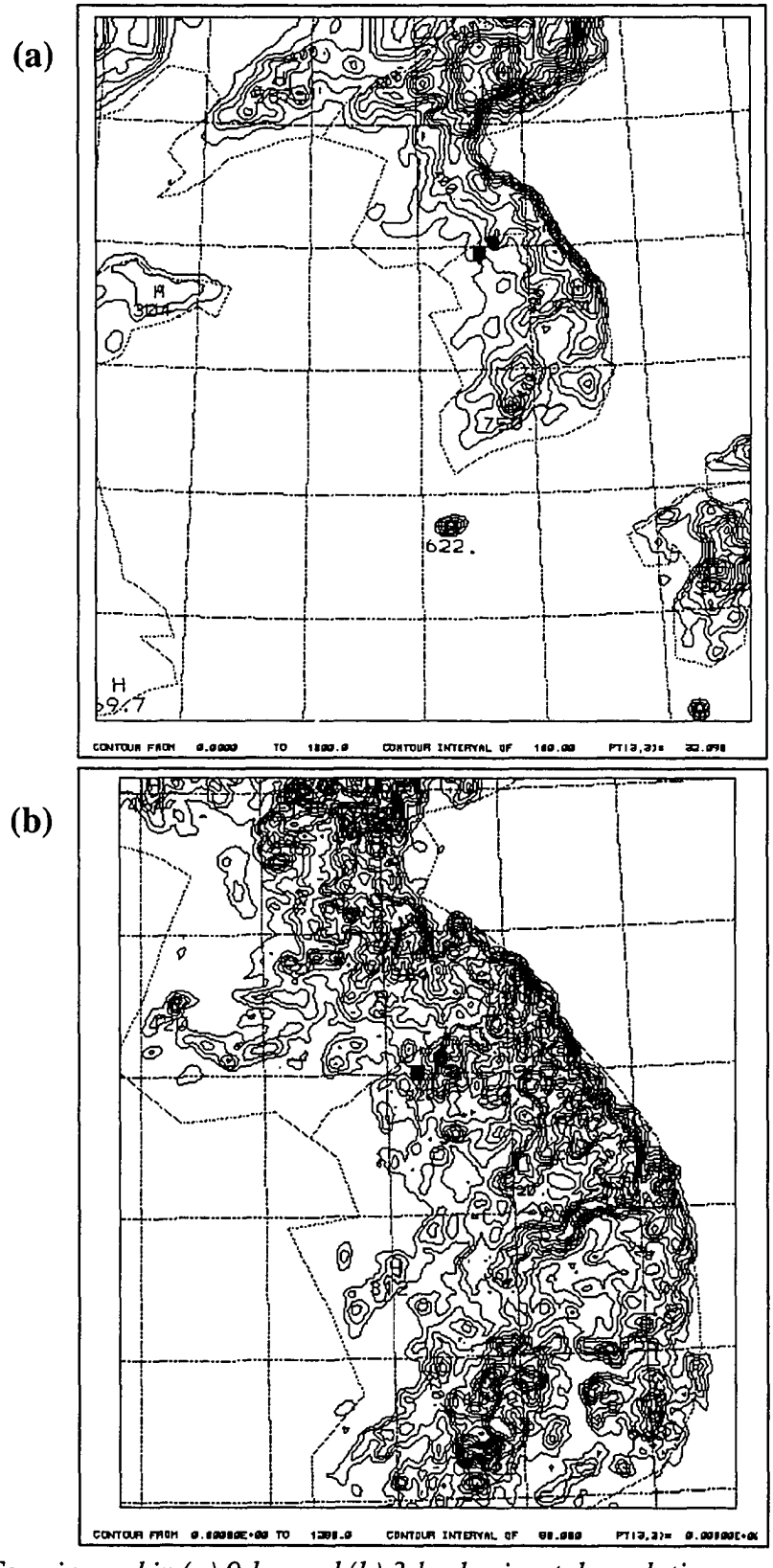

Fig. 4.6 Terrain used in (a) 9-km and (b) 3-km horizontal resolutions experiments, respectively. The filled circle and the filled rectangle indicate the positions of Chorwon and Yonchon respectively.

4.4 NEXRAD (WSR-88D) Radar Data

Data from the WSR-88D radar (commonly referred to as NEXRAD) at the US Air Force Base in Pyoungtaek (RKSG) were used in this study. Table 4.3 presents a brief summary of the Pyoungtaek WSR-88D specifications. In general, two types of WSR-88D data are available for scientific use: Level II (also called "base") data and Level III data. Only Level II data are employed in this study because Level III data contain only the lowest four elevation scans, with the radial velocity and reflectivity values quantized in intervals of approximately 5 units. In contrast, WSR-88D Level II data include reflectivity, mean radial velocity and spectrum width at the full spatial and temporal resolution of the WSR-88D processor. Base reflectivity is a measure of the echo (return) intensity of targets (clouds, water droplets, dust, etc.) in the atmosphere. Mean radial velocity is a measure of the radial component of the velocity within the sampling area. The NEXRAD data were converted to ADAS format by means of the ARPS utility, 88d2ARPS, which remaps the raw radial coordinate NEXRAD data onto an ARPS Cartesian grid, and averages the data within each grid volume as a means of data thinning. Appendix A provides details of this process.

Table 4.3. WSR-88D specification summary (from Kim 2000 and NCDC Radar Data Inventories homepage, 2001).

Location	Pyungtaek (RKSG): 36.9558N, 127.0211E Elevation: 52ft (15.9m)
Coverage	Doppler: 124nm (230km)
	Maximum: 248nm (460km)
Wavelength	10cm S-Band
Power	Operational: 750kW, Maximum: 1MW
Antenna	Radius: 28ft (8.5m), Rotate 360°
Radome	Radius: 39ft (11.8m)
Beam Width	1°
Scan Strategy	Volume Coverage Pattern 11 (Severe Mode): 14 elevations in 5 minutes
	Volume Coverage Pattern 21 (Precipitation Mode): 9 elevations in 6 minutes
	Volume Coverage Pattern 31/32 (Clear Air Mode): 5 elevations in 10 minutes
Data Range	Wind: -64kts (inbound) ~ 64kts (outbound)
	Reflectivity: 0 ~ 75dBZ

4.5 Experiment Design

One way nesting is employed for all experiments using a horizontal resolution of 27-km for the coarse outer grid, 9-km for the middle grid, and 3-km for the inner fine grid. The 26 different experiments may be classified into four principal categories: (1) with and without radar data, (2) different background fields for the outer grid; (3) combinations of radial velocity and reflectivity; (4) different data assimilation strategies applied to radar data. Table 4.4 presents a summary of these experiments, with more detail provided in the following sub-sections.

Figure 4.7 presents a schematic representation of the 27-km and 9-km resolution experiments. Initial and lateral boundary conditions for the 27-km grid ARPS forecast were provided by the KMA 40-km, 18-hour operational Regional Data Assimilation and Prediction System (RDAPS) forecast initialized at 12UTC July 25, 1996. Although we would have preferred to use an analysis for the background field, none was available at the time during which we wished to initialize the ARPS (i.e., prior to the beginning of the heavy rainfall event). The 27-km ARPS control forecast, known as experiment 27R, is integrated for 21 hours (from 0600 UTC on 26 July until 0300 UTC on 27 July) using GTS (surface), AWS (KMA Mesonet), satellite (both IR and VIS) data at the initial time. At 27 km resolution, a numerical model is not capable of resolving convective circulations, and the area covered by the one radar is very small compared to the forecast domain. Thus, no attempt was made to utilize radar data in this case.

Table 4.4 Summary of All Experiments

Name	Horizontal Resolution	Initial Data	Convective Paramet.	Special Features
27R	27 km	GTS, AWS satellite	Kain-Fritsch	first guess field: RDAPS 18-hr forecast initialized at 12UTC July 25 (27 km old f.g.f.)
27R_n	same as 27R but for new first guess filed (RDAPS 6-hr forecast initialized at 00UTC July 26 (27 km new f.g.f.))			
09RNR	9 km	GTS, AWS satellite	Kain-Fritsch	27km old f.g.f.
09RNR_n	same as 09RNR but for 27 km new f.g.f.			
09RYR	9 km	GTS, AWS satellite **radar**	Kain-Fritsch	
09RYR_n	same as 09RYR but for 27 km new f.g.f.			
09RAR	9 km	GTS, AWS Satellite radar	Kain-Fritsch	**radar data assimilation**: **3 times** and **10 min.** data assimilation window
09RAR_n	same as 09RAR but for 27 km new f.g.f.			
03RNR	3 km	GTS, AWS	none	
03RNR_n	same as 03RNR but for 27 km new f.g.f.			
03RYR	3 km	GTS, AWS **radar**	none	using both of radial velocity and reflectivity
03RYR_n	same as 03RYR but for 27 km new f.g.f.			
03RYR_ref	same as 03RYR but for using only reflectivity in radar data			
03RYR_ref_n	same as 03RYR_ref but for 27 km new f.g.f.			
03ROR	3 km	radar	none	only radar data (both of radial velocity and reflectivity) for initial data
03ROR_n	same as 03ROR but for 27 km new f.g.f.			
03ROR_ref	same as 03ROR but for using only reflectivity in radar data			
03ROR_ref_n	same as 03ROR_ref but for 27 km new f.g.f.			
03RAR	3 km	GTS, AWS	none	**radar data assimilation**: **3 times** and **10 min.** (50-00 period) data assimilation window
03RAR_n	same as 03RAR but for 27 km new f.g.f.			
03RAR_1t	same as 03RAR but for only **1 time** data assimilation			
03RAR_1h_rap	same as 03RAR but for 3 times data assimilation **during 1 hour**			
03RAR_initrad	3 km	GTS, AWS **radar**	none	same as 03RAR but for adding **radar** data at initial filed
03RAR_cent10	same as 03RAR but for **10min (55-05 period)** in data assimilation window			
03RAR_cent5	same as 03RAR but for **5min (58-03 period)** data assim. window			
03RAR_cent20	same as 03RAR but for **20min (50-10 period)** data assim. window			

The 9-km control run, which utilizes no radar data, is known as 09RNR (NR = no radar), and was initialized using the 9-hour 27R forecast as a first guess field. Experiment 09RNR was integrated for 12 hours from 1500 UTC on July 26 to 0300 UTC on July 27. As mentioned earlier, this 12-hour time interval was chosen to coincide with the observed rainfall event. GTS and AWS surface observations were used in ADAS for experiment 09RNR. Experiment 09RYR is similar to 09RNR, though with the use of radar data *at the initial time only* to aid in the specification of the moisture and latent heating/temperature fields.

In order to investigate the impact of using more than a single volume scan of radar data as a means for capturing small-scale structures, we perform another experiment, known as 09RAR, that is similar to 09RYR but with the exception that radar data are assimilated at hourly intervals from 1500 UTC to 1800 UTC, July 26 using incremental analysis updating. The first guess field for this run is the same as that for 09RYR, in contrast to the 9-hour forecast from 27R, which was employed in 09RNR.

Figure 4.8 presents a schematic for the 3-km resolution forecasts. As shown in this figure, the methodology for 03RNR, 03RYR, and 03RAR is identical to that for 09RNR, 09RYR, and 09RAR, respectively. As described in Chapter 6, numerous variations are applied to this 3-km methodology, including changes to the data assimilation window, frequency of data inputs, and background fields used. The description of specific design deferred to Chapter 6.

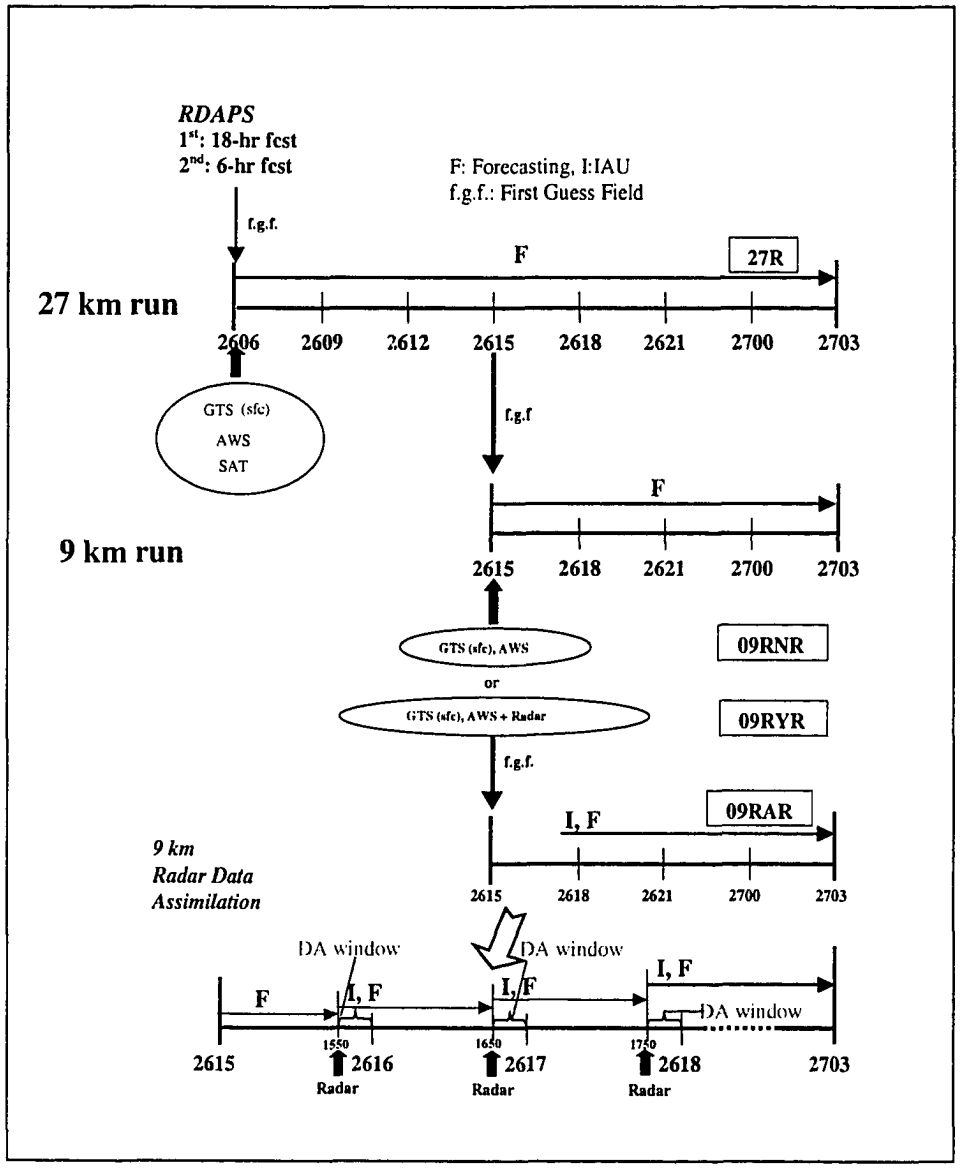

Fig. 4.7 Experiment design for control 27-km and 9-km resolution forecasts.

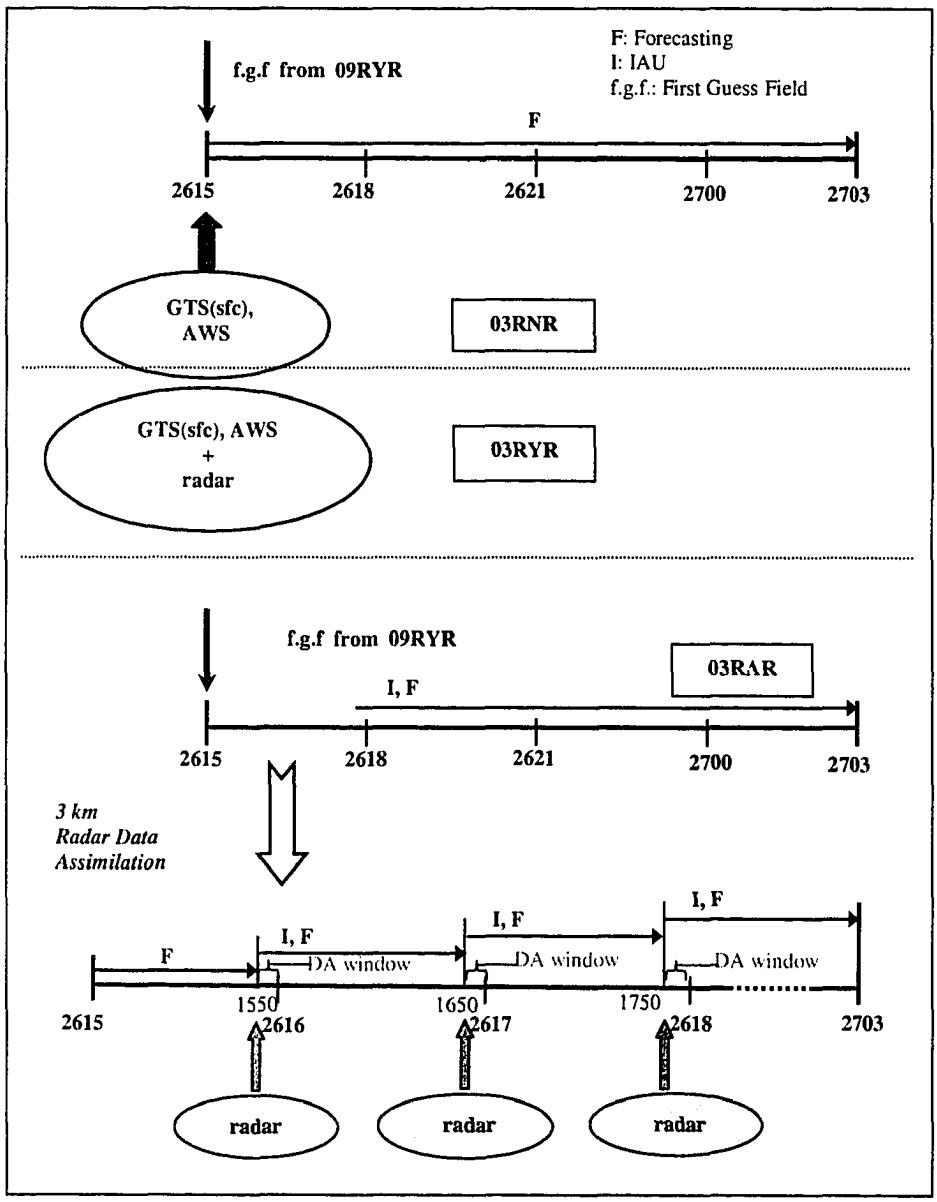

Fig.4.8 Experiment design for 3-km resolution forecasts.

4.6 The Data Assimilation Procedure: Incremental Analysis Updating (IAU)

Incremental analysis updating (IAU), which can be described as belonging to the family of nudging techniques, is designed to gradually incorporate analysis increments (i.e., the analysis minus the background field) into a numerical model as *constant* forcings in prognostic equations over an assimilation period centered on a given analysis time (Bloom et al. 1996; see Figure 4.9). Via linear analysis, Bloom et al. showed that IAU has the advantage of serving as a low-pass time filter. They also found that IAU has a particular effect on the response of the model where analysis increments exist, and that it leaves the model state unaffected where data are not available to be assimilated.

4.6.1 The Scheme and Linear Analysis of IAU

Following Bloom et al. (1996), we present in this section an analysis of the response functions associated with the assimilation of increments into a *linear* model. A general linear system of the dynamics of an assimilation system can be written

$$\begin{aligned} &\frac{d\alpha}{dt} = A\alpha + \mathbf{F}(t), \\ &\alpha = \alpha_0 \ \ at \ t = 0, \end{aligned} \tag{4.3}$$

where t is time, α is a state vector of the atmosphere, and A is a time-independent linear operator representing the dynamics of the system. **F**(t) is a state-independent forcing term which represents *only data forcing* since we focus on the short term impact of the strategy used for assimilating data. Thus, the concern of the linear analysis of IAU is to show "the issue of how the assimilation system reacts to the manner in which analyzed data are *introduced* to that system (Bloom 2003)."

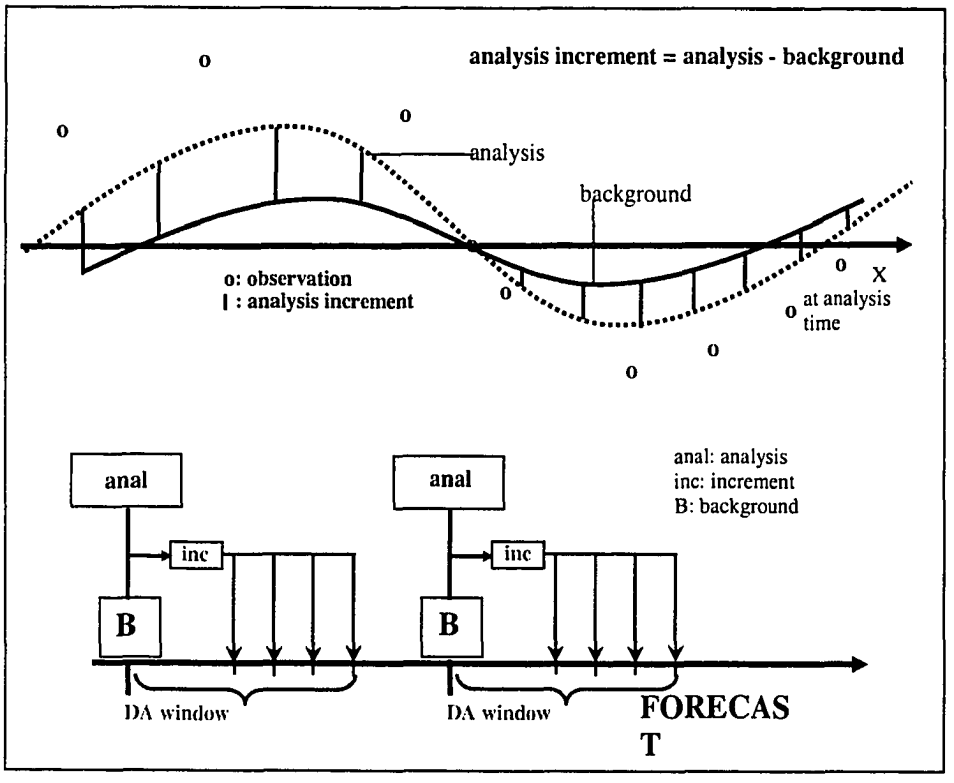

Fig. 4.9 The schematic of IAU technique

For mathematical simplicity, let A be an operator which contains a complete set of eigenvectors and eigenvalues denoted by

$$A\mathbf{u}_j = \lambda_j \mathbf{u}_j, \quad j = 1, \cdots, \infty, \tag{4.4}$$

where $\mathbf{u}_j$ is the jth eigenvector and jth complex eigenvalue $\lambda_j = i\omega_j + \sigma_j$; ω_j is the jth mode frequency and σ_j is the jth mode growth-decay rate. The general solution of Eq. 4.3 is

$$\alpha(t) = e^{At}\alpha_0 + \int_0 e^{A(t-s)}\mathbf{F}(s)ds\,. \tag{4.5}$$

The relationship between the analysis state α_a and the background state α_b is given by

$$\alpha_a = \alpha_b + \Delta\alpha_a\,, \tag{4.6}$$

where $\Delta\alpha_a$ is the analysis increment. Now consider the IAU interval τ (with τ = 2t), within which the background state can be written

$$\alpha_b = e^{A(\tau/2)}\alpha_0\,. \tag{4.7}$$

In this equation, we assume that the model forecast in Eq. 4.3 produces the background state from an initial state α_0 valid at t = 0. Further, we do not consider the *data forcing* in the background state given that the forcing term in Eq. 4.3 is restricted to represent solely the influence of data on the assimilation process. This means that *the background is calculated without the influence of data.* Bloom (2003) denoted a little more detailed explanation of this situation; "we are simply defining the evolution of the background state, which has no data forcing: this is simply the time evolution of the linear system in the absence of data."

In order to compare the performance of the IAU system with an integration of the general linear system (Eq. 4.3) initialized at t = $\tau/2$ with the analysis state α_a as given in equation 4.6, an analysis increment $\Delta\alpha_a$ is employed. This process can approximately be regarded as intermittent assimilation. For the solution, a specific forcing which is proportional to $\delta(t - \tau/2)$, where δ indicates Dirac delta function, is introduced in equation 4.5. Thus, the intermittent solution $\alpha^{INT}(t)$ is given by

$$\alpha^{INT}(t) = e^{At}\alpha_0 + e^{A(t-\tau/2)}\Delta\alpha_a, \tag{4.8}$$

where $t \geq \tau/2$ since $\delta(t - \tau/2) = 0$ in $0 \leq t < \tau/2$ according to the Dirac delta rule.

The framework for examining $\alpha^{INT}(t)$, α_0, and $\Delta\alpha_a$ is provided by using the eigenvectors/eigenvalues (Eq. 4.4) of the general linear system (Eq. 4.3) as follows:

$$\begin{aligned} &\alpha^{INT}(t) = \sum_j \alpha_j^{INT}\mathbf{u}_j, \\ &\alpha_0 = \sum_j b_j\mathbf{u}_j, \quad and \quad \Delta\alpha_a = \sum_j d_j\mathbf{u}_j \end{aligned}, \tag{4.9}$$

where α_j^{INT}, b_j, and d_j are scalar multiplies for $\alpha^{INT}(t)$, α_0, and $\Delta\alpha_a$, respectively. With these frameworks, and replacing A by λ_j, equation 4.8 can be written in mode space as:

$$\alpha_j^{INT}(t) = e^{\lambda_j t}(b_j + e^{-\lambda_j\tau/2}d_j) \tag{4.10}$$

When we consider a constant forcing in the IAU procedure, it can be rewritten as

$$F(t) = \frac{g(t)}{\bar{g}}\Delta\alpha_a, \bar{g} = \int_0^\tau g(s)ds \tag{4.11}$$

where g(t) is a scalar function in which additional analysis increments can be specified in a patchy and sparse manner in time. If we use the forcing of equation 4.11, along with the framework of equation 4.10 and the initial state α_0 at t = 0, the solution of an IAU mode in space can be written

$$\alpha_j^{IAU} = e^{\lambda_j t}[b_j + \gamma(\lambda_j, t)d_j], 0 \le t \le \tau,$$
$$\gamma(\lambda_j, t) = \frac{1}{\bar{g}} \int_0 e^{-\lambda_j s} g(s) ds \tag{4.12}$$

In general, the response function R in a data assimilation state determines whether a wave is amplifying or damping. If |R| > 1 or |R| < 1, the wave is amplifying or damping, respectively (Haltiner and Williams 1980). In the study of Bloom et al. (1996), the response functions were employed to compare the effects of different assimilation strategies. For example, they first obtained a response function (R^{IAU}) comparing to the solutions of intermittent assimilation and IAU. Second, they examined another response function (R^N) for intermittent assimilation and nudging (dynamic relaxation). Finally, they compared R^{IAU} with R^N to find a difference between IAU and nudging method. In the following discussion of each response function, we follow the description of Bloom et al. (1996) without modification.

Compared to the intermittent solution (Eq. 4.10) and IAU solution (Eq. 4.12) employing $t = \tau$ (we used this IAU interval in the present study), the b_j term from the initial state in intermittent assimilation is exactly same as that in IAU. This means that *the analysis increment is the only contributor to assimilation in IAU.* By forming the ratio of the d_j terms from equations 4.10 and 4.12, the R^{IAU} is given by

$$R^{IAU}(\lambda_j, \tau) \equiv \frac{\gamma(\lambda_j, \tau)e^{\lambda_j \tau}}{e^{\lambda_j \tau/2}} = \gamma(\lambda_j, \tau)e^{\lambda_j \tau/2}. \tag{4.13}$$

When g(t) = constant =1, $\gamma(\lambda_j,t)$ in equation 4.12 and equation 4,13 produce

$$R^{IAU}(\lambda_j, \tau) \equiv \rho_j e^{i\theta_j} = \frac{\sinh(\lambda_j \tau/2)}{\lambda_j \tau/2}, \tag{4.14}$$

$$\rho_j^2 = \frac{\sinh^2(\sigma_j \tau/2) + \sin^2(\omega_j \tau/2)}{(\sigma_j \tau/2)^2 + (\omega_j \tau/2)^2}, \tag{4.15}$$

$$\tan(\theta_j) = \frac{\sigma_j \tan(\omega_j \tau/2) - \omega_j \tanh(\sigma_j \tau/2)}{\sigma_j \tanh(\sigma_j \tau/2) + \omega_j \tan(\omega_j \tau/2)}, \tag{4.16}$$

where ρ_j and θ_j are the jth amplitude and phase shift of the complex response function, respectively, ω is mode frequency, and σ is growth-decay rate. Bloom et al. (1996) also explained the characteristics of equations 4.14 to 4.16. The signs of the mode frequency ω and growth-decay rate σ have nothing to do with the amplitude of the response function. The growing disturbances with an e-folding time $1/\sigma$ will be removed in nearly the same amount of time as the decaying disturbances with the same e-folding time for a given frequency.

One of the most interesting characteristics of this response function is that the product of the disturbance complex frequency λ, and the IAU interval τ, can only affect the response function. Figure 4.10a shows the result of Bloom et al. (1996) for the IAU response function amplitude ρ using three values of the growth-decay rate σ. Figure 4.10b depicts the phase shift θ of response function for IAU forcing. They interpreted the result as follows;

> "These linear analysis results indicate that the IAU procedure should behave like a low-pass filter with a cutoff period around one day. Such a behavior would remove fast (e.g. gravity waves) atmosphere motions while having little effect on synoptic-scale and low-frequency atmospheric disturbances. This behavior has the practical result that high-frequency phenomena generated internally by the model (e.g. diurnal cycle, tides) are

not affected by IAU integration; only those high-frequency states excited by imbalances in the analysis increments are affected by the IAU procedure. In the results of the phase shift θ, there is no shift for forced disturbances having periods longer than the IAU period (6 h in this figure). Although the phase behavior does depend on the sign of σ, the-long period behavior of the phase response for both decay and growth converge to the neutral limit. For strong instabilities having e-folding timescales less than 6 h, the phase shift introduced by IAU is very small."

4.6.2 Differenced between IAU and Nudging

Although IAU can be regarded as belonging to the family of nudging techniques, there exist important differences between IAU and classic Newtonian nudging (N). In order to examine these differences, we derive the solution and response functions associated with nudging following the work of Bloom et al. (1996).

A general nudging procedure may be written as

$$\frac{d\alpha}{dt} = A\alpha - G_N(\alpha - \alpha_a) + G_D D^2(\alpha - \alpha_a), \tag{4.17}$$

where G_N and G_D are the scalar constants (not relaxation coefficients) controlling the strength of Newtonian relaxation and diffusion, respectively, and D2 is a diffusion-like operator. This equation can be rewritten as

$$\begin{aligned} &\frac{d\alpha}{dt} = \tilde{A}\alpha + G_N\alpha_a - G_D D^2\alpha_a \equiv \tilde{A}\alpha + F_N + F_D, \\ &\tilde{A} = A - G_N + G_D D^2 \end{aligned} \quad , \tag{4.18}$$

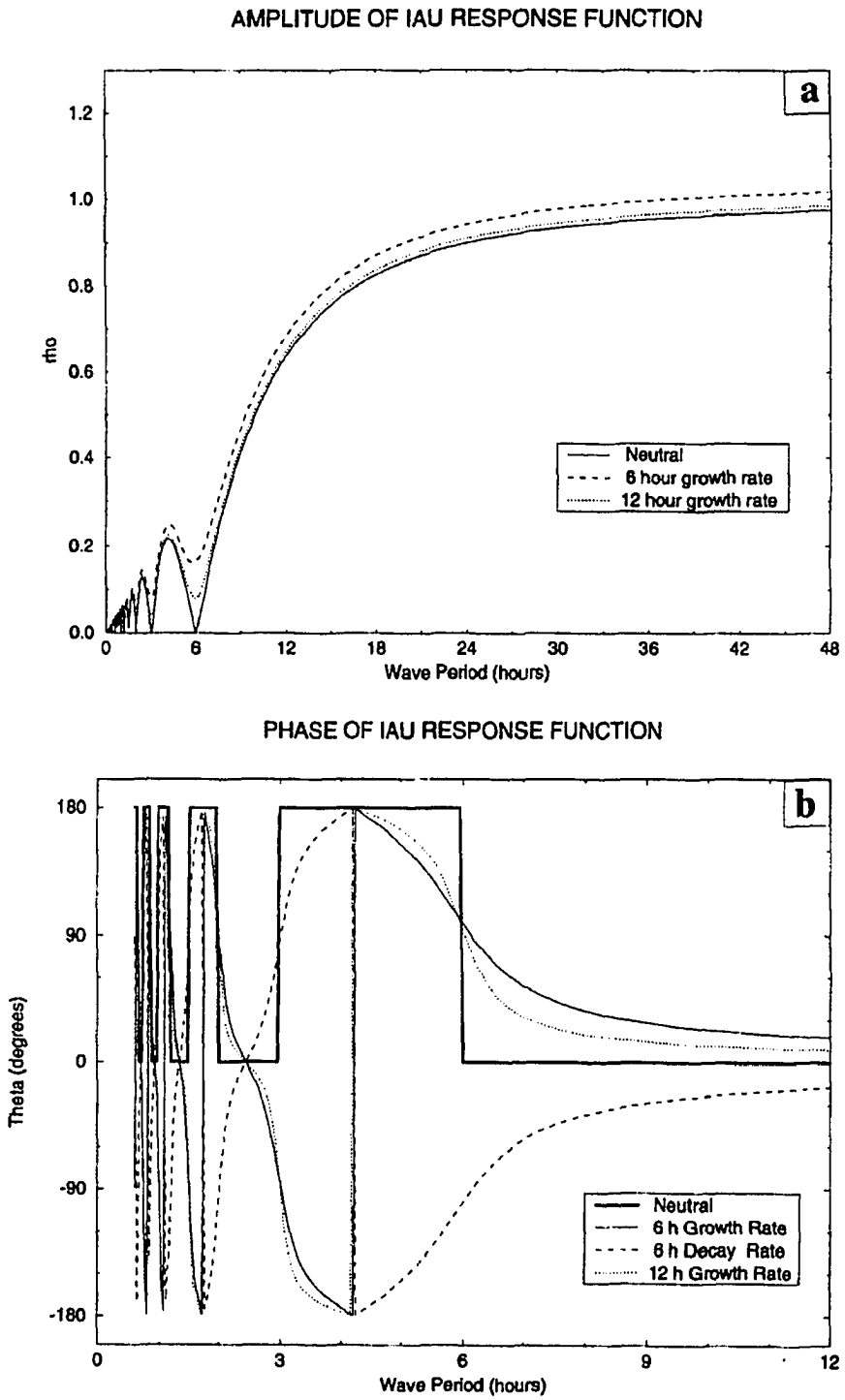

Fig. 4.10 IAU response function for (a) $\rho = |R|$, the amplitude of the response functions for three values of the growth-decay rate, $\sigma = 0$ (neutral case, solid line), $1/\sigma = 12$ h (dashed line) and $1/\sigma = 6$ h (dotted line), (b) the phase θ of the response function R, for four cases, $\sigma = 0$ (heavy solid line), $1/\sigma = \pm 6$ h (light solid line for growth, dashed line for decay), and $1/\sigma = 12$ h (dotted line) (From Bloom et al., 1996).

where $\tilde{A}$ is the modified dynamical operator and $\mathbf{F}_N$ and $\mathbf{F}_D$ are the forcing terms for Newtonian relaxation and diffusion, respectively, which include both background state and the analysis increments. Other variables and notations are same as those used in the IAU process. Following the analysis methodology shown for IAU, we obtain the following general solution of equation 4.18 for nudging

$$\alpha^N(t) = e^{\tilde{A}t}\alpha_0 + \int_0 e^{\tilde{A}(t-s)}(\mathbf{F}_N + \mathbf{F}_D)ds\,. \tag{4.19}$$

For mathematical simplicity, as in IAU, we assume that the eigenvetors of $\tilde{A}$ are the same as the eigenvectors of A, but with shifted eigenvalues

$$\tilde{A}u_j = \tilde{\lambda}_j u_j, \quad \tilde{\lambda}_j \equiv \lambda_j - G_j, \tag{4.20}$$

where Gj is a relaxation coefficient (= $G_N + G_D K_j^2$; here Kj is a scale-selective parameter formally equivalent to a horizontal wave number.) As in the IAU procedure, we obtain the following nudging solution, α_j^N, the analysis increment response function for the nudging procedure, R_A^N, and the background response function for the nudging procedure, R_B^N:

$$\alpha_j^N(\tau) = [1 + G_j e^{\lambda_j \tau/2}\gamma(\tilde{\lambda}_j,\tau)]e^{\tilde{\lambda}_j\tau}b_j + G_j\gamma(\tilde{\lambda}_j,\tau)e^{\tilde{\lambda}_j\tau}d_j. \tag{4.21}$$

$$R_A^N(\lambda_j, G_j, \tau) = G_j\gamma(\tilde{\lambda}_j,\tau)e^{\tilde{\lambda}_j\tau}e^{-\lambda_j\tau/2} = G_j\tau e^{-G_j\tau/2}[\frac{\sinh(\tilde{\lambda}_j\tau/2)}{\tilde{\lambda}_j\tau/2}]. \tag{4.22}$$

$$\begin{aligned} R_B^N(\lambda_j, G_j, \tau) &= [1 + G_j e^{\lambda_j\tau/2}\gamma(\tilde{\lambda}_j,\tau)]e^{-G_j\tau} \\ &= \{1 + G_j\tau e^{G_j\tau/2}[\frac{\sinh(\tilde{\lambda}_j\tau/2)}{\tilde{\lambda}_j\tau/2}]\}e^{-G_j\tau} \end{aligned} \tag{4.23}$$

Although the response functions for the nudging procedure are very similar to those for IAU (cf. 4.14-4.16), the relaxation time scale in the nudging procedure is more important for damping overall amplitude and shifting the eigenvalues to larger growth-decay rates

compared to IAU. Consequently, the IAU scheme adds the analysis increments to the model as a state-independent forcing term to perform the actual filtering only on the response to the analysis increments, whereas the entire model state is relaxed toward an analysis in the nudging technique (Bloom et al. 1996).

The study of Bloom et al. (1996) was focused on the macro-scale forecasting in a GCM model. They used a 6 hr IAU interval using synoptic data and an analysis with a 6 hr interval. However, the IAU procedure employed in our present study is for storm scale forecast using dense radar data with an IAU interval of 10 minutes. Although there exists scale differences in time and space between the study of Bloom et al. (1996) and our present study, one may ask whether difficult exists in applying Bloom's IAU method to storm-scale weather.

As mentioned previously for IAU, the product of the disturbance frequency, λ, and the IAU interval, τ, can only affect the response function. This fact leads to the important result that the IAU interval, and the frequency of observation used for analysis, should appropriately be combined. In light of this, the 10 minute IAU interval using radar data with a 5 minute update frequency is reasonable. For small scales, IAU acts as a low-pass filter to reduce the amplitude of relatively high frequency disturbances.

4.6.3 IAU in ADAS

The ADAS assimilation scheme is designed to gradually apply the ADAS-determined analysis increments over a specified time span during the execution of the ARPS model (Brewster, 2001). Modifications have been made to both the ADAS software and the

ARPS model to enable this capability. The assimilation procedure in ADAS creates a file containing increments that are applied during the model's large time-step, after the other large-time-step forces have been applied. Although the term 'nudging' is used in many places, the method is similar to that described by Bloom et al. (1996) and is more accurately referred to as incremental analysis updating (IAU). For 09RAR and 03RAR experiments ADAS was run at 1500 UTC and IAU was not used at that time. Then increments were calculated at 15:50 using the 1600 UTC data and the ARPS forecast initialized at 1500 UTC. The increments were introduced in a window from 15:50 to 16:00. Similarly, data at 1700 and 1800 UTC were assimilated during the period 16:50 to 17:00 and 17:50 to 18:00 UTC, respectively.

4.7 ARPS Parameters for Radar Data Assimilation

Table 4.5 shows selected ARPS parameters for the 3-km grid spacing radar data assimilation experiment (03RAR), while Tables 4.6 and 4.7 present the same information for the 27-km and 9-km horizontal grid spacing cases, respectively. Because almost all physics options in ARPS were employed for this study, proper choices for parameter values are important. Consequently, many experiments were conducted using various parameter values and physics options, including warm rain versus ice physics and different cumulus parameterizations. Four options for microphysics are included in ARPS: 1) no microphysics processes (warm (liquid) saturation adjustment), 2) Kessler warm rain microphysics, 3) Tao ice microphysics, and 4) Schultz NEM ice microphysics.

ARPS has also four options for convective cumulus parameterization: 1) no convective parameterization, 2) Kuo parameterization scheme, 3) Kuo parameterization scheme using Kessler warm rain microphysics, and 4) Kain-Fritsch cumulus parameterization scheme. After several tests, the Tao ice parameterization was chosen for the 3-km experiments without any convective parameterization - a choice that is consistent with recent studies (e.g., Belair and Mailhot 2001). The Tao ice parameterization is used in both the 27-km and 9-km resolution forecasts for grid-scale precipitation as it includes three categories of frozen precipitation in the form of cloud ice, snow, and hail/graupel (Lin et al. 1983; Tao and Simpson 1993).

In general, the Kain-Fritsch cumulus parameterization scheme is well known as an effective convective parameterization scheme for middle latitudes when using grid spacings of 25 - 40 km. For the 27-km and 9-km resolution forecasts, the Kain-Fritsch scheme is applied, though at 9-km resolution, its use is questionable.

In order to obtain the proper time step sizes, the small time step was first calculated and the large time step size obtained as a multiple. When solving the vertical momentum and pressure equations implicitly in the vertical ('vimplct = 1' in ARPS code), the constraint for small time step size is

,

where cs is the maximum sound speed and x and y are the x and y grid spacings (m), respectively. For our fine grid experiments, x = y = 3000 m and we let cs = 340 m/s. This results in a constraint of dtsml 6.2 sec. Via experiments with dtsml values of 6 s (dtbig 12 s), 5 s (10 s), 4 s (8 s), 4 s (about 70 % of calculated dtsml value), we chose to use 8 s for large time step size and 4 s for the small step for the 3 km resolution forecasts.

Table 4.5 Selected ARPS parameters for 3-km horizontal resolution.

Parameter	Name	Value
Horizontal grid spacing	dx,dy	3 km
Number of vertical levels	nz	37
Mean vertical grid spacing	dz	400. m
Minimum vertical spacing	dzmin	20. m
Vertical stretching option	strhopt	2=tanh profile of dz
Large time step	dtbig	8. s
Small time step	dtsml	4. s
Boundary data interval	tintvebd	3600. s
Boundary relaxation zone	ngbrz	5.0 dx
Boundary relax wgt halfwidth	brlxhw	2.3 dx
Momentum advection	madvopt	2=4th order horiz & 2nd order vert
Scalar advection	sadvopt	2=4th order horiz & 2nd order vert
Hgt to begin Rayleigh damping	zbrdmp	12 km
Turbulent mixing	tmixopt	4=1.5 TKE mixing
Isotropic turbulence	trbisotp	0=anisotropic (dx >> dz)
Vertical mixing	tmixvert	1=vertical components only
Horiz Computational Mixing	cmix4th	1=4th order horiz on
Horiz mixing coefficient	cfcm4h	1.0 X 10^{-4}
Microphysics	mphyopt	2=Tao-Lin Ice
Convective Parameterization	cnvctopt	0=off (no convective parameterization)
Radiation Option	radopt	2=full radiation parameterization
Longwave Radiation Scheme	rlwopt	1=accurate method
Surface physics	sfcphy	4=stability dependent drag
Flux distribution depth	dtqflxdis	200. m
Surface physics time step	dtsfc	60. s

Table 4.6 Selected ARPS parameters for 27-km horizontal resolution.

Parameter	Name	Value
Horizontal grid spacing	dx,dy	27 km
Number of vertical levels	nz	37
Mean vertical grid spacing	dz	400. m
Minimum vertical spacing	dzmin	50. m
Vertical stretching option	strhopt	2=tanh profile of dz
Large time step	dtbig	24. s
Small time step	dtsml	24. s
Boundary data interval	tintvebd	3600. s
Boundary relaxation zone	ngbrz	5.0 dx
Boundary relax wgt halfwidth	brlxhw	2.3 dx
Momentum advection	madvopt	2=4th order horiz & 2nd order vert
Scalar advection	sadvopt	2=4th order horiz & 2nd order vert
Hgt to begin Rayleigh damping	zbrdmp	12 km
Turbulent mixing	tmixopt	4=1.5 TKE mixing
Isotropic turbulence	trbisotp	0=anisotropic (dx >> dz)
Vertical mixing	tmixvert	1=vertical components only
Horiz Computational Mixing	cmix4th	1=4th order horiz on
Horiz mixing coefficient	cfcm4h	1.0 X 10^{-4}
Microphysics	mphyopt	2=Tao-Lin Ice
Convective Parameterization	cnvctopt	3=Kain-Fritsch parameterization
Radiation Option	radopt	2=full radiation parameterization
Longwave Radiation Scheme	rlwopt	1=accurate method
Surface physics	sfcphy	4=stability dependent drag
Flux distribution depth	dtqflxdis	200. m
Surface physics time step	dtsfc	60. s

Table 4.7 Selected ARPS parameters for 9-km horizontal resolution.

Parameter	Name	Value
Horizontal grid spacing	dx,dy	27 km
Number of vertical levels	nz	37
Mean vertical grid spacing	dz	400. m
Minimum vertical spacing	dzmin	50. m
Vertical stretching option	strhopt	2=tanh profile of dz
Large time step	dtbig	18. s
Small time step	dtsml	18. s
Boundary data interval	tintvebd	3600. s
Boundary relaxation zone	ngbrz	5.0 dx
Boundary relax wgt halfwidth	brlxhw	2.3 dx
Momentum advection	madvopt	2=4th order horiz & 2nd order vert
Scalar advection	sadvopt	2=4th order horiz & 2nd order vert
Hgt to begin Rayleigh damping	zbrdmp	12 km
Turbulent mixing	tmixopt	4=1.5 TKE mixing
Isotropic turbulence	trbisotp	0=anisotropic (dx >> dz)
Vertical mixing	tmixvert	1=vertical components only
Horiz Computational Mixing	cmix4th	1=4th order horiz on
Horiz mixing coefficient	cfcm4h	1.0 X 10^{-4}
Microphysics	mphyopt	2=Tao-Lin Ice
Convective Parameterization	cnvctopt	3=Kain-Fritsch parameterization
Radiation Option	radopt	2=full radiation parameterization
Longwave Radiation Scheme	rlwopt	1=accurate method
Surface physics	sfcphy	4=stability dependent drag
Flux distribution depth	dtqflxdis	200. m
Surface physics time step	dtsfc	60. s

Chapter 5.

Results of 27-km and 9-km Resolution Experiments

We discuss in this chapter results from simulations made using grid spacings of 27 and 9 km, the latter as a one-way grid nested within the former. Given that the focus of this research is storm-scale prediction at grid spacings of a few kilometers, our analysis of the 9 and 27 km grid spacing experiments is necessarily limited, with particular emphasis on the former providing the background and boundary condition information for the 3 km experiments.

5.1 Overview of the 27-km Grid Spacing Experiments

As shown in Fig. 4.4 and table 4.3, two experiments at 27-km grid spacing have conducted in this study. Experiment 27R is the 27-km ARPS *control* forecast advanced 21 hours (from 0600 UTC on July 26 to 0300 UTC on July 27) using as a starting point the 18-hour RDAPS forecast initialized at 12 UTC on July 25 (hereafter referred to as the "old" first guess field). Although one would prefer to use an *analysis* as the starting point for forecasts, as well as for boundary conditions, in a research setting, we were forced to use a forecast for both owing to the lack of an operational analysis at 18 UTC, the starting time for our forecasts that was based upon the evolution of the chosen heavy rainfall event. The other experiment, 27R_n, is identical to 27R except for using a newer version of the RDAPS model from a 6-hour forecast initialized at 00UTC on July 26. This particular forecast, which was not available operationally but was produced quite

recently, utilizes an enhanced version of the KMA RDAPS model. Hereafter we refer to this starting point as the "new" first guess field.

5.1.1 Difference Between the Two First Guess Fields

It has long been recognized that the first guess field is of critical importance to forecasting the phase and intensity of mesoscale events (e.g. Janish and Weiss, 1996) as well as of global scale weather phenomena (e. g. Derber et al. 1998). To examine the differences between the two first guess fields described above, we show in figure 5.1 the two analyses (red arrows) compared to the observed surface wind field (black arrows) at the starting time of experiments 27R and 27R_n, i.e., at 06 UTC on July 26. In the case of the old first guess field, large differences between the RDAPS forecast and observations, while a significant improvement is evidenced when using the new version of RDAPS (Fig. 5.1b). For example, the predominant flow in the latter is southwesterly, similar to observations, while the old first guess field indicates southeasterly winds on the middle western side of the KP. The next step is to determine whether the new first guess field has a positive effect on the forecast.

5.1.2 21-hour Total Rainfall Forecast from the 27-km Grid Spacing Experiments

The accumulated rainfall over the 21-hour period ending 03UTC July 27 from experiment 27R is shown in Fig. 5.2 for both first guess fields. The maximum rainfall using the old first guess field is approximately 70 mm (Fig. 5.2a) and is located in the far northwestern part of the Chorwon-Yonchon region. According to the observed rainfall at

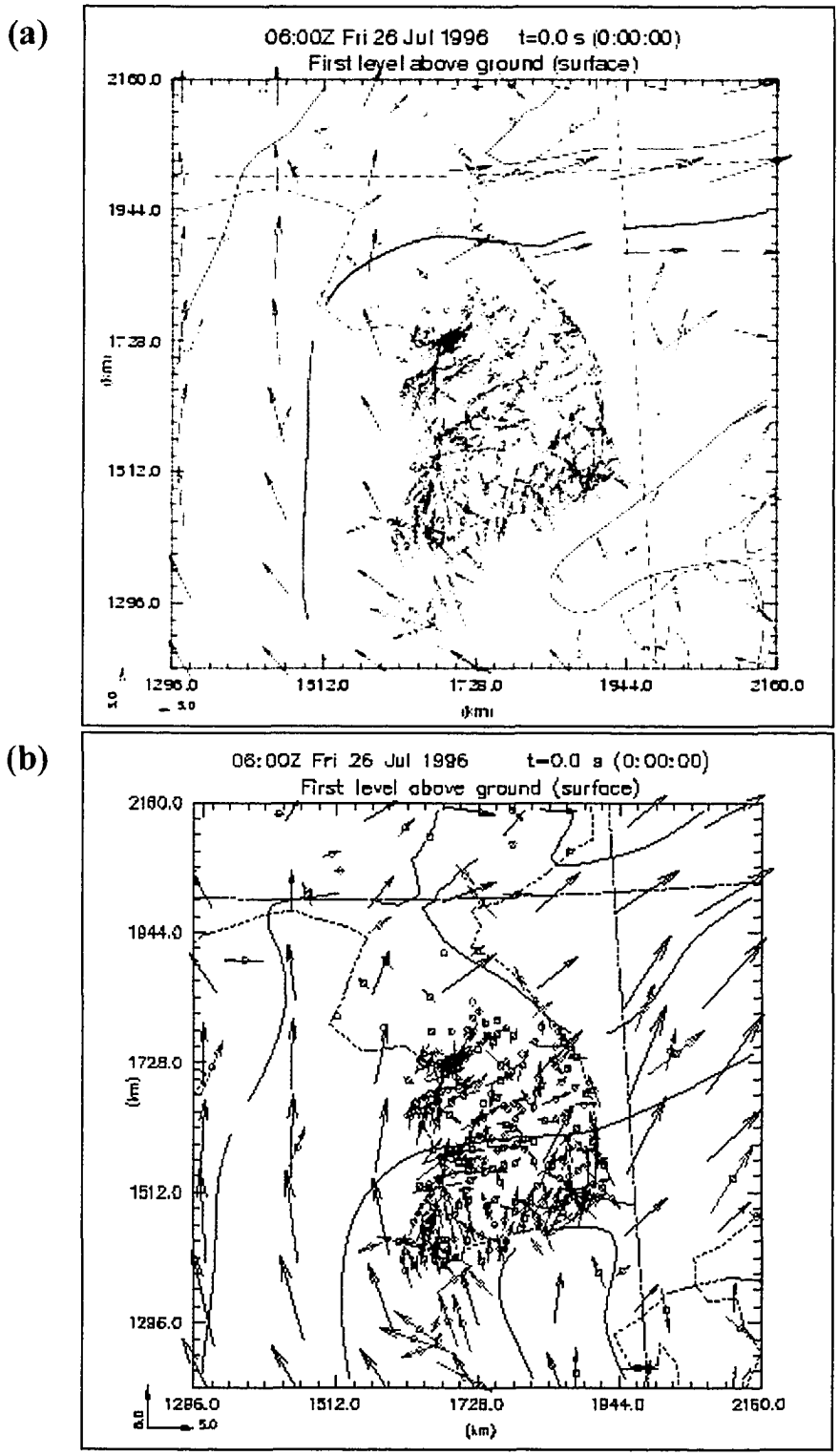

Fig. 5.1 Comparison of the surface wind field from observations at 06UTC July 26 with (a) the old first guess field (RDAPS 18-hour forecast initialized at 12UTC July 25) and (b) the new first guess field (RDAPS 6-hour forecast initialized at 00UTC July 26). Red and black arrows represent observed surface wind and the winds obtained from each first guess filed, respectively.

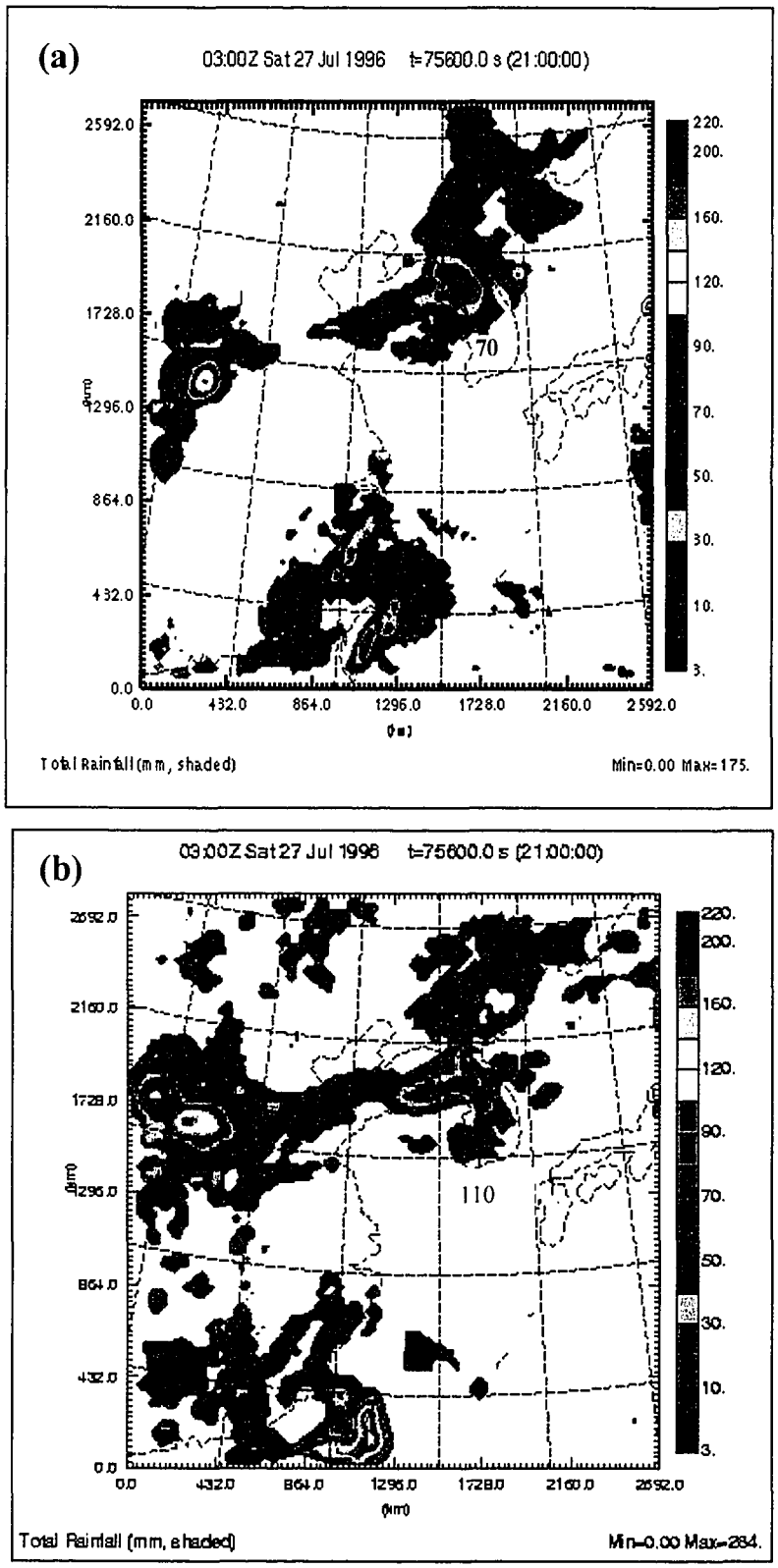

Fig. 5.2 Total predicted rainfall (mm) for 21 hours valid 03UTC July 27 for outer grid (a) for using old first guess field and (b) for using new first guess field.

Chorwon, the total rainfall for this time period is 228.3 mm. Thus, the predicted maximum rainfall amount is approximately 35% of the observed value. However, the predicted rainfall using the new first guess field (Fig. 5.2b) shows substantial improvement, with a peak value of 110 mm, or about 50 % of the observed amount. Furthermore, the forecast using new the first guess field depicts Typhoon Gloria near Taiwan, while the forecast using the old first guess completely misses this feature.

From this and other analyses not shown, the new first guess field leads to improvements in the 27 km grid spacing forecast, though with considerable deviation from the observations. This mismatch is a result of a number of factors, including the coarse resolution of the 27R simulation. Specifically, cumulus parameterization schemes are unable to capture the intense precipitating structure of such localized heavy rainfall events, though they do a reasonably good job in many cases of predicting the location (e.g., Benoit and Mailhot, 2001).

5.1.3 Synoptic Comparison

Although the precipitation prediction using the new first guess field shows the substantial improvement, we need to verify how the results of 27 km compares with observations in the light of synoptic aspects. Figure 5.3 shows predicted 850 hPa synoptic charts at 0000 UTC July 26 for using old first guess filed (Fig.5.3a) and using new first guess field (Fig. 5.3b). In observation (Fig. 3.2c), we find that 1500 gpm height line is on the central Korea. The 18 C isotherm is on the central Korea and is tilted to the direction of southeast to northwest with a strong thermal trough. By comparing observation (Fig. 3.2c) with the predictions (Fig. 5.3a and b), the prediction using the

new first guess field is much closer to observation than the prediction using the old first guess field. Over the central Korea, the prediction using the new first guess field (Fig. 5.3b) depicts 1500 gpm height and 18 C, while the prediction using the old first guess field (Fig. 5.3a) displays 1480 gpm and 17 C. Further, the isotherm over the central part of Korea is also tilted as observation did. Both of them do not show the enough moisture filed as in observation. Considering wind field, however, we find clear reason why the prediction using the new first guess field produced more precipitation than that using the old first guess field. In Fig. 5.3b, it well displays the wind which induces moisture flux into the central part of the KP from the west region of the East China Sea. As shown in Fig. 5.3a, the prediction using the old first guess filed does not depict the wind field which can induce moisture flux. Overall, it is very clear that the improved first guess field led to substantial improvement for the prediction on 27 km resolution.

5.2 Overview of the 9-km Grid Spacing Experiments

Six experiments were conducted at 9-km grid spacing, the detailed construction of which was provided in Chapter 4. All forecasts were of 12 hour duration from 1500 UTC on July 26 to 0300 UTC on July 27 (Fig. 4.4). As noted earlier, 9-hour forecasts from both 27-km experiments (27R and 27R_n) were employed for the 9 km first guess fields.

5.2.1 Results Using the Old First Guess Field

Figure 5.4 shows the 12-hour accumulated rainfall for each 9-km grid spacing experiment. The 'C', 'Y', and 'm' in each image depict, respectively, the location of

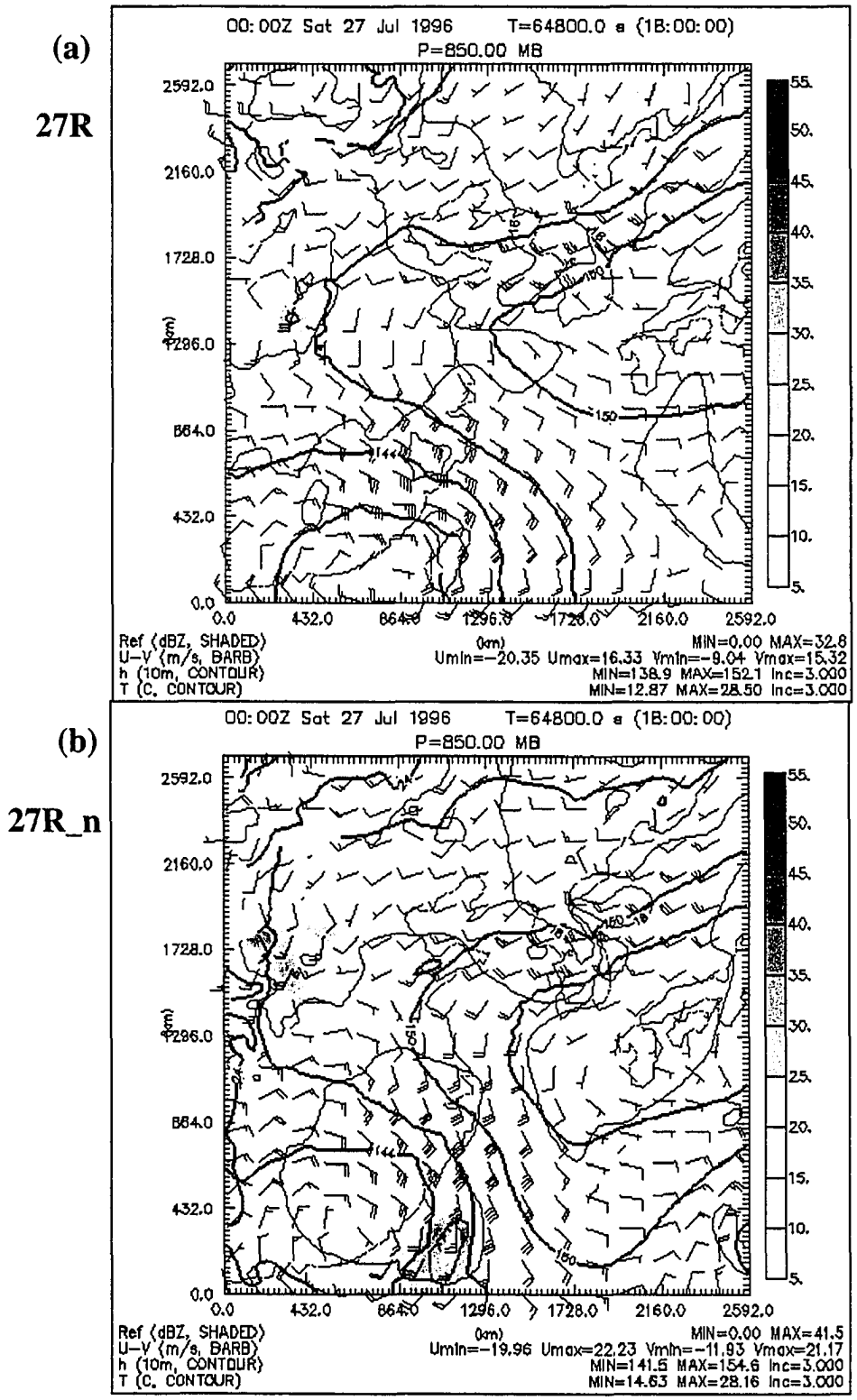

Fig.5.3 Forecasted 850 hPa height, temperature, wind field, and reflectivity at 0000 UTC July 27 for (a) 27R and (b) 27R_n.

Chorwon, Yonchon, and the actual maximum rainfall position estimated from NEXRAD Level II data (see Chapter 7 for details regarding radar data processing). Experiment 09RNR (Fig. 5.4a), which does not utilize any radar data, began with 27R background information, but was able to spin-up precipitation at an accelerated pace compared to experiment 27R. This shows the importance of increased resolution for the prediction of intense weather events (e.g., Bélair and Mailhot, 2001; Mass et al., 2001). The maximum predicted rainfall is approximately 130 mm, nearly double that from experiment 27R. In addition, the location of the maximum is improved over that predicted in 27R, though still is located to the west of the observed maximum ('m').

Increasingly slightly the level of complexity and presumable accuracy, experiment 09RYR had the benefit of radar data in the *initial* analysis. Figure 5.4b shows the 12-hour accumulated rainfall, and compared 09RNR (Fig. 5.4a), the maximum is approximately 145mm, or approximately 30% of the observed maximum (according to the estimated rainfall from NEXRAD data, the maximum amount for the 12 hr forecast period is approximately 518 mm at 'm'). Although the forecasted position of the maximum also is located west of the observed maximum, it is slightly closer than in experiment 09RNR. Many factors can affect on the correct positioning of heavy rainfall, including initial conditions and model physics. This simple experiment indicates that the use of radar data shows promise in improving the prediction of significant weather events, principally in the context of diabatic initialization (i.e., when the model grid spacing is too coarse to resolve explicitly convective-scale features but is sufficiently fine to benefit from improved specification of latent heating from radar data).

For comparison, Figure 5.4c shows the total accumulated rainfall from experiment 09RAR experiment, which is identical to 09RYR but with radar data assimilated rather than used only in the initial analysis. The maximum predicted rainfall over the KP is approximately 120 mm, or about 23% of the observed value. The position and maximum amount disagree more with observations than in 09RYR, which is a bit surprising. Although experiment 09RAR is more costly in terms of computer resources and is unable to improve upon 09RYR, it does exhibit more detailed structure in the rainfall pattern.

The above results, though obviously limited to a single case and a specific experiment design philosophy, indicate that radar data potentially can add value to a forecast, though cannot necessarily correct phase or amplitude errors (perhaps requiring phase-correcting data assimilation, e.g., Brewster 2003). However, the assimilation of radar data at 9 km grid spacing, at least for this case and in the manner applied, does not appear to improve the results significantly. Note, however, that in applying IAU at 9 km grid spacing, we have not utilized Doppler winds or wind retrieval algorithms. Further, 9-km grid spacing is still quite coarse for representing the type of deep and intense convection present in this heavy rainfall event.

5.2.2 Results Using the New First Guess Field

Fig. 5.5a, b, and c depict results from experiments 09RNR_n, 09RYR_n, and 09RAR_n, respectively, which are identical to the experiments described above but using results from the 27 km experiment initialized with the new background field.

In all cases, the predicted total rainfall is considerably larger than when using the old first guess field.

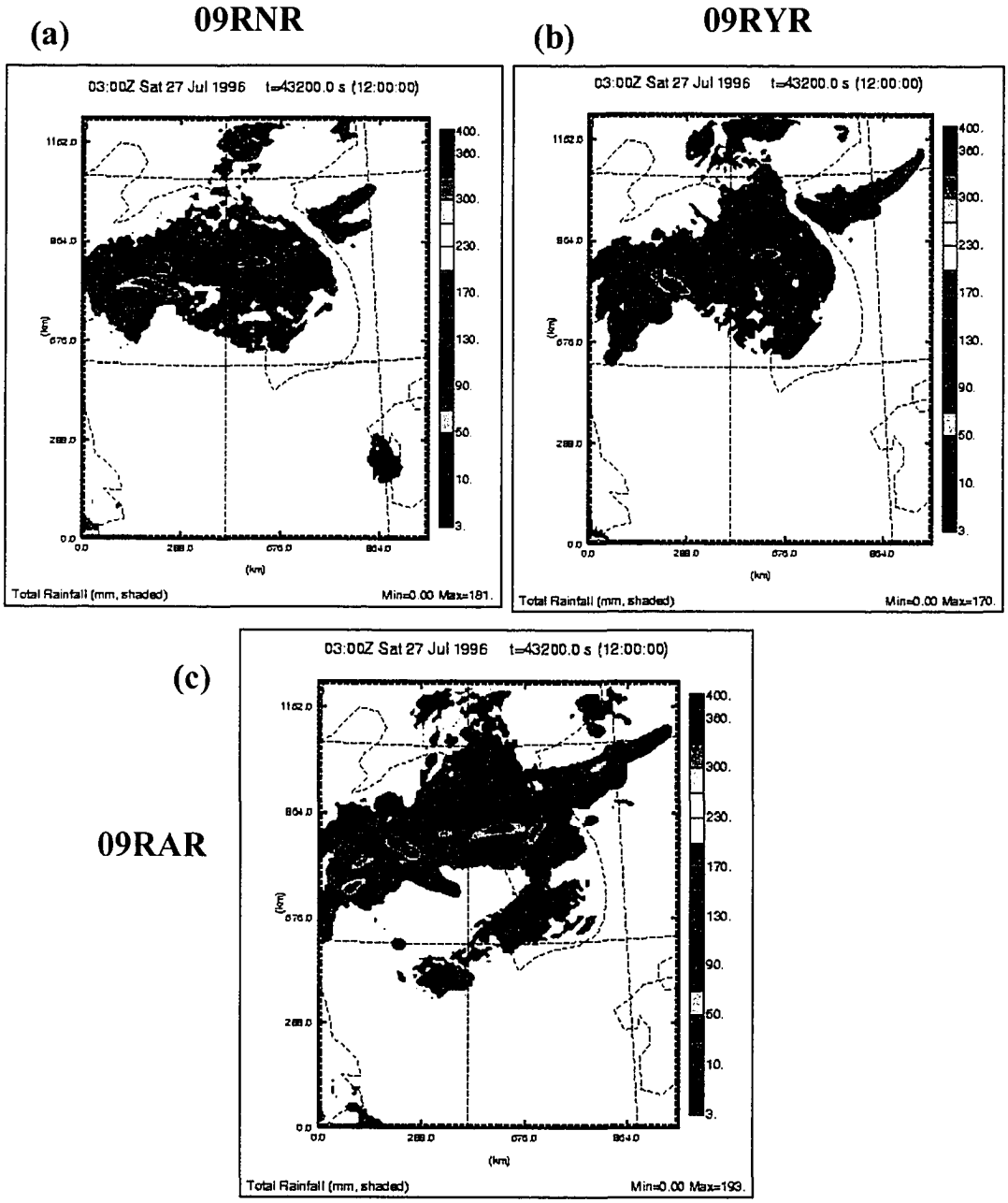

Fig. *5.4 12-hour accumulated rainfall for (a) 09RNR, (b) 09RYR, and (c) 09RAR forecasts. ('C': Chorwon position, 'Y': Yonchon position, 'm': observed maximum position)*

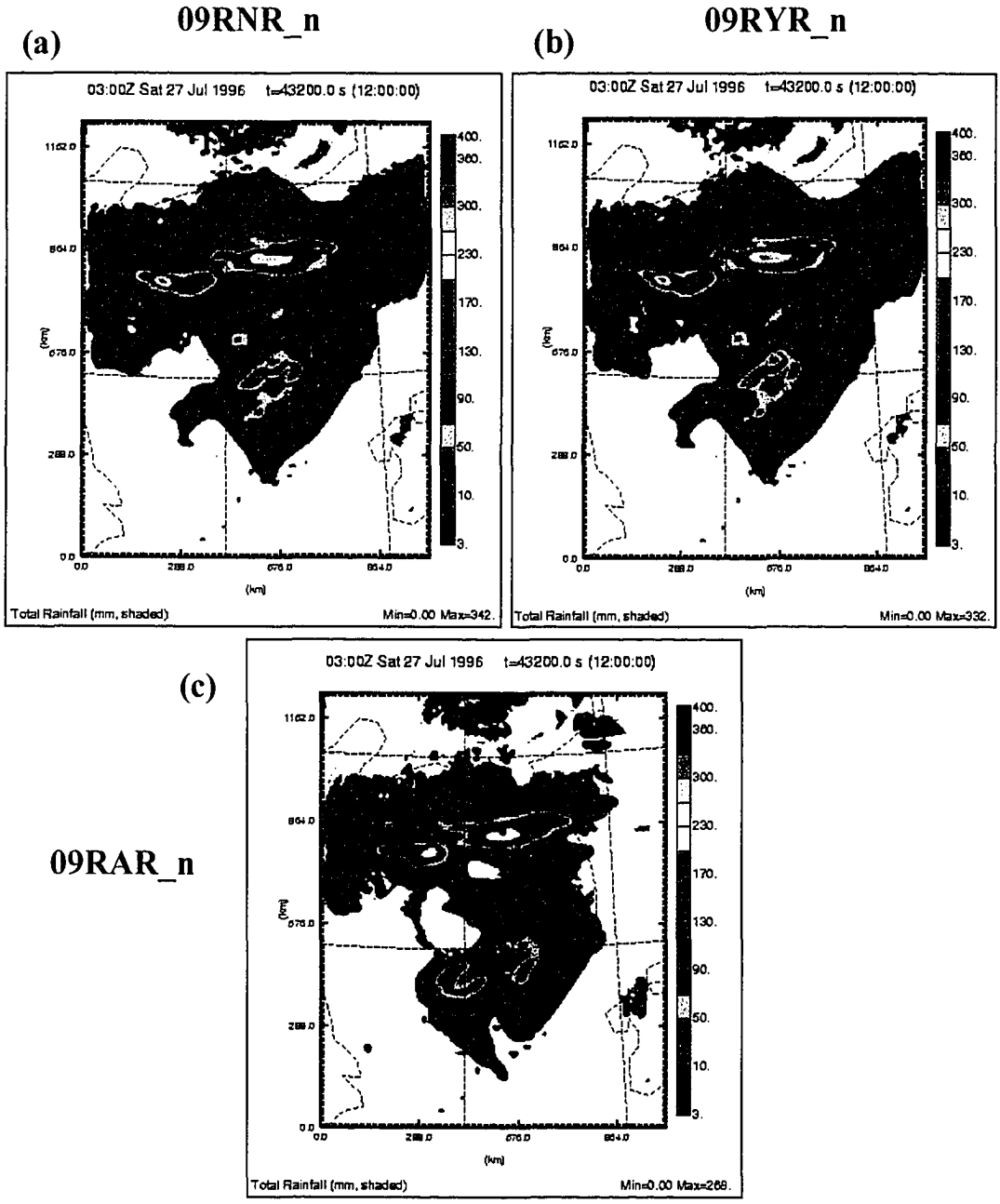

Fig. *5.5 12-hour accumulated rainfall for (a) 09RNR_n, (b) 09RYR_n, (c) 09RAR_n forecasts. ('C': Chorwon position, 'Y': Yonchon position, 'm': observed maximum position)*

Specifically, the predicted maximum rainfall amounts over the KP are 300 mm for 09RNR_n, 320 mm for 09RYR_n, and 260 mm for 09RAR_n – a considerable improvement over the runs discussed above. However, these results also show that rainfall is increasing not only locally, but throughout the entire domain, with no improvement in the location of the maximum. Indeed, as noted above, the new first guess field is considerably moister, thus producing increased precipitation rates and accumulated rainfall throughout the forecast period. As in the experiments using the old first guess field, radar data assimilation does not appear to improve the forecast. Considered qualitatively, these results at 9-km grid spacing suggest that the improved first guess field from the 27 km run has a positive effect at 9 km, though at the expense of increased biases. Note that we make no quantitative precipitation comparisons here because, as noted earlier, our focus is on the 3 km grid spacing experiments.

5.2.3 Grid-Scale Precipitation and Parameterized Convection Precipitation

The precipitation predicted by numerical weather models consists of grid-scale (resolvable) precipitation and parameterized sub-grid scale convective precipitation. In the 27 km experiment, precipitation produced by the cumulus convection scheme (not shown) is much larger than that produced by the explicit grid-scale cloud microphysics scheme – a result consistent with other studies (e.g., Bélair and Mailhot, 2001). Indeed, between approximately 15 and 5 km grid spacing, no clear scale separation exists for convective clouds, i.e., they cannot be resolved explicitly, and closure assumptions regarding their representation as sub-grid scale phenomena are not applicable (Molinari, 1993). As noted in section 4.7, a horizontal grid spacing of 9 km thus is ambiguous with

regard to cumulus parameterization, for example our Kain-Fritsch scheme (designed for grid spacings of approximately 25 km), though we use it on the 9 km grid per conventional wisdom (e.g., Bélair and Mailhot, 2001).

In this section we evaluate the partitioning of accumulated rainfall in a representative 9 km grid forecast between grid-scale precipitation and parameterized convection. Figure 5.6 shows the 12-hour accumulated rainfall for (a) the grid-scale precipitation and (b) parameterized cumulus, with panel (c) showing the sum for experiment 09RYR. The heaviest precipitation is produced by the grid-scale microphysics scheme, though cumulus convection contributes to broader and somewhat weaker precipitation. This reinforces the points made by Molinari (1993) and is similar to the study of Bélair and Mailhot (2001), which showed that intense precipitation is better represented by grid-scale cloud physics at a horizontal grid spacing of 6 km.

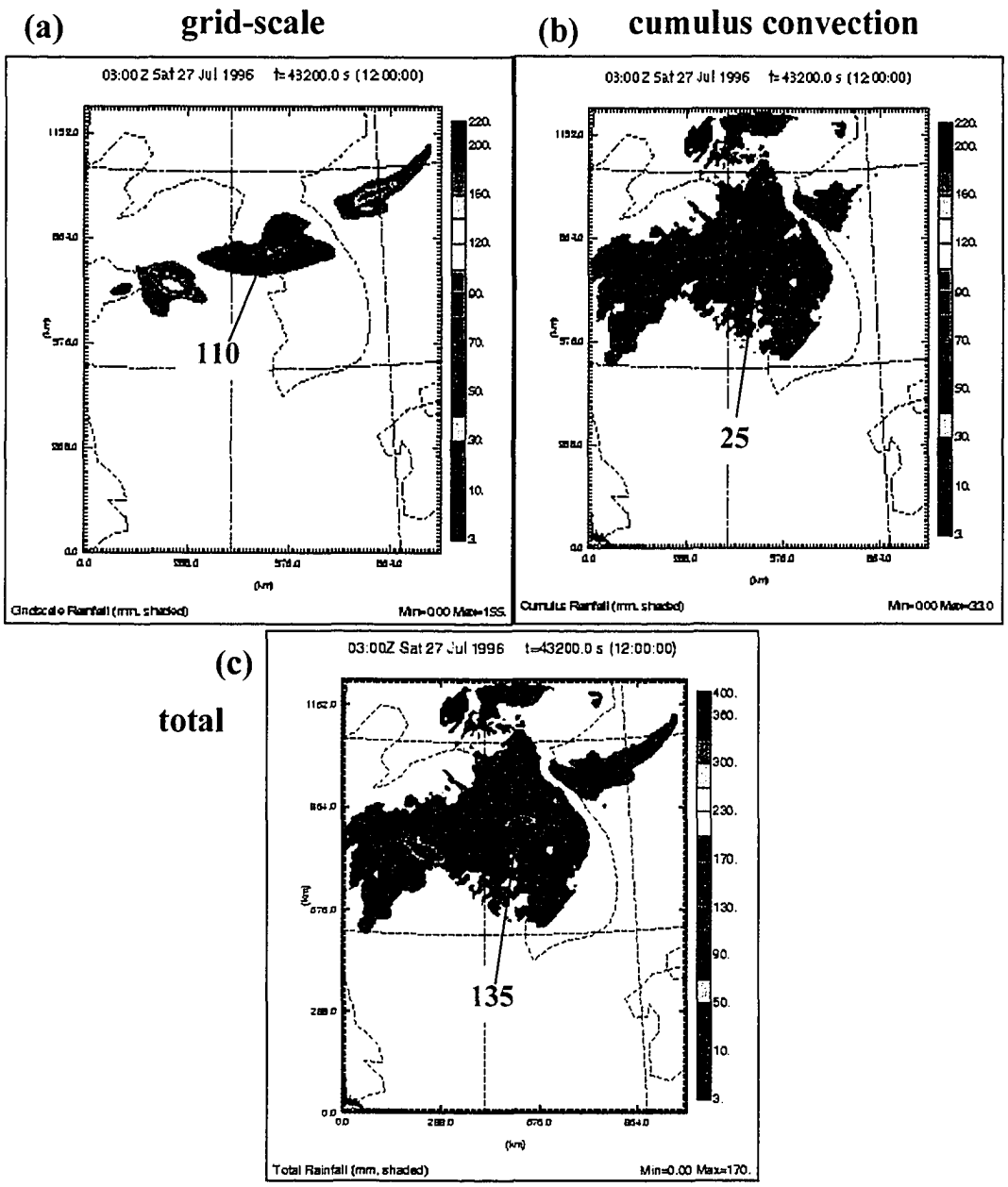

Fig. *5.6 12-hour accumulated rainfall for (a) grid-scale precipitation, (b) cumulus convection precipitation, and (c) grid-scale plus cumulus convection precipitation in 09RYR experiment.*

Chapter 6.

3-km Resolution Experiments

Although this study utilized numerical predictions at three different grid spacings, our principal goal is to evaluate the impact of NEXRAD data on forecasts at the highest resolution, or 3 km spacing. We describe in chapter the methodology behind the design these experiments and present a variety of analyses to assess the effectiveness of and physical response of the model to radar data assimilation.

6.1 Methodology of the 3-km Resolution Experiments

As mentioned in section 4.5, 18 experiments were performed using 3 km horizontal grid spacing. For ease of reference, they may be classified into four principal categories: (1) use of a different background field to initialize the outermost (27 km) grid; (2) experiments with and without radar data (03RNR, 03RYR, and 03ROR); (3) differences in radar data used, i.e., radial velocity only, reflectivity only, and both; and (4) use of different data assimilation strategies, e.g., length of assimilation interval, number of data sets assimilated. We describe below the results of experiments in the latter two categories given that the former two were discussed in section 4.5.

6.1.1 Assessing the Relative Value of Reflectivity and Radial Velocity

In general, both radial velocity and reflectivity data may be assimilated into a numerical model. Use of the former alone is expected to be less effective than using either reflectivity alone, or using both reflectivity and radial velocity, because of the absence of diabatic forcing, even though information about the horizontal wind field is known to be more important than the vertical wind field (Nascimento, 2003). In an effort to understand the tradeoffs, we conducted comparative experiments in which only one of the Doppler moments was used as well as both. The extension '_ref' in the name of the experiment (See table 4.3) means that only reflectivity information was assimilated.

6.1.2 Assessing Different Data Assimilation Strategies

To assess the impact of various assimilation strategies applied to NEXRAD data for the Chorwon-Yonchon heavy rainfall event, we start with a simple scenario in which assimilation is performed during the following three time windows: 15:50-16:00 UTC, 16:50-17:00, and 17:50-18:00 UTC (03RAR, Fig. 6.1a). Only a single volume scan of radar data, collected during the interval closest to the start of the assimilation window, is used for each period, i.e., data collected from 15:51-15:56 UTC, 16:51-16:56 UTC, and 17:51-17:56 UTC. Note that no radar data are used at the initial time (1500 UTC). We regard 03RAR as the control experiment and first wish to assess whether the chosen 10-minute assimilation window, with three hourly insertions of radar data, has any meaningful impact for a model run at 3 km grid spacing for 9 hours. We are particularly interested in the time period during which the radar data has a discernable and hopefully positive impact.

Building upon experiment 03RAR, six additional assimilation strategies are used, as shown in Figures 6.1 and 6.2. In experiment 03RAR_initrad, radar data are used at the initial time (1500 UTC). Only a single insertion of radar data is used in experiment 03RAR_1t to determine whether one or three assimilation cycles has the greatest impact. An experiment using rapidly updated assimilation cycle (03RAR_1h_rap) was performed to determine if a more continuous assimilation (three times within an hour) strategy provides any improvement, or causes the model to respond differently in terms of its adjustment to increments. We will focus in detail on 03RAR_1h_rap in the next chapter.

The final set of experiments focuses on the impact of the length of the data assimilation window. Lengths of 5 minutes, 10 minutes, and 20 minutes are employed (Figure 6.2), corresponding to assimilation windows of 15:58-16:03 UTC, 1658-17:03 UTC, and 17:58-18:03 UTC for experiment '03RAR_cent5' and 15:50-16:10 UTC, 16:50-17:10 UTC, and 17:50-18:10 UTC for experiment '03RAR_cent20'. Experiment '03RAR_cent10' is similar to 03RAR_initrad in that it uses data at the initial time and the same window length of 10 minutes; however, '03RAR_cent10' also uses different data assimilation windows: 15:55-1605 UTC (as opposed to 15:50-16:00 UTC in 03RAR_initrad), 16:55-17:05 UTC (as opposed to 16:50-17:00 UTC in 03RAR_initrad), and 17:55-18:05 UTC (as opposed to 17:50-18:00 UTC in 03RAR_initrad). By comparing the results of 03RAR_cent10 with those of 03RAR_initrad, we can determine whether any differences exist solely due to changes in the placement of the data assimilation window.

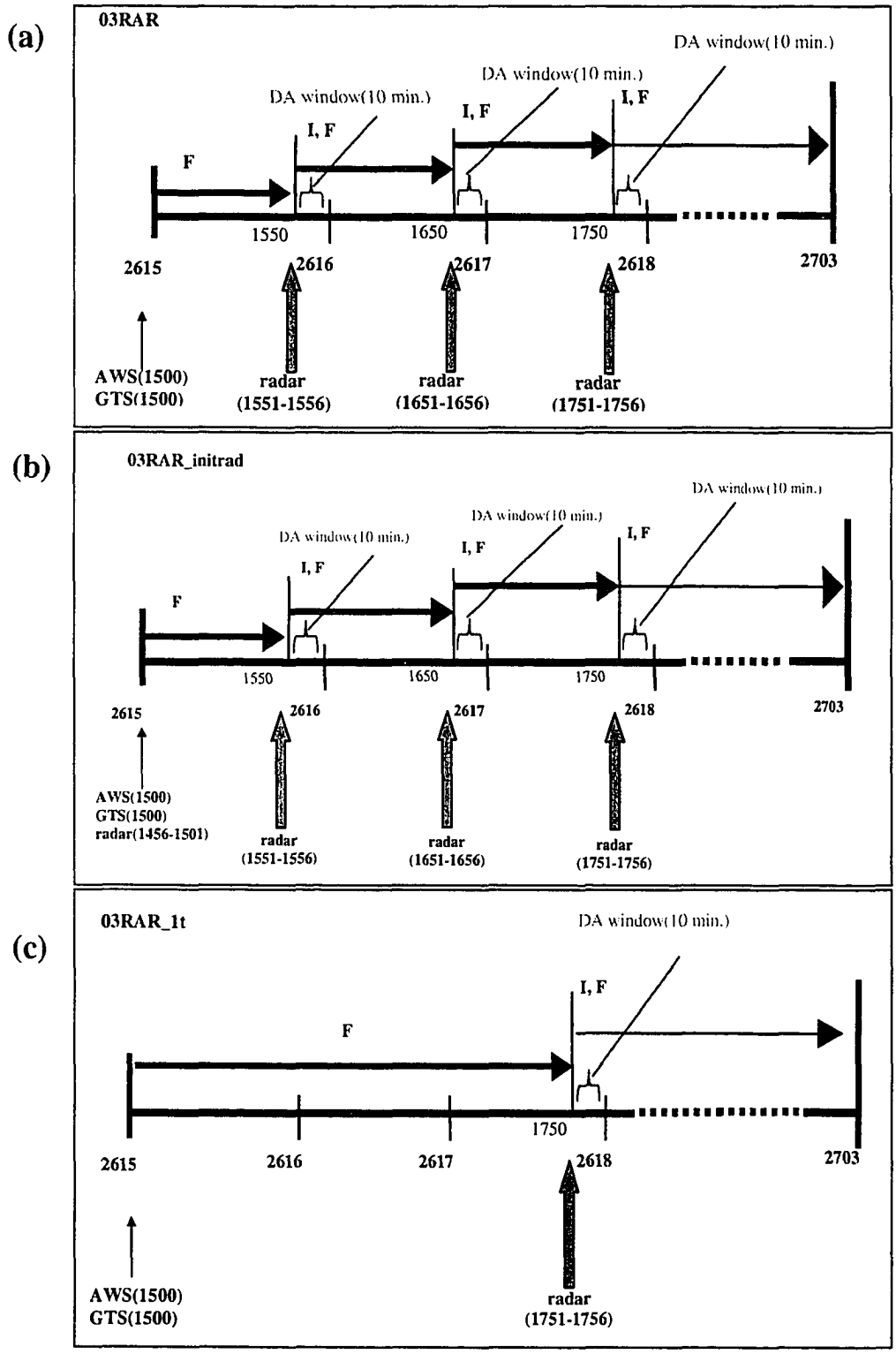

Fig. 6.1 Experiment design for different data assimilation strategies; (a) 03RAR, (b) 03RAR_initrad, (c) 03RAR_1t, and (d) 03RAR_1h_rap. Each thick arrow indicates the radar data assimilation and the numbers in parentheses mean the data time. For example, AWS(1500) and radar(1551-1556) mean AWS data at 1500 UTC and one volume scan radar data for 5 minutes from 1551 UTC to 1556 UTC, respectively.

(d)

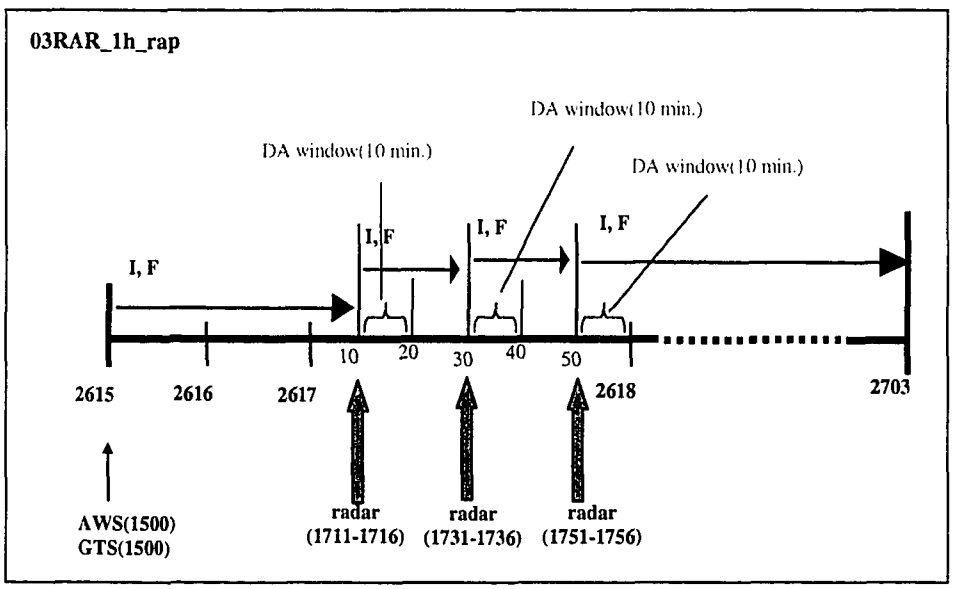

Fig. 6.1 (Continued)

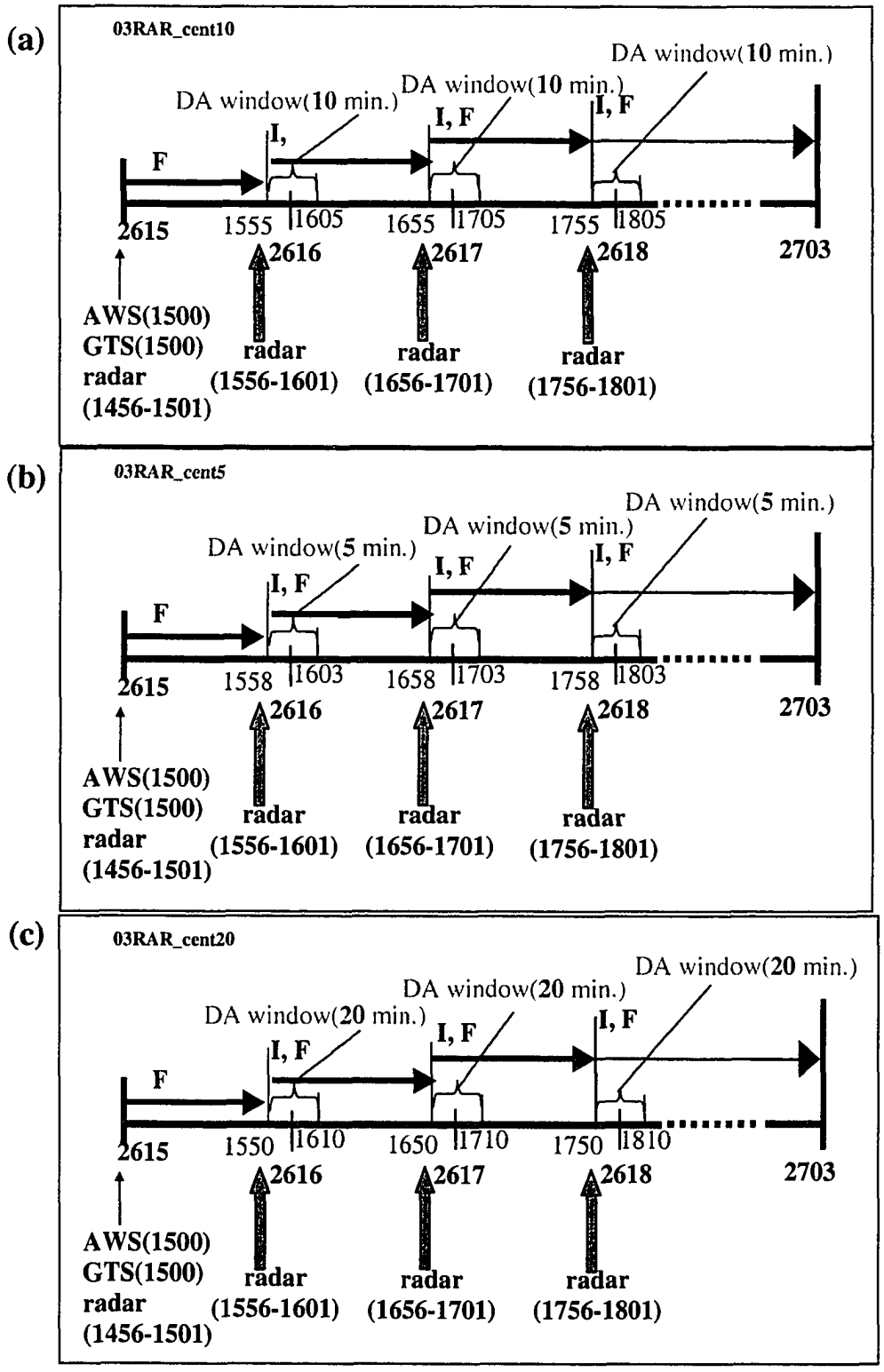

Fig. 6.2 Same as Fig. 6.1 but for (a) 03RAR_cent10, (b) 03RAR_cent5, and (c) 03RAR_cent20.

6.2 Results of 3-km Resolution Experiments

In an effort to verify, in the most quantitative manner possible, the results from our 3 km grid spacing forecasts in the four experiment categories described in the previous section, we compare forecasted precipitation accumulation against estimates of the same quantity obtained from the WSR-88D radar at Pyoungtaek, the latter provided courtesy of Vieux and Associates, Inc and shown in Figure 6.3 for the 6-hr and 12-hr accumulations. Prior to discussing in the next chapter how these estimates were computed, along with detailed precipitation skill scores, we present here more qualitative comparisons between the model accumulated rainfall and observations.

6.2.1 Use of Different Background Fields to Initialize the Outermost Grid

As mentioned previously, all 27 km grid spacing simulations made for this study utilized for a background field output from the KMA forecasting system that was operational at the time of the heavy rainfall event. A new first guess field, based upon a more recent version of the model, was noted to be much more moist. We felt compelled to test this new background field, even though it appeared to be of lesser quality than the original one when compared against observations. Surprisingly, it led to improvements in the 27-km grid spacing forecast and to a positive impact on the 9-km grid spacing forecast, though at the expense of increased biases. That is, the moister environment produced greater amounts of precipitation everywhere, increasing the skill score because of an increase in the bias. The question is whether a positive impact can be shown in the finest grid spacing forecast using this new first guess field.

(a)

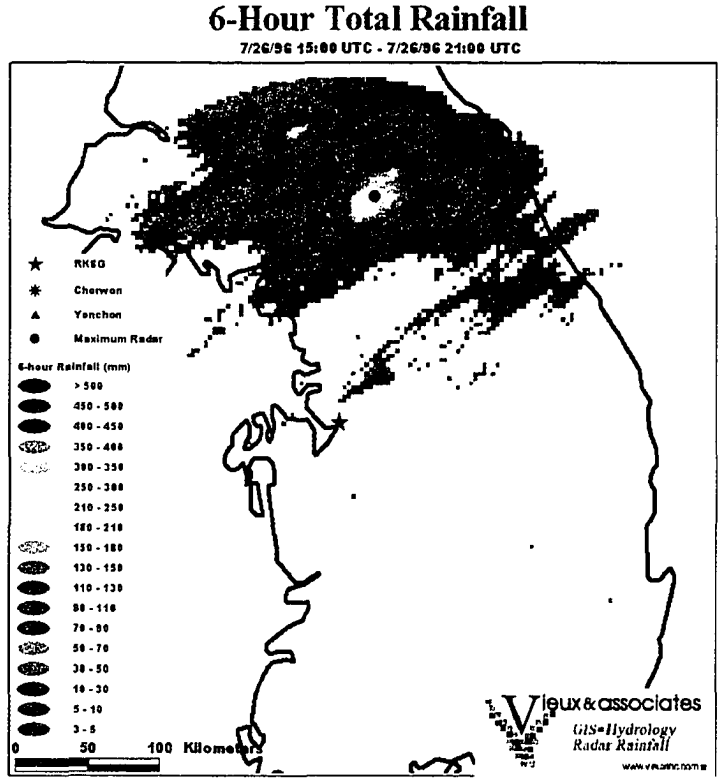

(b)

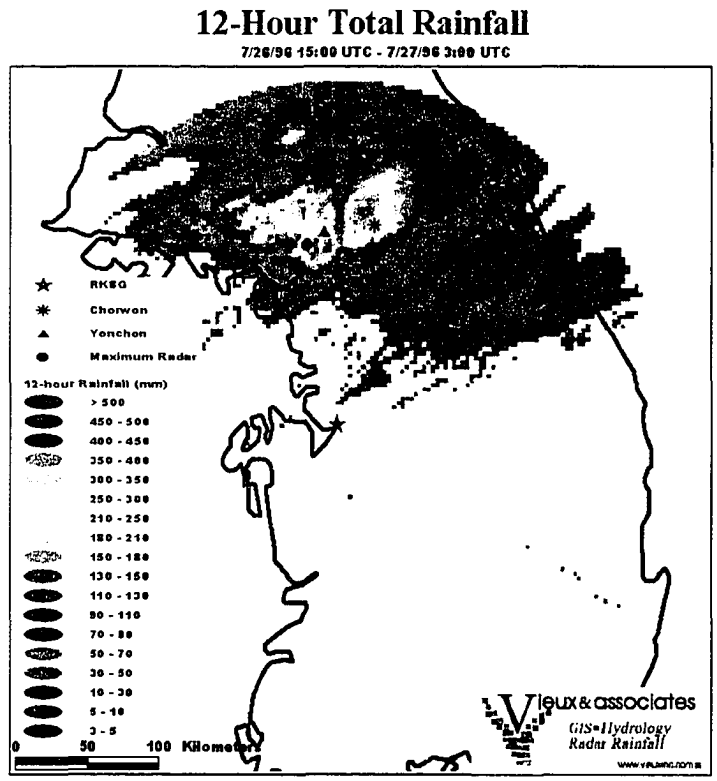

Fig. 6.3 Observed accumulated rainfall estimated from NEXRAD Level II data (a) 6 hour accumulated rainfall for 1500-2100 UTC and (b) 12 hour accumulated rainfall, 15-03UTC. Star, asterisk, filled triangle, and filled circle mean the positions of Pyoungtaek radar, Chowon, Yonchon, and observed maximum rainfall, respectively.

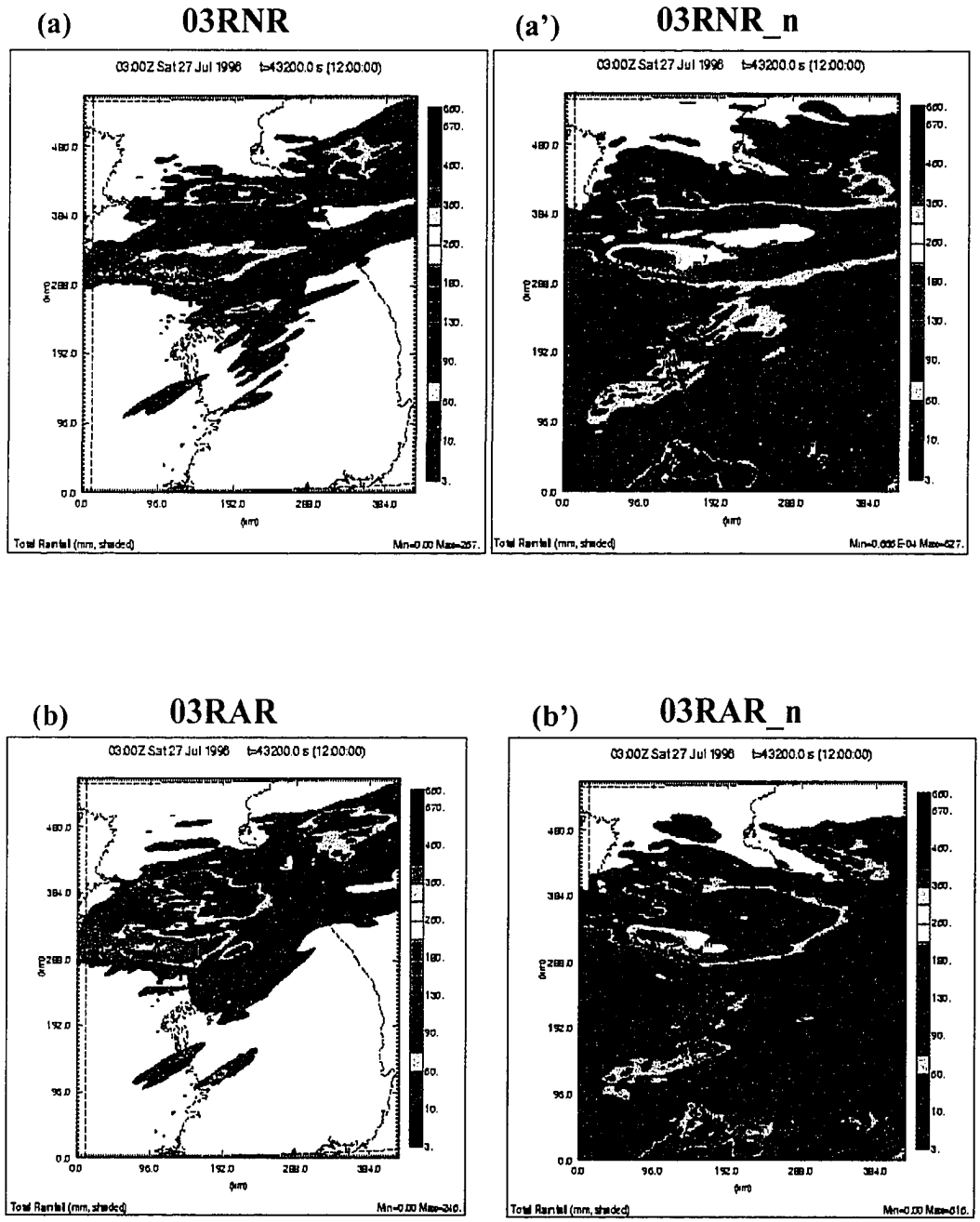

Fig. 6.4 Predicted accumulated rainfall for 12 hr valid at 0300 UTC July 27 for (a) 03RNR, (a') 03RNR_n, (b) 03RAR, and (b') 03RAR_n experiments. Left panels are the results using old first guess field and right panels are the results using new first guess field. 'c', 'y', and 'm' mean the positions of Chorwon, Yonchon, and the position of observed maximum rainfall, respectively.

For this purpose we examined the predicted rainfall using the old background field and the new background field. Figure 6.4 shows the forecasted 12-hr accumulated rainfall for experiments 03RNR and 03RAR, along with 03RNR_n and 03RAR_n. The left panels depict the result using the old first guess field while the right panels show the result using the new first guess field. It is clear that the predicted accumulated rainfall using the new first guess field is considerably larger than when using the old first guess field over almost the entire KP. The 9-km results for assessing this same impact (Fig. 5.3) were similar and in fact slightly better. However, the 3-km results do not show a positive impact, but rather a substantial negative one. Note in particular the nearly uniform light rainfall over most of the domain, in addition to the especially intense amounts off the west coast.

The predicted maximum rainfall for 03RNR and 03RNR_n experiments is 49 % (257 mm to 518 mm) and 102 % (527 mm to 518 mm) of the observed maximum, respectively. The results of 03RAR and 03RAR_n, namely, 47 % (245 mm to 518 mm) and 99 % (516 mm to 518 mm), are similar to those of 03RNR and 03RNR_n. The much more accurate maximum rainfall (102 % and 99 %) using the new first guess field can be regarded as a significant improvement. However, it is clear that these results cannot support use of the new first guess field for the following reasons: (1) the predicted accumulated rainfall increased not only locally, but throughout the entire domain; (2) the predicted maximum rainfall for 6-hr and 9-hr (figures not shown) do not exhibit any improvement; for example, the predicted rainfall for 6-hr in 03RAR_n is 163 % (462 mm to 284 mm) of the observed maximum, while 03RAR is 87 % (245 mm to 284 mm); (3) the distances between the locations of maximum forecasted and observed rainfall position.

The 'm' in Fig. 6.4 shows the location of maximum observed rainfall. Also shown are the positions of the maximum forecasted rainfall for all experiments. The distances between the two for 03RNR and 03RAR are 56 km and 51 km, respectively, while those of 03RNR_n and 03RAR_n are 77 km and 74 km, respectively. The greatest error occurs when using the new first guess field to initialize 27-km grid spacing experiment. Consequently, it is very difficult to support using the "improved" background field to initialize the outermost grid. In other experiments, such as 03RYR_n, 03ROR_n, 03RNR_n and 03RAR_n described in this sub section, the results (not shown) are very similar. Thus, all of our experiments are made using the operationally-available RDAPS forecast to initialize the 27 km grid spacing ARPS forecast.

6.2.2 Relative Impact of Reflectivity and Radial Velocity

Radial velocity, or the velocity component directed parallel to the radar beam, and reflectivity are the major observational data available from Doppler radars. Both are used for assimilation into numerical models, though retrieval techniques often must be used to obtain other necessary information (Sun et al. 1991, Shapiro et al. 1995; Sun and Crook 1997). Coordinate transformations of radial velocity, sampled in spherical coordinates, often must be made for compatibility with a numerical model's coordinate system and sometimes poses additional difficulty (Sun et al. 1994). Considering the potential impact, via the use of reflectivity, of diabatic heating on model initialization (section 6.1.1), it is valuable for us to assess the relative importance of radial velocity and reflectivity on the accuracy of forecasts in the present study.

In what follows, experiments using both radial velocity and reflectivity data, i.e., 03RYR, 03ROR, 03RAR, 03RYR_n, 03ROR_n, and 03RAR_n, are compared against their counterparts that employed only reflectivity, i.e., 03RYR_ref, 03ROR_ref, 03RAR_ref, 03RYR_ref_n, 03ROR_ref_n, and 03RAR_ref_n. Figure 6.5 shows the forecasted 12-hr accumulated rainfall for 03RYR and 03ROR, along with 03RYR_ref and 03ROR_ref. The left panels show results using both radial velocity and reflectivity, while the right panels show results using reflectivity alone. Little difference is evident in the overall pattern, and the predicted maximum rainfall amounts for 03RYR and 03RYR_ref are 50 % (259 mm to 518 mm) and 47 % (245 mm to 518 mm) of the observed maximum rainfall, respectively. The results of 03ROR and 03ROR_ref show predicted maximum rainfall amounts of 49 % (251 mm to 518 mm) and 49 % (254 mm to 518 mm), respectively, and therefore also show little change.

The distances between the locations of maximum forecasted and maximum observed rainfall are similar to the above, i.e., 50 km and 56 km in 03RYR and 03ROR, respectively, and in 03RYR_ref and 03ROR_ref, 52 km and 59 km. Although the results using both radial velocity and reflectivity are slightly better than using reflectivity alone, the differences are not viewed as significant in light of the many processes associated with a storm-scale forecast (in Chapter 7, we will examine the behavior of the increments in an attempt to explain this behavior).

In other experiments, e.g., 03RAR_ref, 03RYR_ref_n, 03ROR_ref_n, and 03RAR_ref_n, the results (not shown here) are essentially the same. Consequently, both radial velocity and reflectivity are employed in the different data assimilation strategies

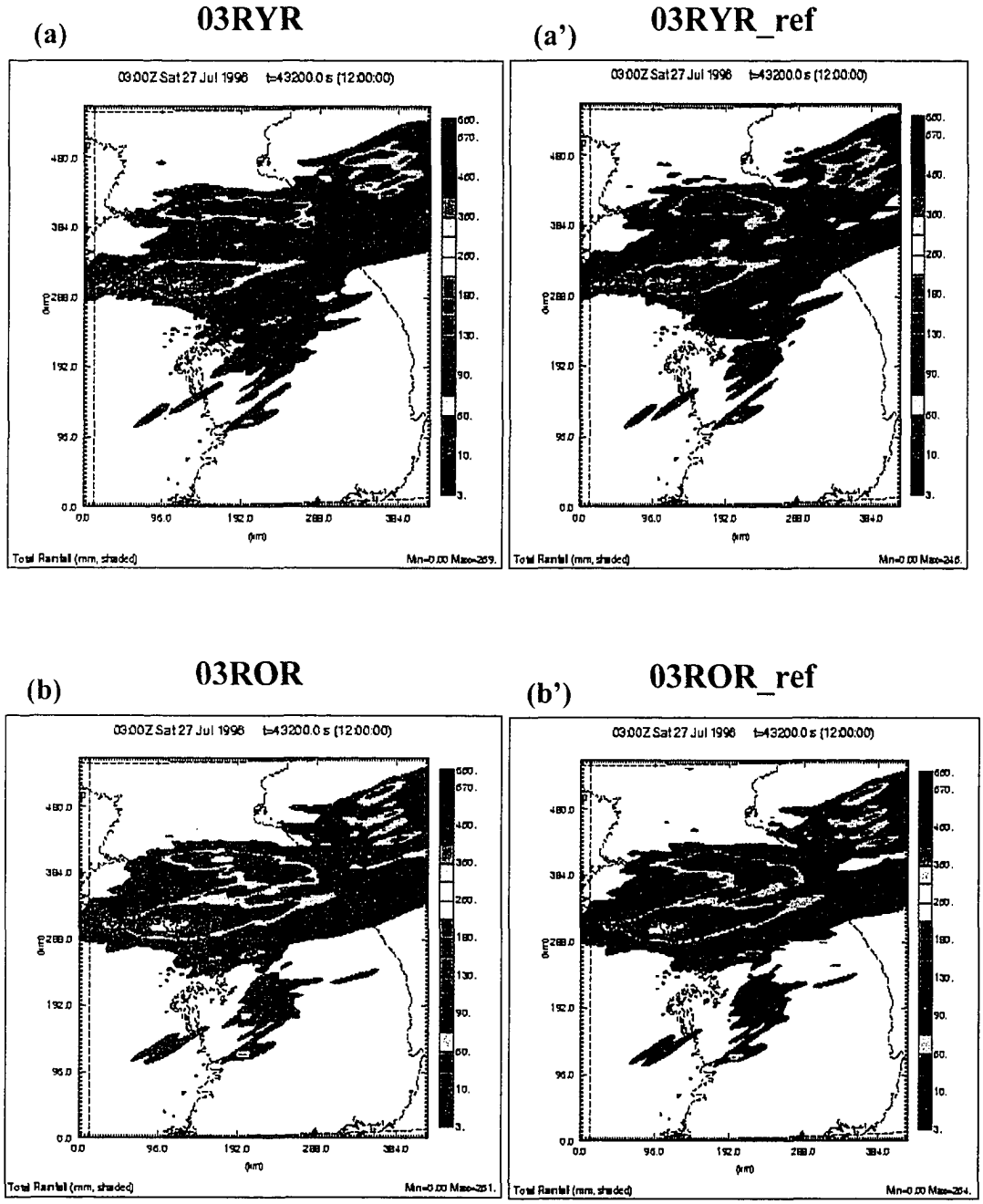

Fig. 6.5 Predicted accumulated rainfall for 12 hr valid at 0300 UTC July 27 for (a) 03RYR, (a') 03RYR_ref, (b) 03ROR, and (b') 03ROR_ref experiments. Left panels are the results using both reflectivity and radial velocity and right panels are the results using reflectivity alone. 'c', 'y', and 'm' mean the positions of Chorwon, Yonchon, and the position of observed maximum rainfall, respectively.

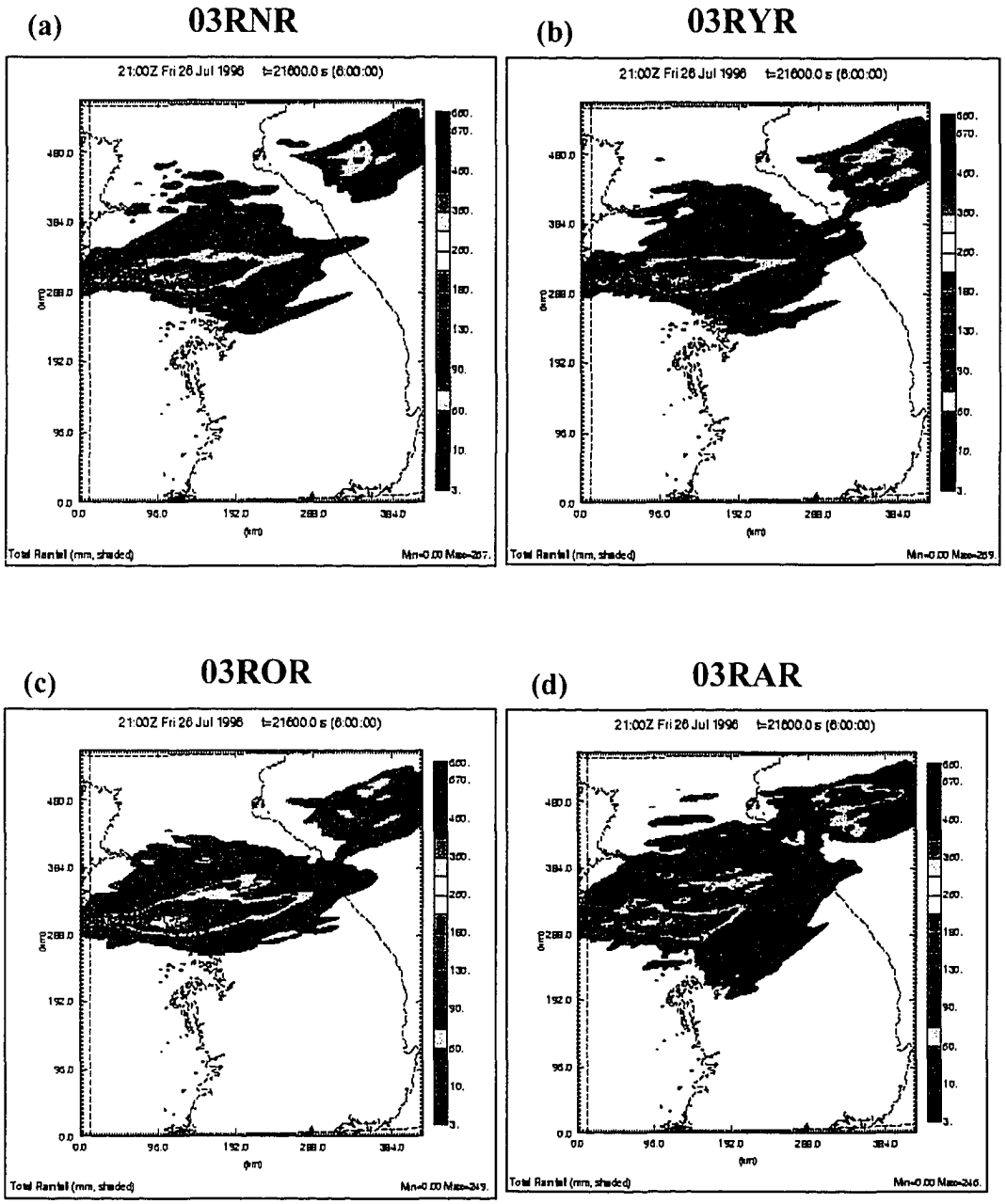

Fig. 6.6 Predicted accumulated rainfall for 6 hr valid at 2100 UTC July 26 for (a) 03RNR, (b) 03RYR, (c) 03ROR, and (d) 03RAR experiments. 'c', 'y', and 'm' mean the positions of Chorwon, Yonchon, and the position of observed maximum rainfall, respectively.

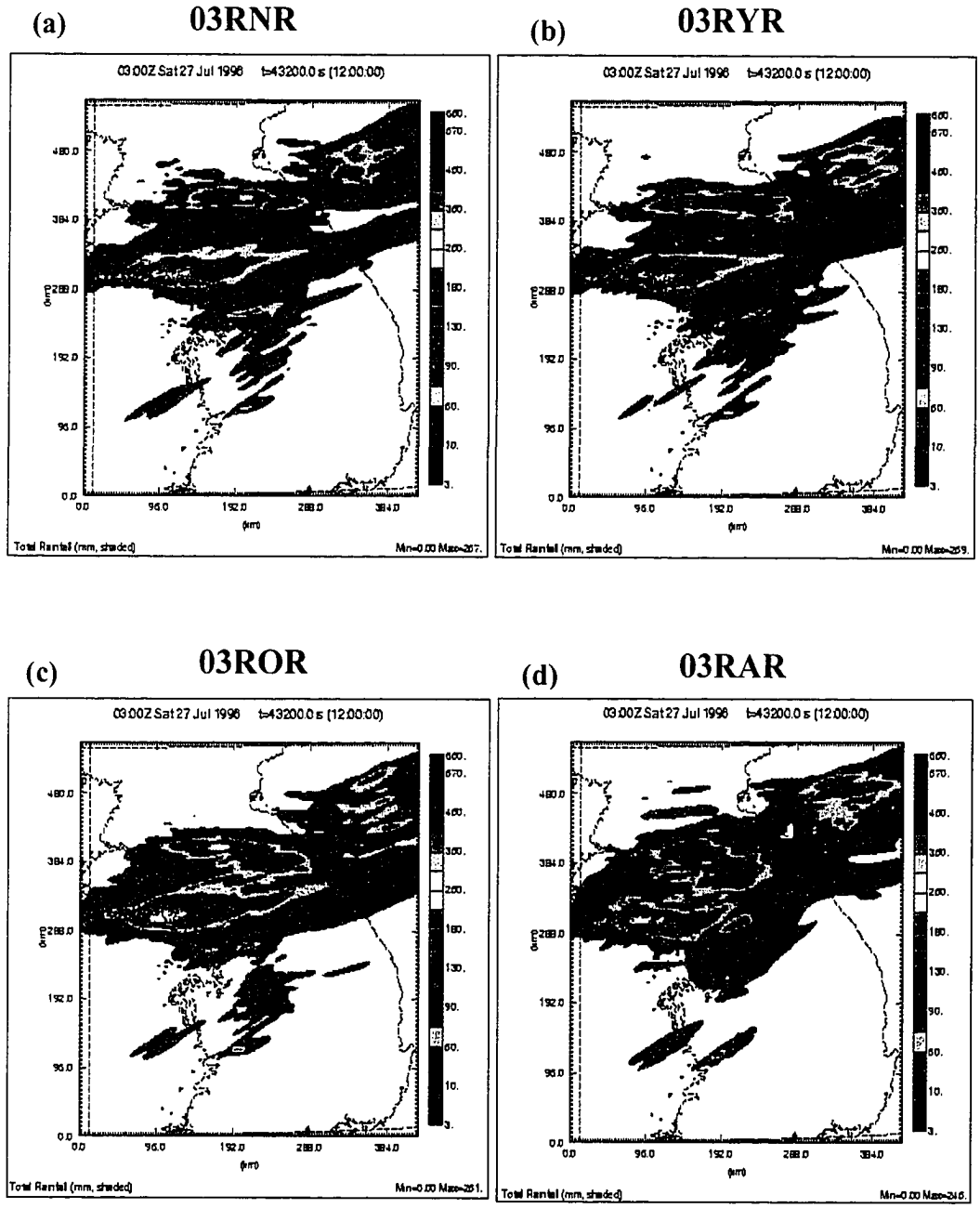

Fig. 6.7 Predicted accumulated rainfall for 12 hr valid at 0300 UTC July 27 for (a) 03RNR, (b) 03RYR, (c) 03ROR, and (d) 03RAR experiments. 'c', 'y', and 'm' mean the positions of Chorwon, Yonchon, and the position of observed maximum rainfall, respectively.

that follow. The more detailed description about the relationship between radial velocity and reflectivity will be explained in the quantitative verification (Chapter 7).

6.2.3 Experiments with and without Radar Data

In this section, we focus on the results of experiments made with and without radar data. To explain these results qualitatively, we first compare the predicted accumulated rainfall with observations. Figures 6.6 and 6.7 show the former over 6 hours valid at 2100 UTC July 26, and over 12 hours valid at 0300 UTC July 27, for experiments 03RNR, 03RYR, 03ROR, and 03RAR. In these figures, 'c', 'y', and 'm' refer to the positions of Chorwon, Yonchon, and the maximum observed rainfall. At 6 hours (Fig. 6.6), the position of the observed maximum is located north of Chorwon (marked 'c'), while at 12 hours (Fig. 6.7), it is located southeast of Yonchon (marked 'y').

Qualitatively, there exists no clear difference at 6 hours among the results of these experiments with regard to the shape and location of the predicted maximum rainfall, except that 03RAR (Fig. 6.6d) shows an increased bias and more detailed structure. Compared to the observed accumulated rainfall (fig. 6.3a), the shapes of predicted rainfall have a more east-west orientation and are less localized in their maximum values. The observed rainfall shows a clear boundary between the rain region and the no rain region about 40 km south of Chorwon and Yonchon. However, the predicted results show the boundary significantly further south. The 12-hr accumulated rainfall is similar to that at 6 hours, with 03RAR (Fig. 6.7d) relatively closer to the observations than the other experiments when considering the boundary between the rain region and the no rain region.

For a more detailed verification, we use the predicted maximum rainfall amounts and the distances between the locations of the maximum forecasted and observed rainfall in all experiments (hereafter DIS). The accumulated rainfall and the DIS for 6-hr, 9-hr, and 12-hr are shown in Table 6.1. These results also do not show clear differences among the experiments. The DIS in 03RAR for the 6-hr forecast is 93 km, while for the others it ranges from 96 km to 106 km. In 03RAR, the DIS is slightly better. However, the DIS differences between 03RAR and other experiments occur over only one to four grid points. The predicted maximum rainfall at 6-hr is much better than that at other times. The ratios of the predicted maximum to observed rainfall (hereafter RAT) for 6-hr are 87 % to 91 %, while the ranges for 9-hr and 12-hr are 56 % to 58 % and 47 % to 50 %, respectively. What is the reason for this large difference?

Figure 6.8 shows the time evolution of observed and predicted accumulated rainfall from 1600 UTC July 26 (1-hr forecast) to 0300 UTC July 27 (12-hr forecast). The observed rainfall increased rapidly throughout the entire period, while the predicted rainfall for all experiments increases only until 1900 UTC (4-hr forecast). It appears that the numerical model in this study, regardless of the details of the individual simulations, produces most of the precipitation within the first 4 hours. Thus, it is very difficult to determine which experiment is best. Is it then impossible to assess the differences in experiments with and without the use of radar data, and to predict longer than 4 hours?

It is very difficult to compare the forecasted results to observations using only the maximum rainfall amount and its position simply because the forecasted rainfall from a numerical model usually has large error in both amplitude and phase, especially when

Table 6.1 Predicted and observed maximum rainfall and the distances between the locations of maximum forecasted and observed rainfall position for the experiments with or without radar data.

		03RNR	03RYR	03ROR	03RAR
6-hr (1500-2100 UTC)	Obs. Max.(mm)	284			
	Fcst. Max. (mm)	257	259	249	245
	Fcst./Obs. (%)	90	91	88	87
	Distance (km)	96	96	106	93
9-hr (1500-0000 UTC)	Obs. Max.(mm)	441			
	Fcst. Max. (mm)	257	259	249	245
	Fcst./Obs. (%)	58	59	56	56
	Distance (km)	56	50	56	51
12-hr (1500-0300 UTC)	Obs. Max.(mm)	518			
	Fcst. Max. (mm)	257	259	251	245
	Fcst./Obs. (%)	49	50	48	47
	Distance (km)	56	50	56	51

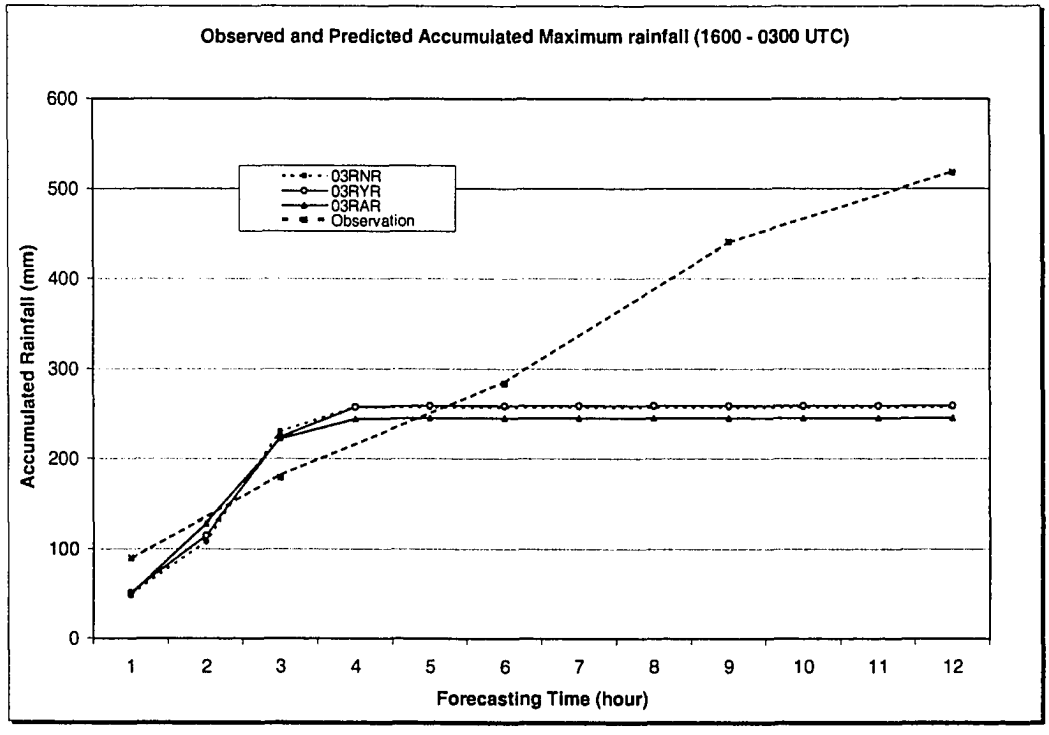

Fig. 6.8 Time evolution of observed and predicted accumulated maximum rainfall from 1600 UTC (1 hour) July 26 to 0300 UTC (12 hour) July 27 for observation (dashed line with filled rectangles), 03RNR (dotted line with filled circles), 03RYR (solid line with open circle), and 03RAR (solid line with filled triangles) experiments.

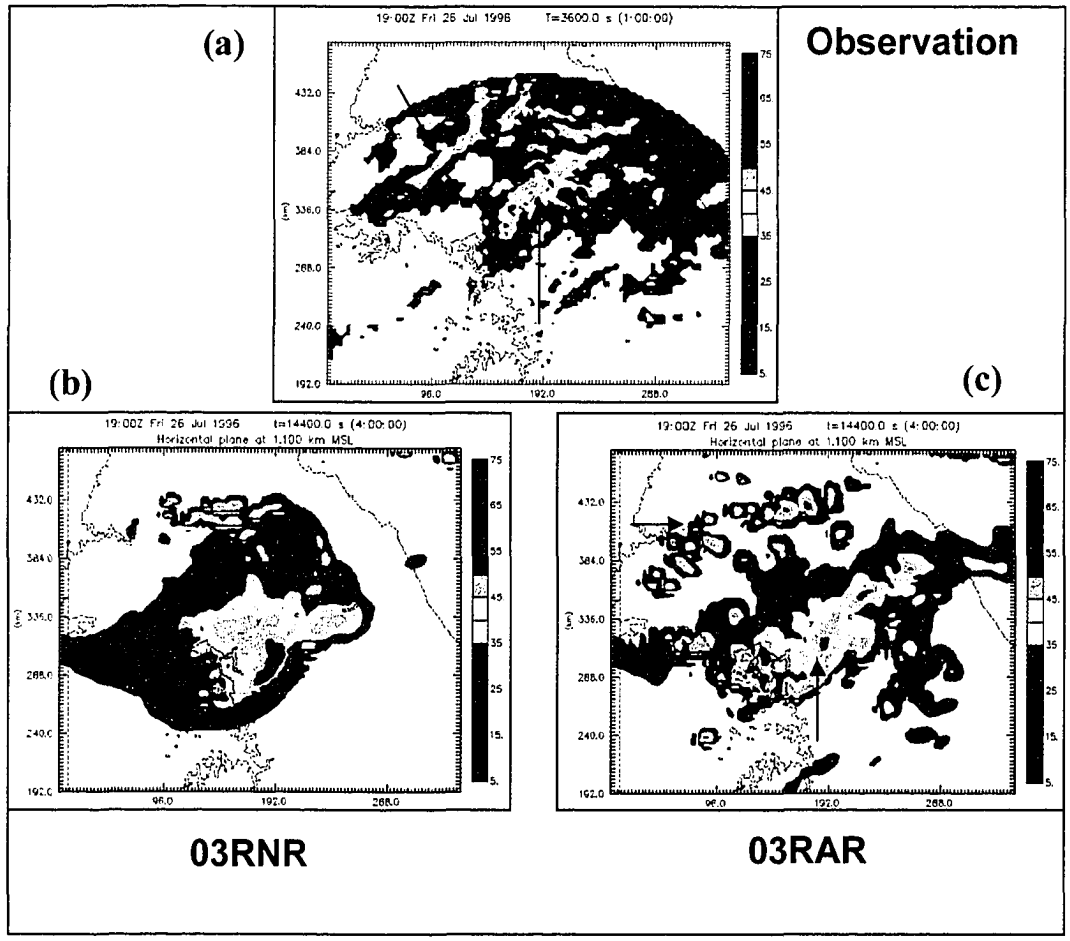

Fig. 6.9 Observed and predicted radar reflectivity at 1900 UTC July 26 (4-hr forecast, 1 hour after finishing data assimilation for 03RAR experiment). (a) is observed horizontal reflectivity at lowest elevation angle (0.48°), (b) and (c) are the predicted horizontal reflectivity at 1.1 km height from sea level for 03RNR and 03RAR experiments, respectively.

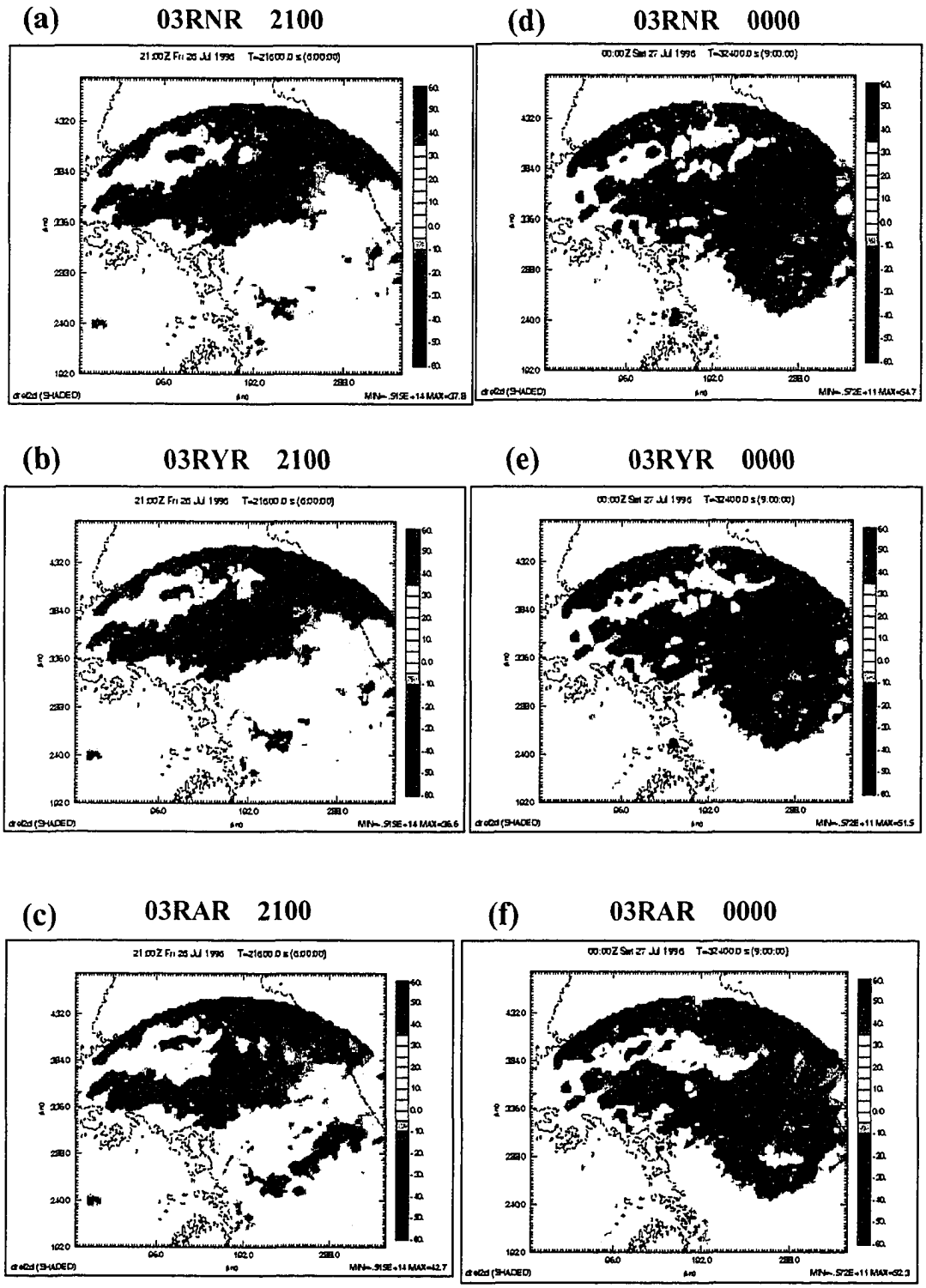

Fig. 6.10 The reflectivity difference between forecasted and observed reflectivity (forecast – observation) for 03RNR (upper panels, a, d, and g), 03RYR (middle panels, b, e, and h), and 03RAR (lower panels, c, f, and i) experiments at 2100 UTC (left panels of first page, a, b, and c), 0000 UTC (right panels of first page, d, e, and f), and 0300 UTC (g, h, and i in second page). Red and blue color means over predicted and under predicted reflectivity, respectively.

(g) 03RNR 0300

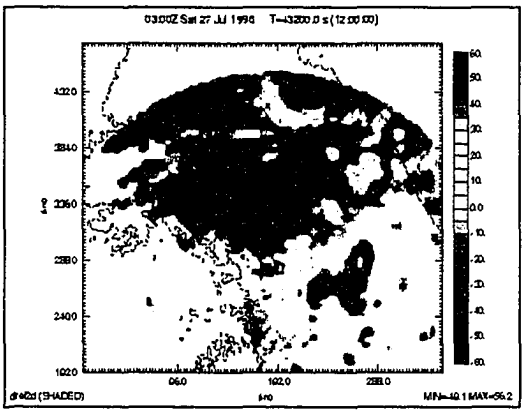

(h) 03RYR 0300

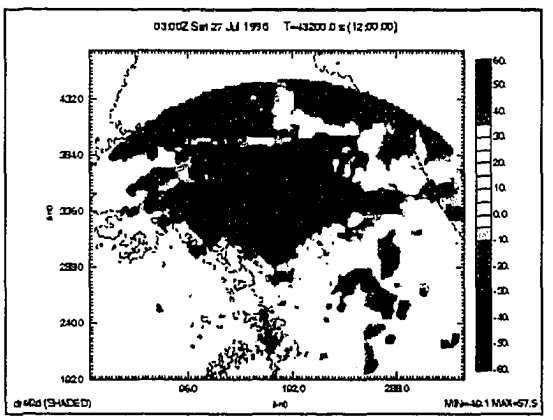

(i) 03RAR 0300

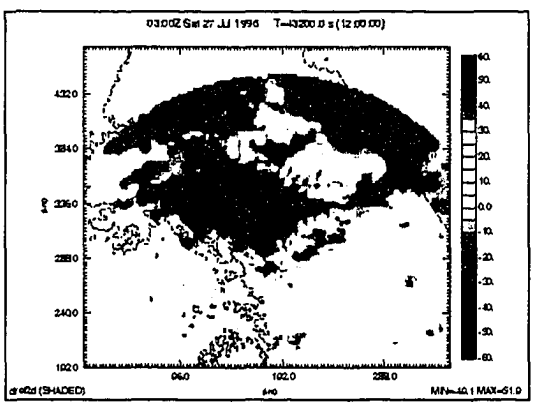

Fig. 6.10 (Continued)

considering fine scales. As the next step toward assessing the quality of our experiments compared with observations, we compare observed and predicted radar reflectivity.

Figure 6.9 shows observed and predicted radar reflectivity at 1900 UTC on July 26. This time is 4 hours after the start of the simulation (1500 UTC), and 1 hour after the end of the data assimilation period in 03RAR. The observed reflectivity used (Fig. 6.9a) is the horizontal reflectivity at the lowest elevation angle (0.48°). The predicted reflectivity image is for the horizontal reflectivity at a height of 1.1 km above sea level. The latter is used to avoid errors in the difference between observed and predicted reflectivity by considering the distance between the Pyoungtaek radar site and the Chorwon and Yonchon region where the heavy rainfall occurred – about 135 km, at which the height of the radar beam is approximately 1.1 km MSL.

As shown in Figure 6.9, the results of experiment 03RAR are much better than those of 03RNR. The former depicts well the line of echoes in the observed reflectivity (see the arrows in Fig. 6.9a and 6.9c), while 03RNR shows only rough outlines and does not exhibit a linear structure. This is of course only one demonstration of the effect of radar data assimilation. Although the results are disappointing when considering the maximum rainfall amount and location, we do find a positive impact of radar data assimilation considering only the predicted and observed reflectivity. To confirm this and to better understand why, we compute the reflectivity difference fields (forecast minus observations, hereafter RD).

Figure 6.10 shows the RDs for 03RNR, 03RYR, and 03RAR at 2100 UTC on July 26 (6 hours after starting the simulations or 3 hours after finishing data assimilation), at 0000 UTC (9 hours after starting the simulations or 6 hours after finishing data

assimilation), and at 0300 UTC July 27 (12 hours after starting the simulations or 9 hours after finishing data assimilation). Red and blue colors represent over-forecasted and under-forecasted region, respectively, while white areas represent perfect agreement between observations and forecast. We focus on two points for this evaluation using the RD.

First, we seek to document and understand differences among the experiments and second, we wish to understand how the impact of radar data diminishes as the forecast proceeds. Focusing on Fig. 6.10a, b, and c at 2100 UTC July 26, 03RAR shows a much improved forecast compared to the other cases across the entire domain. The result at 0000 UTC on July 27 (Fig. 6.10d, e, and f) is similar to that at 2100 UTC, although the improvements in 03RAR are somewhat less. At 0300 UTC on July 27, the results of 03RAR (Fig. 6.10i) continue to be superior to the other experiments (Fig. 6.10g and h). For example, reflectivity is over-forecasted over the southeast part of the domain in 03RNR and 03RYR (Fig. 6.10g and h), and this problem is reduced greatly in 03RAR, though the latter produced stronger reflectivity over the southwest part of the domain (on the west sea and coast area).

Overall, three main findings are evident from this evaluation of difference fields. First, 03RYR provides no obvious benefits compared to 03RNR. Second, radar data assimilation shows a positive impact on the forecast compared to no radar data assimilation. Finally, *we note that the effect of radar data assimilation diminishes with time throughout the forecast*, perhaps for about 3 hours. This result is, however, questionable because the above analysis is purely qualitative. We will use quantitative verification in the next chapter to confirm the impact of radar data assimilation.

6.2.4 The Results Using Different Data Assimilation Strategies

Six additional assimilation strategies, representing extensions or modifications of 03RAR, are used to assess the impact of radar data on the prediction of the Chorwon-Yongchon heavy rainfall event. Figures 6.11 and 6.12 show the same information as Figures 6.6 and 6.7, except for the six additional data assimilation strategies described earlier, and Tables 6.2 and 6.3 show the accumulated rainfall amounts and the DISs for 6-hr, 9-hr, and 12-hr in comparison with observed values.

Experiment 03RAR_initrad uses radar data at the initial time (which was note the case in 03RAR) owing to the fact that storms present in the initial conditions can affect the subsequent location and amount of precipitation. The results of the 03RAR_initrad (Figs. 6.11b and 6.12b) are very similar to those of 03RAR (Figs. 6.11a and 6.12a), especially for 12-hr accumulated rainfall. A difference is, however, noted in the 6-hr accumulated rainfall (Fig. 6.11b), where heavy rainfall is predicted north of the observed position in 03RAR_initrad and not in 03RAR. The RATs of 03RAR_initrad for all forecasting times are slightly better than those of 03RAR, with a 2 % margin of difference (Table 6.2). There is no major difference in DIS between these two experiments (Table 6.2). Considering these results, we find only a slight (probably not meaningfully significant) positive impact for radar data assimilation when using radar data at the initial time.

Building in complexity, the next experiment assesses the number of new data updates within the assimilation cycle. Experiment 03RAR_1t uses only a single insertion of radar data within one hour while the 03RAR uses three assimilation cycles during

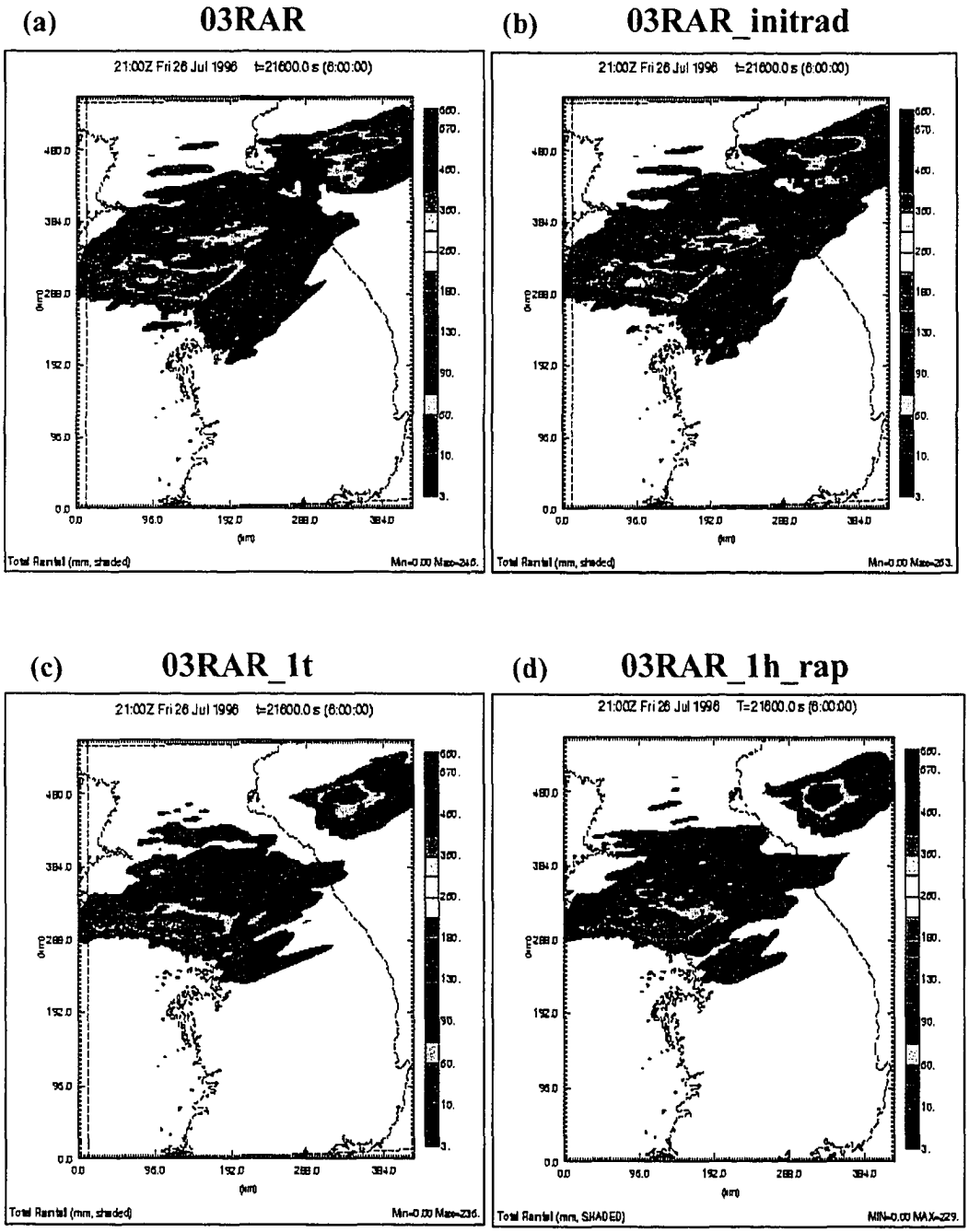

Fig. 6.11 Predicted accumulated rainfall for 6 hr valid at 2100 UTC July 26 for (a) 03RAR, (b) 03RAR_initrad, (c) 03RAR_1t, (d) 03RAR-1h_rap, (e) assi_cent5, (f) assi_cent10, and (g) assi_cent20 experiments. 'c', 'y', and 'm' mean the positions of Chorwon, Yonchon, and the position of observed maximum rainfall, respectively.

(e) 03RAR_cent5

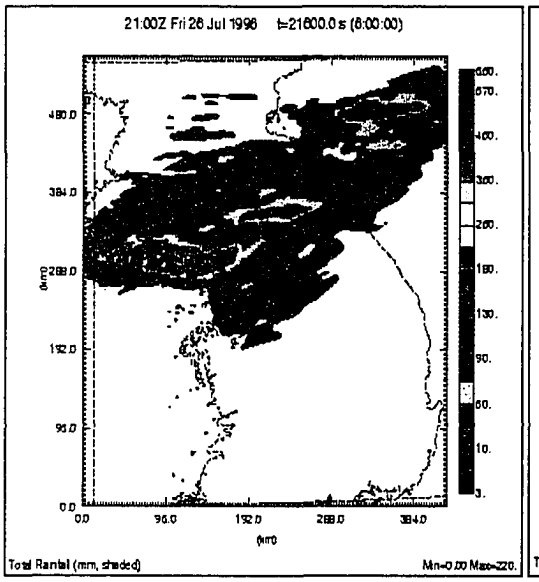

(f) 03RAR_cent10

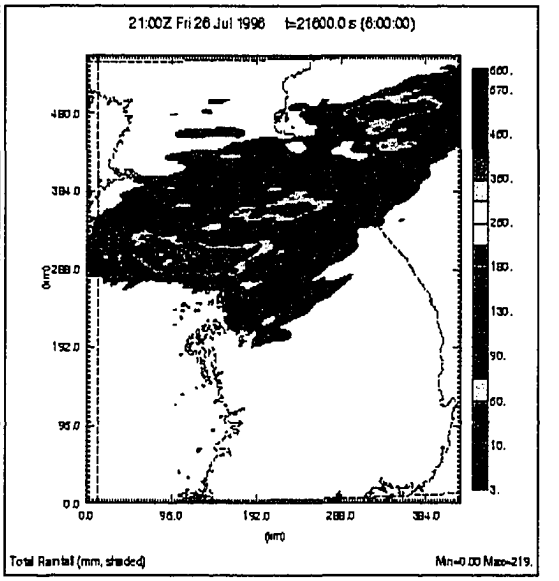

(g) 03RAR_cent20

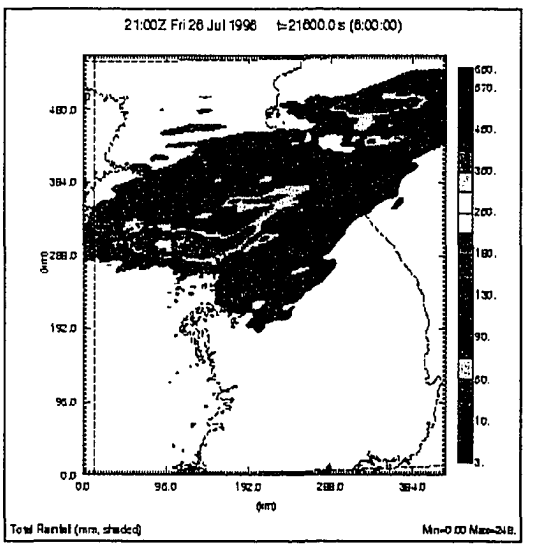

Fig. 6.11 (Continued)

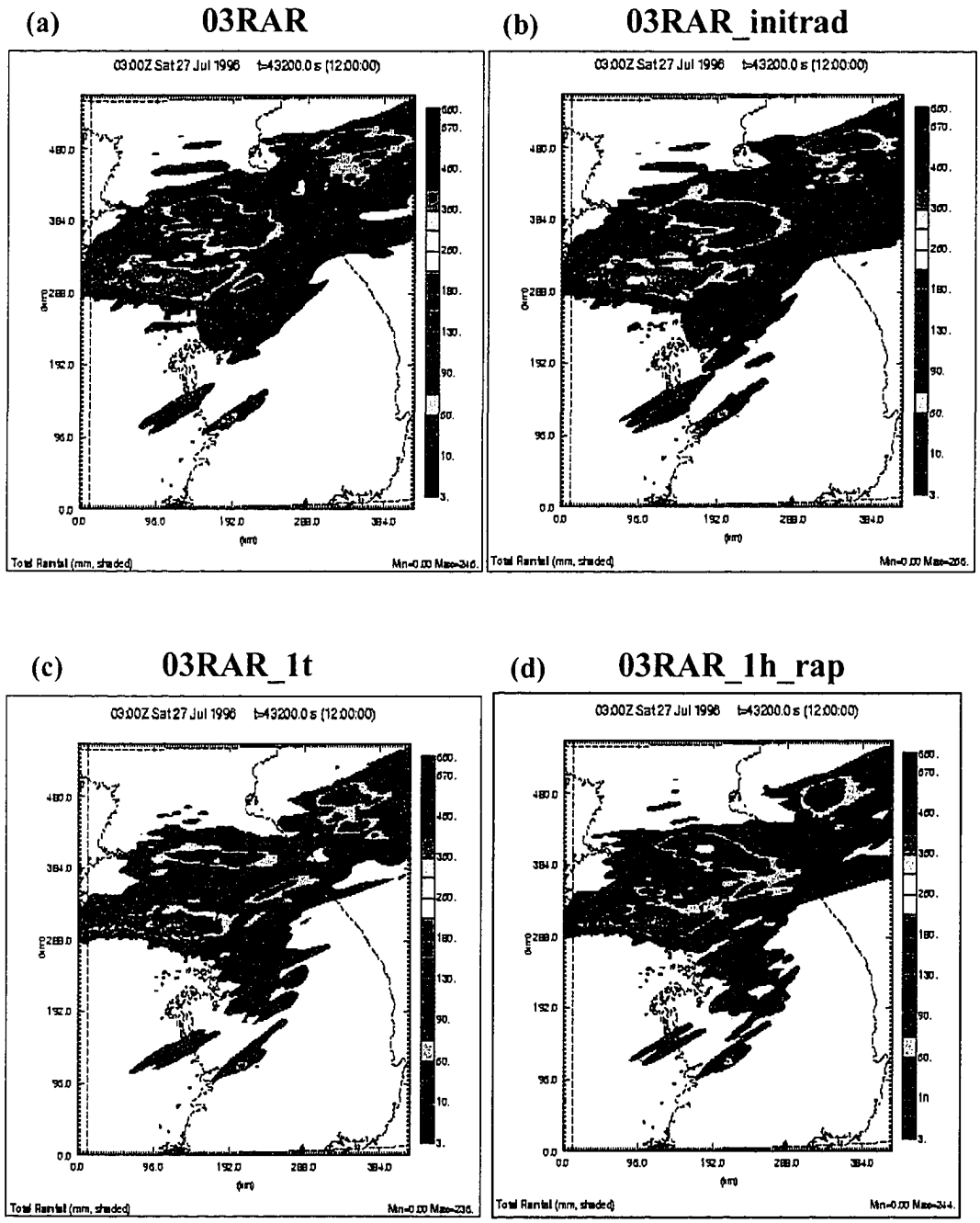

Fig. 6.12 Predicted accumulated rainfall for 12 hr valid at 0300 UTC July 27 for (a) 03RAR, (b) 03RAR_initrad, (c) 03RAR_1t, (d) 03RAR-1h_rap, (e) assi_cent5, (f) assi_cent10, and (g) assi_cent20 experiments. 'c', 'y', and 'm' mean the positions of Chorwon, Yonchon, and the position of observed maximum rainfall, respectively.

(e) 03RAR_cent5

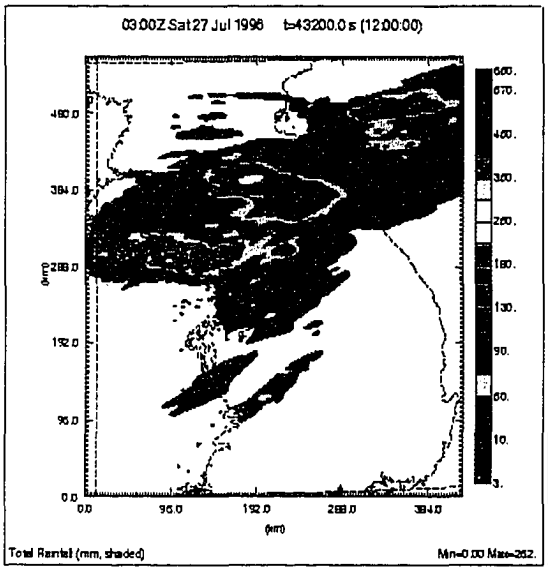

(f) 03RAR_cent10

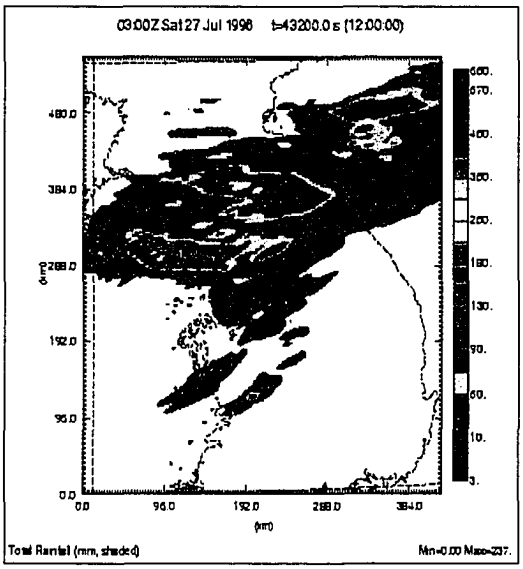

(g) 03RAR_cent20

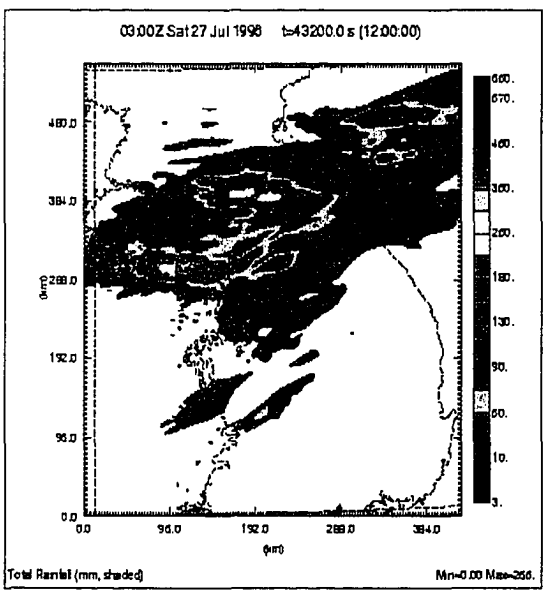

Fig. 6.12 (Continued)

three hours. Compared to 03RAR (Fig.6.11a and 6.12a), 03RAR_1t shows less bias for both the 6-hr and 12-hr forecasts. The RATs of 03RAR_1t are 82 %, 53 %, and 45 % for 6-hr, 9-hr, and 12-hr forecast, while those of 03RAR are 87 %, 56 %, and 47 %, respectively. The DISs of 03RAR_1t are also a bit (about one grid point) worse than those of 03RAR (Table 6.2). Although the differences between 03RAR_1t and 03RAR are not considerable, the use of three assimilation cycles of radar data appears to be more effective than using only a single insertion. Again, a more quantitative evaluation will be made in the next chapter.

To assess the effect of more rapid assimilation of observations, experiment 03RAR_1h_rap was performed. It uses three assimilation cycles during one hour, while 03RAR assimilates data once every hour for three hours. The singular feature of the former is the change in position of the maximum rainfall amount in the 12-hr forecast. In 03RAR_1hr_rap, it is far to the north of the observed maximum ('m' in Fig. 6.12d) as opposed to the west of the maximum in the 6-hr forecast (Fig. 6.11d). Other experiments, i.e., 03RAR, 03RAR_initrad, and 03RAR_1t, kept the maximum rainfall position west of 'm' regardless of forecasting time. Although the RATs of 03RAR_1hr_rap are worse than for the other experiments, the DISs (89 km and 44 km in 6-hr and 9-hr forecast, respectively) are better (Table 6.3), and the uncommon features are too ambiguous to assess any improvement.

Figure 6.13 shows the RDs of 03RAR and 03RAR_1h_rap at 2100 UTC on July 26 (6 hours after starting simulation or 3 hours after finishing data assimilation), at 0000 UTC (9 hours after starting simulation or 6 hours after finishing data assimilation), and at

0300 on UTC July 27 (12 hours after starting simulation or 9 hours after finishing data assimilation). This figure has the same configuration as Fig. 6.10. The RD of 03RAR_1h_rap is superior to that of 03RAR at 2100 UTC, although this result doesn't hold at 0000 UTC and 0300 UTC. Recalling the RD evaluation of the previous section, 03RAR exhibited the best results overall. Because the results of 03RAR_1h_rap are better than 03RAR at 2100 UTC (6 hours after starting simulation or 3 hours after finishing data assimilation), *this more continuous assimilation strategy can be regarded as the best method for short range forecasts about 3 hour duration.* More specific discussion of the quantitative verification of 03RAR_1h_rap is deferred to the next chapter.

To examine the impact of the length of the data assimilation window on forecast quality, we use value of 5, 10, and 20 minutes. Crook (1994) conducted numerical simulations of gust fronts to determine the sensitivity to the length of the data assimilation window and also performed other sensitivity tests using window lengths of 5, 10, 15, and 20 minutes. He showed that the normalized root mean square error (RMSE) increases as the window length increases. Specifically, he found that the RMSE increased smoothly from 20 % for a 5 minute assimilation window to 34 % for a 20 minute assimilation window. He presumed that this increase resulted from the assumption of linearity, which becomes less valid as length of data assimilation window increases. Figures 6.11e,f,g and 6.12e,f,g, indicate no substantial difference among our three results with regard the shape of accumulated rainfall except that the experiment with the longest data assimilation window shows more detailed structure at 0300 UTC July 27(12 hours after starting simulation or 9 hours after finishing data assimilation, Fig.

6.12e, f, and g). At 0300 UTC, the maximum rainfall positions for these three experiments are also far north of the observed maximum, as in 03RAR_1h_rap. Comparing RATs and DISs among these experiments, our results are found to differ from those of Crook. Experiment 03RAR_assi20, using the longest data assimilation window, shows the most improvement. The RATs of 03RAR_assi20 are better than those of other two experiments (03RAR_cent5 and 03RAR_cent10). For DIS, experiment 03RAR_assi20 is slightly better than the others for the 6-hr forecast. Consequently, the strategy using a longer data assimilation window does not appear to be worse than the strategies using a shorter assimilation window and may even be better, even for a short range forecast. As discussed in the next chapter, the explanation may lie in the time required for the model to adjust to new data in comparison to the time scale of the events being predicted.

As the final step for assessing different data assimilation strategies, we compare 03RAR_initrad with 03RAR_cent10 to determine whether any differences exist due to changes in the placement in time of the data assimilation window. However, there exist two other related differences: the volume scan of radar data used and different background fields. As shown in Figs. 6.1 and 6.2, there exists a five minute interval between the radar volume scans used in 03RAR_initrad and 03RAR_cent10. 03RAR_initrad uses the volume scan collected from 1551 to 1556 UTC, while 03RAR_cent10 uses that from 1556 to 1601 UTC. For the IAU assimilation method used in this study, a background field is necessary for creating an analysis increment. At the first data assimilation time the background of 03RAR_initrad uses the 50-minute forecast

from 1500 UTC to 1550 UTC, while that of 03RAR_cent10 uses the 55-minute forecast from 1500 UTC to 1555 UTC.

With regard to the RATs, 03RAR_initrad shows 89 %, 58 %, and 49 % for 6-hr, 9-hr, and 12-hr forecasts, respectively. These values are higher, especially for the 6-hr forecast, than those of 03RAR_cent10, which are 77 %, 50 %, and 46 %. The results of DISs are similar to the results of RATs. It is interesting that differences exist between these two experiments, though they are not deemed significant.

The increment used in this study is the difference between the analysis and background. Thus, any improvement depends upon the quality of the background and the observations. At this time, we cannot easily determine which of the above experiments is "best." Generally, the shorter the forecast the smaller the error. Thus, we might assume that the background of 03RAR_initrad from the 50 minute forecast is better than that of 03RAR_cent10 from the 55 minute forecast. Therefore, the improved results of the 03RAR_initrad could be associated only with the background field. A more quantitative analysis is presented in the next chapter.

Table 6.2 Predicted and observed maximum rainfall and the distances between the locations of maximum forecasted and observed rainfall position for different data assimilation strategies, especially for 03RAR_initrad, 03RAR_1t, and 03RAR_1h_rap experiments.

		03AR	03RAR_initrad	03RAR_1t	03RAR_1h_rap
6-hr (1500-2100 UTC)	Obs. Max.(mm)	284			
	Fcst. Max. (mm)	245	253	236	229
	Fcst./Obs. (%)	87	89	82	81
	Distance (km)	93	95	95	89
9-hr (1500-0000 UTC)	Obs. Max.(mm)	441			
	Fcst. Max. (mm)	245	256	236	229
	Fcst./Obs. (%)	56	58	53	52
	Distance (km)	51	52	54	44
12-hr (1500-0300 UTC)	Obs. Max.(mm)	518			
	Fcst. Max. (mm)	245	256	236	244
	Fcst./Obs. (%)	47	49	45	47
	Distance (km)	51	52	54	60

Table 6.3 Predicted and observed maximum rainfall and the distances between the locations of maximum forecasted and observed rainfall position for the experiments of different length of data assimilation window.

		03RAR_cent5	03RAR_cent10	03RAR_cent20
6-hr (1500-2100 UTC)	Obs. Max.(mm)	284		
	Fcst. Max. (mm)	220	219	248
	Fcst./Obs. (%)	77	77	87
	Distance (km)	116	113	110
9-hr (1500-0000 UTC)	Obs. Max.(mm)	441		
	Fcst. Max. (mm)	220	219	248
	Fcst./Obs. (%)	50	50	56
	Distance (km)	72	71	69
12-hr (1500-0300 UTC)	Obs. Max.(mm)	518		
	Fcst. Max. (mm)	262	237	265
	Fcst./Obs. (%)	50	46	51
	Distance (km)	66	66	67

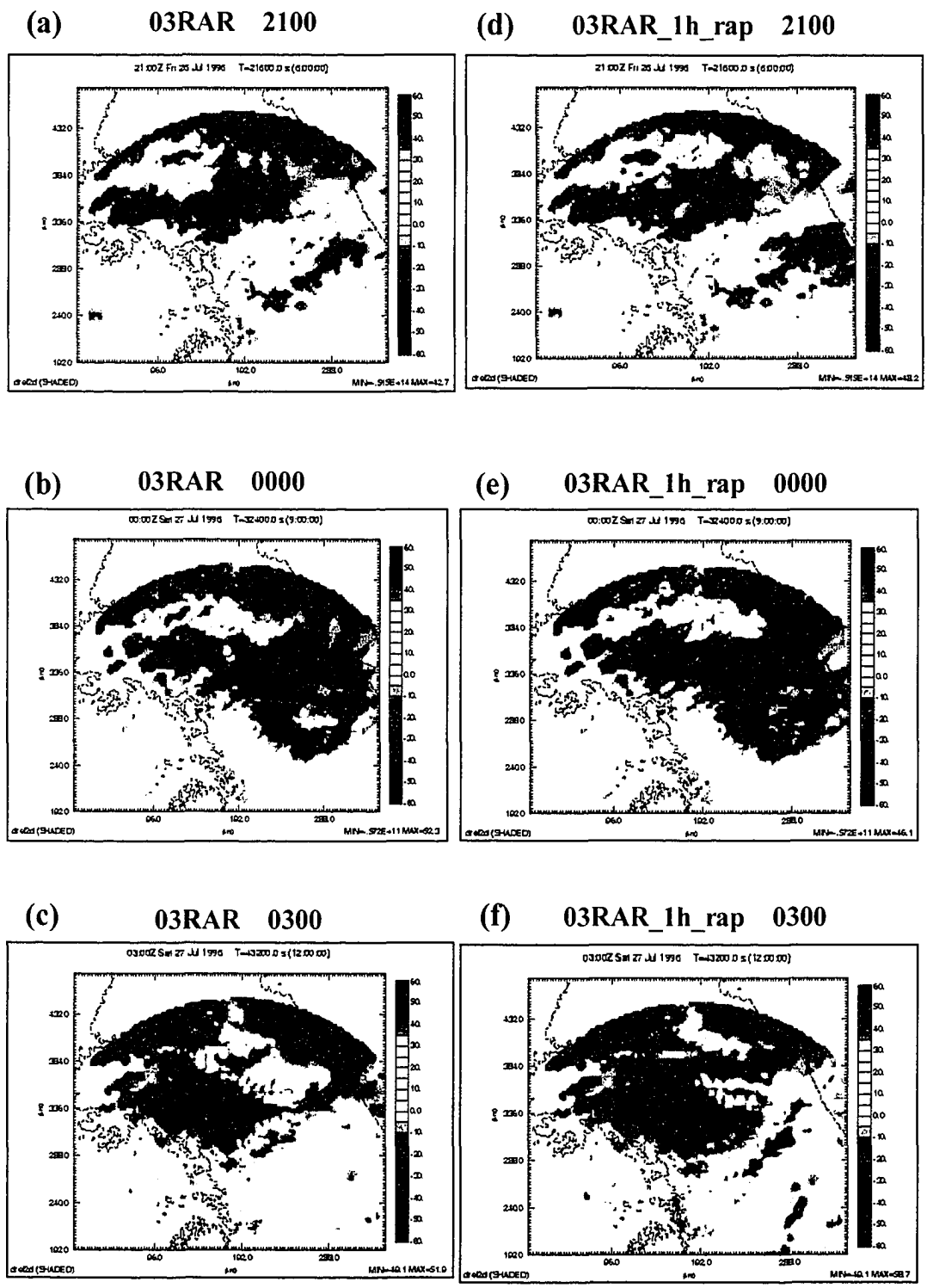

Fig. 6.13 The reflectivity difference between forecasted and observed reflectivity (forecast – observation) for 03RAR (left panels, a, b, and c) and 03RAR_1h_rap (right panels, d, e, and f)) experiments at 2100 UTC (upper panels, a and d), 0000 UTC (middle panels, b and e), and 0300 UTC (lower panels, c and f). Red and blue colors mean over predicted and under predicted reflectivity, respectively.

Chapter 7

Quantitative Verification of 3-km Grid Spacing Experiments

7.1 Methodology

We use conventional verification scores in this study for quantitative verification of forecasts at 3 km grid spacing. Although these traditional verification scores have been successfully employed to verify forecasts on larger scales, Carr et al. (1996) showed that they may not render useful information for small scale forecasts, e.g., of convection by a nonhydrostatic model, due to differences of spatial resolution between observations and the model. Thus, they suggested non-traditional measures such as sounding verification for the quantitative verification of non-hydrostatic model forecasts of convective phenomena. However, as discussed below, use of these scores in the present case remains valid despite the fine grid spacing used. We thus briefly describe their formulation and application.

7.1.1 Bias Score

The bias score B quantifies the tendency of a model to over- or under-predict an area of a given amount of precipitation. In terms of precipitation area, it is defined as

$$B = \frac{fa}{oa}, \tag{7.1}$$

while in terms of stations (points) it can be defined as

Table 7.1 Contingency 2 x 2 table for calculating Bias, Threat, and Equitable Threat scores.

		OBSERVATIONS	
		Yes	*No*
FORECASTS	*Yes*	**H** (Absolute Frequency of Hits)	**FA** (Absolute Frequency of False Alarms)
	No	M (Absolute Frequency of Misses)	**CN** (Absolute Frequency of Correct Nulls)

$$B = \frac{F}{O}, \tag{7.2}$$

where fa is the forecast area, oa is the observed area, F is the number of stations (points) forecast, and O is the number of stations (points) observing the amount. From a practical standpoint, we use a contingency table (Table 7.1) to obtain verification scores such as Bias, Threat, and Equitable threat. By comparing observed precipitation estimated from the radar data at each point (detailed explanation in the next section) with the predicted precipitation at each grid point, the scores are calculated following the contingency table.

As described in Wilkes (1995) and other standard texts, the contingency table utilizes the following nomenclature. Positive (Yes) forecasts that are matched with positive (Yes) observations are true-positives, or hits (H), while those matched with negative (No) observations are false-positives, or false alarms (FA). Negative (No) forecasts that are matched with 'Yes' observations are false-negatives, or misses (M), while those matched with 'No' observations are true-negatives, or correct nulls (CN). Therefore we define a computationally practical B using the above four frequencies in Table 7.1 as

$$B = \frac{H + FA}{H + M}, \tag{7.3}$$

If the value of B is greater than unity, this indicates over-forecasting based upon a specified threshold.

7.1.2 Threat Score

The threat score TS is a measure of the skill in predicting an area of precipitation amount over any given threshold. It is defined as

$$TS = \frac{cfa}{(fa + oa - cfa)}, \tag{7.4}$$

or

$$TS = \frac{C}{(F + O - C)}, \tag{7.5}$$

where cfa is the correctly forecasted area bounded by a given precipitation amount, fa, oa, F, and O are same as in the definition of Bias score, and C is the number of stations (grid points) correctly forecast to receive a threshold amount of precipitation. As in the calculation of B, we need a computationally practical definition of TS as well. The alternative form is

$$TS = \frac{H}{(H + M + FA)}, \tag{7.6}$$

where H, M, and FA are same as in section 7.1.1. TS has values ranging from 0 to 1. If TS is unity, it indicates a perfect forecast, while a zero value of TS indicates no skill.

7.1.3 Equitable Threat Score

The Equitable threat score (ETS) is similar to TS, but also accounts for forecasts that verify by chance. In that regard, the ETS measures 'the correctly forecasted area to exceed a given threshold' divided by 'observed area plus the incorrectly forecasted area to exceed a given threshold'. The area that would be correctly forecasted by random chance is subtracted from these areas. It is defined as

$$ETS = \frac{C - E}{F + O - C - E}, E = \frac{F \times O}{T}, \tag{7.7}$$

where E and T are the correctly forecasted area by random chance and the total number of grid points in the verification domain, respectively. Other notation is the same as in B and TS. As in B and TS, we use an alternative definition of ETS for practical computation, defined as

$$ETS = \frac{H - HR}{H + M + FA - HR}, HR = \frac{(H + M) \times (H + FA)}{H + M + FA + CN}, \tag{7.8}$$

where all variables are the same as in B and TS. ETS has values ranging from $-\infty$ to unity, where the latter indicates a perfect forecast, 0 indicates no skill (accuracy equivalent to that from random forecasts), and negative numbers mean accuracy less than that from random forecasts. The ETS values are usually lower than those of the TS.

7.1.4 Mean Absolute Error

One scalar measure of forecast accuracy is the mean absolute error (MAE), defined as (Wilkes 1995)

$$MAE = \frac{1}{N} \sum_{i=1}^{N} |f_i - o_i|, \tag{7.9}$$

where N is the total number of points considered in the calculation and f_i and o_i are forecast and verification fields, respectively. The MAE is the average of the values of the differences between forecast and observations. If the MAE is zero, it means a perfect forecast, while a large value of the MAE means an increasing discrepancy between observations and forecast.

7.1.5 Root Mean Square Error

Another scalar measure of forecast accuracy is the mean squared error (MSE). The MSE is very similar to MAE except for a fact that the errors are squared rather than the absolute value function in MAE. Wilkes (1995) explained that MSE can be more sensitive to large errors than MAE because the MSE is computed by squaring errors of the forecast. The MSE is usually used as its square root, or the root mean square error (RMSE), which has the benefit that it preserves the units of the forecast variables so that it can be interpreted more easily as a typical error magnitude (Wilkes 1995). The RMSE is defined by

$$RMSE = \left[\frac{1}{N} \sum_{i=1}^{N} (f_i - o_i)^2 \right]^{\frac{1}{2}}, \tag{7.10}$$

where N is the total number of points considered in the calculation, and f_i and o_i are forecast and verification fields, respectively.

7.2 Quantitative Precipitation Estimation from WSR-88D Level II Data

7.2.1 The Limitations of Observed Surface Rain Gauge Data

To evaluate forecasted precipitation by numerical prediction using conventional verification scores such as B, TS, and ETS, the observed values should be converted to values on the grid having the same spatial scale and variance (e.g., Tustison et al. 2003). As noted by Carr et al. (1996), however, the resolution difference between the observations and the forecast, when using fine grid spacing in models, may not produce reliable results. Such is the case here.

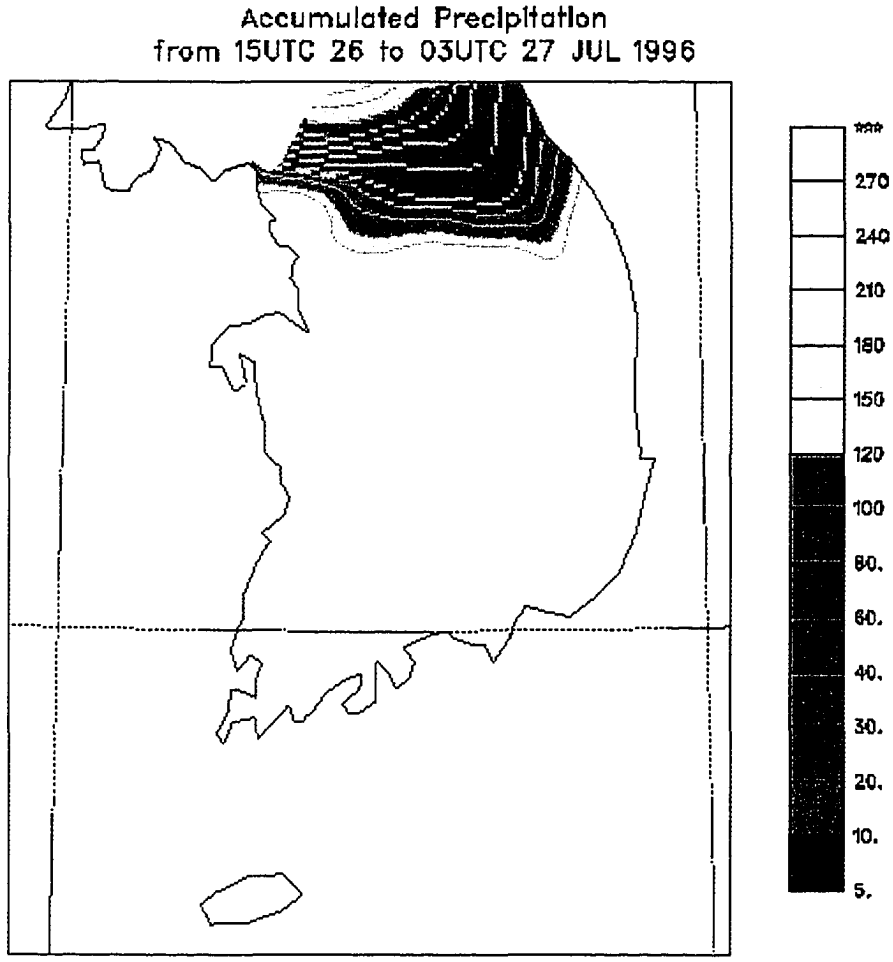

Fig. 7.1 Observed accumulated rainfall for 12-hr from 1500 UTC July 26 to 0300 UTC July 27 made by the data of surface rain gauge at official statios and AWS of KMA.

Figure 7.1 shows the observed accumulated rainfall for 12 hours valid at 0300 UTC on July 27 produced by precipitation data from surface rain gauges operated by the KMA. A two-pass Barnes scheme was employed by the KMA in creating this image, and unfortunately, a great deal of fine-scale detail has been lost, making this information of limited value for comparison against our model results. Thus, another more appropriate source of estimated precipitation is needed, for which we turn to WSR-88D Level II data and apply a commercial software package developed by Vieux and Associates, Inc.

7.2.2 Estimation of Surface Accumulated Precipitation From WSR-88D Level II Data

To provide a rigorous comparison between surface accumulated precipitation estimated from observations and that predicted by the ARPS model, we employ a commercial software package, known as RainVieux (Version 1.0; hereafter RV1.0), developed by Vieux and Associates, Inc. It creates calibrated (against surface gauges) hourly surface precipitation estimates from WSR-88D Level II data. Although RV1.0 is proprietary and cannot be described in detail, it employs a modification of the mean field bias (MFB) method described by Wilson and Brandes (1979). The MFB takes the sum of surface precipitation (rainfall) captured by a set of gauges and dividing by the sum of the sampled radar pixels over the same gauges. In other words, the MFB is the ratio of the true area-averaged rainfall obtained from surface rain gauges to the corresponding radar rainfall (Smith and Krajewski 1991). This ratio serves as calibration for the radar data. For example, an MFB of 1.5 can be interpreted as a 33% underestimation of accumulated precipitation by the radar (Jean Vieux, personal communication, 2003).

Wilson and Brandes (1979) discussed three parameters used to quantify MFB: (1) average difference (AD), (2) calibrated average difference (CAD), and (3) relative dispersion (RD). All three of these parameters are expressed as an absolute percentage about the mean. AD expresses the uncertainty between the non-adjusted radar estimate and the gauge-based estimate, whereas CAD expresses the uncertainty due to random errors once the bias (systematic error) is removed. For example, a calibrated average difference of 10% means that the gauges are ±5% about the mean. Gauges are a point measurement and radar is an area-averaged measurement, so complete agreement would not be expected. The CAD also may be interpreted as describing the closeness of the gauges to calibrated radar estimates. A CAD lower than the AD indicates improvement in the adjusted radar estimate. RD expresses the scatter distribution of the radar/gauge (RG) pairs to a one-to-one relationship. As the relative dispersion decreases, the scatter of the RG pairs tightens and vice versa. It should be noted that it is possible to obtain a relatively low CAD with a relatively high RD when the scatter of the radar/gauge (RG) pairs balance each other out. These three parameters are mathematically defined as (Wilson and Brandes 1979)

$$AD = 100\% \times \frac{\sum_{i=1}^{N} \left| \frac{G_i - R_i}{G_i} \right|}{N}, \tag{7.11}$$

$$CAD = 100\% \times \frac{\sum_{i=1}^{N} \left| \frac{G_i - \overline{(G/R)} R_i}{G_i} \right|}{N}, \tag{7.12}$$

$$RD = 100\% \times \frac{\sigma[G/R]}{\overline{G/R}}, \tag{7.13}$$

Table 7.2 The statistics of parameters for radar data calibration used in the present study and used in the study of Wilson and Brandes (1979).

	Number of gauges	MFB	AD (%)	CAD (%)	RD (%)
Present study	7	1.10	30.6	30.4	42.3
Wilson and Brandes	223	1.04	63	24	30

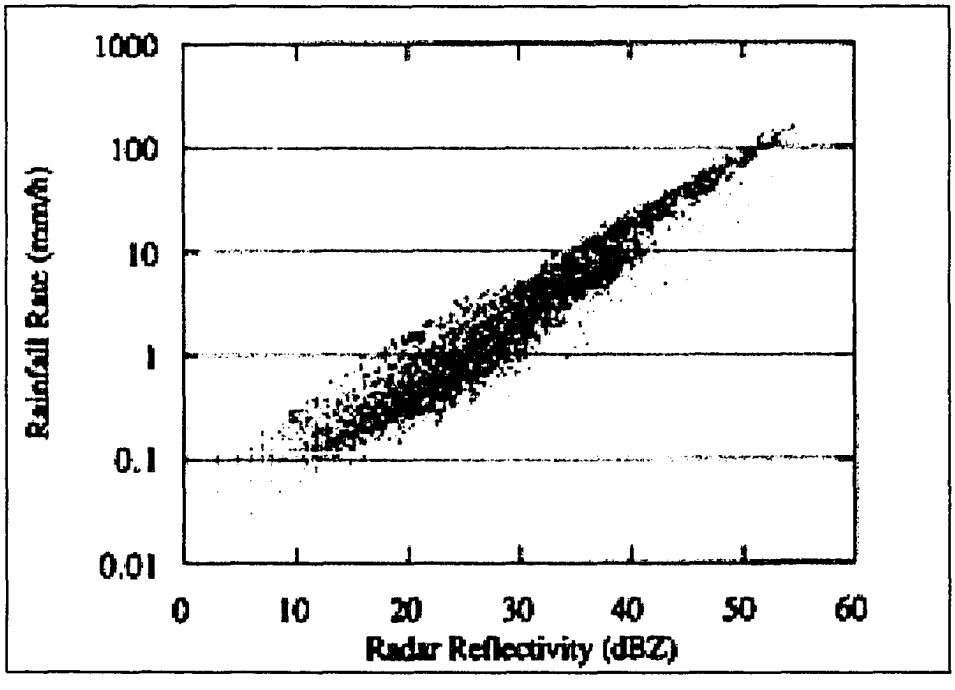

Fig. 7.2 An example of the relationship between rainfall rate and radar reflectivity (from Short et al. 1990).

where N is the number of gauges, and σ[G/R] means the standard deviation of the ratio of surface gauge rainfall to radar rainfall.

For the heavy rainfall event studied here, 72 surface rain gauges were utilized for calibration, 55 of which were removed because their gauge or radar *storm total* was less than 2.54 mm (0.10 inches), thus leaving 17 gauges. Next, inspection of the gauge locations compared to obvious radar blockages and tilt discontinuities led to the removal of eight more gauges leaving, nine gauges for outlier identification. Of the nine remaining gauges, two were identified as outliers and thus were discarded. *The seven remaining gauges were used for calibration of the radar.*

Table 7.2 shows statistics of parameters used in this study (the calculation for these statistics was conducted by Jean Vieux and Eddie Koehler of Vieux and Associates Inc.) and those used in the study of Wilson and Brandes (1979). Comparatively, the present study has a few weak points. For example, the CAD is a little bit lower than the AD, which means there exists only a slight improvement in the adjusted radar estimate. Considering the RD value of 42.3 %, the scatter of the RG pairs in the present heavy rainfall event is considerable. Furthermore, we note that after removal of the bias, the CAD of 30.4% indicates an error of about ±15% in the radar rainfall estimates. This leads to significantly erroneous estimates in the high reflectivity region considering the relationship between radar reflectivity and rainfall rate.

Figure 7.2 shows an example of the relationship between radar reflectivity and rainfall rate as determined by Short et al (1990). They obtained this result using observational raindrop size distribution data in Darwin, Australia. When considering a 15% error at around 50 dBZ, the difference in rainfall rate is at least 50 mm/h, while it is

less than 1 mm/h at 20 dBZ. We note that the results in the present study, which use estimated rainfall from WSR-88D level II data, must be interpreted carefully in light of the logarithmic relationship between rainfall rate and reflectivity.

A total of 113 AWS gauges were analyzed as well, but were not used for calibration due to large inconsistencies between gauge and radar estimates (note that AWS data are known to be of questionable quality).

We now describe briefly how RV1.0 estimates precipitation from NEXRAD Level II data (Jean Vieux, personal communication, 2003). First, NEXRAD reflectivity values at the lowest elevation angle (approximately 0.5 degrees) in native spherical coordinates are compared to surface rain values for calibration. Once the calibration correction has been applied to the radar data, they are interpolated from the spherical coordinate system to the 3 km spacing ARPS Cartesian grid, which accounts for factors such as the Lambert conformal map projection. Each volume scan of data is processed in this manner, and the accumulated precipitation at any particular time is obtained by summing the incremental rainfall amounts from previous successive volume scans and multiplying by the elapsed time. Any rainfall potentially affected by ground clutter is excluded through the calibration procedure.

The tropical convective Z-R relationship, developed by Rosenfeld et al. (1993), is used to relate reflectivity to rainfall rate: $Z = 250R^{1.2}$, where Z is reflectivity factor (mm^6/m^3, $dBZ = 10 \log(Z)$) and R is rainfall rate (mm/h), with 0 to 65 dBZ thresholds in RV1.0. Although the Marshall-Palmer Z-R relationship (Marshall et al. 1955), denoted by $Z = 200R^{1.6}$, and the default WSR-88D convective Z-R relationship (NOAA 1990), denoted by $Z=300R^{1.4}$, are commonly used for rainfall estimation, we employ the tropical

convective Z-R relationship in this study owing to the fact that the Chorwon-Yonchon heavy rainfall case occurred during the summer monsoon season and was decidedly tropical in behavior.

Consequently, the rainfall amount for each grid, which is same as the ARPS grid with 3 km x 3 km resolution, is produced using RV1.0. Figure 7.3 displays the ARPS grid and the coverage area of the NEXRAD radar at Pyoungtaek. For computing verification scores, the predicted precipitation is compared to the observed precipitation at each grid. A comparison of Figure 6.3 in the previous chapter with Fig. 7.1 shows significant differences, with notably more detail evident in the radar-based rainfall estimates, as one would expect. The local maxima from these estimates agree quite well with the location of surface-based heavy rainfall, as we demonstrate below.

7.2.3 Validation of Estimation of Surface Accumulated Precipitation From RV 1.0

To validate the accuracy of rainfall estimates from NEXRAD Level II data, we compare them with surface rain gauge observations at four surface stations: Chorwon (38.15N, 127.32E), Chunchon (37.90N, 127.73E), Seoul (37.57N, 126.97E), and Kanghwa (37.70N, 126.45E). Figure 7.4 shows the ratio of gauge measured total rainfall to NEXRAD estimated total rainfall for this time period (G/R). This ratio is greater than unity if the radar underestimates and is less than unity in case of overestimation. As shown in this figure, the G/R ratios range from 0.74 to 2.75. According to Klazura et al. (1999), the estimated rainfall from NEXRAD has a large range of G/R (0.36 to 3.92). Compared to the results of Klazura et al., our G/R ratio is reasonable and the pattern of estimated rainfall at every hour is similar to that of the surface rain gauges.

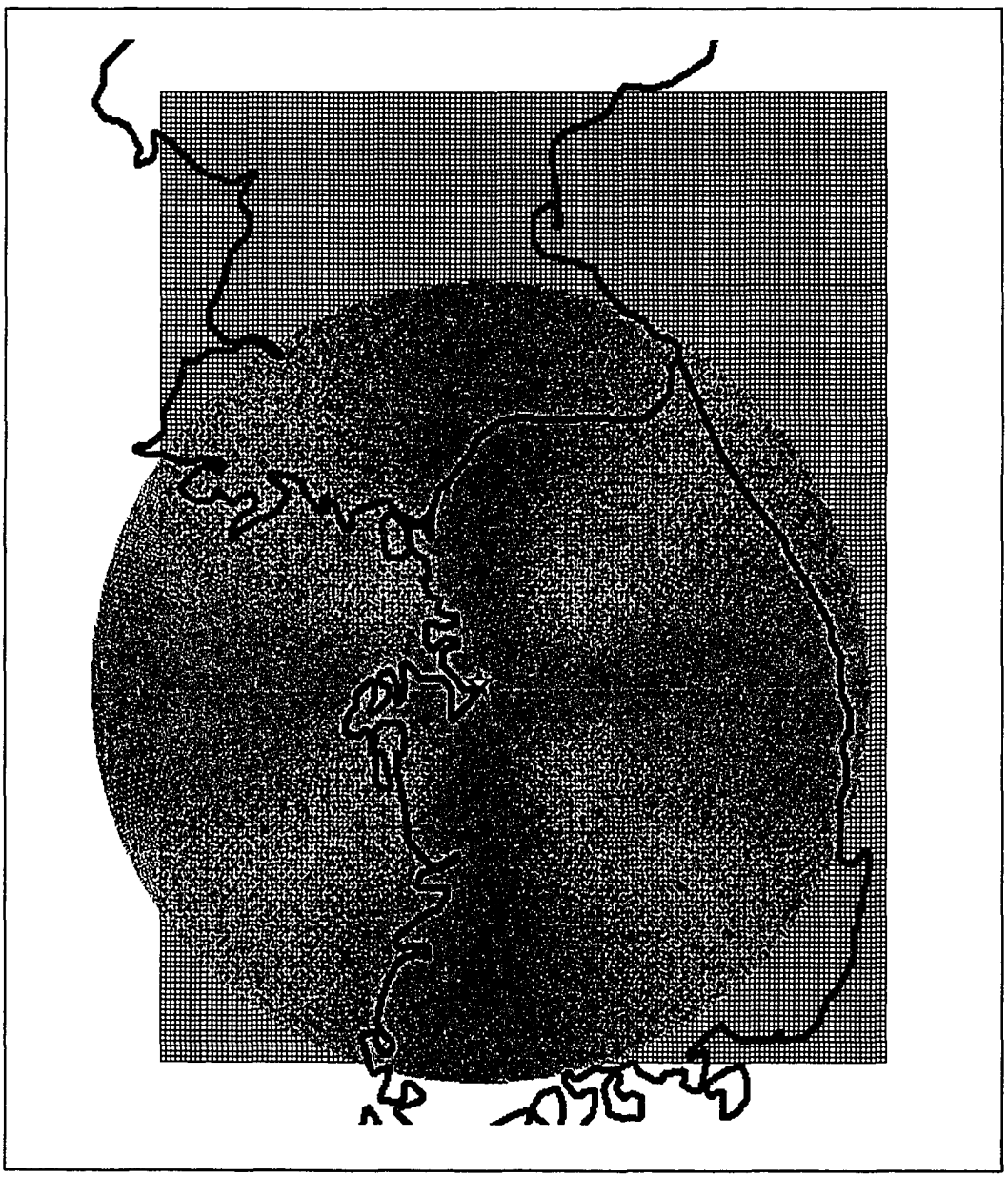

Fig. 7.3 Domain and grid of 3-km horizontal resolution and NEXRAD range. Each small rectangles means the grid with 3 km x 3km, while large rectangles including each small rectangles displays the domain of the experiment on 3 km horizontal resolution. Small circles and star indicate Chorwon position and NEXRAD position in Pyungtaek, respectively.

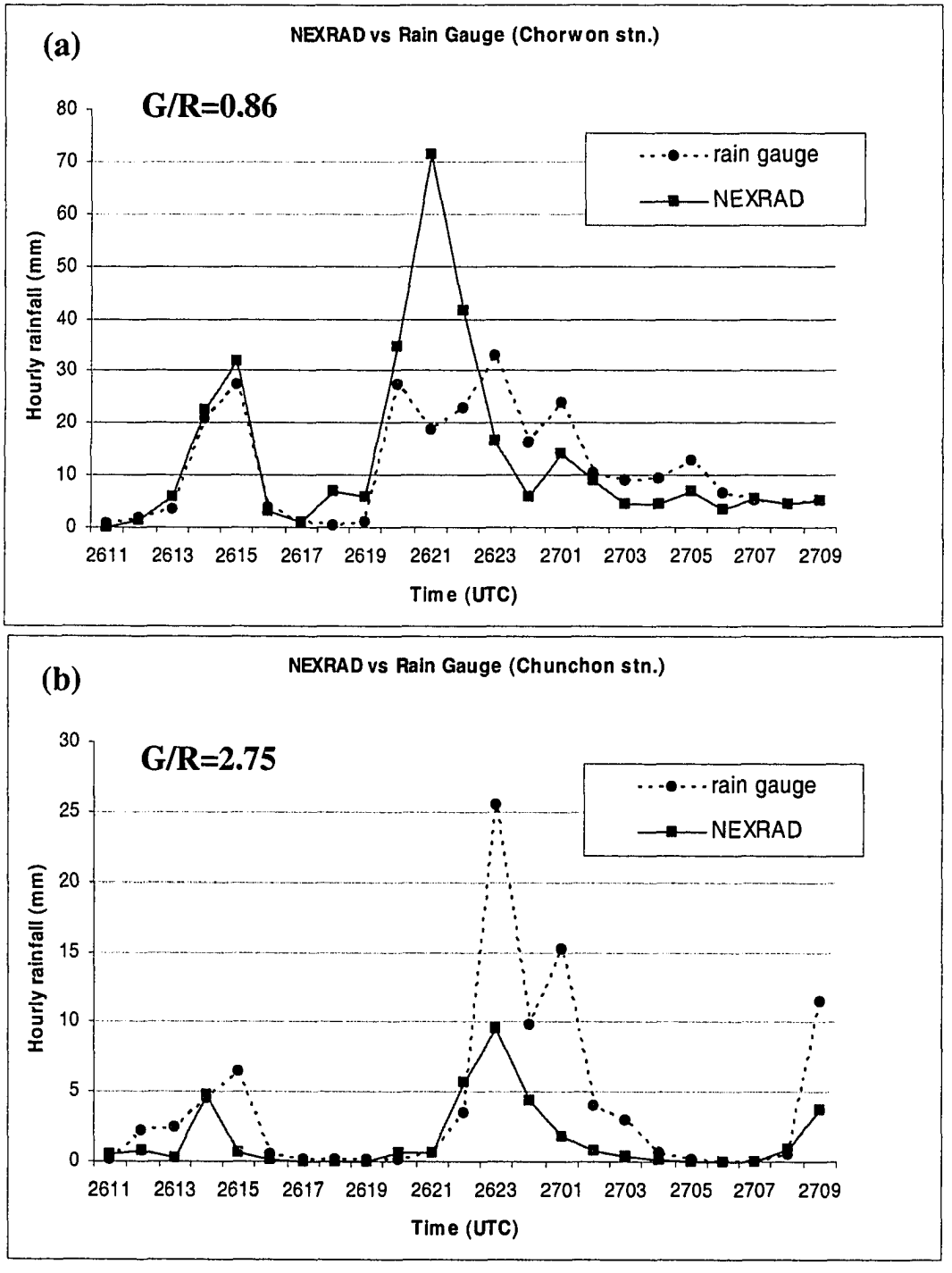

Fig. 7.4 Gauge-measured hourly rainfall at a weather station versus NEXRAD-estimated hourly rainfall at a grid which includes the station point from 1000 UTC July 26 to 0900UTC July 27 in (a) Chorwon, (b) Chunchon, (c) Seoul, and (d) Kangwha (G/R value means the ratio of gauge measured total rainfall to NEXRAD estimated total rainfall for this time period).

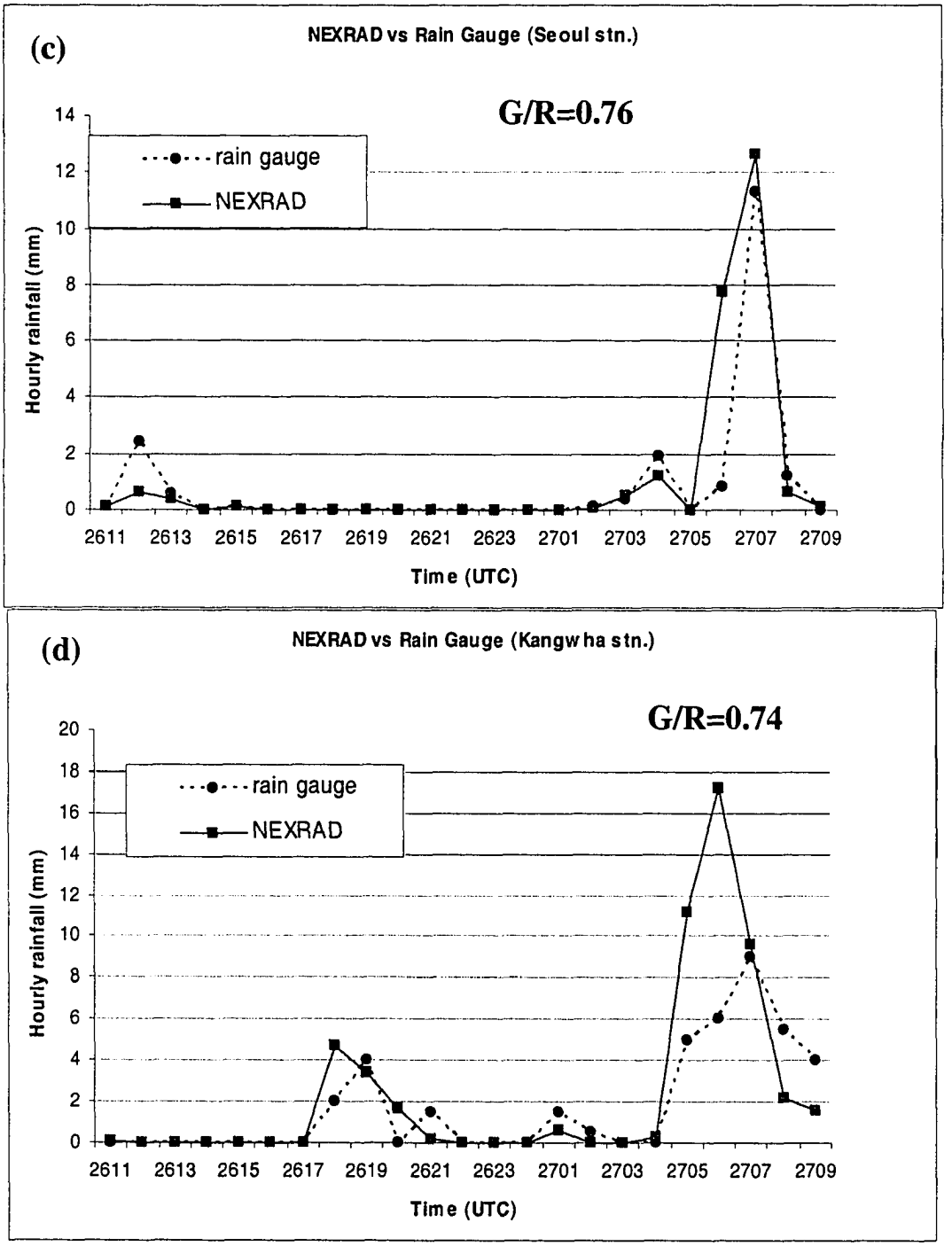

Fig. 7.4 (Continued).

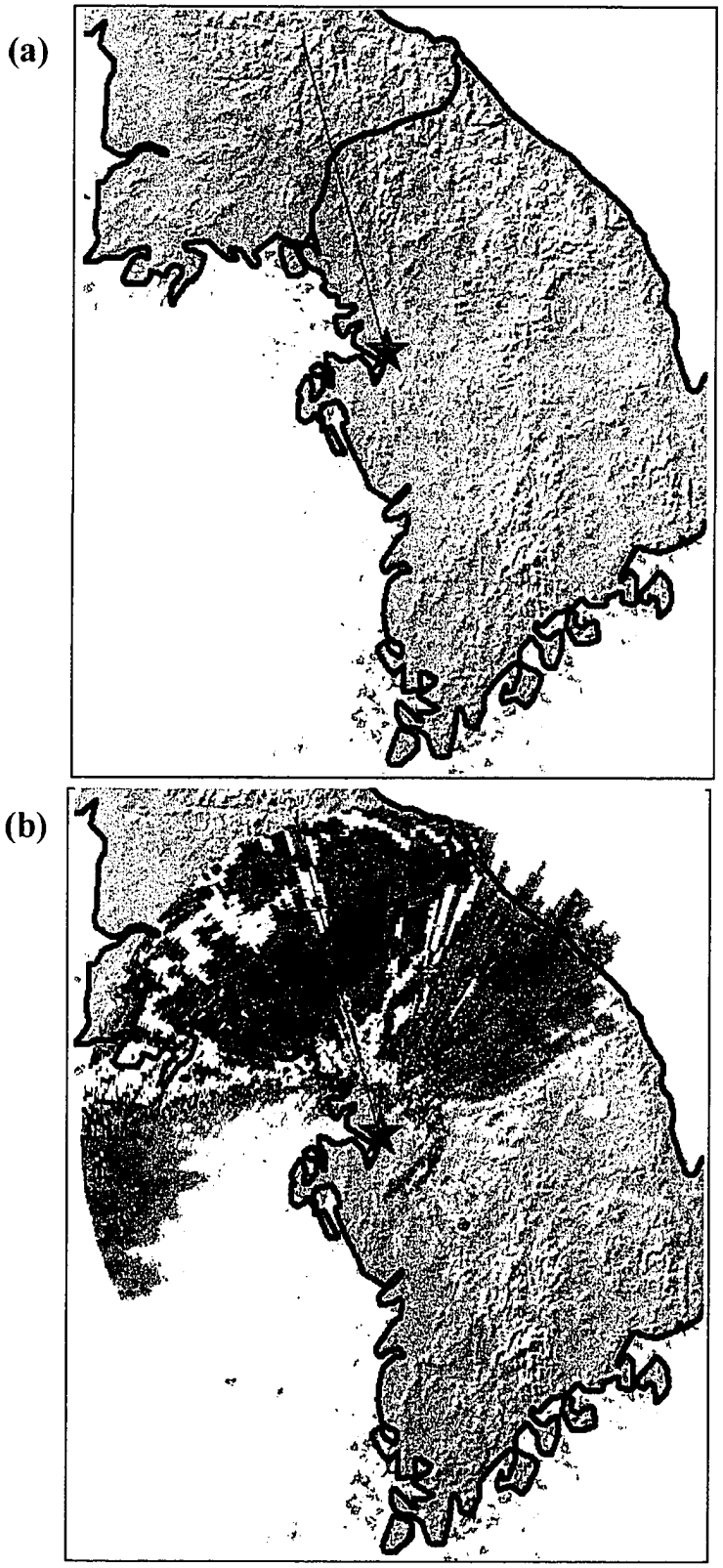

Fig. 7.5 Schematic for blockage problem (a) radar and topography and (b) the result of blockage problem.

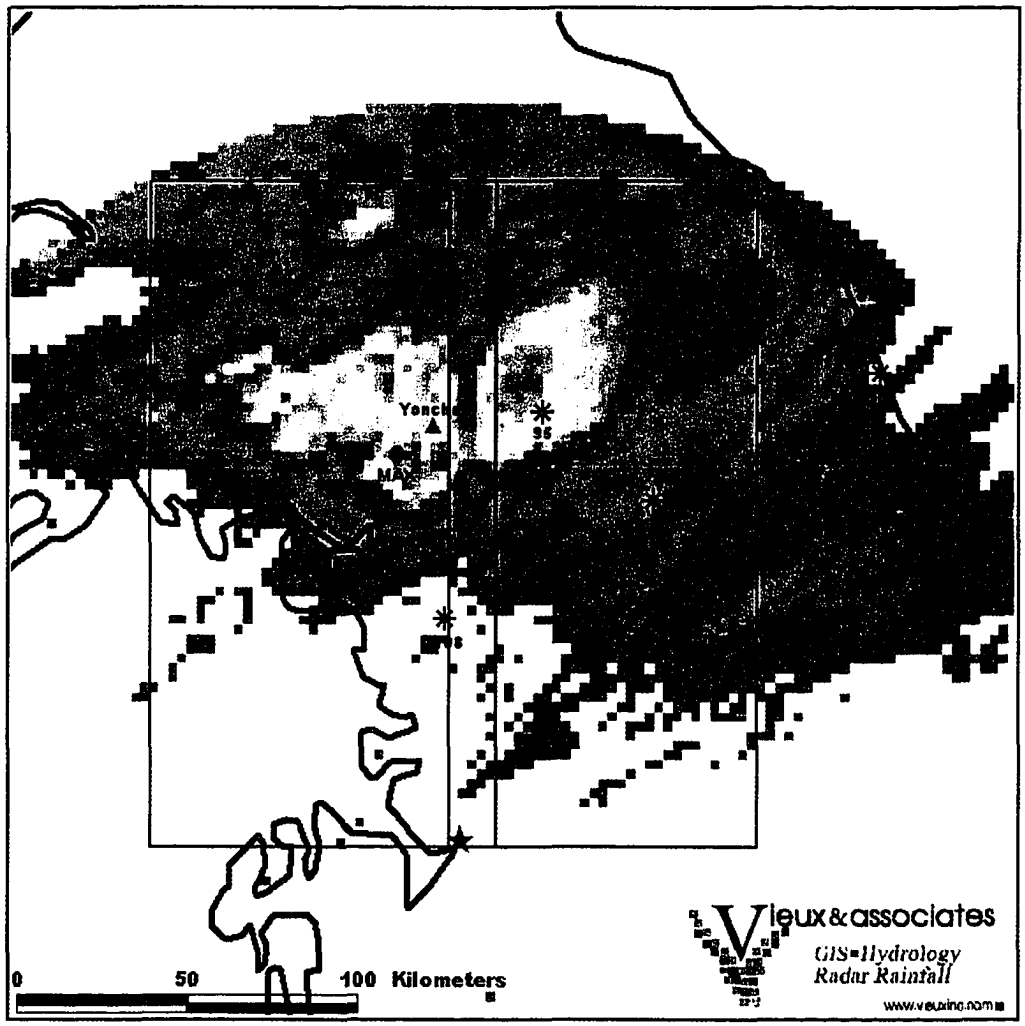

Fig. 7.6 Verification domain (large rectangles) and erroneous area which is removed for the verification (small rectangles in the center of verification domain)..

However, this validation work suffers from two principal limitations. The first is that estimated rainfall produced by RV1.0 cannot be well matched with the station values since the estimated value represents a 9 km^2 (3 km x 3 km) area, while the station value is a point value. The other limitation is that the estimated rainfall from radar data is already correlated to the rain gauge data through calibration work using RV1.0 mentioned in the previous section. Thus, this correlation naturally renders a more positive relationship. With this in mind, the radar estimated rainfall amount is, in an overall sense, larger than for the surface gauges, and thus we assume that the NEXRAD estimates are appropriate for verification.

7.2.4 Radar Beam Blockage

Owing to terrain effects, the Pyoungtaek radar beam suffers from blockage at certain azimuths, particularly toward the north. Fig. 7.5 demonstrates this blockage by the Gwanak mountain located about 60 km from the Pyoungtaek radar site with a height of 632 m. This blockage led to obviously erroneous rainfall estimates (Fig. 7.5b). By simple geometry, if terrain exceeds 500 m in height 60 km from the radar site, the radar beam at the lowest elevation angle will be blocked. To deal with this problem, we discarded the erroneous estimates by dividing the verification domain into two areas – one on the east and one on the west – separated by a gap containing bad data. The rectangular region (12 km (4 grids) x 207 km (69 grids)) at the center of entire verification domain (large rectangular region in Fig. 7.6, 195 km (65 grids) x 207 km (69 grids) thus is not used in our verification work.

7.3 Quantitative Verification of 3 km Grid Spacing Forecast

7.3.1 Impact of Radar Data Assimilation

In the previous chapter, we showed qualitatively that radar data assimilation appears to have a positive impact on the 3 km grid spacing forecasts. In this chapter, we use quantitative verification measures to determine how experiment 03RAR compares to others in which radar data were or were not used, e.g., 03RNR, 03RYR, and 03RYR_ref. In addition, we investigate whether the effects of radar data assimilation are limited to a certain forecast time period.

For quantitative verification, we employ conventional statistical scores such as B, TS, and ETS, as described earlier. They are computed using various thresholds over three different time periods: 3-hr (1800 UTC to 2100 UTC July 26), 6-hr (1800 UTC July 26 to 0000 UTC July 27), and 9-hr (1800 UTC to 0300 UTC July 27). Although the 3 km simulations are initialized at 1500 UTC on July 26, we use 1800 UTC as the starting point for examining accumulated rainfall. Because data assimilation concludes at 1800 UTC on July 26, the actual forecast starts from that time. The scores for the other experiments are also computed during the above time periods in order to compare with those of 03RAR.

Multiple thresholds are usually employed in precipitation verification to provide increasingly stringent tests of the forecast model. In general, higher thresholds produce verification scores having lower skill. Thresholds used for the 3-hr accumulation period range from 2.5 mm to 20 mm, and those for the 6-hr and 9-hr periods range from 2.5 mm

to 50 mm. The higher extreme value for the latter accounts for the possibility of heavier accumulations over these longer time periods.

Figure 7.6 shows bias scores for experiments 03RAR, 03RYR, 03RYR_ref, and 03RNR over all three time periods. A significant finding is that 03RAR exhibits the best overall skill, i.e., a score close to unity, for all verification periods (Fig. 7.7a-c), although it shows some bias, with values near 1.2 for low thresholds (2.5 mm and 5 mm), in the 3-hr period (Fig. 7.7a). This suggests that 03RAR provides a good representation of the forecasted rainfall over the entire verification domain. Although radar data assimilation shows a positive impact it is difficult to determine the time window over which this impact exists.

In our earlier qualitative verification procedure (section 6.2.2), the differences arising from the use of both radial velocity and reflectivity versus reflectivity only were not significant (only slight improvement in 03RYR compared to 03RYR_ref). However, Fig. 7.7 shows that the difference between 03RYR and 03YR_ref is notably significant. The effect is greater for the shorter precipitation accumulation windows (compare 3-hr and 6-hr accumulations in Fig. 7.7a-b with those for 9-hr in Fig. 7.7c), as would be expected. This suggests that radial velocity data have a positive impact on the forecasts, presumably by reinforcing the humidity and latent heating adjustments associated with assimilation of radar reflectivity, especially at early times, although radial velocity is limited in its subsequent effect upon the horizontal wind field, as discussed further below.

Figures 7.8 and 7.9 show the TS and the ETS for the above four experiments. The results are similar in a relative since given that ETS differs from TS only in that the former includes the effects of a hit by chance. Considering these scores, the effect of

radar data assimilation is perhaps even more significant than suggested from the bias scores. Because the TS provides a measure of how accurately the location of precipitation is forecasted for a given threshold, it demonstrates that radar data assimilation improves the forecasted rainfall *location* more than the forecasted rainfall *amount*. The other results are also consistent with the results of the bias scores. For example, 03RNR (Figs. 7.8 and 7.9) has the worst scores, while 03RYR is better than 03RYR_ref. Although the TS and the ETS of 03RAR are better than for the other experiments across all accumulated precipitation periods, the scores for the first 3-hr period (Figs. 7.8a and 7.9a) are higher for both of the higher thresholds (15 mm and 20 mm), while the scores for the 6-hr and 9-hr periods (Figs. 7.8b-c and 7.9b-c) converge to those of the other experiments at higher thresholds. That the scores maintain relatively higher values for higher thresholds is important because we are more interested in accurately forecasting heavy rainfall. Therefore, we can tentatively conclude that radar data assimilation indeed has a quantitatively verifiable positive impact, and that this impact is greatest during the first few hours of the forecasts.

We conducted another quantitative verification to confirm the positive impact of radar data assimilation. Similar to the method of Carr et al. (1996), simulated sounding data were examined for each experiment and key instability indices compared against those of actual soundings taken at Osan (RKSO, 47122, 37.11N, 127.03E) at 00 UTC on July 27.

Table 7.3 displays these instability indices for each experiment as well as the observed values. Although discrepancies exist, these results are encouraging and suggest a positive impact of radar data assimilation at 3-km resolution. For example, comparing

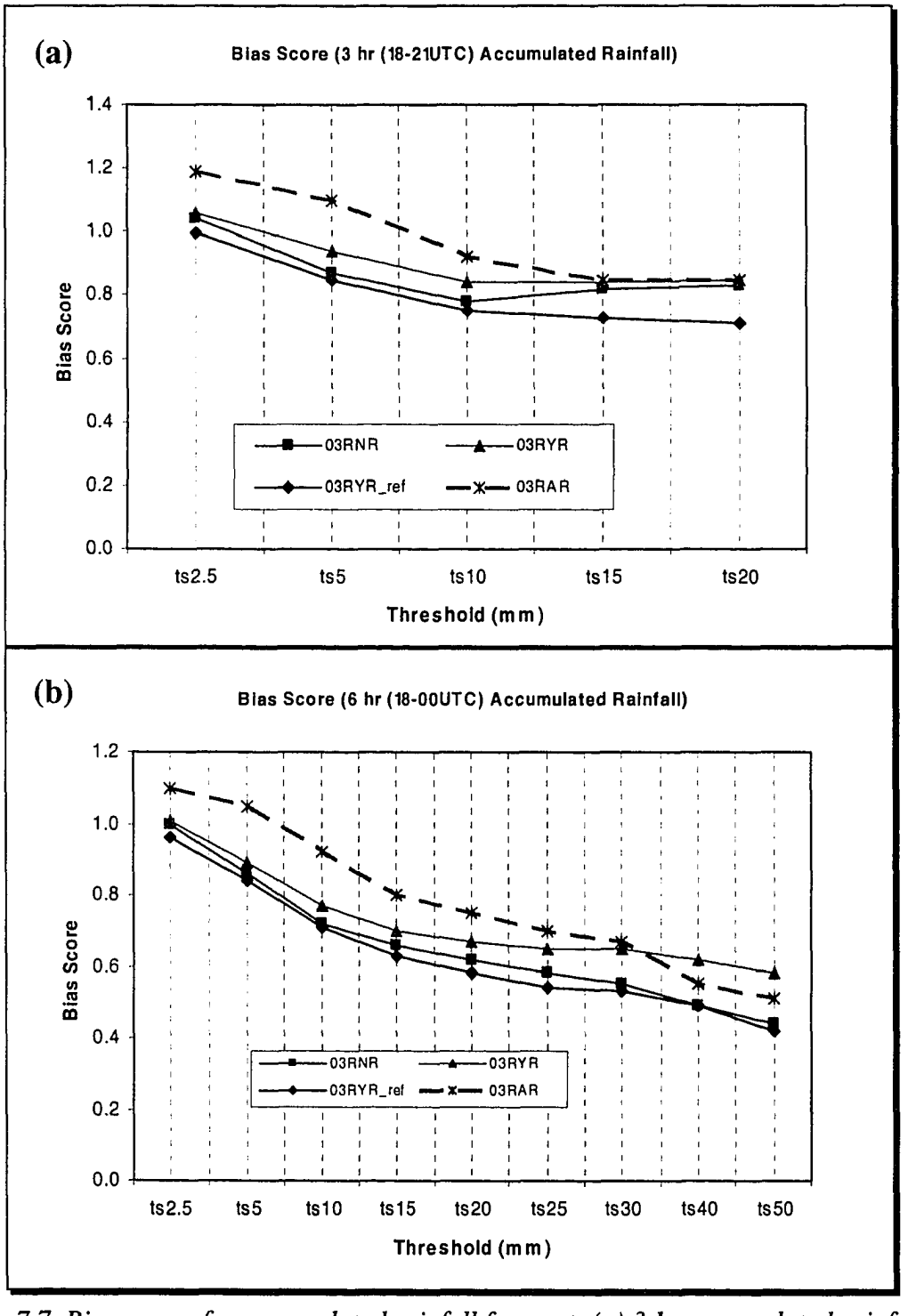

Fig. 7.7 Bias scores for accumulated rainfall forecast; (a) 3-hr accumulated rainfall from 1800 UTC to 2100 UTC July 26, (b) 6-hr accumulated from 1800 UTC July 26 to 0000 UTC July 27, and (c) 9-hr accumulated rainfall from 1800 UTC July 26 to 0300 UTC July 27. Thick dashed line with asterisk, solid line with filled triangles, solid line with filled diamonds, and solid line with filled rectangles indicate 03RAR, 03RYR, 03RYR_ref, and 03RNR, respectively. And, the ts in x-axis stands for threshold. Namely, ts2.5 means the threshold with 2.5 mm.

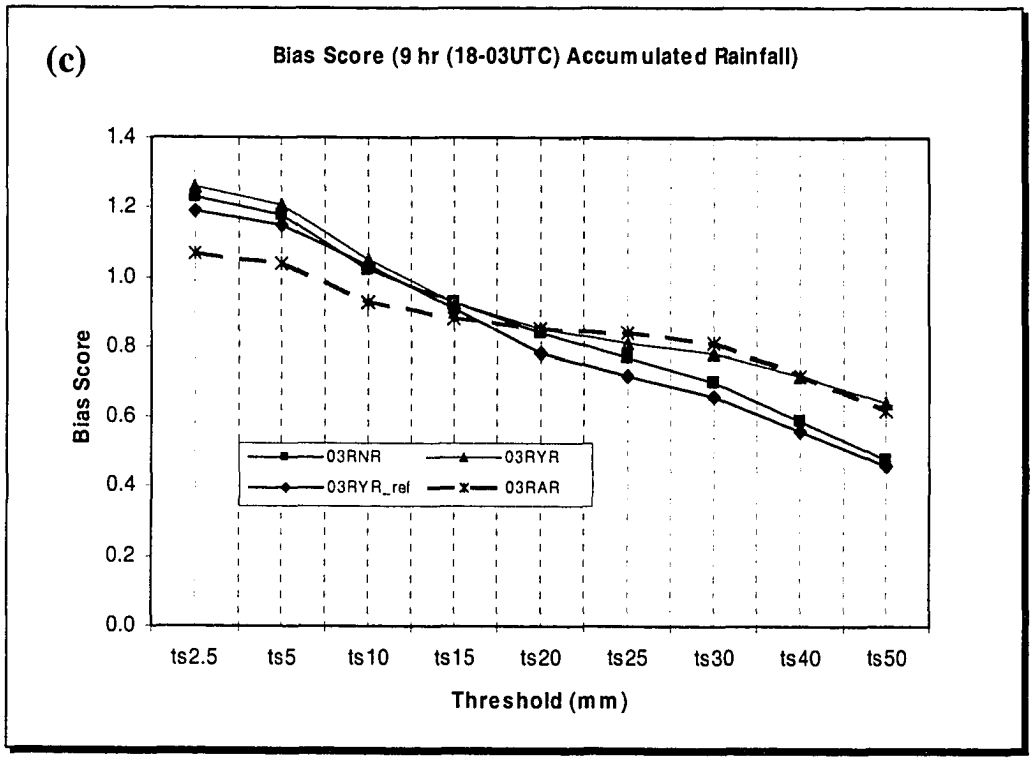

Fig. 7.7 (Continued)

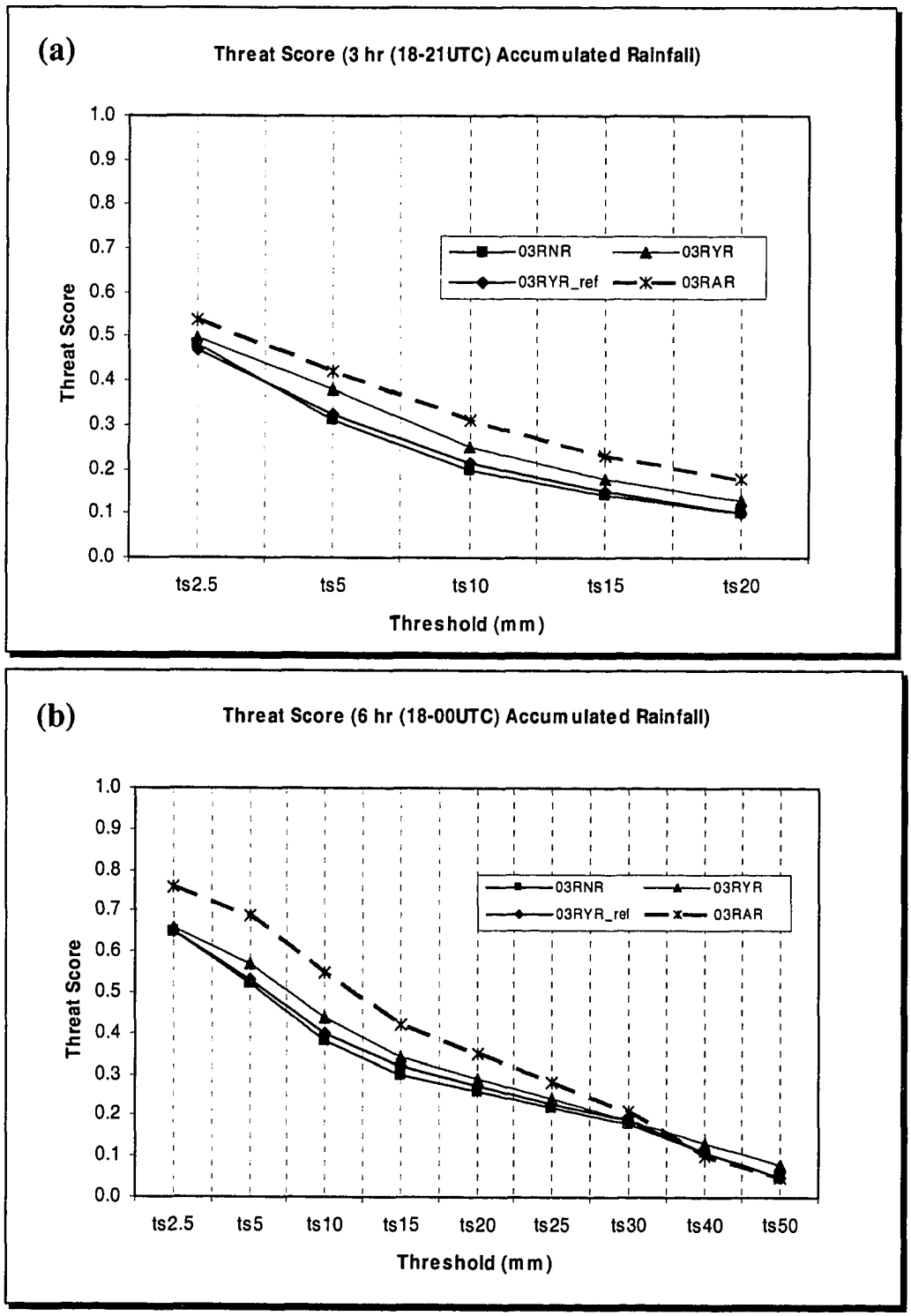

Fig. 7.8 Same as in Fig. 7.7 except for threat scores (TS).

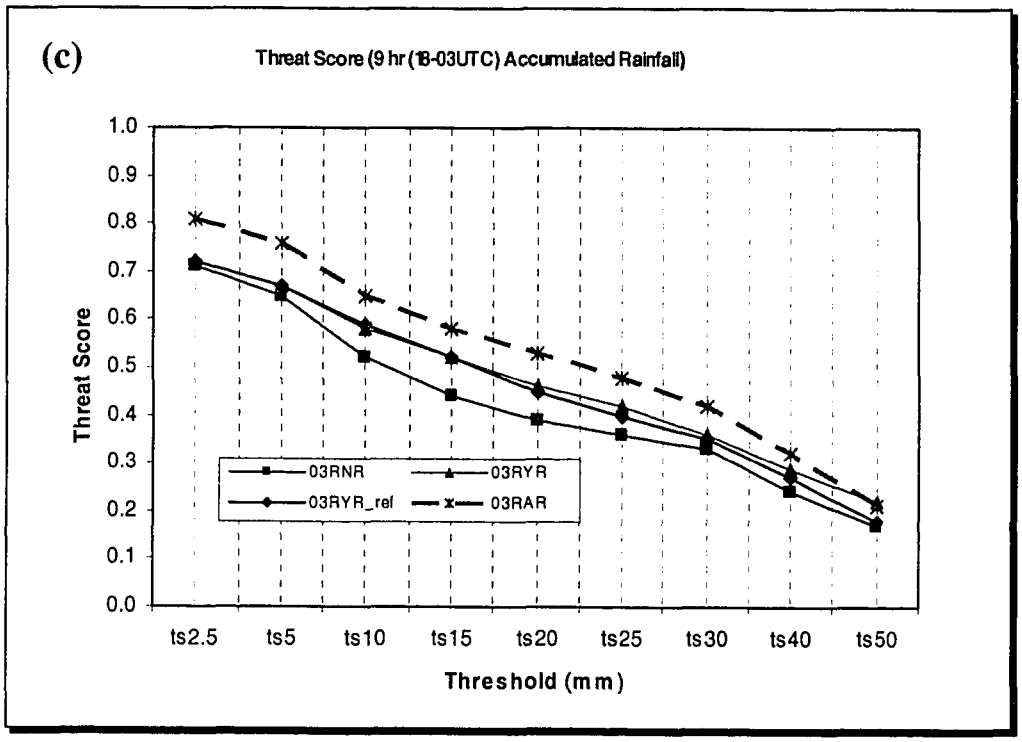

Fig. 7.8 (Continued).

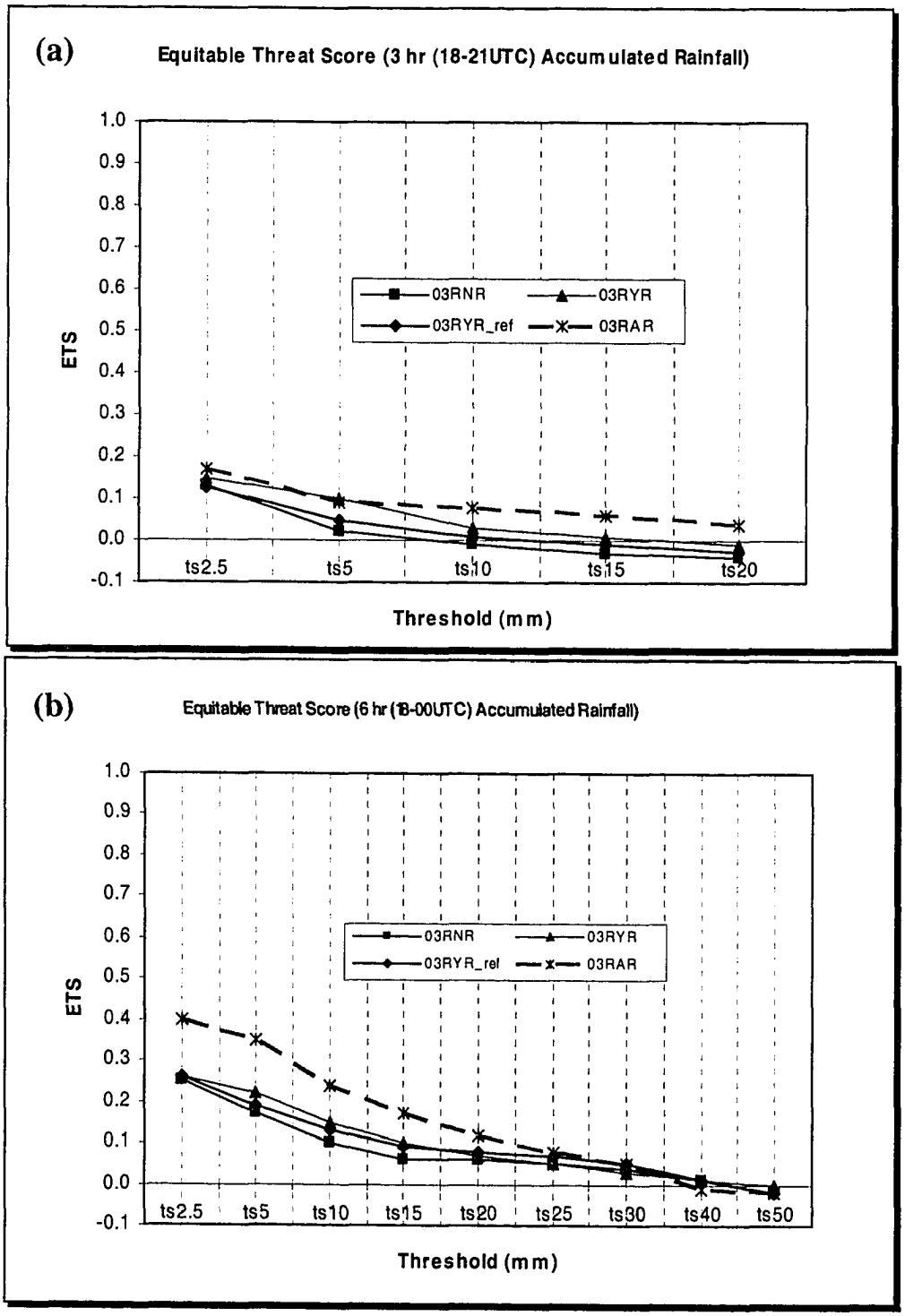

Fig. 7.9 Same as in Fig. 7.7 except for equitable threat score (ETS).

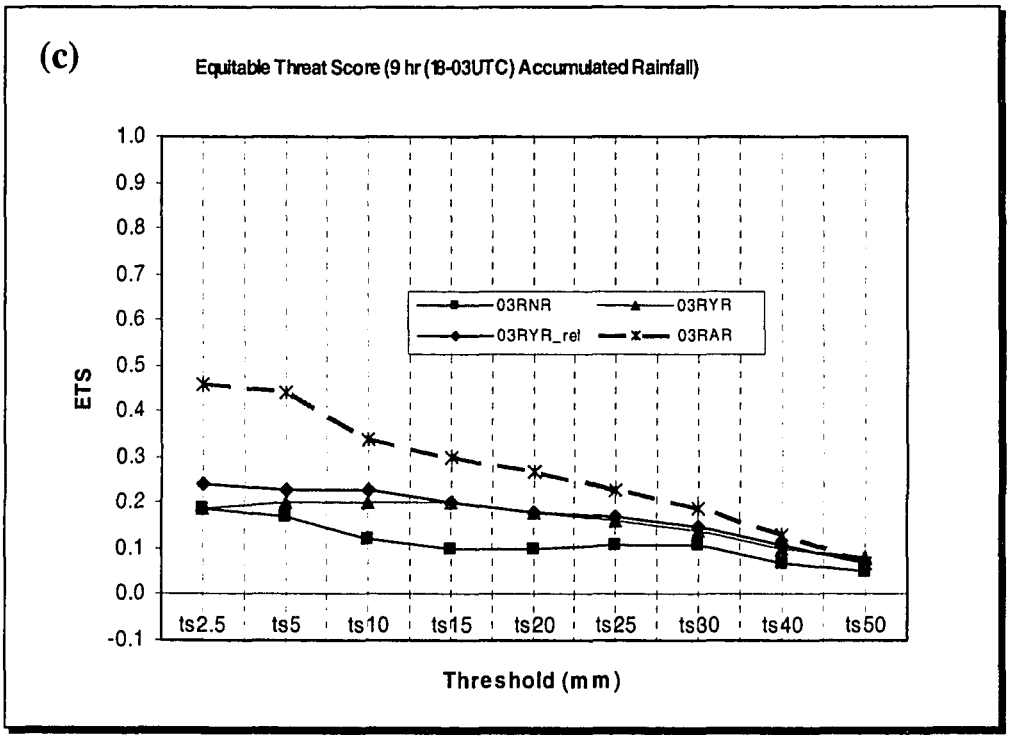

Fig. 7.9 (Continued).

Table 7.3 Instability indices for each experiment and observation at Osan, 00 UTC July 27.

	CAPE (J/kg)	LI (C)	SI	KI	SR Helicity (m^2/s^2)
03RNR	306	-0.7	-1.7	37	170.0
03RYR	401	-1.1	-1.5	38	156.2
03RAR	633	-1.8	-3.6	36	67.4
03RAR_1h_rap	1812	-4.1	-4.2	38	106
Observation	1102	-4.4	-4.1	36	63.1

•CAPE: Convective Available Potential Energy.
The larger value, the more severe weather (if CAPE > 1000, high possibility of severe thunderstorm)

• LI: Lifted Index.
The less value, the more unstable.

• SI: Showalter Index.
The less value, the more unstable

• KI: K Index.
The larger value, the more unstable. (over 30 is associated with severe thunderstorm)

• SR Helicity: Storm-Relative Helicity.
Potential for updraft rotation if convection occurs. The larger value, the more severe weather.

03RAR with 03RNR and 03RYR (03RAR_1h_rap will be described in the next section), the CAPE, lifted index, and Showalter index of 03RAR are closest to observations and clearly suggest the potential for severe weather. The storm-relative helicity and K-index of 03RAR are also close to observations, even though their values tend to indicate stable weather. In summary, these results provide evidence for the positive impact of radar data assimilation on the 3-km grid spacing run.

To confirm that 03RAR is better the other experiments and also has a forecast time limitation with regard to the impact of radar data assimilation, we examine the behavior of the domain-maximum updraft. It is well known that strong updrafts are related to heavy precipitation, and it is assumed that experiments using radar data assimilation will produce stronger and sustained updrafts, which in a qualitative sense would be in agreement with observations (though no direct computation of vertical velocity from observations was attempted).

Figure 7.10 shows the time evolution of the domain-wide maximum updraft for the aforementioned 3-km simulations. As expected, 03RAR produces stronger maxima during the first 3 hours (1800 UTC to 2100 UTC) after radar data assimilation, though at later times the velocity tends to be smaller than in the other experiments. The long-term average vertical motion of about 12 m/s is weak compared to the expected intensity of the convection, and is a factor of 3 or more weaker than would be expected from simple parcel theory. However, a grid spacing of 3 km is barely sufficient to capture such intensity, and if any grid cell had an updraft of even 25 m/s, the associated energy over a 9 km square region would be quite large. Thus, we view these results as generally

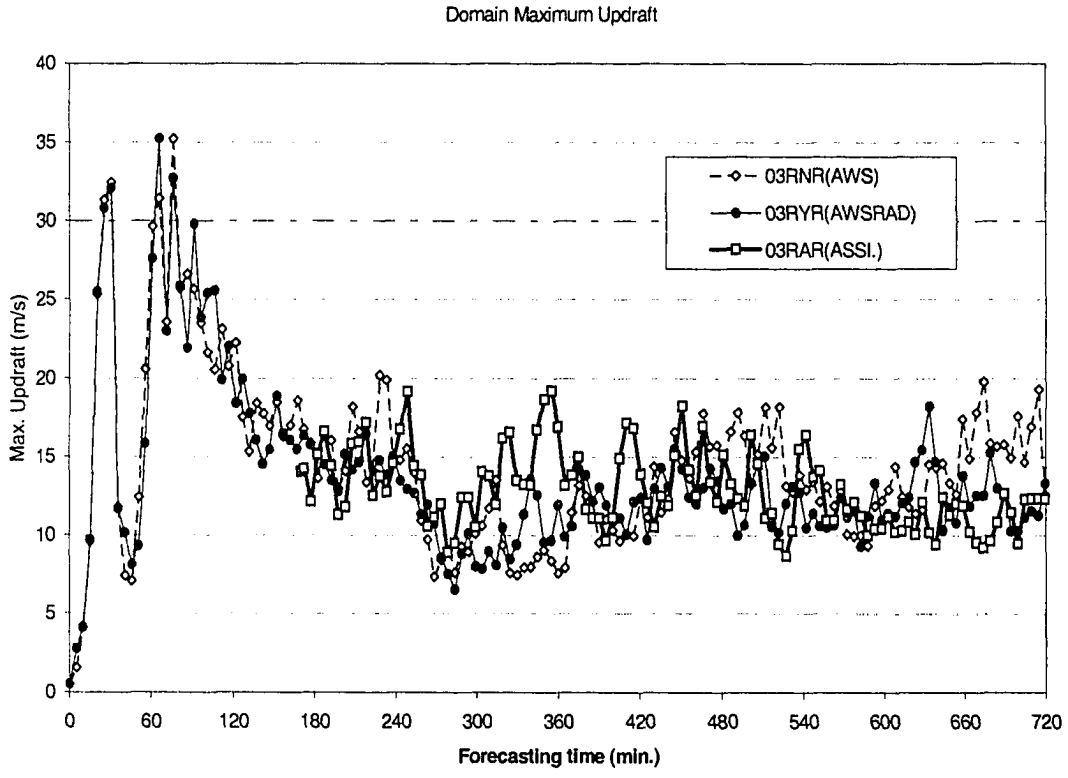

Fig. 7.10 Time evolution of domain maximum updraft from 1500 UTC July 26 to 0300 UTC July 27 (12 hours) for 03RNR (dashed line with open diamonds), 03RYR (solid line with filled diamonds), and 03RAR (thick solid line with open rectangles).

reasonable in the context of model resolution, though cannot say with certainty that the higher values of vertical motion associated with 03RAR are superior to the other cases.

7.3.2 Use of Different Data Assimilation Strategies

In this section we assess the impact of different data assimilation strategies on quantitative forecast skill and attempt to confirm whether frequent assimilation of data leads to notable improvements in skill. A total of seven experiments employing different data assimilation strategies are evaluated: 03RAR, 03RAR_initrad, 03RAR_1t, 03RAR_1h_rap, 03RAR_cent5, 03RAR_cent10, and 03RAR_cent20. The verification methods used are the same as in the previous section.

Figure 7.11 shows bias scores for these seven experiments. Experiment 03RAR_1t (Fig. 7.11), using only a single insertion of radar data, performs the worst, whereas 03RAR_cent5 (Fig. 7.11), using the shortest data assimilation window, is slightly better. A more continuous assimilation strategy, 03RAR_1h_rap (Fig. 7.11), shows more bias, with values near 1.2 for high precipitation thresholds (15 mm and 20 mm) for the 3-hr accumulation period (Fig 7.11a). However, there exists no difference between this experiment and the others for the 6-hr and 9-hr accumulation time periods (Figs. 7.11b-c). This suggests that 03RAR_1h_rap produces more rainfall in the early periods of the forecast.

It is difficult to find meaningful differences between experiments 03RAR and 03RAR_initrad (Fig 7.11) in the context of using radar data at the model initialization time. It is also difficult to find differences between 03RAR_cent10 and 03RAR_cent20 (Fig. 7.11) in order to assess the impact of the length of the data assimilation window.

Similarly, comparing experiments 03RAR_initrad and 03RAR_cent10 (Fig. 7.11), which deal with the placement of the data assimilation window, the differences in bias scores are relatively small. It should be noted that these results are valid for a single case study and thus may not be broadly applicable.

Figures 7.12 and 7.13 show the TS and the ETS for the different data assimilation strategies noted above. We see very clearly that *03RAR_1h_rap has substantially higher skill for all thresholds during the 3-hr accumulation period.* This is a very encouraging result as it strongly suggests that a more continuous data assimilation strategy is optimal, which agrees with intuition. It also confirms that the impact of radar data is confined to the first few hours of the forecast, i.e., because 03RAR_1h_rap shows substantial improvement only during the 3-hr accumulation period.

As was true for the bias scores, 03RAR_1t has the worst TS and ET (Figs. 7.12 and 7.13). Comparing 03RAR with 03RAR_initrad to assess the impact of using radar data at the initial time, we find only a slight positive impact for 03RAR_initrad. This result is consistent that from our qualitative examination in section 6.2.4. Unlike the bias scores, 03RAR_cent20 is slightly better than 03RAR_cent10 concerning the length of data assimilation window, and 03RAR_initrad is also slightly better than 03RAR_cent10 (assessing the change of displacement of radar data assimilation). These results are also consistent with the qualitative assessment made in section 6.2.4. Therefore, we surmise that, for this case, a data assimilation window of 20 minutes is slightly better than 5 or 10 minutes. Considering the differences between 03RAR_initrad and 03RAR_cent10, radar data assimilation can be quite sensitive to a change in the position of the data assimilation window or the selection of a particular volume scan.

The major results from the above quantitative verification are that radar data assimilation yields a positive impact upon our 3-km grid spacing forecasts, and that more continuous assimilation using a rapid update cycle (03RAR_1h_rap) produces the best results. The instability indices shown in Table 7.3 also confirm this. All indices of 03RAR_1h_rap are close to the observations and they clearly demonstrate the potential of severe weather. *We note that the skill scores are quite good because IAU is killing incorrect convection – not building correct convection.* We now examine the MAE of the reflectivity difference in order to confirm whether 03RAR_1h_rap is a better method and to better document the finite time duration for which radar data yields a benefit.

Figure 7.14 shows the MAE of the principal 3-km grid spacing experiments. The MAE of 03RAR_1h_rap is smaller than that of the other experiments. Specifically, during the three assimilation periods, 1710 - 1720 UTC, 1730 - 1740 UTC, and 1750 - 1800 UTC, the MAE decreases rapidly in response to the incremental insertion of observations. *It is also clear that after one IAU and before the next the MAE grows rapidly. Obviously we know that forecast errors grow with the time, but the behavior in this figure may indicate limitations in the model itself, i.e., improper formulation of surface drag that is creating spurious convection along the coast, etc. If the model is more perfect, after one IAU and before the next the MAE may not grow rapidly than current results.* Experiment 03RAR also shows the effect of data assimilation between 1750 and 1800 UTC. Comparing 03RAR_1h_rap with 03RAR, the former does not show improved results until the start of the second assimilation period at 1730 UTC, after which the effect of data assimilation appears to be maximized. From this time onward, 03RAR_1h_rap preserves the positive impact until the end of the simulation at 0300 UTC

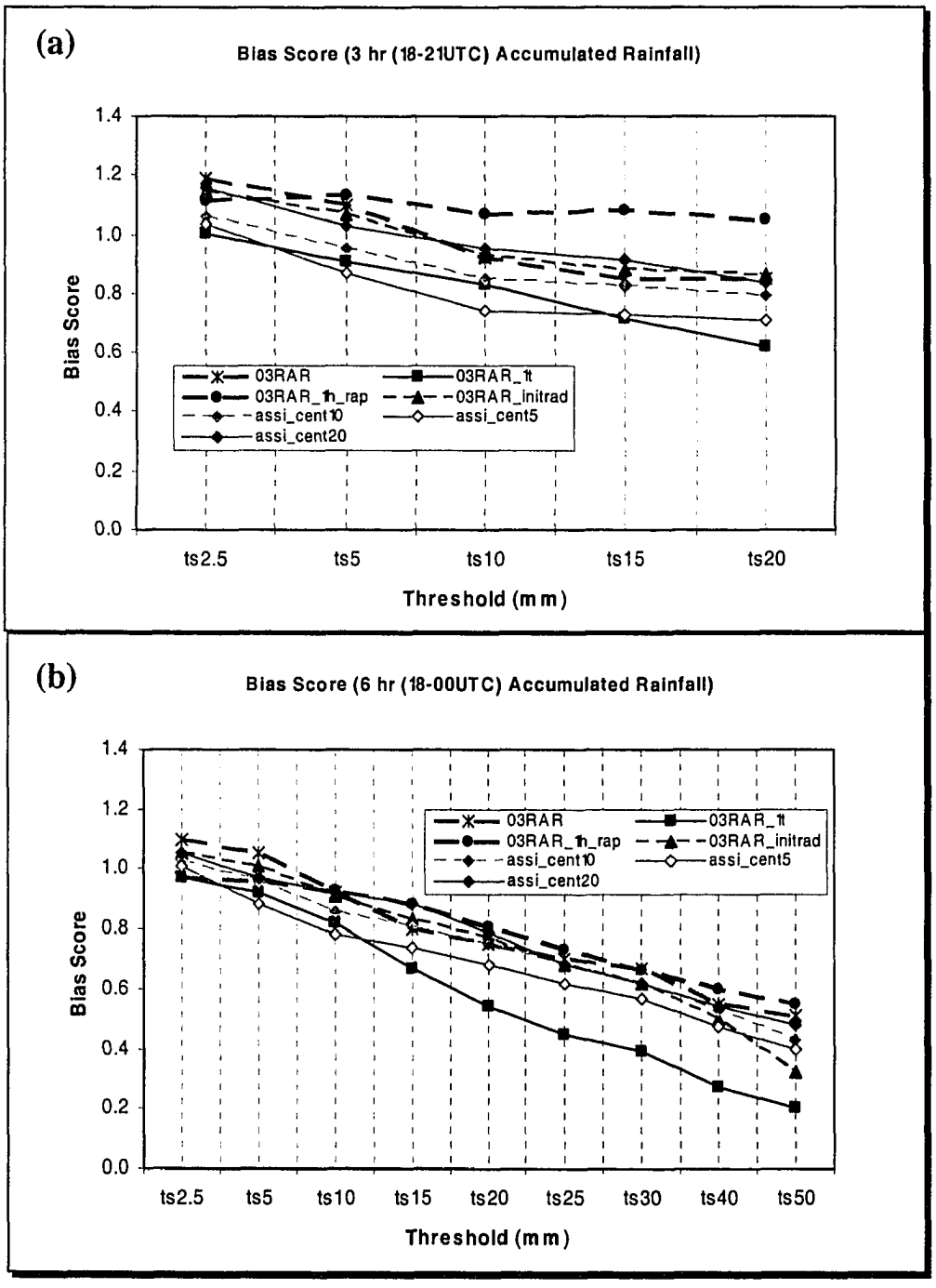

Fig. 7.11 Bias scores for accumulated rainfall forecast; (a) 3-hr accumulated rainfall from 1800 UTC to 2100 UTC July 26, (b) 6-hr accumulated from 1800 UTC July 26 to 0000 UTC July 27, and (c) 9-hr accumulated rainfall from 1800 UTC July 26 to 0300 UTC July 27. Thick dashed line with asterisk, solid line with filled rectangles, thick solid line with filled circles, dashed line with filled triangles, dashed line with filled diamonds, solid line with open diamonds, and solid line with filled diamonds indicate 03RAR, 03RAR_1t, 03RAR_1h_rap, 03RAR_initrad, 03RAR_cent10, 03RAR_cent5, and 03RAR_cent20 and 03RNR, respectively. And, the ts in x-axis stands for threshold. Namely, ts2.5 means the threshold with 2.5 mm.

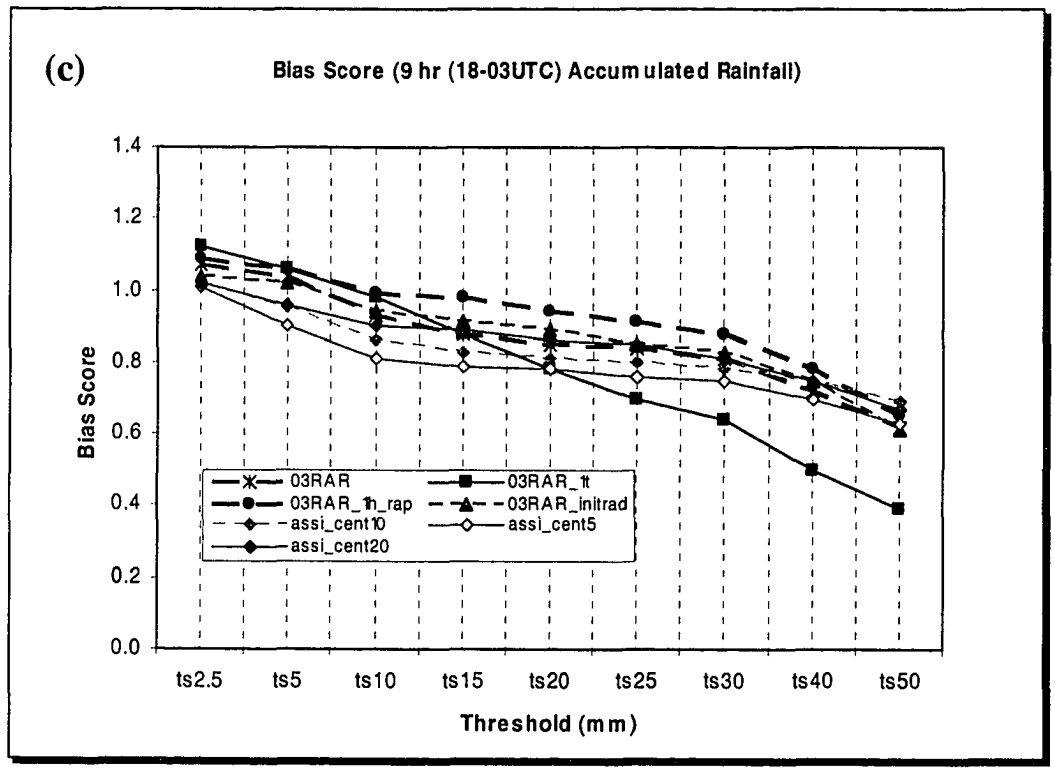

Fig. 7.11 (Continued).

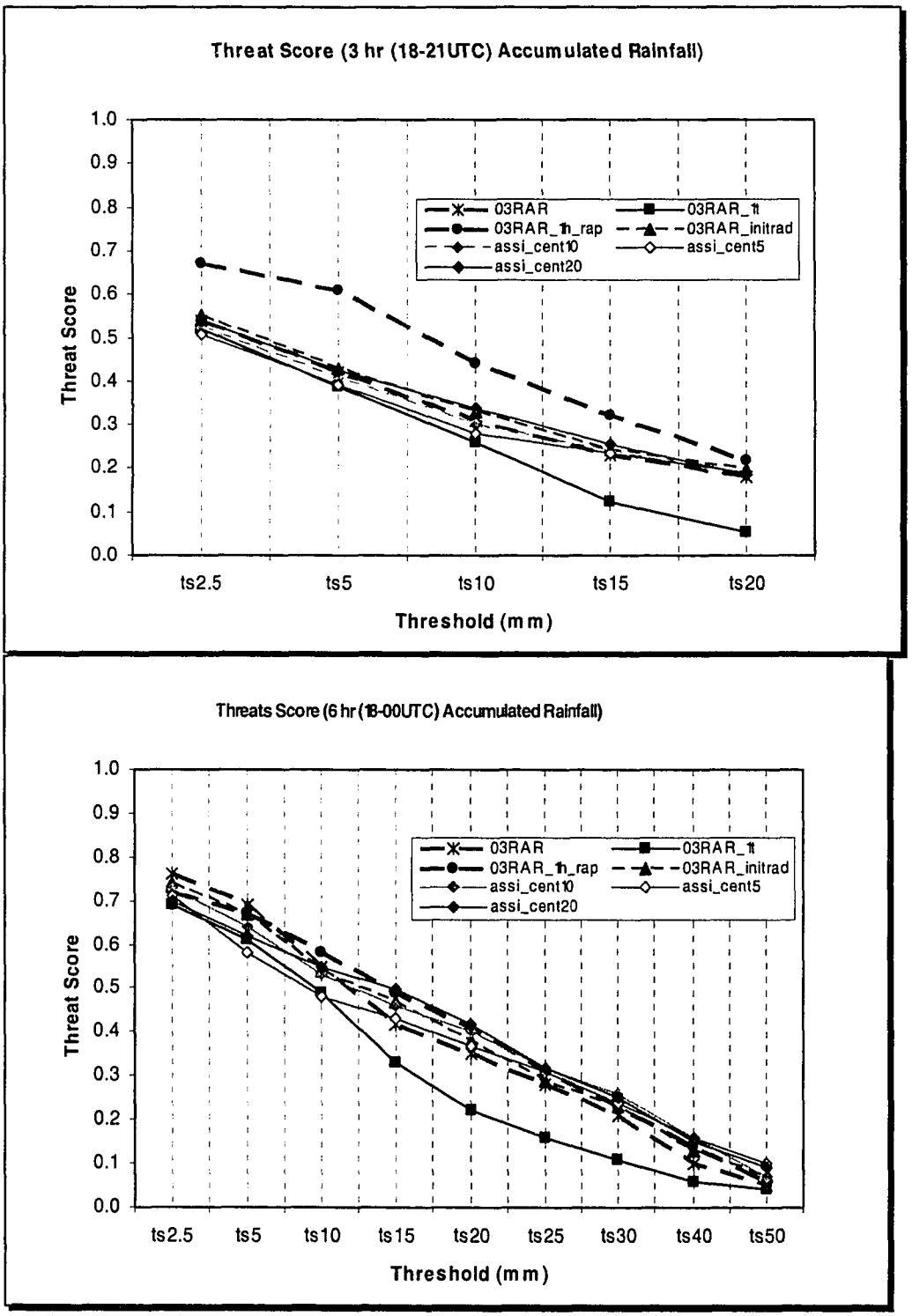

Fig. 7.12 Same as in Fig. 7.11 except for threat scores (TS).

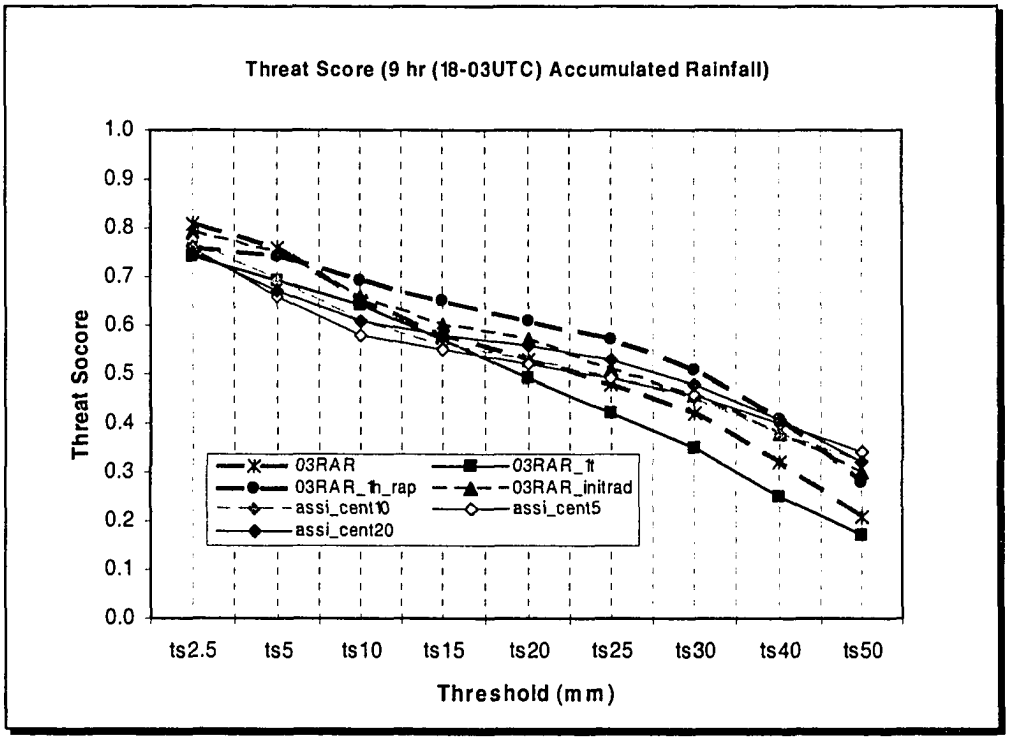

Fig. 7.12 (Continued).

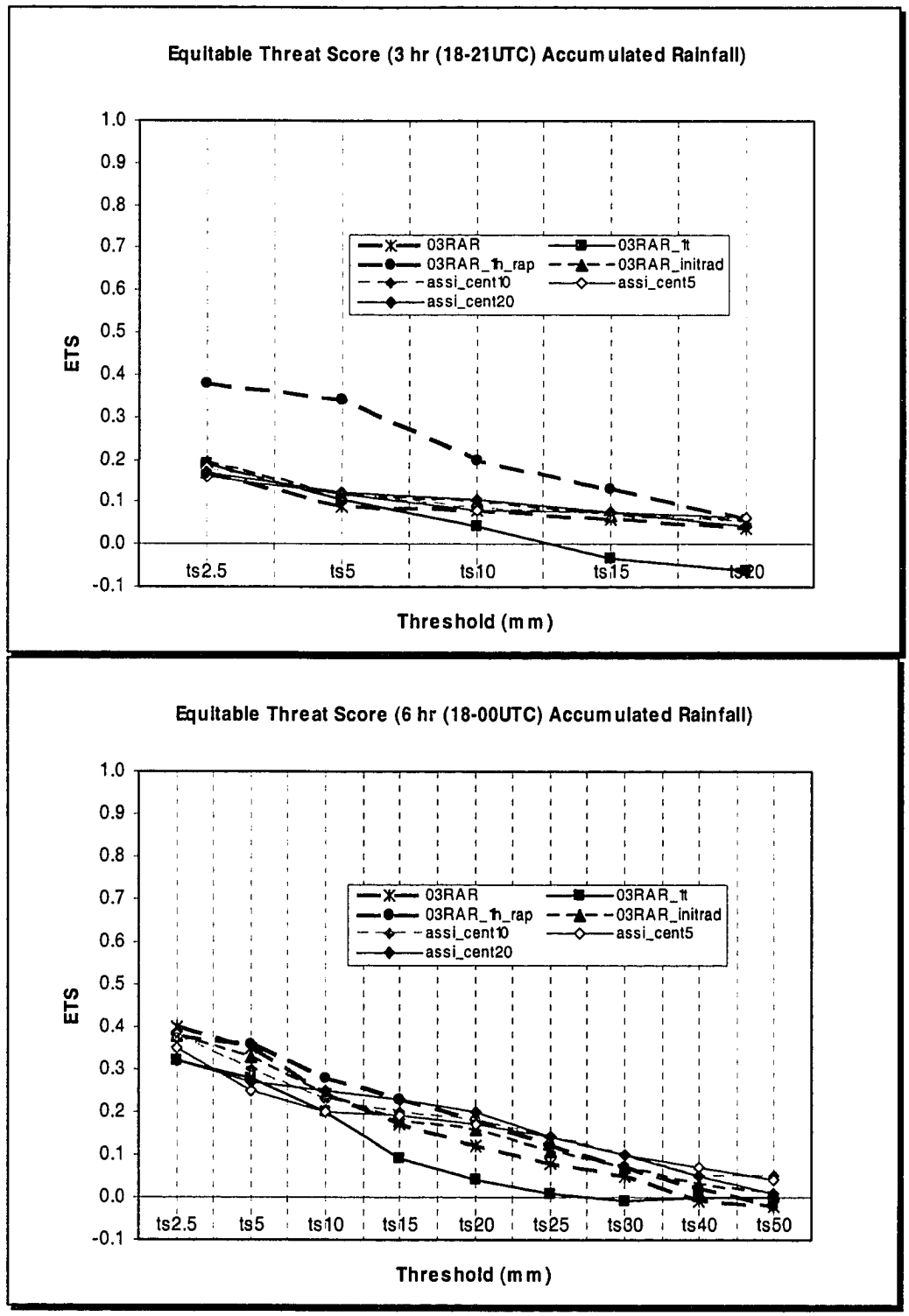

Fig. 7.13 Same as in Fig. 7.11 except for equitable threat scores (ETS).

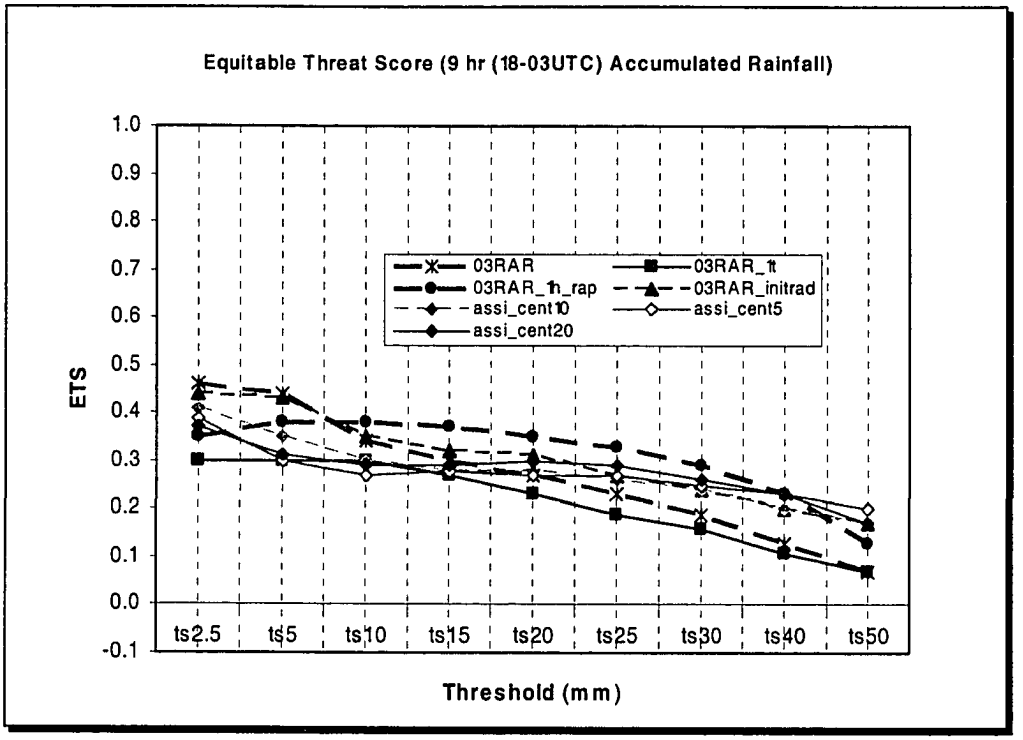

Fig. 7.13 (Continued).

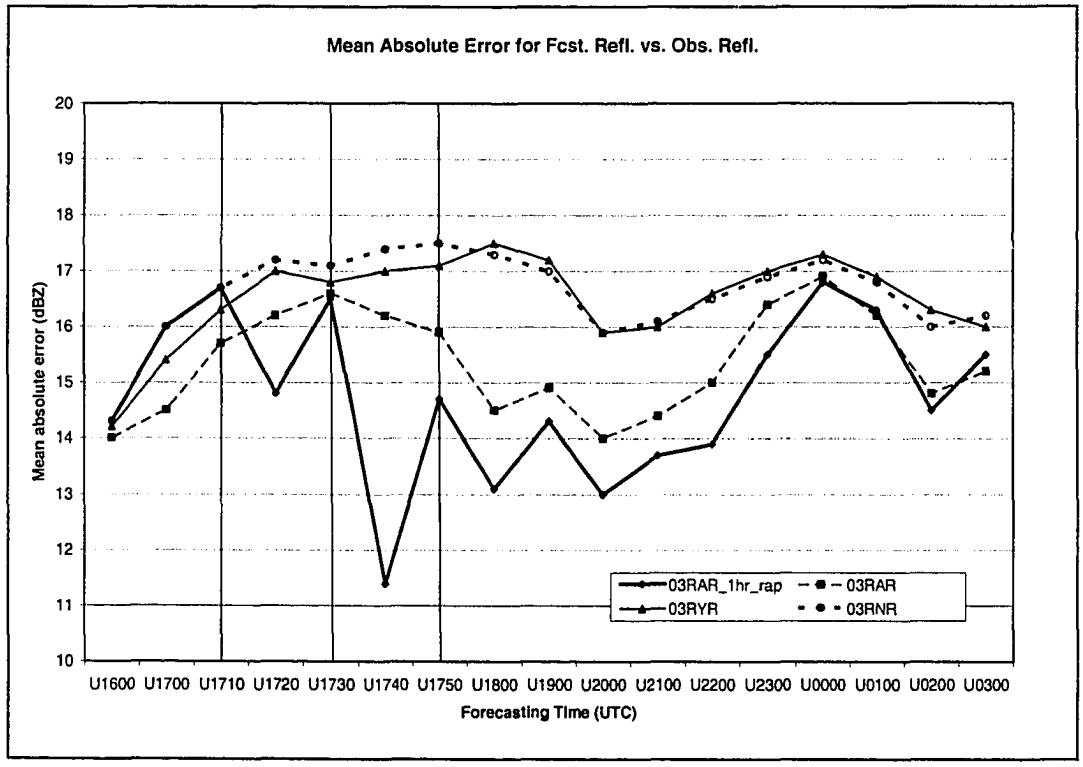

Fig. 7.14 Mean Absolute Error from the forecasted and observed radar reflectivity for 03RAR_1h_rap (heavy solid line with filled circles), 03RAR (dashed line with filled rectangles), 03RYR (solid line with filled triangles), and 03RNR (dashed line with open circles). U1600 means 1600 UTC and others are same as this.

July 27. Although the superior performance of 03RAR_1h_rap continues until the end of the simulation, the trend shows some time dependence. The MAE increases rapidly from 2200 UTC, similar to the trend in 03RAR.

Considering these results, it is clear that there exists a finite time during which radar data assimilation exerts a positive impact upon the forecast – nominally 3 or perhaps 4 hours. This is consistent with the previous results and begs the following question: what is the mechanism by which 03RAR_1h_rap yields such improvements? This experiment applied IAU three times, each over a 10-minute period, within an hour. Therefore, the next assimilation cycle begins before the adjustments produced by the previous cycle disappear. In contrast, the one-hour period between data insertions in 03RAR is too long to preserve adjustments from one assimilation period to the next. In summary, it is clear that 03RAR_1h_rap provides the best results from both qualitative and quantitative perspectives, and we therefore focus on a detailed analysis of this experiment in the next section.

7.4 Analysis of IAU for Experiment 03RAR_1h_rap

From both quantitative and qualitative verification of our results, we have determined that a more continuous assimilation strategy (03RAR_1h_rap) is superior to the other strategies described previously. In this section, we attempt to quantify the effect of incremental analysis updating (IAU) upon the corresponding prediction. We will examine reflectivity differences and the analysis errors of the wind and temperature fields.

7.4.1 Forecasted and Observed Radar Reflectivity

Figure 7.15 displays the reflectivity difference, or RD (forecasted reflectivity minus observed reflectivity), both before IAU (left panels) and after IAU (right panels). The RD's decrease rapidly after IAU for all data assimilation periods, and in particular, the erroneous convection over the western sea and coastal areas is correctly eliminated. However, the under-forecasted regions in the north do not show any significant change in RD. This is most likely a result of the fact that, at longer distances, the radar beam is at higher elevations; consequently, changes induced by the radar data will be confined to higher levels, where their impact would be expected to be smaller.

During the first IAU (Fig. 7.15a and b), from 1710 to 1720 UTC, the RD improves significantly. However, this improved RD is degraded during the next forecasting period, from 1720 to 1730 UTC (Fig. 7.15c), as the storms re-intensify. Although the forecast produces a worse RD (Fig. 7.15c), it is still better than the first RD (Fig. 7.15a). This suggests that the adjustment effectuated by radar data assimilation, and the assimilation of other quantities as made possible by the ADAS cloud analysis, is beneficial. Subsequent IAU/forecast cycles further improve the RD (Fig 7.15, right column).

Figure 7.16 shows the distributions of forecasted and observed reflectivity before (1730 UTC, Fig. 7.16a) and after the second IAU (1740 UTC, Fig. 7.16b). Although the absolute correlation is not very high, the correlation is significantly improved after the IAU. The correlation between forecasted and observed reflectivity for each forecasting time are shown in Fig. 7.17. This result is consistent with the MAE (Fig. 7.14), with the correlation decreasing until the first IAU begins at 1710 UTC, then rapidly increasing

thereafter through all three cycles. Similar to the trend in MAE (Fig. 7.14), the correlation increases to its maximum value of 25.4% after the second IAU (1740 UTC).

Once the IAUs are completed, the correlation again decreases. After 2200 UTC (4 hours after data assimilation), the correlation decreases very rapidly, reaching almost 0 % during the last 3 hours (0100, 0200, and 0300 UTC). Once again, the absolute values of the correlation are low overall. However, they do show a substantial positive impact of radar data assimilation. These results are quite similar to those of section 6.2.4 (see Fig. 6.13) in that the effect of radar data assimilation in the more continuous assimilation strategy diminishes with time throughout the forecast (for approximately 3 or 4 hours).

7.4.2 Analysis Error

In this section, we examine the analysis error (observation minus objective analysis values interpolated to observing stations) to determine the quantitative effect of radar data assimilation in experiment 03RAR_1h_rap. Wind and temperature fields at 20 stations (Table 7.4) are employed, and the analysis before IAU is compared with that after IAU for all IAU periods. The closest observed data at each station are used for the analysis. For example, observations collected "at" 1700 UTC are applied for the comparison at 1710 UTC and 1720 UTC, while observations at 1800 UTC are used for other times. Because 1700 UTC is not a regular time for observations, only AWS surface data are used.

The temperature analysis error, shown in Fig. 7.18, shows a substantial decrease from prior to data insertion (1710 UTC) to just after IAU (1720 UTC) (Fig. 7.18a). At 1710 UTC, the analysis errors are greater than 3° K at most stations. These large errors

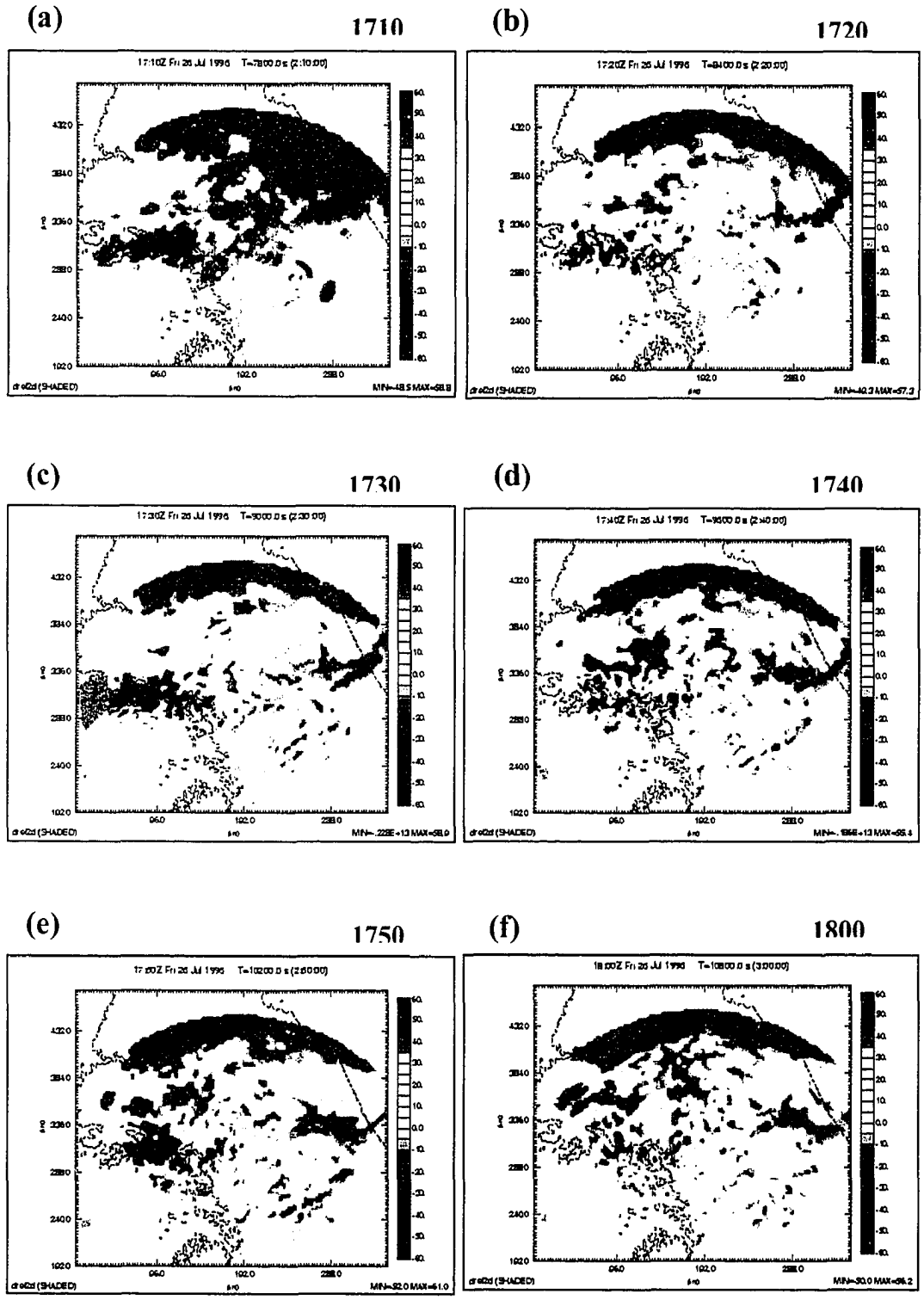

Fig. 7.15 The reflectivity difference between forecast and observation (forecast minus observation) for 03RAR_1h_rap experiment at before IAU (left panels) and after IAU (right panels).

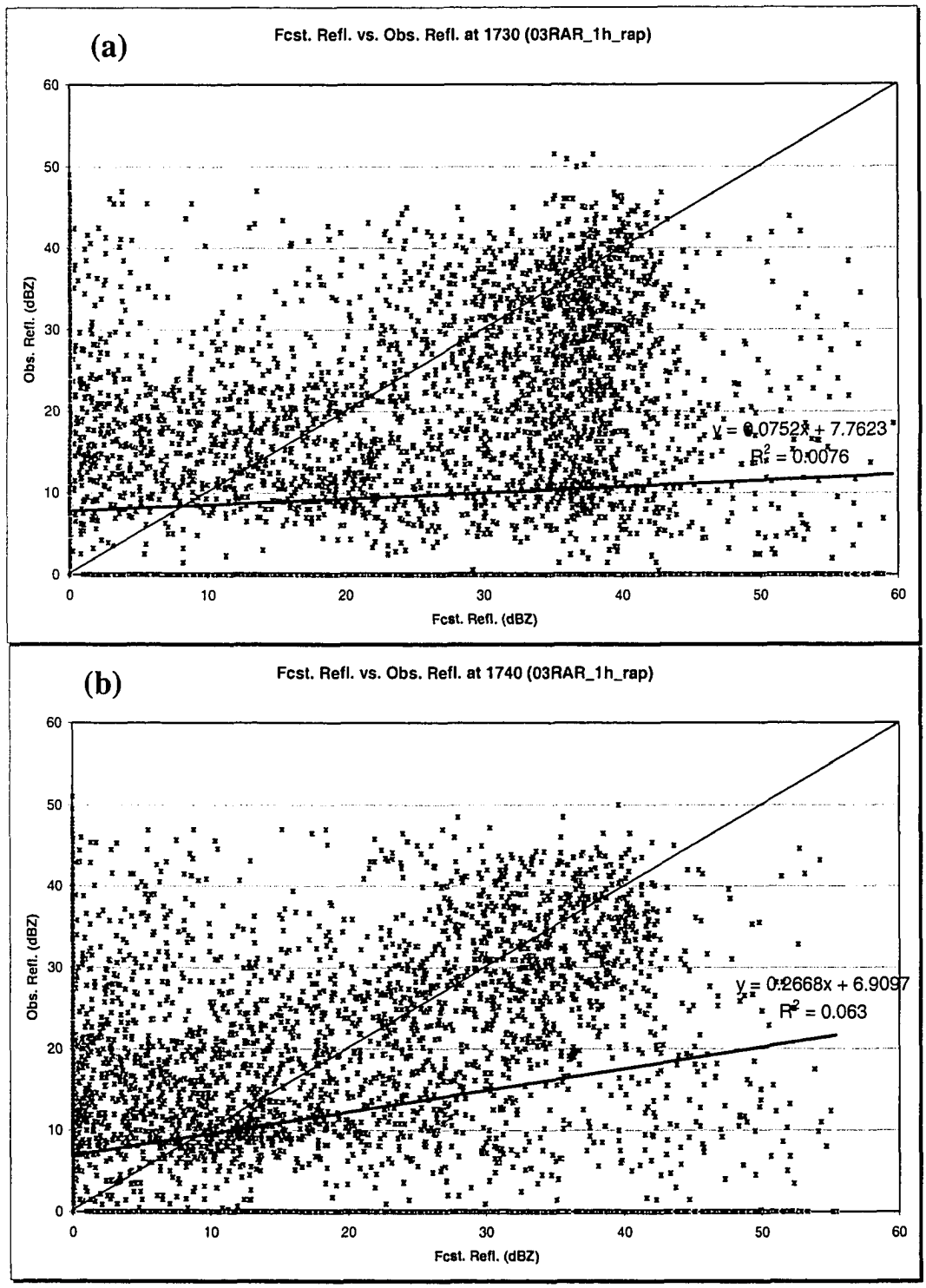

Fig. 7.16 Forecasted reflectivity from 03RAR_1h_rap versus observed reflectivity at (a) before 2nd IAU, 1730 UTC and (b) after 2nd IAU, 1740 UTC July 26.

Table 7.4 AWS and official observation stations used in the analysis error. A and S stand for AWS station and official surface station, respectively

Stn. No.	Latitude(N)	Longitude(E)
A400	37.51	127.05
A401	37.48	127.02
A402	37.55	127.15
A404	37.55	126.85
A407	37.62	127.09
A409	37.58	127.09
A410	37.49	126.92
A411	37.54	126.93
A412	37.57	126.95
A508	37.57	127.97
A523	37.90	128.83
A526	37.37	128.42
A706	35.30	126.97
A708	35.13	126.80
A713	34.98	127.58
S090	38.25	128.56
S100	37.68	128.76
S105	37.75	128.90
S106	37.50	129.13
S130	36.98	129.41

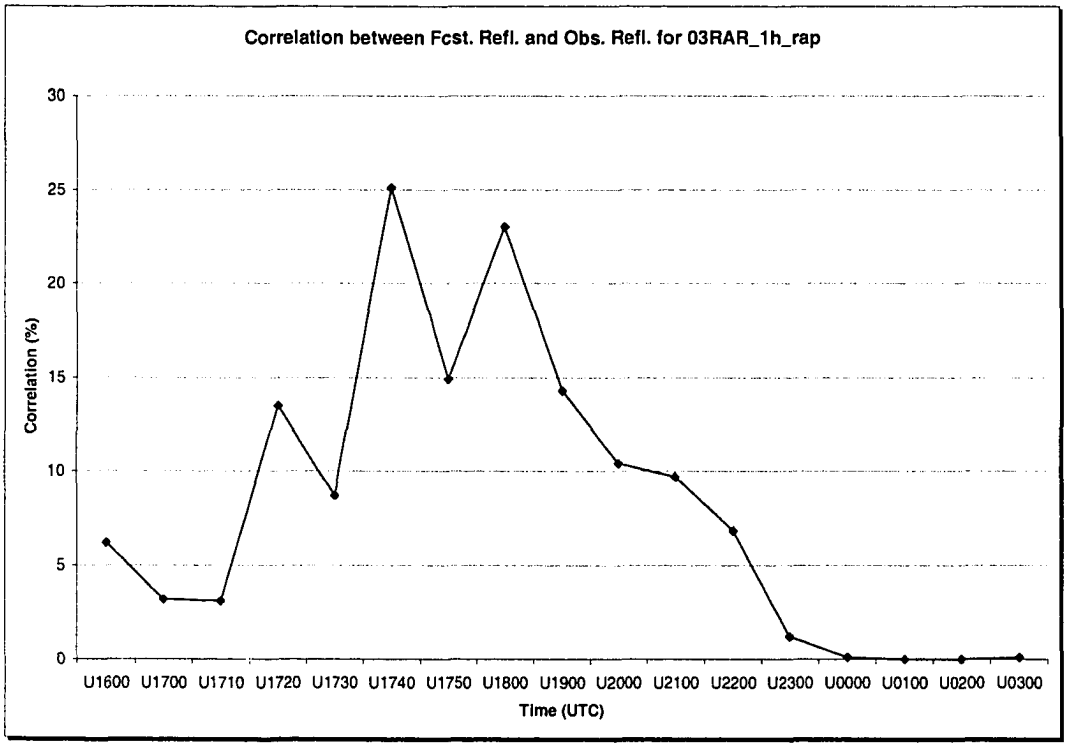

Fig. 7.17 Time evolution of the correlation between forecasted reflectivity by 03RAR_1h_rap and observed reflectivity.

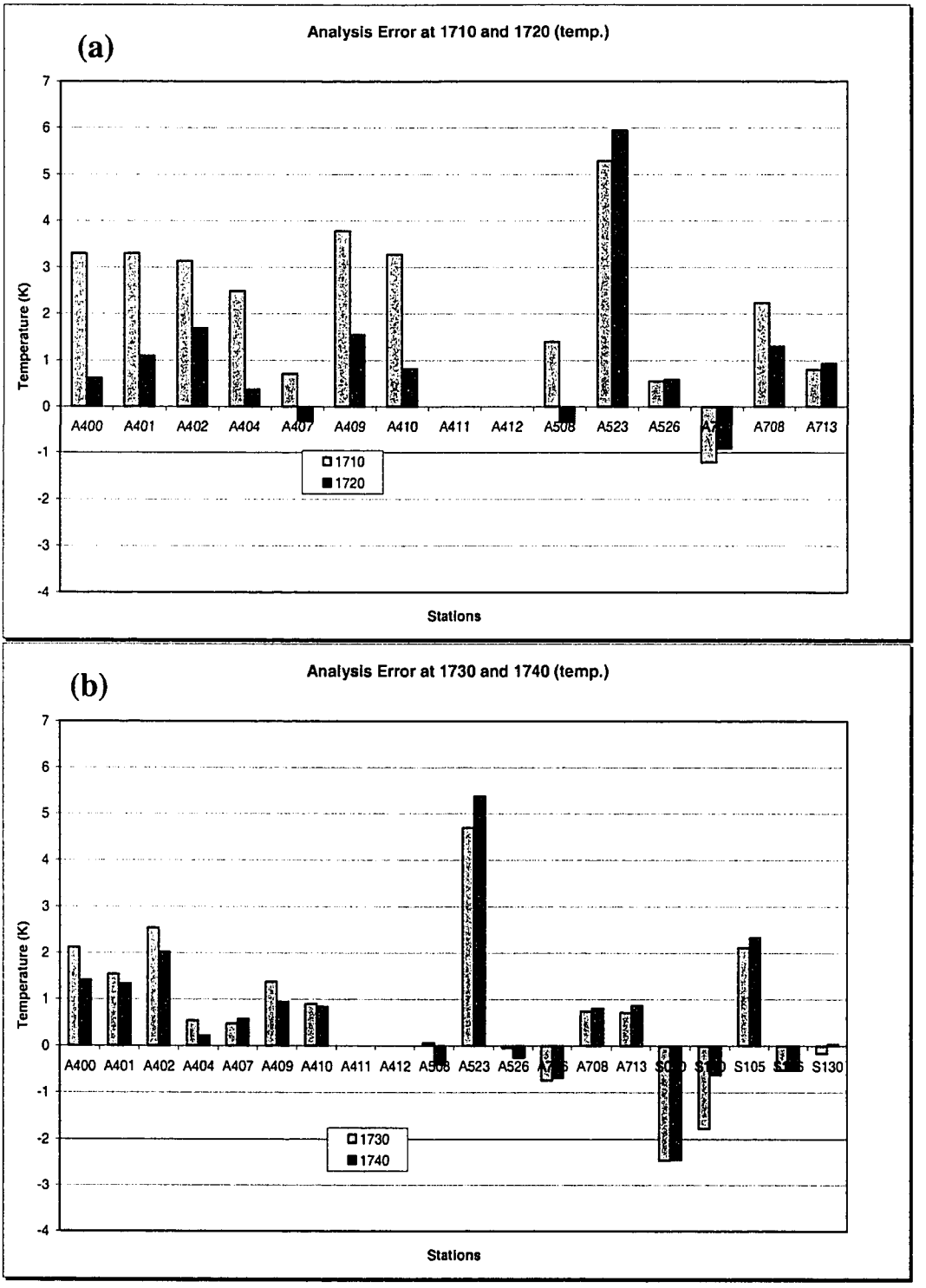

Fig. 7.18 Temperature analysis error at (a) the first IAU period (1710 UTC and 1720 UTC), (b) the second IAU period (1730 to 1740 UTC), and (c) the third IAU period (1750 to 1800).

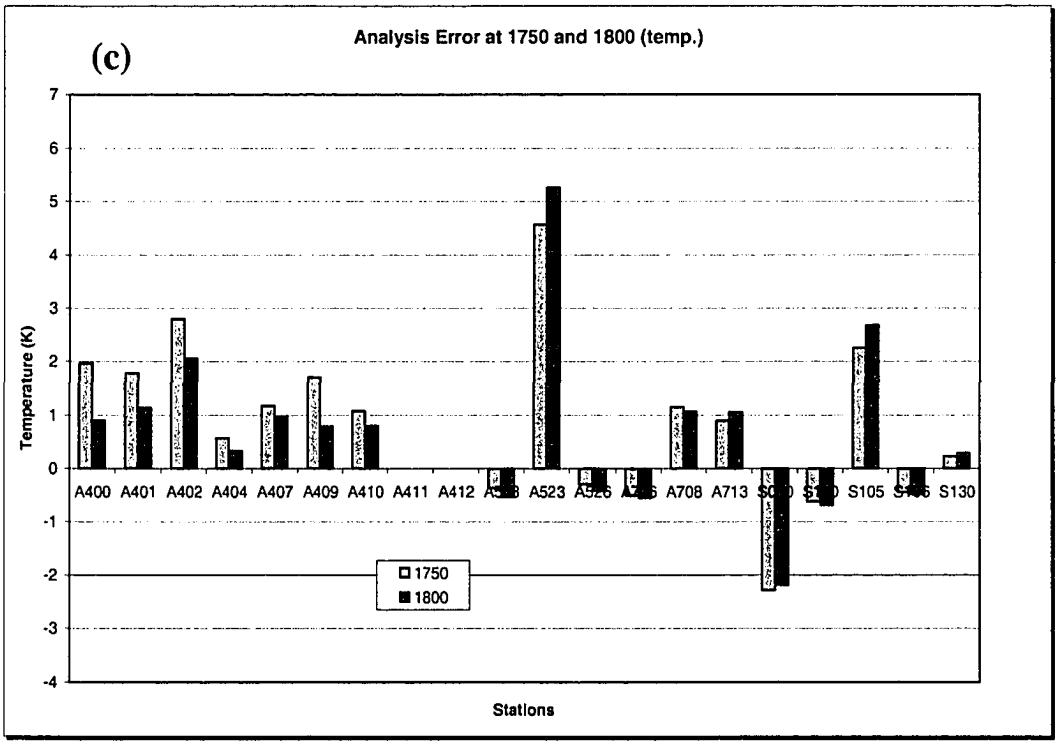

Fig. 7.18 (Continued).

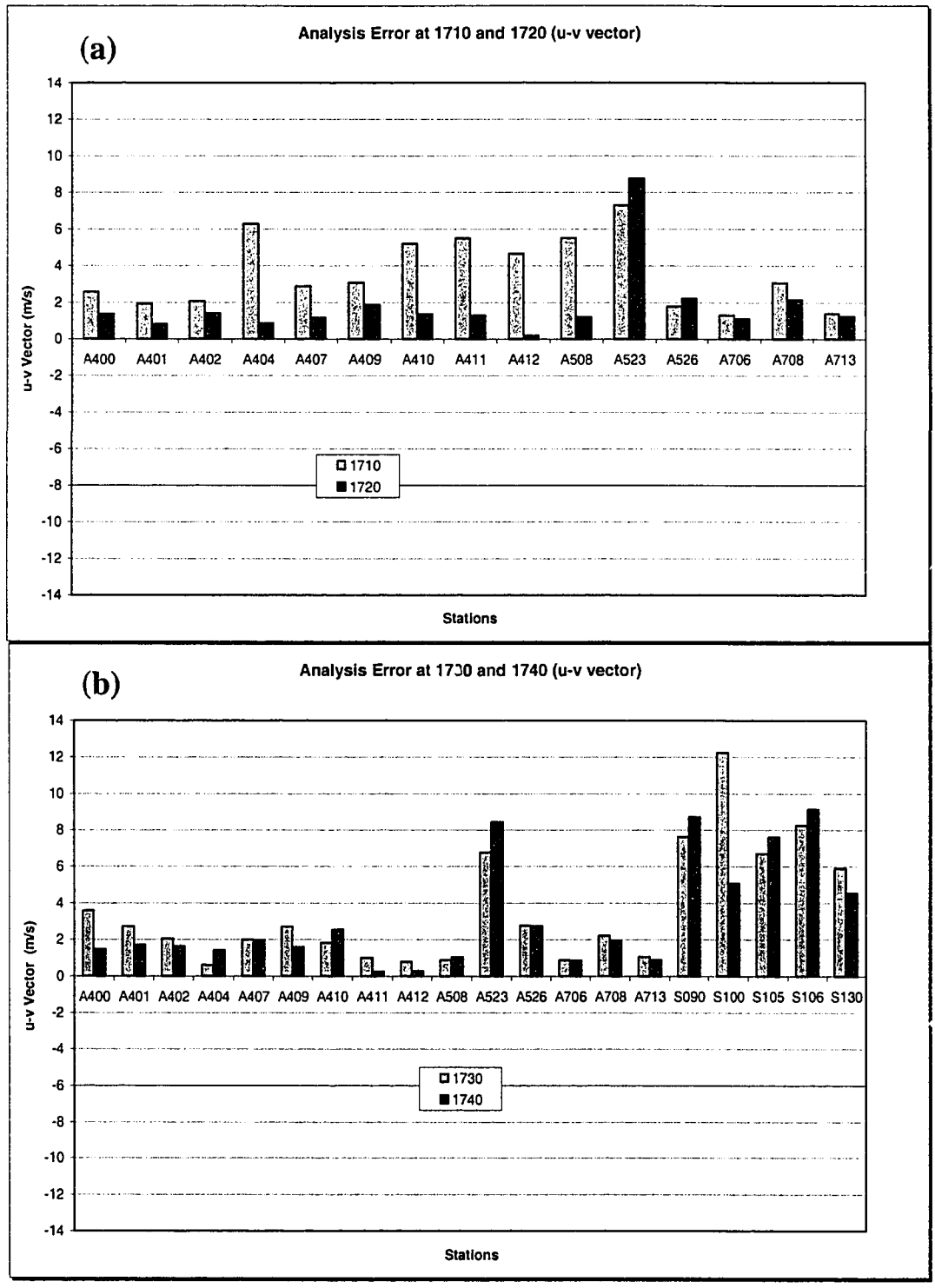

Fig. 7.19 Same as in Fig. 7.18 except for u-v vector.

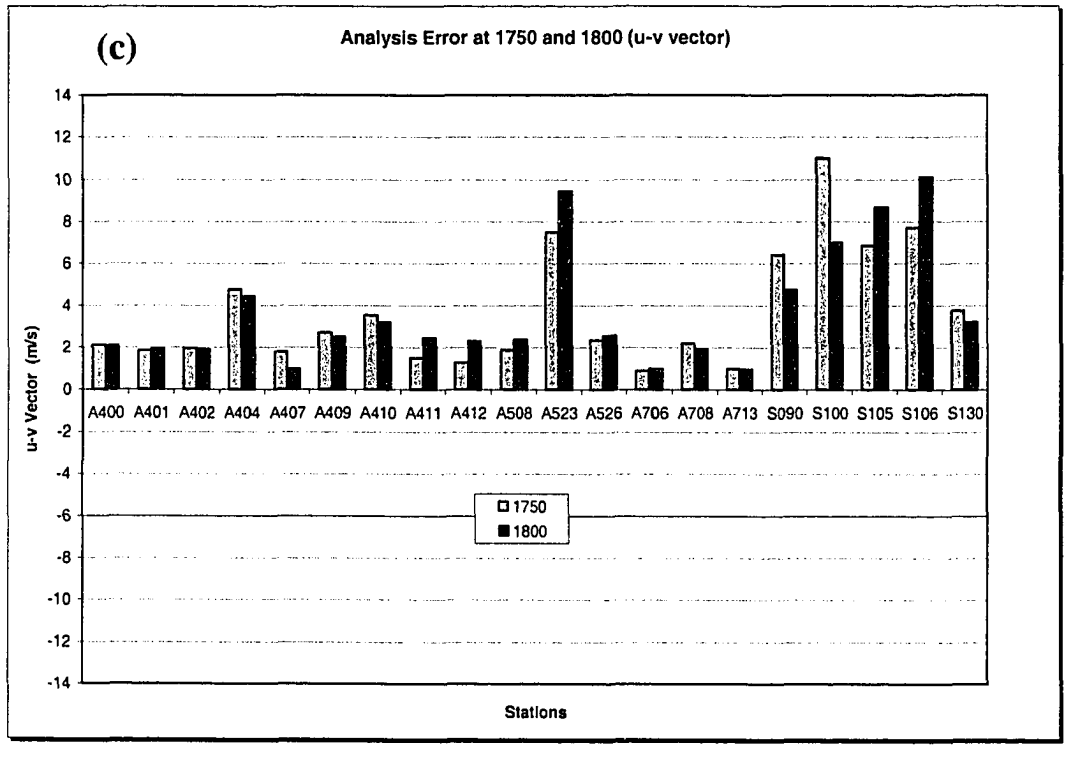

Fig. 7.19 (Continued).

rapidly decrease after the first IAU. The analysis errors at 1720 UTC are less than 1° K at most stations, and the results for the other IAU periods are consistent with those of the first. However, the analysis error difference (before and after the IAU) for the second and third IAU periods (Fig. 7.18b and c) is smaller, as it should be, given that the forecast following each IAU starts with an analysis more accurate than the preceding time. In other words, the analysis errors should decrease with each subsequent data insertion as the model is driven toward the observations.

As shown in the Fig. 7.18b, the analysis error at 1730 UTC is less than that at 1710 UTC. When we compare the analysis error difference between 1710 UTC and 1730 UTC with the analysis error difference between 1730 UTC and 1750 UTC, the former is better than the latter. This result suggests that the effect of radar data assimilation is decreasing as the number of assimilation cycles is increasing. Therefore, more data assimilation cycles may not always produce better results, and therefore it is important to find the optimal number of insertions.

The analysis error results for the wind vector magnitude (Fig. 7.19) are similar to those for the temperature field. However, the outcome of the third IAU period (Fig. 7.19c) is inconsistent because improvement, and in fact some degradation, occurs after the IAU. Because only radial wind information is being inserted into the analysis, the gradual wind adjustment owing to radar data assimilation probably diminishes in comparison to that associated with other variables, principally those related directly to thermodynamic effects.

As shown in Figures 7.18 and 7.19, several stations such as A523, S090, S100, S105, S106, and S103 show unacceptable results. To examine the cause of these errors,

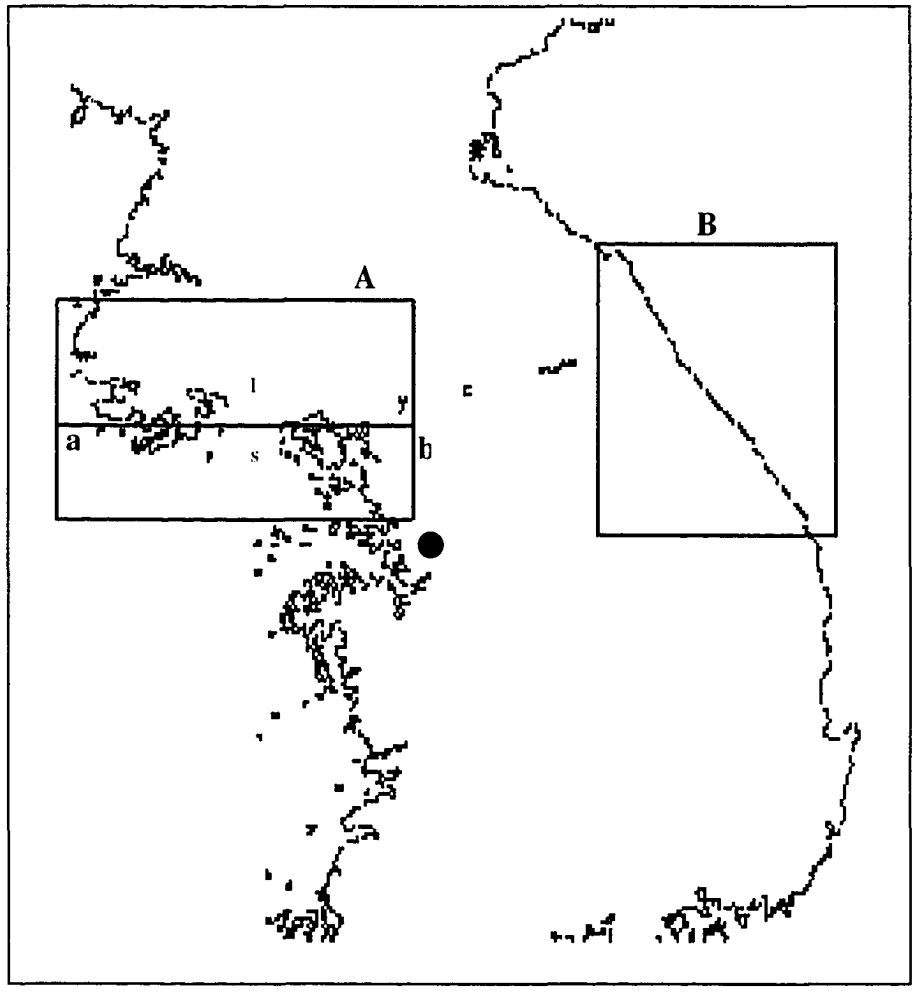

Fig. 7.20 The domains for analysis (The filled circle indicates Osan position).

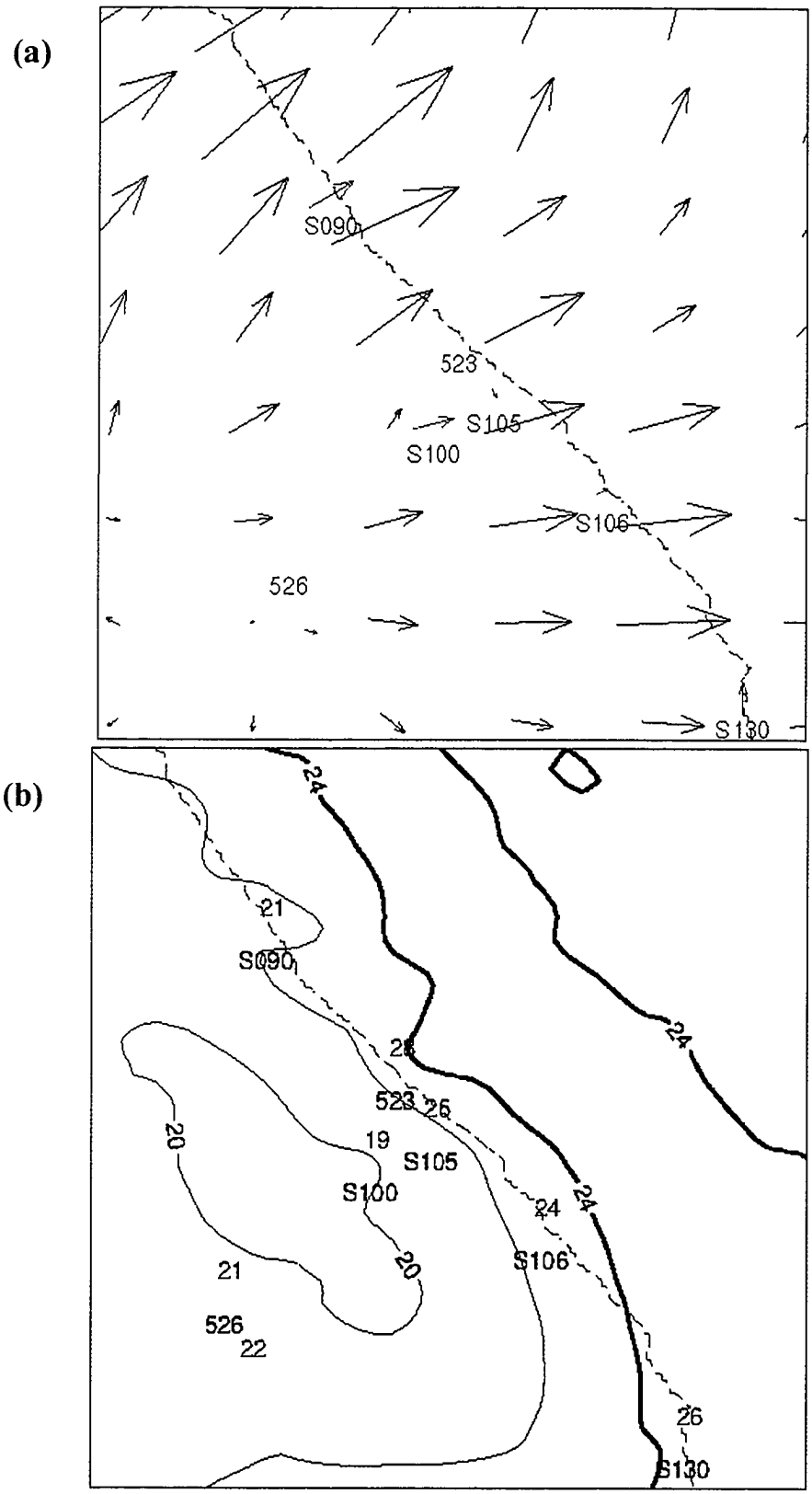

Fig. 7.21 Observations (red arrows and red characters) at 1800 UTC and ADAS analysis at 1700 UTC. 523 and 526 indicate the number of AWS stations and S stands for the official surface station (a:wind, b:air temperature).

Fig. 7.21 shows the analysis at 1750 UTC, and the observations of horizontal wind and temperature, at 1800 UTC, along with the locations of these stations. Area B in Fig. 7.20 indicates the domain of Fig. 7.21. Figure 7.21 confirms the existence of large differences between observations and the analysis. One common characteristic is that all stations exhibiting significant error are near the coast, with high terrain to their west. We assume that these observations are not in error because they passed the quality control process in the ADAS scheme. The observed winds (Fig, 7.21a) are weaker and more variable than in the analysis. This behavior might result from a sea-land breeze circulation or from mountain waves induced by the complex terrain. However, the numerical model does not seem to capture this detailed structure in its prediction.

In summary, we can state with quantitative certainty that radar data assimilated at reasonably rapid intervals has a positive impact on the forecast of the Chorwon-Yonchon heavy rainfall event. In the next section, we examine how the increments used in radar data assimilation affect the forecast.

7.4.3 Origin of Erroneous Coastal Convection

We discuss there the origin of erroneous convection predicted consistently by all forecasts, especially those using 3 and 9 km grid spacing, over the western sea and coastal areas. For example, Figure 7.22 shows surface horizontal reflectivity and surface wind vectors at 1500 UTC on (a) July 26 and (b) 1700 UTC in experiment 03RAR_1h_rap. Although the analysis at 1500 UTC (Fig. 7.22a) shows no reflectivity in this region, the model forecast clearly produces intense spurious convection in the area of the western sea and coastal regions at 1700 UTC (Fig. 7.22b).

Although no definitive reason exists for this spurious convection, one important characteristic is that it occurs along the coastal region as thus likely results, at least in part, from the rapid frictional slowing of southerly wind as it passes from the sea onto land over the western part of the KP (Fig. 7.22). Thus, the frictionally-induced convergence occurs in the region joining moist, warm tropical air over the water and relatively dry and cold continental air over the land. In experiment 03RAR_1h_rap, we employed AWS data and GTS surface data at the initial time, along with the 09RYR analysis as the first guess field, in an attempt to correct any mis-specified structure of the environment. It appears, however, that the environment is sufficiently unstable for any such correction to have a significant impact. It also appears that the assimilation of radar data into such an environment is effective only locally, i.e., the assimilation process is unable to overcome the potentially erroneous background state on a broad scale, and is effective locally only after repeated insertions.

We also examined soundings over land and sea near the coastal area at 1800 UTC July 26 (Fig. 7.23) in an effort to determine the degree of disagreement between the model and observations in the relatively undisturbed environment, and the propensity of land-sea contrasts to explain the spurious convection in the light of frictionally-induced convergence forcing. The annotations 'l' and 's' in Fig. 7.20 indicate the position of the model land and sea soundings, respectively, and it is clear that significant differences exist between the soundings on land and at sea. The latter (Fig. 7.23b) clearly is more unstable, with a CAPE of 1510J/kg. In contrast, the CAPE over land at this time is zero. The surface wind over the sea is also stronger (about 8 m/s) than that over the land (about

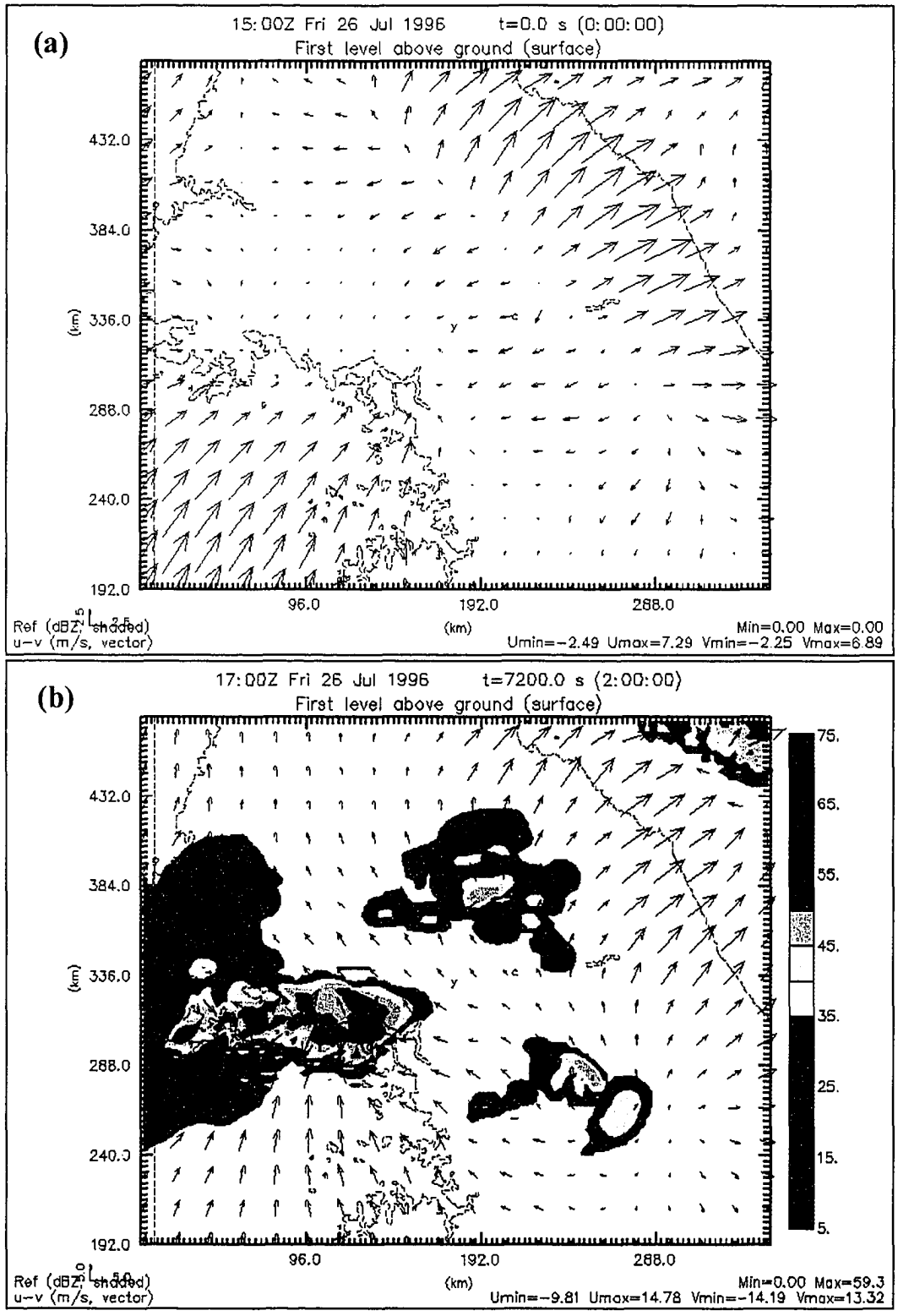

Fig. 7.22 Surface horizontal reflectivity and surface wind vector at 1500 UTC July 26 (a) and 1700 UTC (b) simulated from 03RAR_1h_rap experiment.

1800 UTC July 26 (03RAR_1h_rap at LND)

(a)

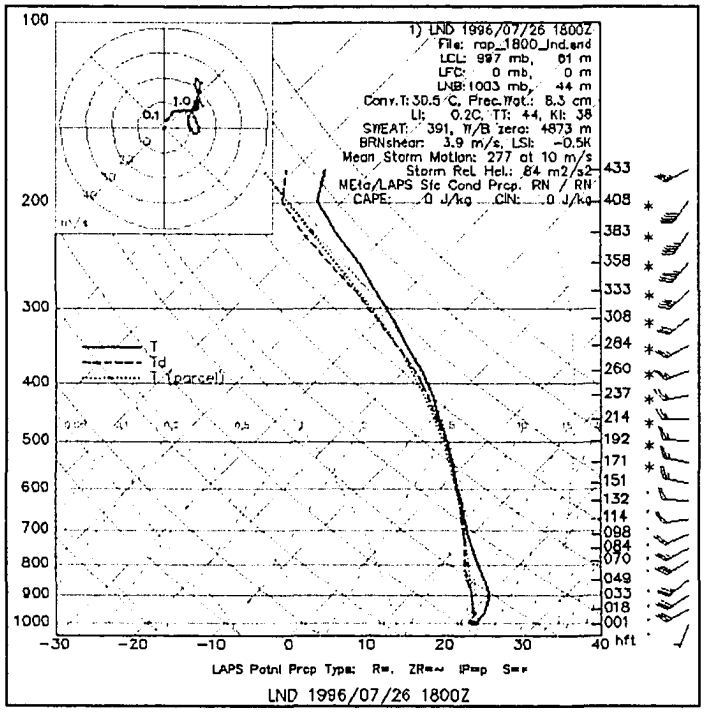

1800 UTC July 26 (03RAR_1h_rap at SEA)

(b)

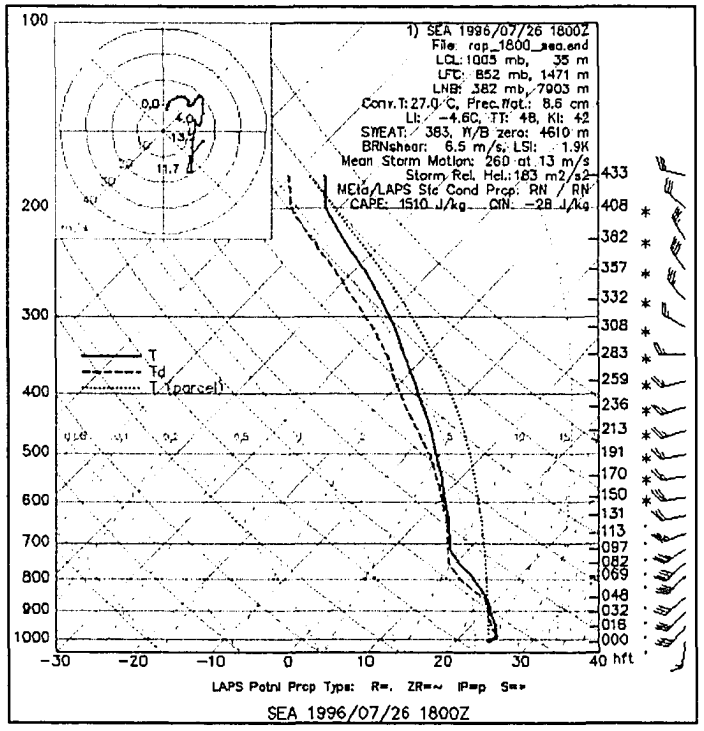

Fig. 7.23 Skew-T plot of sounding over a land position (a) and a sea position (b) near coastal are (Fig. 7.19 displays the exact land position and the sea position).

1800 UTC July 26 (Observation at Osan)

(a)

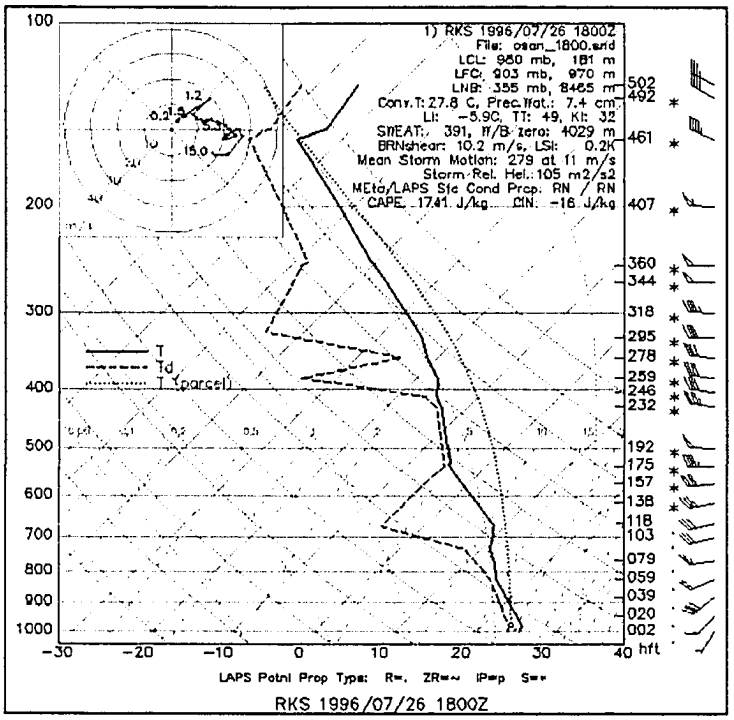

1800 UTC July 26 (03RAR_1h_rap at Osan)

(b)

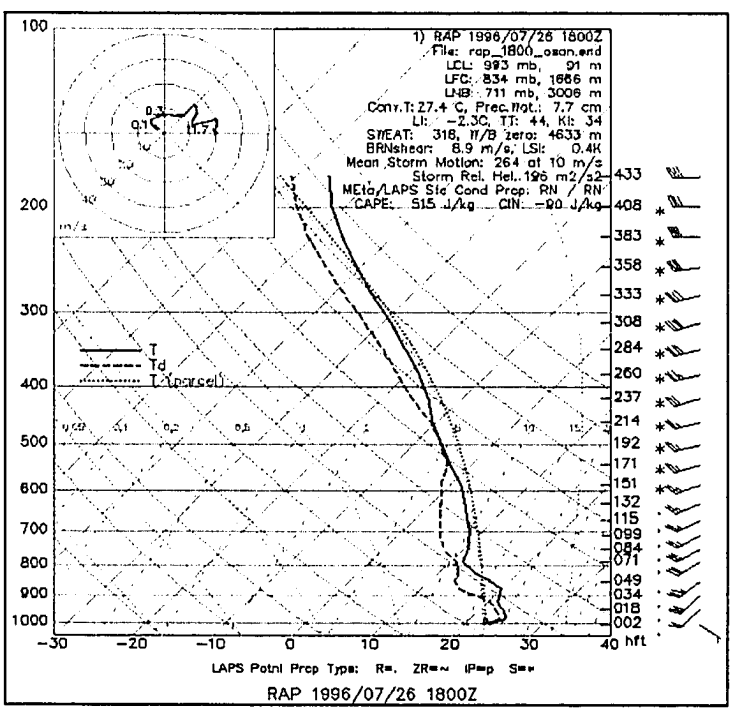

Fig. 7.24 *Skew-T plot of sounding at Osan (the filled circle in Fig. 7.20) for observation and 03RAR_1h_rap (b).*

4 m/s). One factor contributing to the spurious convection along the coastal region in the model is an *overestimate by the model of instability upstream over the sea.*

Verifying this conjecture requires a comparison of model and observed soundings at the same location. Unfortunately, the only location for doing so is at Osan, which is located southeast of the spurious convection (Fig. 7.20). Nonetheless, such a comparison in the relatively undisturbed environment should prove useful for determining whether the model is accurately representing the physics of the flow (which of course depends upon the quality of the background field provided by the operational KMA model). Figure 7.24a shows the 1800 UTC sounding from Osan, with the model counterpart from experiment 03RAR_1h_rap shown in Figure 7.24b. Interestingly, the model environment is more stable than observations, with a CAPE of 545 J/kg compared to the observed value of 1741 J/kg. Note, however, that the model profile is significantly moister between 700 and 500 mb, and that it contains a strong surface-based capping inversion.

Although the above results are not conclusive, they do suggest that the spurious convection along the western part of the KP – which was evident in all 9 and 3 km grid spacing experiments – resulted from strong frictional convergence in the presence of a conditionally unstable environment. That this convection was present in all high resolution runs suggests that the flow from the sea to the land was too large (unfortunately, no verifying observations exist), and that the environment in the vicinity of the convection may have been too unstable, though such was not the case further inland at Osan.

7.5 Structure and Effect of Increments on Experiment 03RAR_1h_rap

When using IAU, it is important to understand the structure of the increments and the manner in which they physically impact the model solution during and after their application. We again focus on experiment 03RAR_1h_rap because of its superior qualitative and quantitative forecast performance, and examine 1) the increment between the analysis and the background field before IAU (the increment introduced into radar data assimilation, hereafter "the increments") and 2) the difference between the forecast after IAU and the background before IAU (hereafter "D"). Figure 7.25 illustrates the schematic of this increment examination. We examine these quantities for seven meteorological variables: potential temperature (θ, deg K), cloud water mixing ratio (q_c, g kg^{-1}), rain water mixing ratio (q_r, g kg^{-1}), specific humidity (q_v, g kg^{-1}), and the three wind components u (m s^{-1}), v (m s^{-1}), and w (m s^{-1}). The increments and D's are examined for all IAU periods and are plotted on x-z cross sections along the line segment a_b in region A of Figure 7.20. The latter covers the location where spurious convection develops vigorously in 03RAR_1h_rap. Figures 7.26 through 7.35 depict selected cross sections of the increments and the D's.

Focusing first on the θ fields (Figs. 7.26 and 7.27), first IAU increments (Fig. 7.26a) show negative values over nearly the entire domain (i.e., colder temperatures are being assimilated into the model), with a range from -1.7 K to 0.5 K. The increment difference between the maximum and minimum, hereafter "IR", has a magnitude of 2.2 K (Fig. 7.26a). The first increments for θ were gradually introduced via IAU during 10 minutes (from 1710 UTC to 1720), producing the D shown in Fig. 7.26b, i.e., the

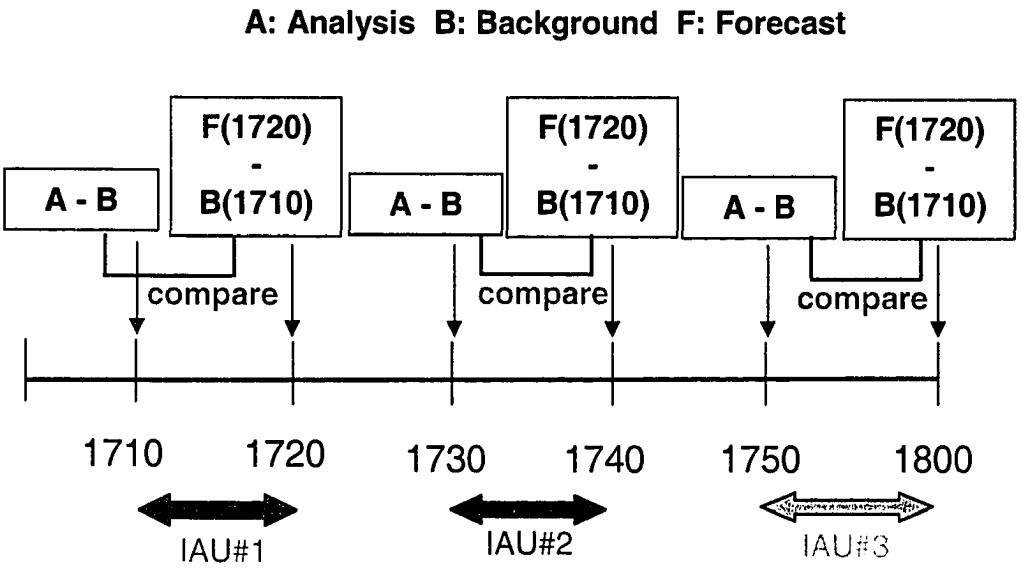

Fig. 7.25 Schematic illustration of examination of analysis increments for 03RAR_1h_rap.

difference between the forecast at the end of the IAU and the starting background. Ideally, these fields should be reasonably close, though will not be identical because they are valid at different times. Positive D's are evident in the lower parts of the domain, especially in the boxed region of Fig. 7.26b. The difference between maximum and minimum magnitude (hereafter "DR") is 8.7 K (4.6 K at maximum minus -4.1 K at minimum). In a later section, we will use the ratio of DR to IR to evaluate how much an increment affects the next forecast through the IAU period.

The positive θ produced by the model during the first IAU is driven toward negative values at the start of the second IAU (1730 UTC, Fig. 7.27a). The D after the second IAU (Fig. 7.27b) once again shows positive values, similar to the first IAU though with a somewhat reduced magnitude. The results for the third IAU are similar and not shown. In a convective system, the temperature and other fields respond mutually (Nascimento, 2002). Because the relationships among them are linked in a complex manner, we need to compare θ with other fields such as cloud water (q_c), rainfall water (q_r) and vertical velocity (w).

In Figure 7.28a, positive increments of q_c are evident over nearly the entire domain at 1710 UTC. Because these increments are the difference between the ADAS analysis and the background, positive increments denote cloud water that was provided by the analysis. In general, conventional data such as surface observations do not provide condensate fields such as cloud water (Xue et al. 1998). Therefore, the ultimate source of this positive increments of q_c is radar data. When these increments are applied over the first 10 minute IAU interval(1710 to 1720 UTC), they produce strongly positive D of q_c in the region x =45 km and z = 6 km (Fig. 7.28b). At this time, the DR of q_c, with a

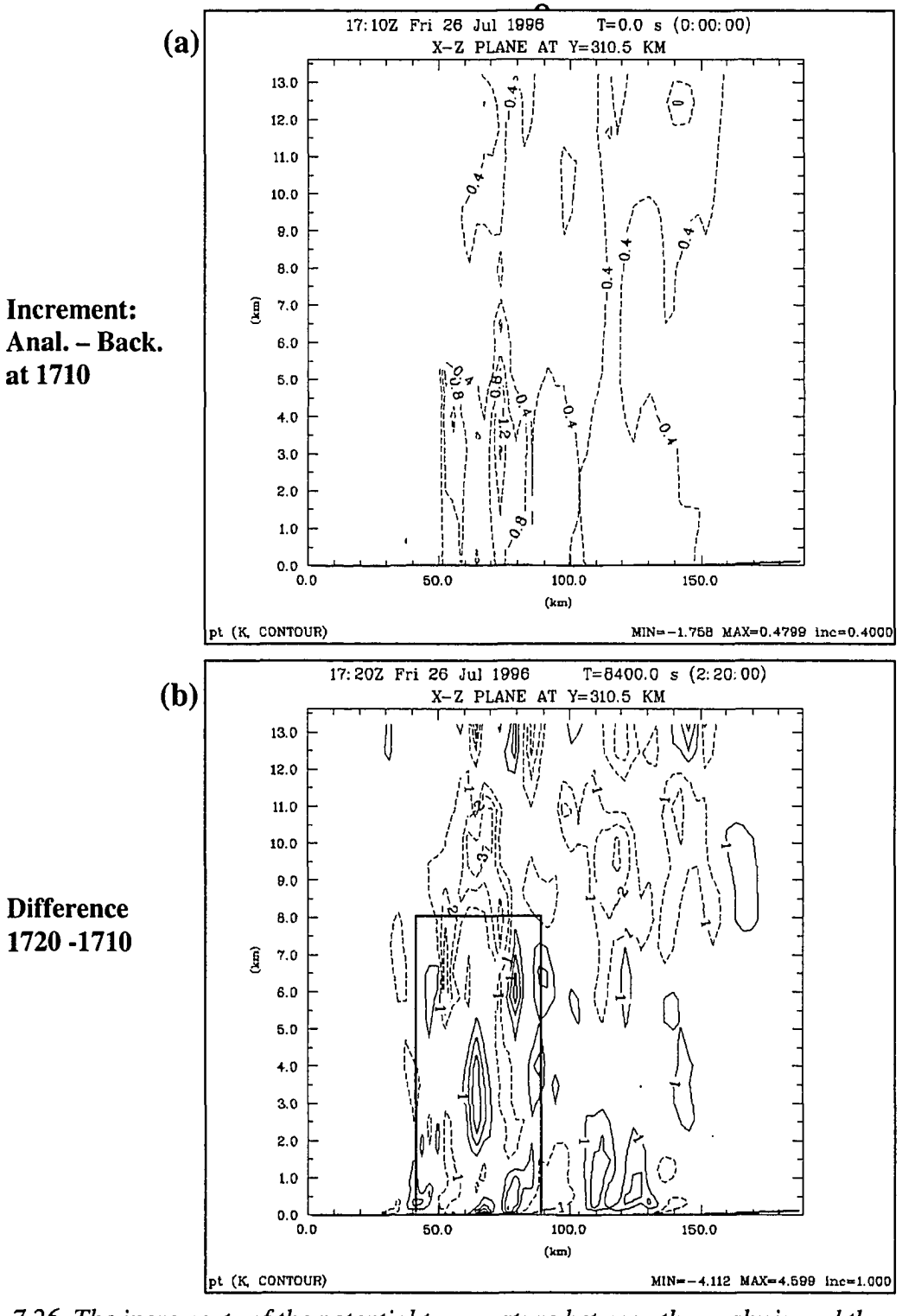

Increment: Anal. – Back. at 1710

Difference 1720 -1710

Fig. 7.26 The increments of the potential temperature between the analysis and the background (analysis –background) at 1710 UTC (a) and the difference of the potential temperature between the forecast at 1720 UTC and the analysis at 1710 UTC (b). The box in (b) will be used for zooming work.

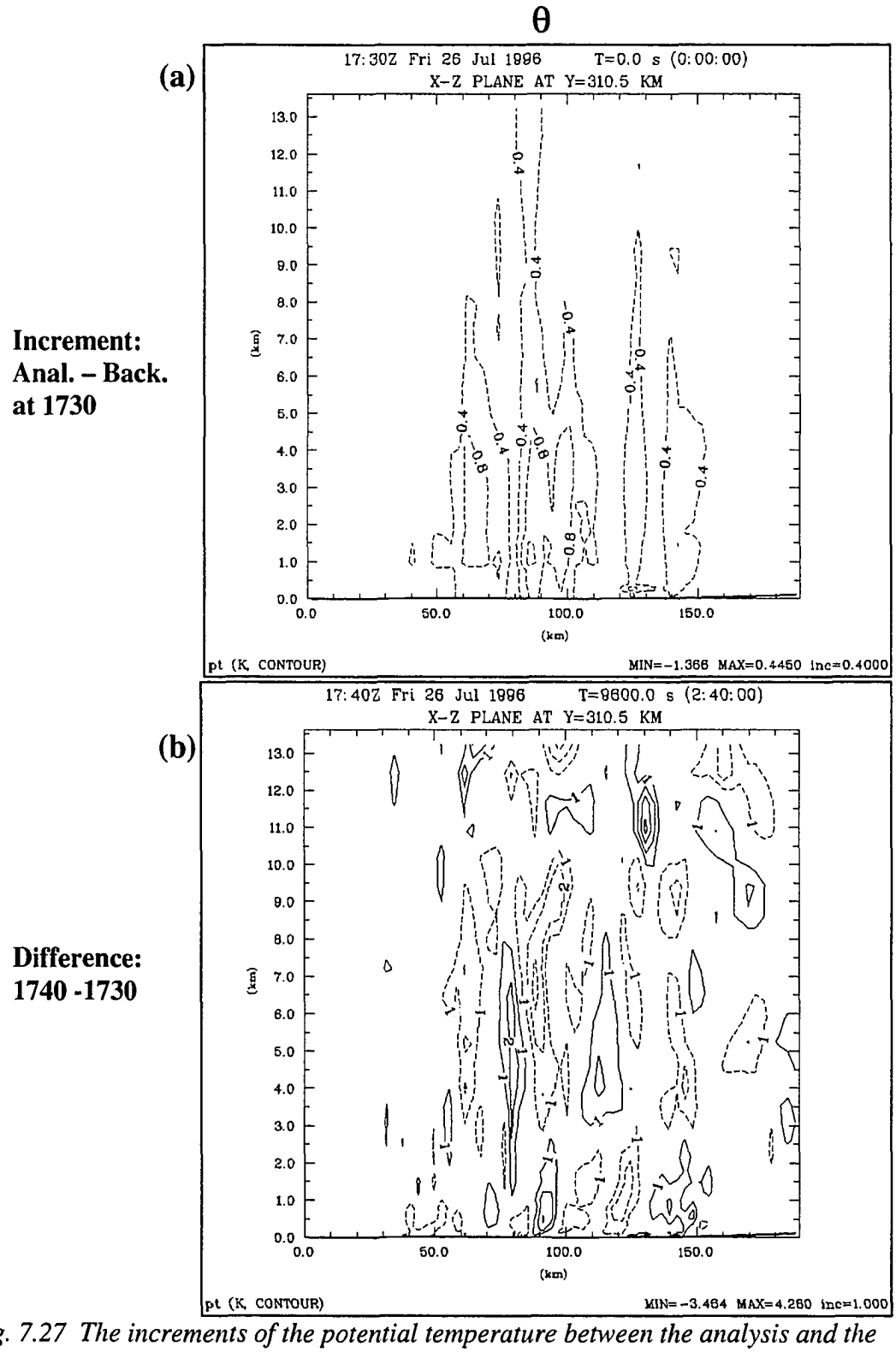

Increment: Anal. – Back. at 1730

Difference: 1740 -1730

Fig. 7.27 The increments of the potential temperature between the analysis and the background (analysis –background) at 1730 UTC (a) and the difference of potential temperature between the forecast at 1740 UTC and the background at 1730 UTC (b).

magnitude of 3.40 g kg^{-1} (2.11 g kg^{-1} at maximum minus -1.29 g kg^{-1} at minimum), is higher than the IR of q_c, with a magnitude of 2.94 g kg^{-1} (2.19 g kg^{-1} at maximum minus -0.75 g kg^{-1} at minimum). This suggests that the increments amplified te q_c during the IAU period. For the second (Fig. 7.29a and b) and third periods (not shown), the results are similar. The increments of q_v (not shown) also show positive values in the lower levels. The other analysis values for the q_v are similar to those of q_c.

Next, we consider rainwater (q_r). As shown in Fig. 7.30a, the increments of q_r show negative values at 1710 UTC, meaning that the analysis does not contain as much rain water as present in the background field (indicating that the model overforecasted convection, as indicated earlier). Although the increments are entirely negative, relatively large amount of q_r are produced at x = 65 km and z = 4 km through the first IAU period from 1710 to 1720 UTC (Fig. 7.30b). Despite the reduction in rainfall from IAU, the model quickly tends to re-generate convection in the affected regions. The increments of q_r are again adjusted negatively at the start of second IAU period (1730 UTC, Fig. 7.31a), and this increment is introduced into the third cycle. The net result is a reduction in precipitation in the region of spurious convection, as hoped for, though IAU alone, as currently applied, does only a marginal job. The reasons for this behavior are discussed below.

Figure 7.32a shows the increments of w at 1710 UTC. The value of IR is relatively small at 9.7 m s^{-1}. Through the first IAU period using these increments, w increases in absolute magnitude, producing clear updraft and downdraft regions (Fig. 7.32b). Relatively strong updrafts are evident at x = 47 km, z = 5 km, at x = 65 km, z = 3.5 km, and at x = 75 km, z = 6 km. These regions will be evaluated with other variables

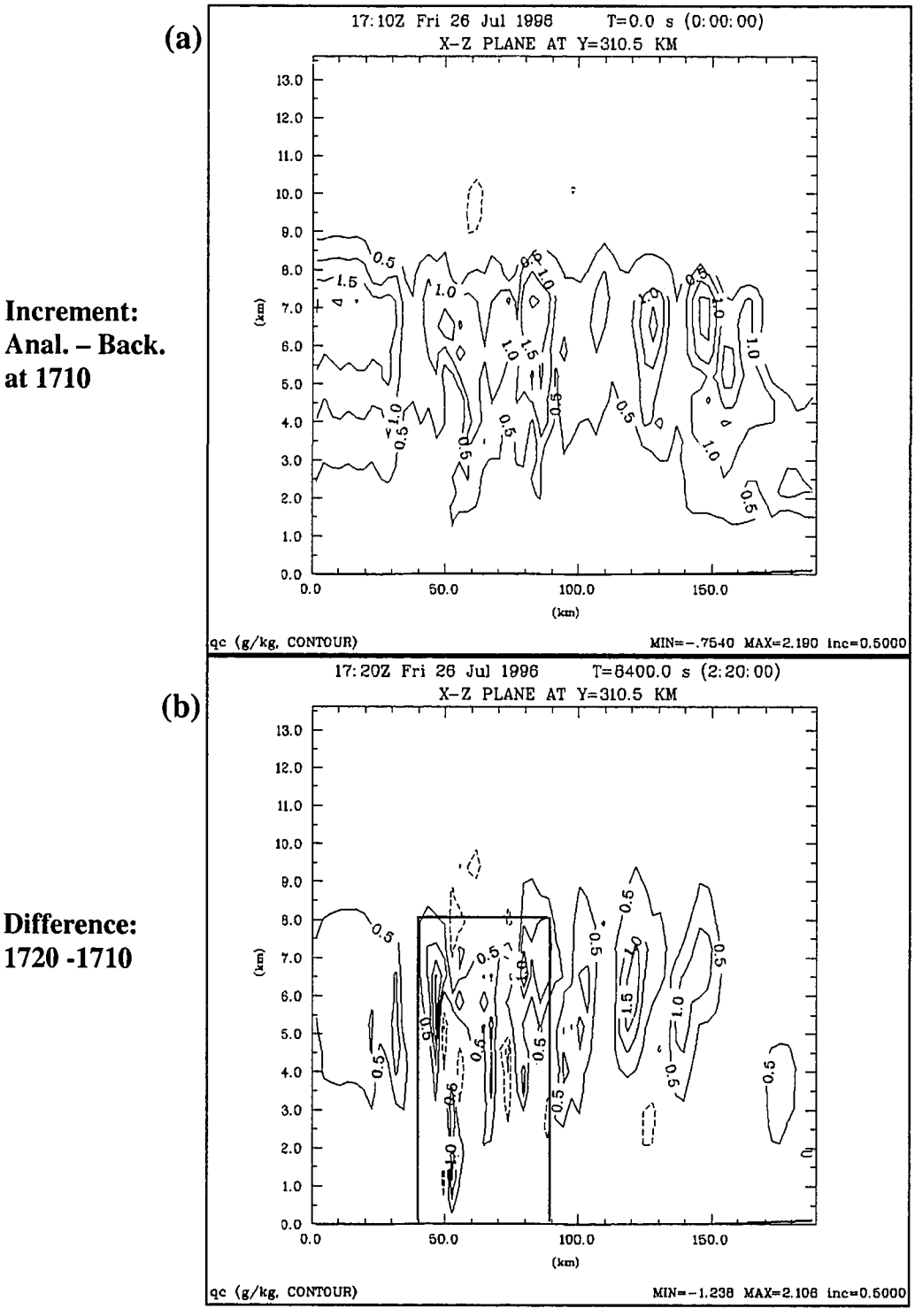

Fig. 7.28 The increments of the qc between the analysis and the background (analysis – background) at 1710 UTC (a) and the difference of the qc between the forecast at 1720 UTC and the background at 1710 UTC (b). The box in (b) will be used for zooming work.

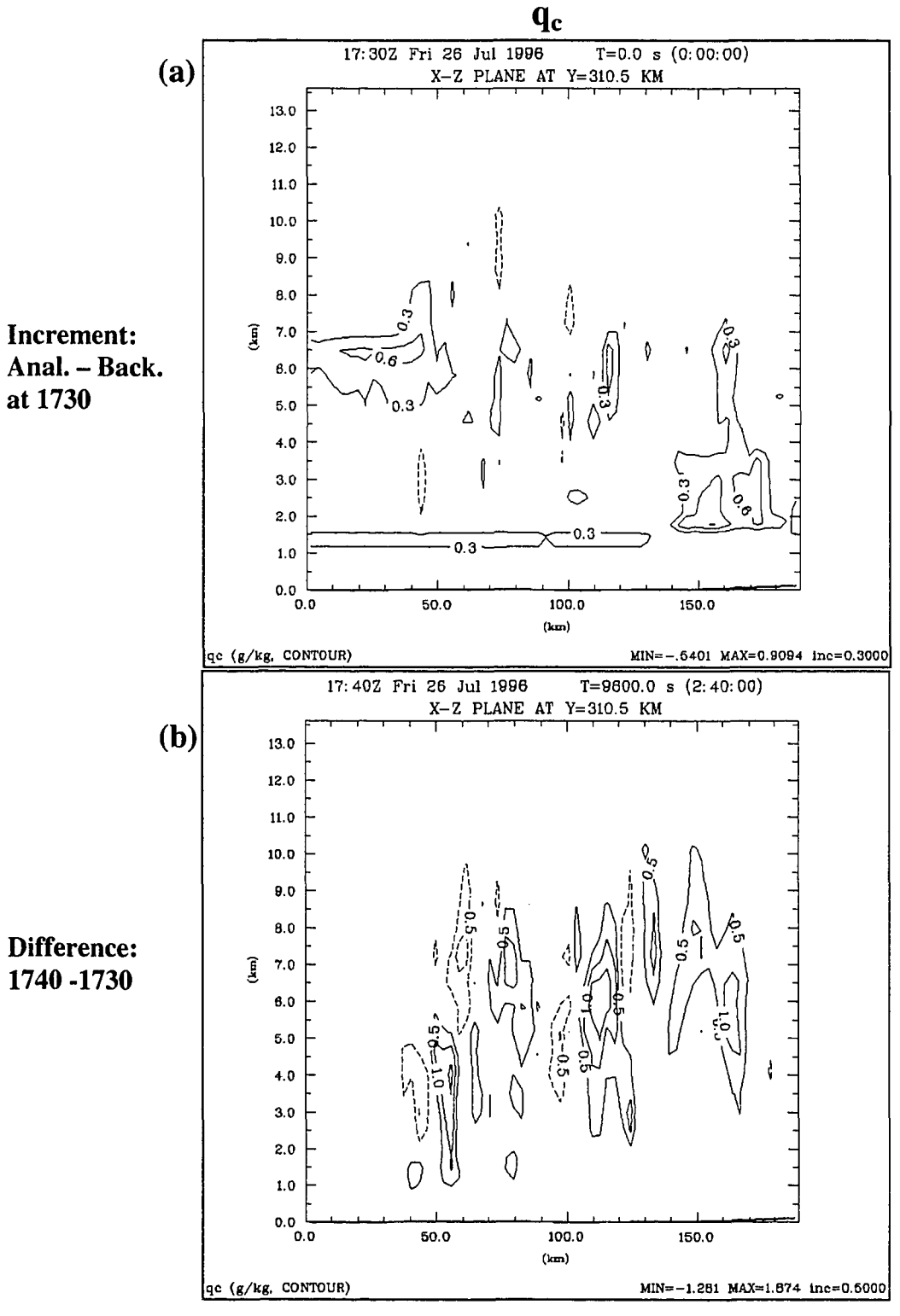

Fig. 7.29 The increments of the qc between the analysis and the background (analysis – background) at 1730 UTC (a) and the difference of the qc between the forecast at 1740 UTC and the background at 1730 UTC (b).

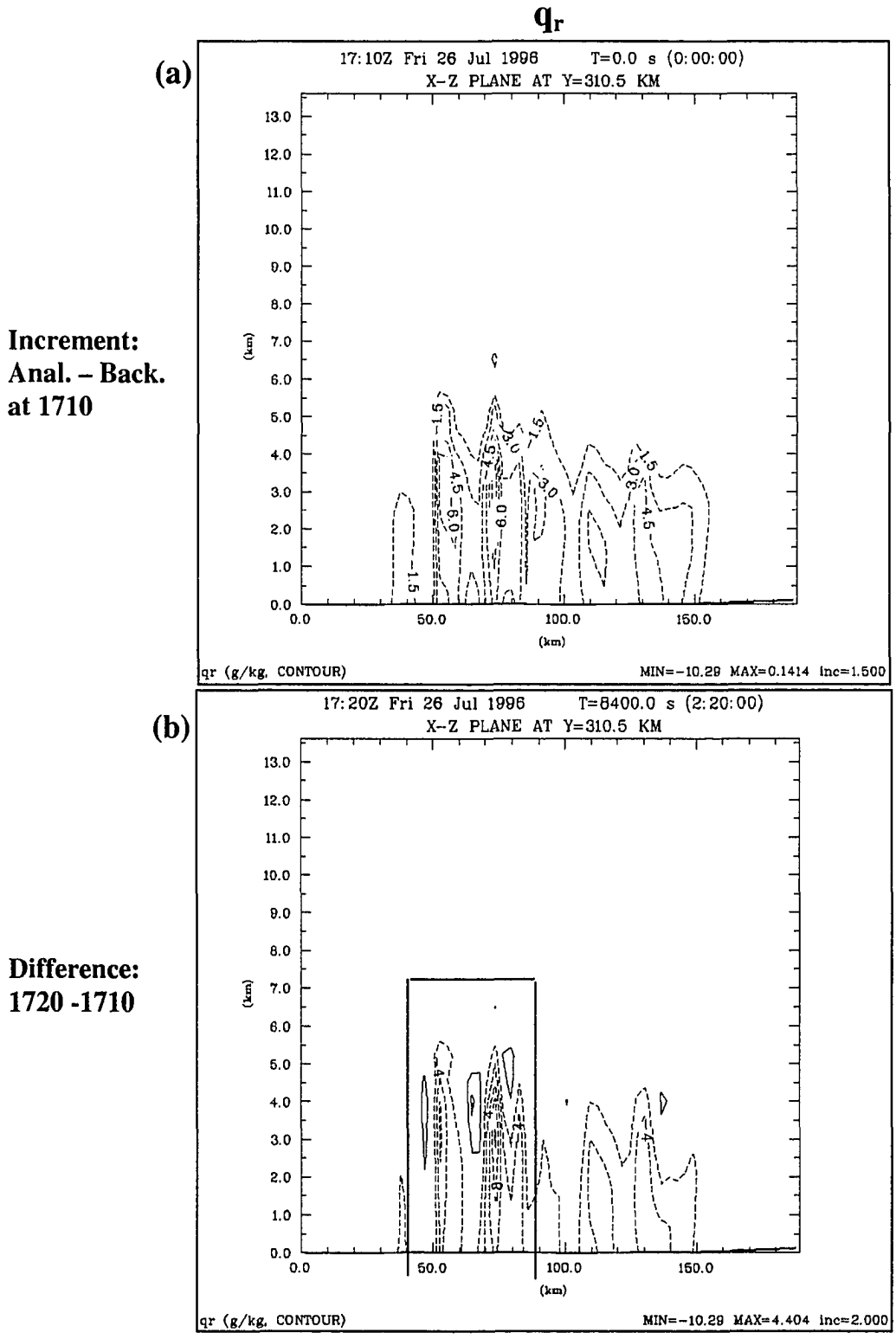

Fig. 7.30 The increments of the qr between the analysis and the background (analysis – background) at 1710 UTC (a) and the difference of the qr between the forecast at 1720 UTC and the background at 1710 UTC (b). The box in (b) will be used for zooming work.

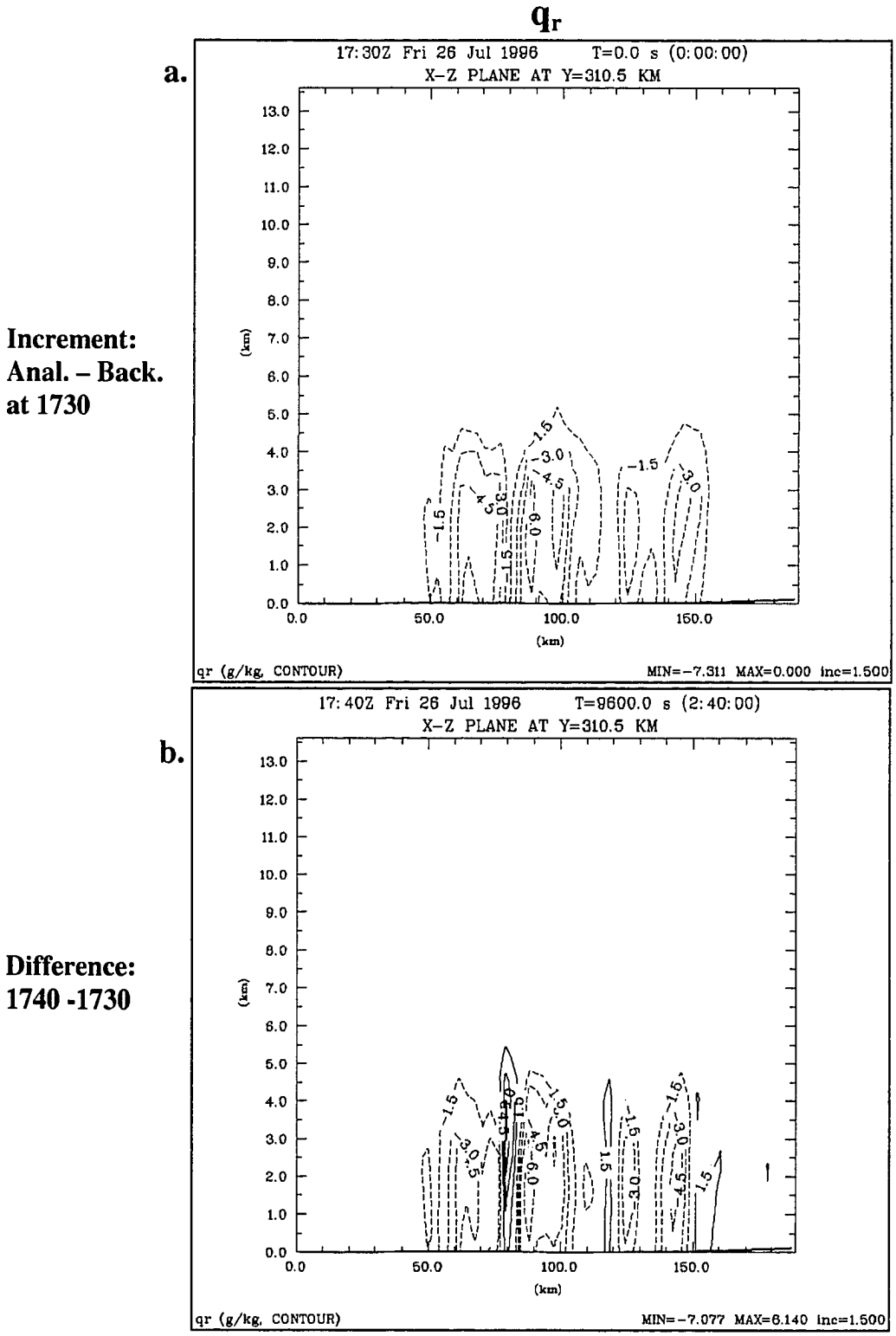

Fig. 7.31 The increments of the qr between the analysis and the background (analysis – background) at 1730 UTC (a) and the difference of the qr between the forecast at 1740 UTC and the background at 1730 UTC (b).

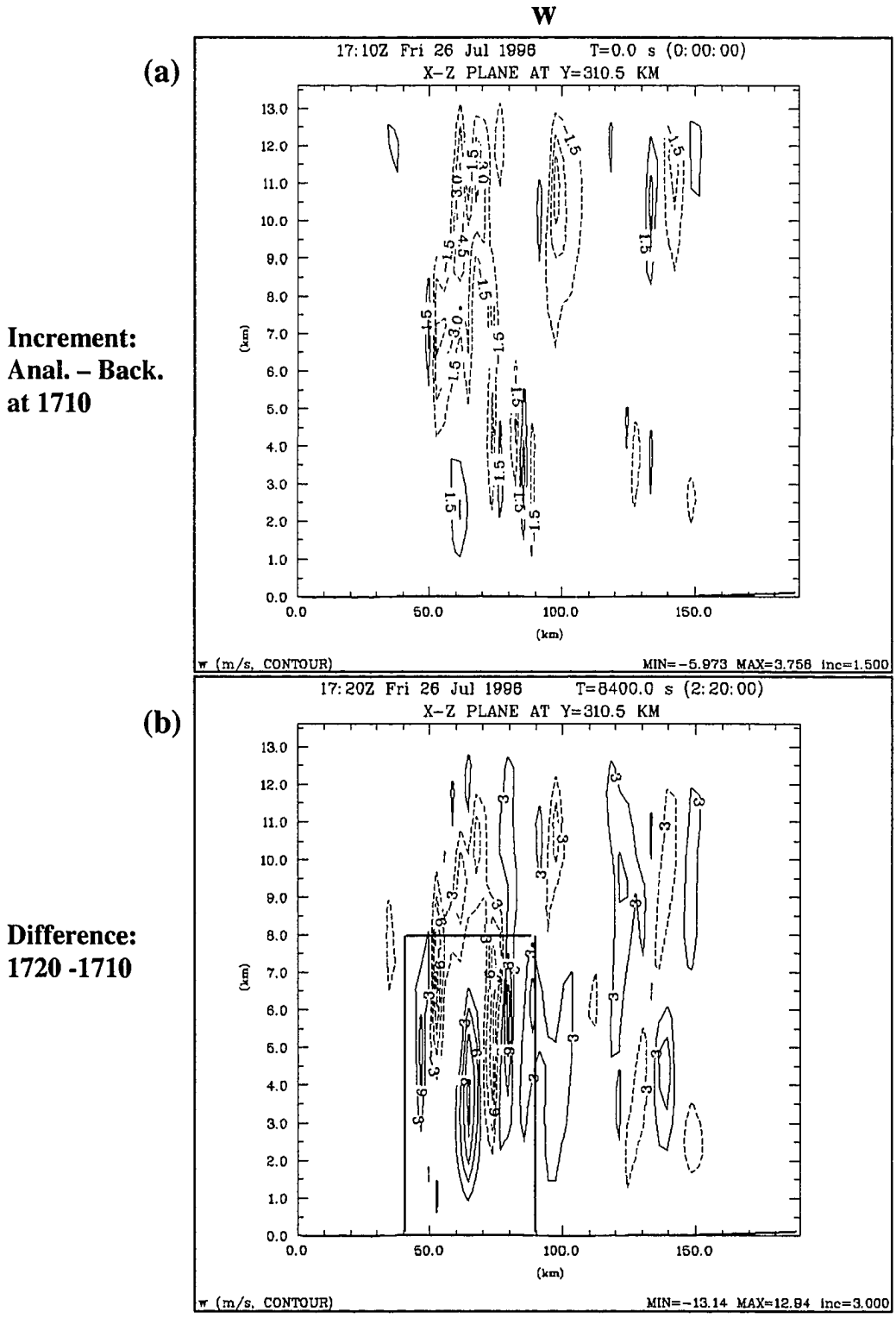

Fig. 7.32 The increments of the w between the analysis and the background (analysis – background) at 1710 UTC (a) and the difference of the w between the forecast at 1720 UTC and the background at 1710 UTC (b). The box in (b) will be used for zooming work.

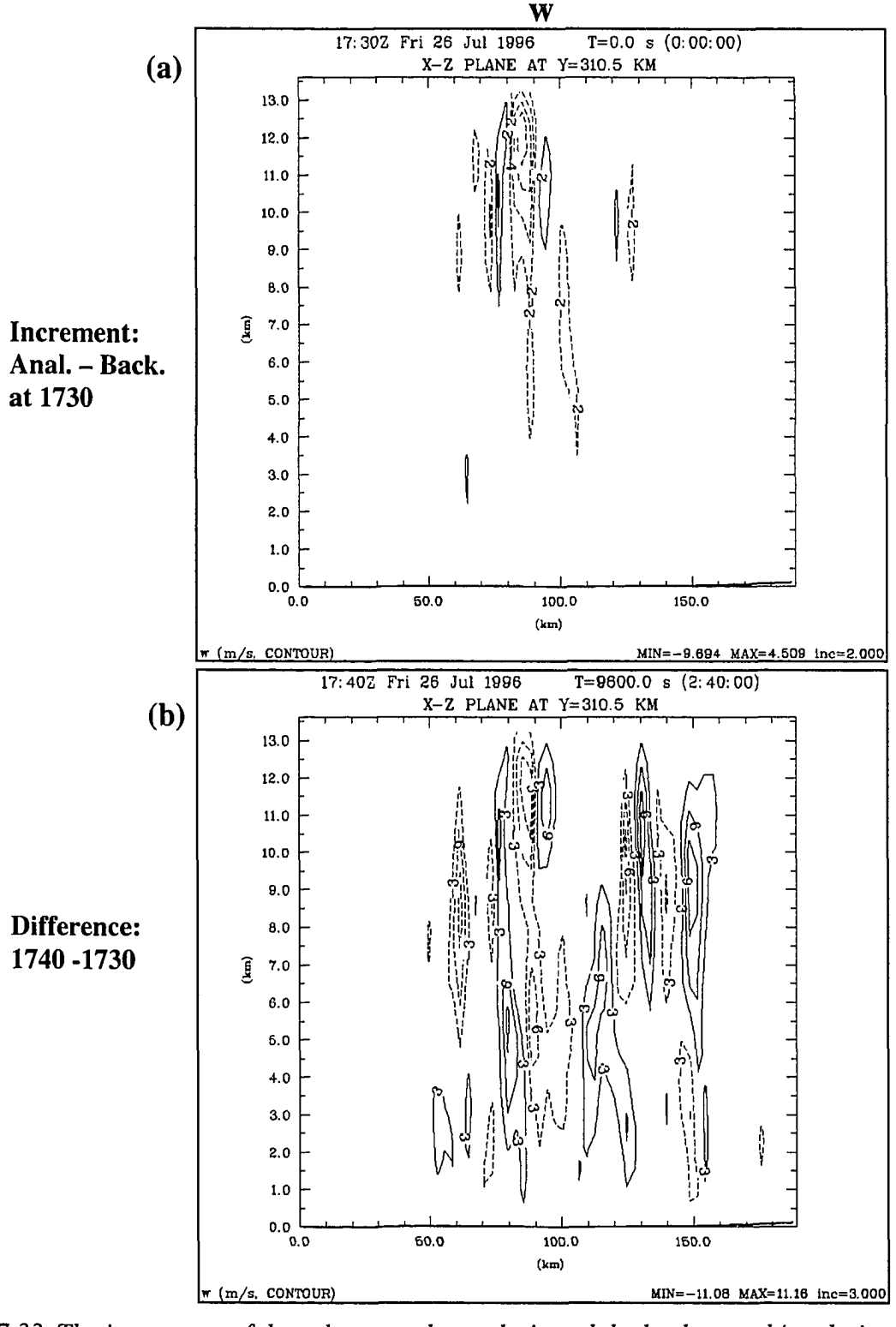

Fig. 7.33 The increments of the w between the analysis and the background (analysis – background) at 1730 UTC (a) and the difference of the w between the forecast at 1740 UTC and the background at 1730 UTC (b).

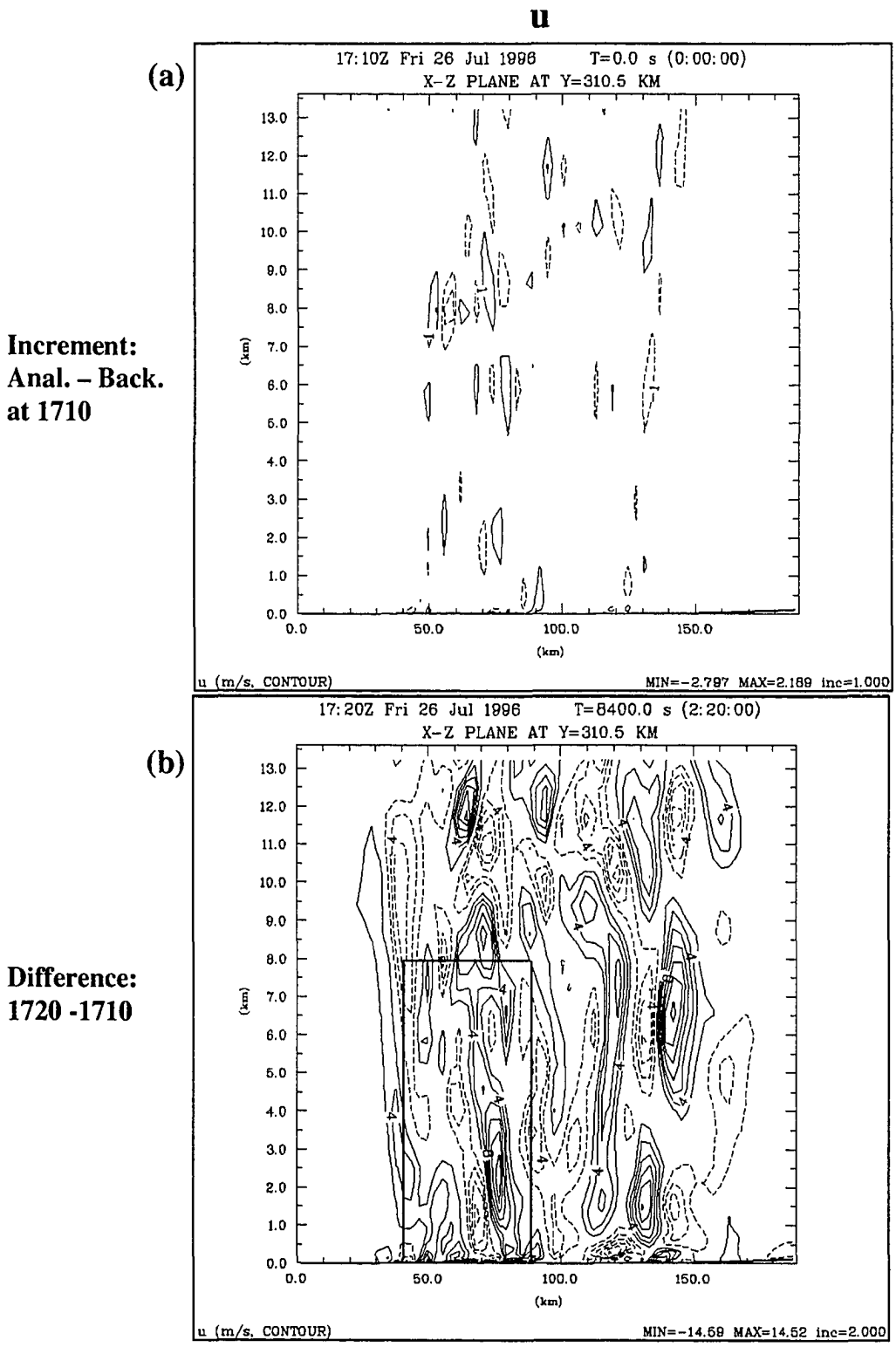

Fig. 7.34 The increments of the u between the analysis and the background (analysis – background) at 1710 UTC (a) and the difference of the u between the forecast at 1720 UTC and the background at 1710 UTC (b). The box in (b) will be used for zooming work.

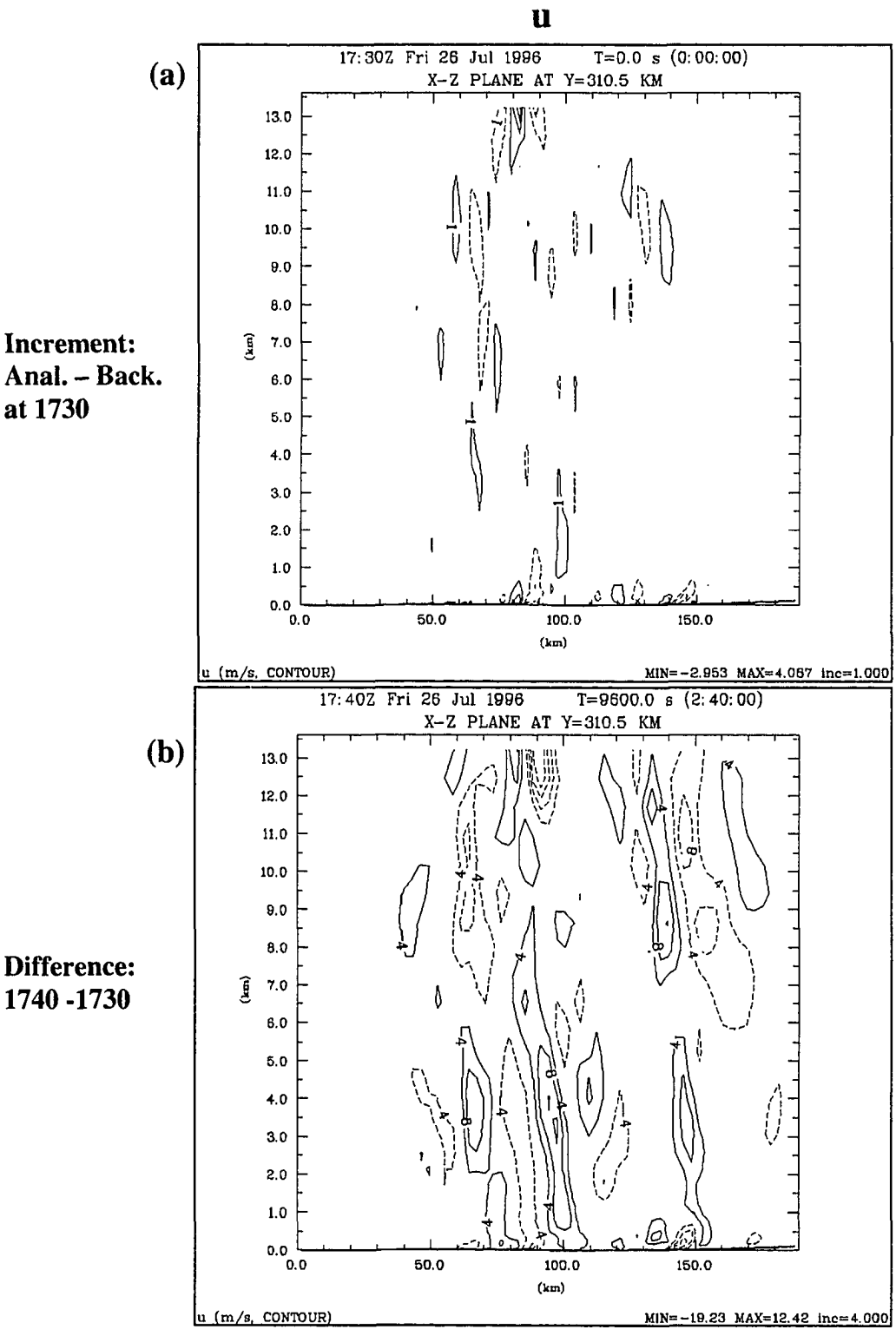

Fig. 7.35 The increments of the u between the analysis and the background (analysis – background) at 1730 UTC (a) and the difference of u between the forecast at 1740 UTC and the background at 1730 UTC (b).

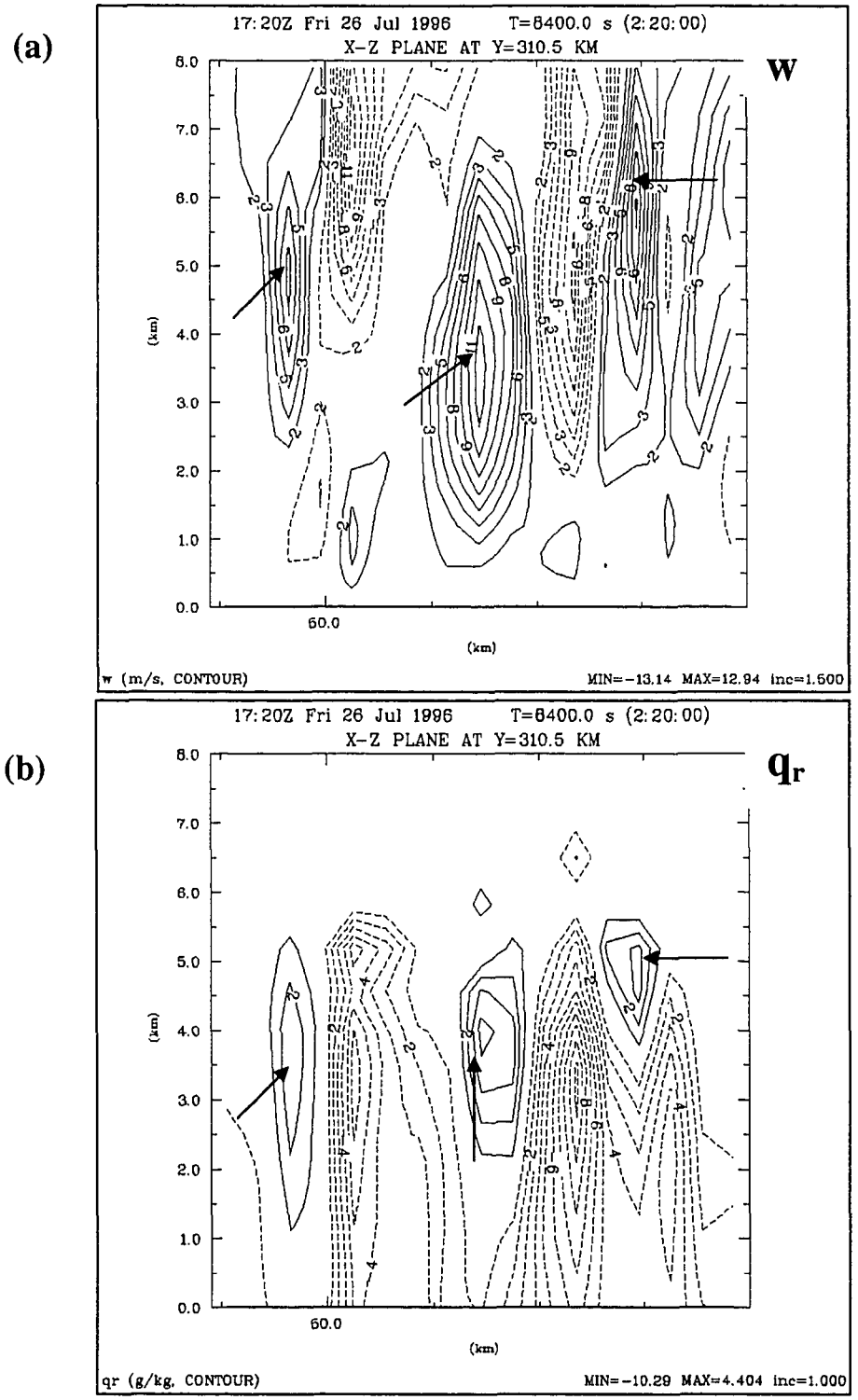

Fig. 7.36 The difference of (a) w, (b) qr, (c) pt, (d) qc, and (e) u between the forecast at 1720 UTC and the background at 1710 UTC.

(c)

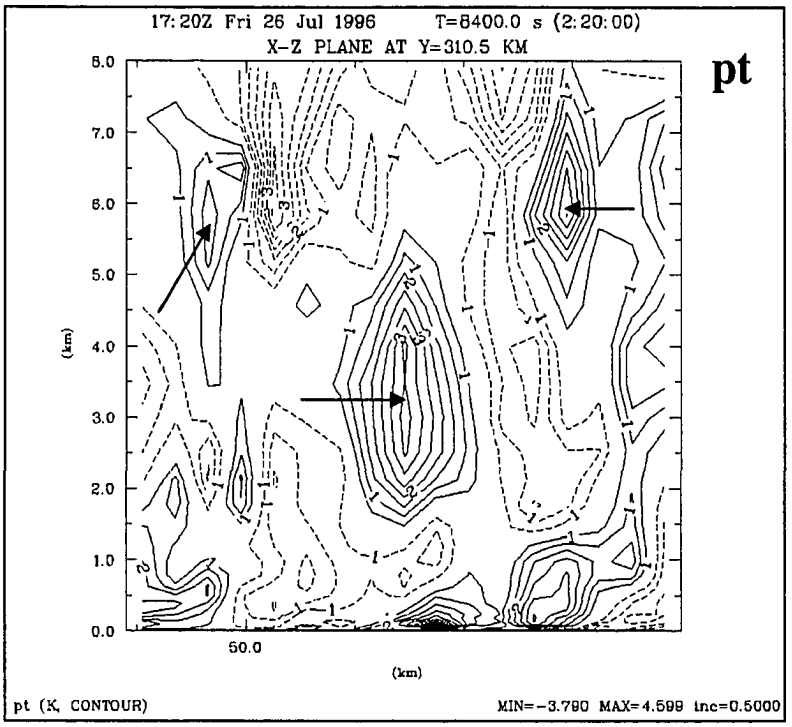

(d)

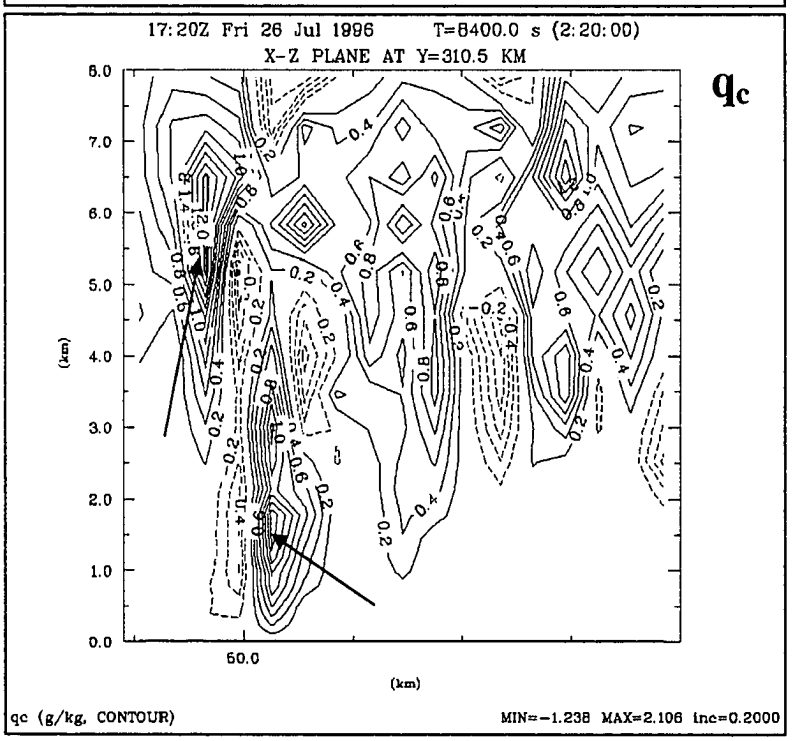

Fig. 7.36 (Continued)

(e)

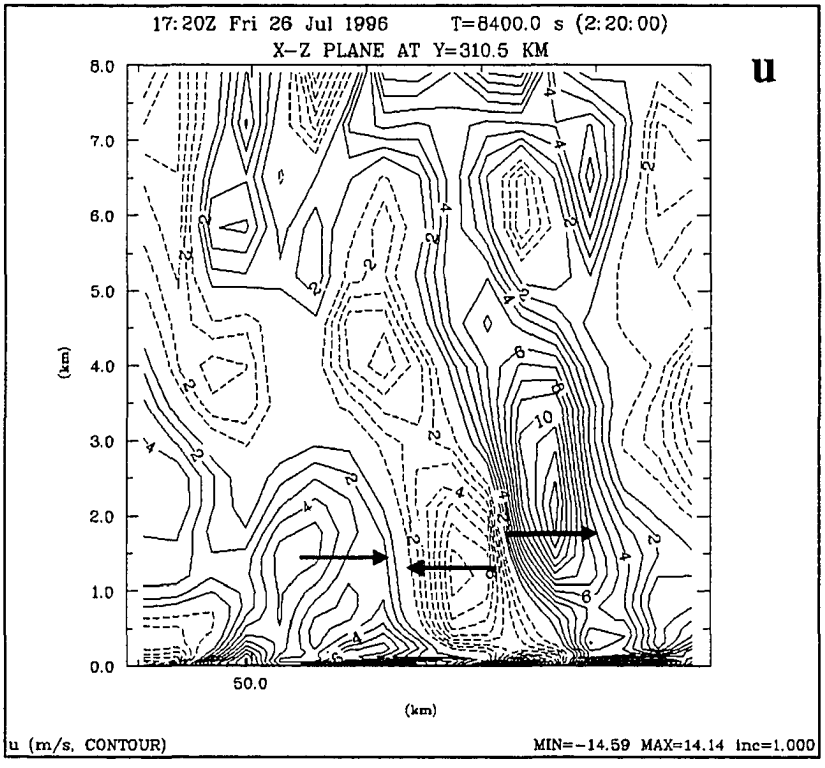

Fig. 7.36 (Continued)

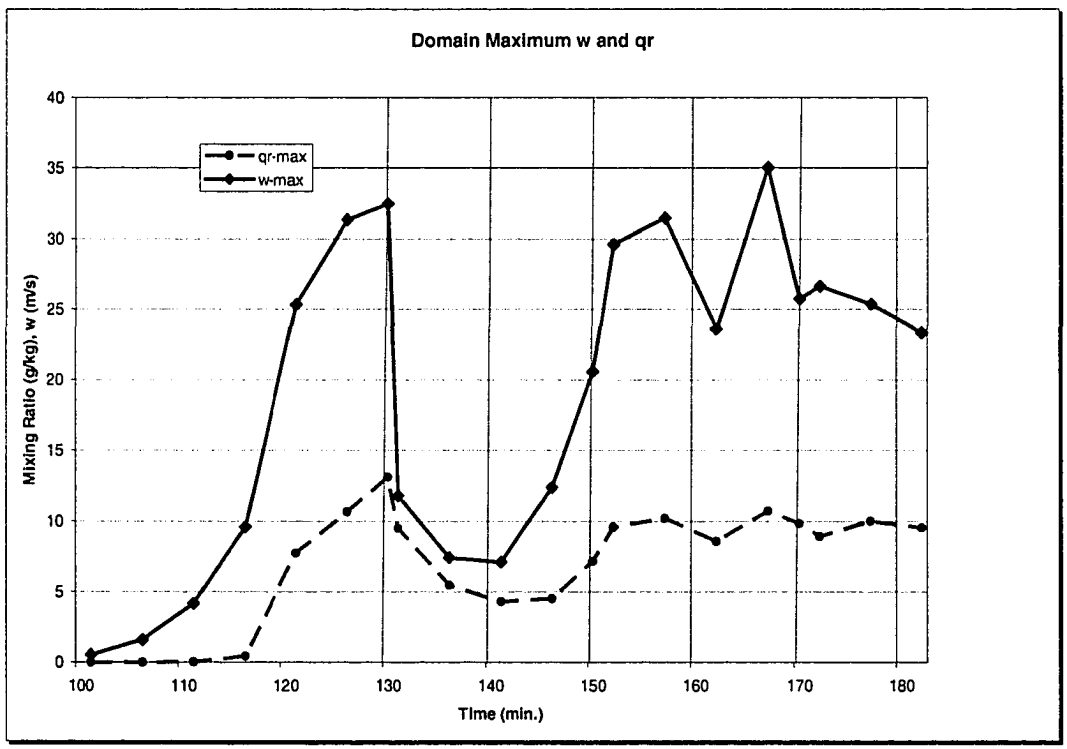

Fig. 7.37 Time evolution of the domain maximum qr and w in the 03RAR_1h_rap. Each data assimilation period indicates the periods of 130 min. (1710 UTC) to 140 min. (1720 UTC), 150 min. (1730 UTC) to 160 min. (1740 UTC), and 170 min. (1750 UTC) to 180 min., (1800 UTC) indicate the first, second, and third data assimilation period, respectively. Two different units of Y axis are used in this figure: 'g/kg' for qr and 'm/s' for w.

later. The updraft and downdraft in this DR are distributed in narrow bands such that they can produce rain in a very localized manner.

The increment of w at the start of second IAU period (1730 UTC) is shown in Fig. 7.33a and is distributed through higher levels. When this increment is introduced into the next IAU cycle, it produces a large DR. For future comparison with the other variables, we especially note the maximum updraft region at x = 80 km and z = 5.5 km during the second IAU period from 1730 to 1740 UTC (Fig. 7.33b).

The horizontal wind fields (u and v) appear quite erratic. The DR's during both the first and second periods (Figs. 7.34b and 7.35b) show complicated shapes although the increments are not variable (simple shape) and are small in magnitude (Figs. 7.34b and 7.35b). The v fields are similar to the u fields (not shown). We find one consistent feature among variables, namely, a convergence region at x = 75 km and z = 4 km during the second IAU period (1740 to 1750 UTC, Fig. 7.35b). Such a feature at low levels should be accompanied by upward motion at higher levels. The w field (Fig. 7.33b) shows upward motion associated with this convergence, and it agrees quite well with pt (Fig. 7.27b), q_r (Fig. 7.31b) and q_c (Fig. 7.29b), although q_c is phase shifted to the west (x = 55 km, while the others are near x = 75 km). This phase difference is not surprising, as the cloud water condenses, produces rain, then falls downward while being advected horizontally by the local winds. (This phase shift will be discussed in more detail below).

Diabatic initialization (i.e., initialization which includes the adjustment of thermal fields) is necessary for producing spatially and temporally accurate precipitation forecasts (Zhang 1999). From this point of view, we wish to investigate how the increments for each variable behave and adjust interactively during the IAU. For example, negative

buoyancy produced by initialized cloud water and rain water in the precipitation region can be compensated by upward motion that develops convection. Therefore, we next examine the mutual interactions among the thermal fields.

To provide a more detailed examination of the mutual behavior among model variables, we show in Figure 7.36 zoomed-in sections of the differences between the forecast at 1720 UTC and the background at 1710 UTC of pt (Fig. 7.26b), qc (Fig.7.28b), qr (Fig. 7.30b), w (Fig. 7.32b), and u (Fig.7.34b. Comparing w, q_r, and pt (Fig. 7.36a, b, and c, respectively), there exists significant consistency among these fields (see maxima indicated by arrows). The relationship between w and q_r is more highly correlated than the relationship between pt and other variables. The domain-maximum q_r and w from 1640 UTC to 1805UTC, including the three data assimilation periods, is shown in Fig. 7.37. The two fields have a very similar pattern and they also clearly display the impact of data assimilation. Why do the above three fields produced by the increments have the highest consistency?

This behavior can be explained by a positive feedback mechanism of convective systems (Bluestein 1993). First, heating ($\Delta\theta > 0$) exists at upper levels, and upward motion ($w > 0$) accompanied by convergence at low levels is produced by it. This upward motion draws moist air from low levels and the moisture continually condenses ($\Delta q_r > 0$). This condensation produces latent heating, which functions as a temperature source at upper levels. The variables mentioned above match well, keeping this positive feedback mechanism operating.

The region of maximum q_c (Fig. 7.36d) is located in the western and upper parts of the domain. It shows a phase shift, in contrast to the above three variables. The

maximum of this field (located at x = 47 km and z = 5.8 km) and the w field (7.36a) show a region of strong updrafts located at z = 4.7 km height. This cloud water rises in the upward motion, condenses, and forms rain water, thereby helping to develop convection despite the phase shift. According to this process, the rain water maximum in the center of the domain (Fig. 7.36b) was probably produced by two mechanisms: one is directly by the upward motion, the other is from cloud water, although it is not located near the rain water region.

Upward motion is usually accompanied by convergence at another level. However, the u field does not show such consistency. As shown in Fig. 7.36e, the u field does not agree with the other fields except in one convergence region and in one divergence region (see the arrows in Fig. 7.36e). The problem is worse at higher levels. Although it is difficult to evaluate the increment effect exactly, the wind field looks worse than the others. As mentioned earlier, we can examine DR/IR. If this ratio is greater than 1, the forecast varies more than the increments (and vice versa). In other words, a larger value of DR/IR is more sensitive and can make the error larger. Figure 7.38a shows the DR/IR ratio for seven variables. High values for u and v are seen. The ratio for the v field during the third IAU period is greater than 10. This indicates that small incorrect increments for the horizontal winds can result in large errors for the forecast.

A previous result (section 7.4.2) showed that the effects of radar data assimilation are decreasing as the number of assimilation cycles is increasing. To verify this result, we examine the ratio of DR's for the second and third IAU periods to the range value (maximum minus minimum) of the difference between the forecast after the IAU and the

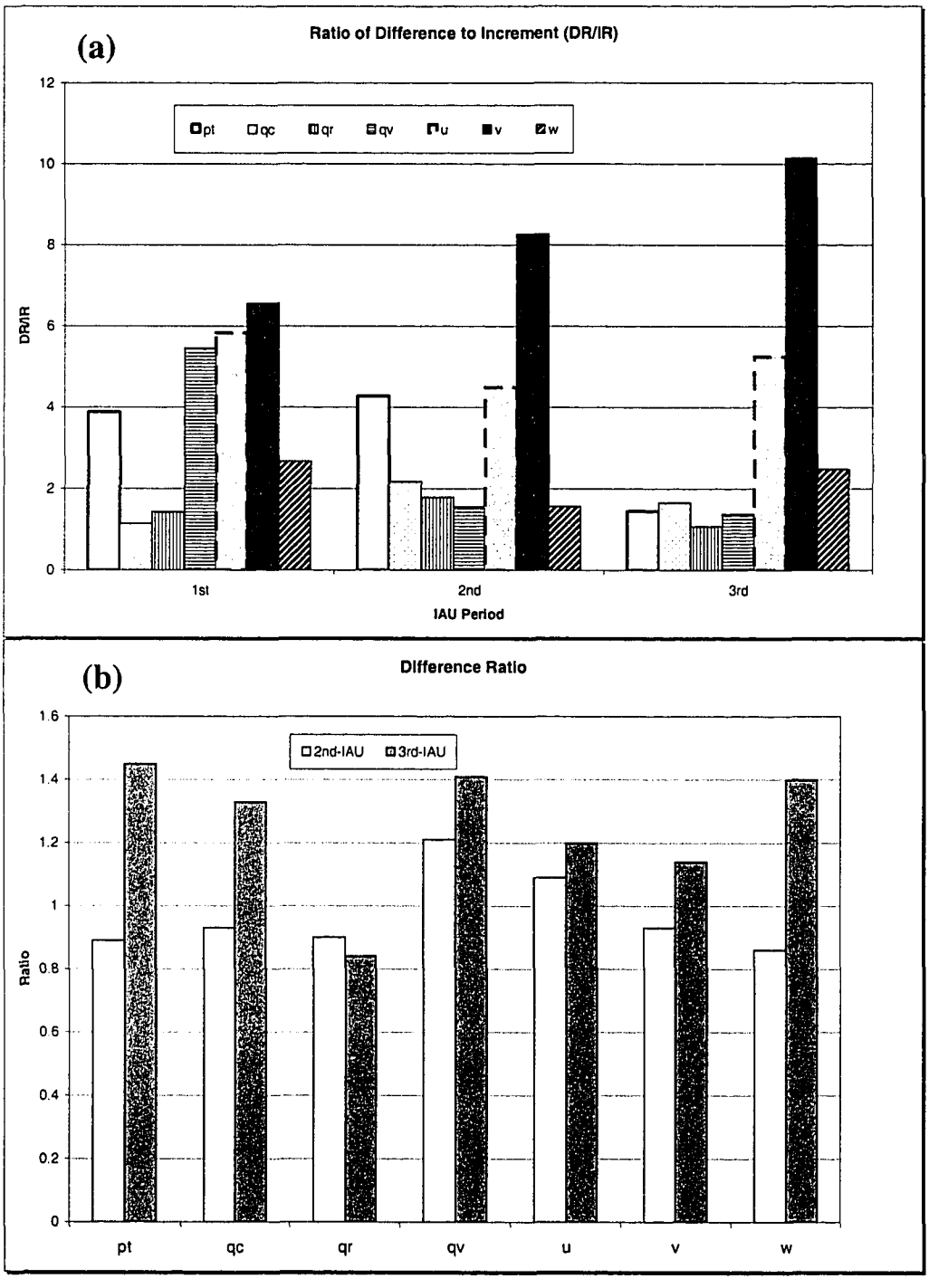

Fig. 7.38 (a) The ratio of 'the range value (max. minus min.) of the difference between forecast after IAU and the background before IAU (DR)' to 'the range value (max. minus min.) of the increment between analysis and background(IR)' for each variable. (b) The ratio of 'the range value (max. minus min.) of the difference between the forecast after IAU and the background before IAU for 2nd and 3rd IAU periods' to 'the range value (max. minus min.) of the difference between the forecast after IAU and the background before IAU for 1st IAU period'.

background before the IAU for first IAU period. For example, if the DR at the second IAU period (DR2) is larger than the DR at first IAU period (DR1), the ratio DR2/DR1 > 1, meaning that the variation of a variable during the second IAU period is larger than that during the first IAU period. Figure 7.38b shows these ratios. In the second IAU period, the ratio for almost all variables are less than one, while the ratio increases for the third IAU period. Considering this observation and the previous results of section 7.4.2, the number of assimilation cycles should be carefully considered. More is not always better.

In summary, pt, q_r, q_c, q_v, and w incorporate well into the model forecast when employing radar data assimilation using increments. They contribute to the positive feedback mechanism of the convective system. However, the horizontal wind fields obtained from only radar data have problems to be employed enough in the radar data assimilation process since the radial velocity has a serious limitation not to produce full vector field of winds. We also note that rain field is compact while the other fields such as θ and wind fields have global structure. This different structure between rain field and the other fields is because rain field directly comes from radar data while the other fields pass through ADAS scheme.

7.6 Summary

Quantitative verifications were conducted to confirm if the radar data assimilation has an advantage compared to the other experiments. For the quantitative verification, we used conventional verification scores such as B, TS, and ETS. The estimated

precipitation produced by RV1.0 was compared to predicted precipitation for computing verification scores. Using the observed precipitation produced by RV1.0, we found a blockage problem due to terrain effects. We therefore discarded the erroneous area produced by this blockage problem in the verification domain.

We computed B, TS, and ETS by various thresholds in order to determine whether radar data assimilation can positively affect the forecast and to find if each experiment has specific features. The major results are as follows:

1. The radar data assimilation shows clear improvement for precipitation forecast quantitatively.
2. The radar data assimilation improves the forecasted rainfall location more than the forecasted rainfall amount, as shown from the B and the TS.
3. The radial velocity data can positively affect the forecast, though the effect is not great, especially at early forecast times.
4. The radar data assimilation appears to have a time limitation of approximately 3 hours in its positive impact on the forecast.
5. The 03RAR_1t experiment, using only a single insertion radar data, is the worst one of the different radar data assimilation strategies.
6. A data assimilation window length of 20 minutes (03RAR_cent20) is slightly more appropriate than 5 minutes and 10 minutes (5 minutes is the worst).
7. *A more continuous data assimilation strategy (03RAR_1h_rap) shows the best results, and presents a forecasting time limitation of about 3 hours.*

8. The radar data assimilation can be sensitive to a change in the position of the data assimilation window or the selection of a particular volume scan, as shown from 03RAR_initrad and 03RAR_cent10.
9. The radar data assimilation using radar data at the initial time (03RAR_initrad) is slightly better than 03RAR.

Through the evaluation of the verification scores, we strongly confirmed that the 03RAR_1h_rap is the best method. We attempted to quantify the effect of the data assimilation upon the corresponding prediction in the results of 03RAR_1h_rap. The RD (forecasted reflectivity minus observed reflectivity) and analysis error (observation minus analysis) for wind fields and temperature at 20 stations were employed for quantification. We compared the RD and the analysis error before the IAU with those after the IAU. From this, we confirmed that the *radar data assimilation effect can last for 3 or 4 hours.* In addition, we found that the effect of radar data assimilation decreased as the number of assimilation cycles increased. The last important finding was a basic limitation in introducing horizontal wind from radial velocities. Thus, the gradual wind adjustment from the radar data assimilation was probably not enough (or appropriate) when compared with the adjustment of other variables such as temperature.

We also attempted to know the effects of the increments used in the IAU. The increments for seven variables such as pt, q_c, q_r, q_v, u, v, and w, were examined. Consequently, we found that the increments of thermodynamic variables and vertical wind are introduced well into the IAU process and that the increments of these variables contribute to the positive feedback mechanism in a storm. We also confirmed that the increment of horizontal wind fields has limited utility in the radar data assimilation

process since the source of the horizontal wind fields is the radial velocity from radar data.

Chapter 8.

Summary, Conclusions, and Future Work

8.1 Summary

In order to improve the initial conditions for numerical models, considerable attention has been given to improving data assimilation techniques and using new sources of remotely sensed data. One of the most powerful tools for remote sensing of the atmosphere at fine scales is Doppler radar. Despite the importance of radar data for use in warning and numerical simulations, little effort has been made to include analyzed radar data in the data assimilation cycle of the operational numerical weather prediction models of Korea. *The first step in bringing Korean radar data into a numerical model for the forecasting of heavy rainfall has been undertaken in this study. Our purpose is to assess the impact of NEXRAD Doppler radar data in the numerical forecast of a highly convective, localized heavy rainfall event in Korea, the so-called "Chorwon-Yonchon event", and to evaluate a relatively new data assimilation technique for small scale flows, increment analysis updating (IAU).* We hypothesize that the assimilation of WSR-88D data into a model operated with relatively fine horizontal grid spacing (3 km) will improve the prediction of the convective event noted above. In this study the complete Advanced Regional Prediction System (ARPS) developed by the Center for Analysis and Prediction of Storms at the University of Oklahoma, in combination with NEXRAD Level II data gathered by the US Air Force in Pyungtaek, Korea, is applied to the Chorwon-Yonchon heavy rainfall event.

The Chorwon-Yonchon heavy rainfall event occurred over the middle part of the Korean peninsula during 26-28 July 1996, with total rainfall accumulations exceeding 650 mm in many regions. Four main synoptic features contributed to this event: (1) the presence of the northwest boundary of a stationary north Pacific front, located in the central part of the Korean peninsula, (2) the presence of a boundary between two air masses, the Okhotsk maritime Pacific and north Pacific maritime tropical masses, (3) the presence of a continuous strong moisture flux into the middle part of the Korean peninsula, and (4) the passage of two upper-level short-wave troughs over the Korean peninsula.

The heavy rainfall was not directly associated with the Changma (East Asian summer monsoon) front and was highly localized, with strong storms developing locally and moving very little. Orographic effects can be inferred as one of the causes of this heavy rainfall event. The Q-vector field at 850 hPa showed Q-vector convergence and frontogenesis in the region of heaviest rainfall.

For our experiments, one-way grid nesting was employed with a horizontal grid spacing of 27 km for the coarse outer grid (99 x 103 x 37 points), 9 km for the middle grid (115 x1 39 x 37 points), and 3 km for the inner fine grid (144 x 187 x 37 points). A total of 26 experiments served to test the effect of model resolution, the impact of radar data, and the difference between a cold start and data assimilation methodologies. Initial and lateral boundary conditions for the 27-km grid ARPS forecast were provided by the Korea Meteorological Administration 40 km, 18-hour and 6-hour operational Regional Data Assimilation and Prediction System (RDAPS) forecasts.

Incremental analysis updating (IAU), a type of nudging technique, is designed to gradually incorporate analysis increments into a model integration by using the increments as constant forcings in the prognostic equations during an assimilation period centered on the analysis time (Bloom et al. 1996). IAU has the advantage of serving as a low-pass time filter, having a particular effect upon the response of the model where analysis increments exist; it leaves the model state unaffected where no data is available to assimilate. The IAU scheme adds the analysis increments to the model as a state-independent forcing term, performing the actual filtering only in response to the analysis increments. This is in contrast to classic nudging, where the entire model state is relaxed toward an analysis.

Two experiments at 27 km grid spacing, 27R and 27R_n, were conducted. Experiment 27R was the 27 km ARPS forecast integrated for 21 hours using the 18-hour RDAPS forecast as a starting point (the "old first guess field"). 27R_n was identical to 27R except for the use of a newer version of the RDAPS model from a 6-hour forecast (the "new first guess field"). Comparing the predicted total rainfall over the 21-hr period for both first guess fields, *that obtained using the new first guess field* showed substantial improvement.

Six experiments of 12-hour duration were conducted at a grid spacing of 9 km, using the 9 hour forecasts from both 27 km experiments as first guess fields. Experiment 09RNR was utilized with no radar data. Experiment 09RYR was similar to 09RNR, but with the use of radar data only at the initial time to aid in the specification of the moisture and temperature fields via diabatic initialization using the ARPS Data Assimilation System (ADAS). Experiment 09RAR was identical to 09RYR, but with radar data

assimilated over a period of 3 hours rather than used only in the initial analysis. Comparing predicted total rainfall amounts, 09RNR was better than 27R. This indicated that increasing resolution results in an improved forecast over 12 hours, as shown in other studies (e.g., Benoit and Mailhot 2001; Mass et al. 2001). Comparing 09RNR with 09RYR, the latter was more accurate in terms of total maximum rainfall owing to the benefit of radar data in the initial analysis. However, the forecasted position of the rainfall maximum in did not show any significant improvement. Although 03RAR was computationally more costly, the location and maximum value of the peak rainfall did not improve relative to 09RYR.

When using the new first guess field, the predicted total rainfall was considerably greater, and its area larger, than when using the old first guess field. As in the results using the old first guess field, the impact of radar data assimilation was nominal.

A total of 18 experiments were conducted at 3 km grid spacing in order to evaluate the impact of NEXRAD data on high-resolution forecasts in four principal categories. The results were evaluated both qualitatively and quantitatively. For verification (especially quantitative), we used precipitation estimates derived from NEXRAD Level II data using a commercial software package developed by Vieux and Associates.

Qualitative verification showed that the new first guess field did not lead to any improvements at 3 km grid spacing, although the predicted maximum rainfall amounts were close to those observed. The predicted rainfall exhibited a greater positive bias over the entire domain than in the 9 km grid spacing simulation. *Quantitative* verification demonstrated that the use of *both* radial velocity and reflectivity led to a discernible

improvement compared to the use of reflectivity only, especially early during the forecast. This suggests that radial velocity can exert a positive impact upon the forecast despite the fact that it represents only one component of the full three-dimensional wind field.

Comparing experiments with and without the use of radar data, the radar data assimilation case (03RAR) was the most skillful, while 03RYR and 03RNR followed in that order. This suggests that radar data can potentially add value to a forecast.

Six additional experiments were employed to assess four data assimilation strategies: (1) use of radar data only at the initial time, (2) variation in the rate at which data are assimilated; (3) variation in the length of the data assimilation window; and (4) the use of different placements in time of the data assimilation. For the first case, we found that there exists only a slight difference when radar data are or are not used at the initial time. A data assimilation window of length 20 minutes was slightly better than 5 or 10 minutes, with 5 minutes being clearly the worst. This is in contrast to the results of Crook (1994). For the fourth set of experiments, we found that radar data assimilation can be quite sensitive to a change in the position of the data assimilation window or the selection of a particular volume scan. *Overall, it was clear that an experiment using three data inserts within a one-hour period, as compared to three inserts over a three hour period, produced the most skillful forecast.*

By examining the mean absolute error and difference fields for the most skillful case noted above, we confirmed that the positive impact of radar data for this particular event, using a grid spacing of 3 km, is approximately 3 to 4 hours process presented a limitation as forecast time increased.

The structure and physical impact of the increments were examined for the rapid data assimilation case as well. The potential temperature, water substance, and vertical motion were incorporated well into the model forecast when employing radar data assimilation using IAU. This also led to a positive feedback mechanism in the convective system.

8.2 **Concluding Remarks and Future Work**

Although this study shows that Doppler radar data assimilated into a cloud-resolving forecast model, using incremental analysis updating, has a significant positive impact, a number of limitations exist, some of which limit the generalization of these results.

1. The best forecast produced in this study still exhibited considerable error in the position and maximum amount of total rainfall.

2. The lack of availability of conventional data, and the use of 3 km model grid spacing, likely contributed to these results, as well as the use of IAU in a rather conventional manner. With regard to the latter, changes in the weighting of the increments over time, and phase-correcting assimilation, may have proved beneficial.

3. Although the precipitation estimated from NEXRAD Doppler radar was in reasonable agreement with surface gauges, its overall quality remains questionable given that it was calibrated using only seven surface stations.

It is important to recognize that the forecasting improvement brought about by Doppler radar data assimilation, and measured by objective skill scores, is due mostly to a reduction in falsely-prediction convection rather than the creation of correct convective structures in the region where they actually were observed.

Finally, and perhaps most importantly, no Doppler wind retrieval was applied in this study, i.e., only the radial velocities were used rather than the radial velocities combined with estimates of the polar and azimuthal wind components. Because many studies have shown that the 3D wind field can be retrieved with reasonable accuracy from Doppler radar data (e.g., Shapiro et al., 1995; Weygandt et al., 2002a,b; Gao et al. 2001), we would expect that the use of such complete fields, coupled with thermodynamic and microphysical retrieval using model grid spacings of 1 km, might lead to significant improvements for the present case.

APPENDIX A Using the ARPS WSR-88D Data Remapper

A.1 Introduction

Because this study involves the assimilation of WSR-88D Doppler radar data, which is important for others to reproduce our results, we report here the steps involved in incorporating radar data into ADAS. This description is based upon internal documentation at CAPS (Brewster, 2001)

One of the ARPS programs, 88d2arps, reads data from WSR-88D archive Level II tapes, from disk files, or from the RIDDS live circular buffer (a device used to collect Level II data in real time but no longer in service). All data located within each ARPS grid volume are averaged to produce the remapped fields. One output file is produced for each radar data "volume scan." Data returned are averaged reflectivity factor (dBZ), radial velocity (ms^{-1}), spectrum width (ms^{-1}), and local Nyquist velocity. In the averaging process, the data within each grid volume are checked to ensure that they lie within the same Nyquist interval, but they are not unfolded. Unfolding is performed within ADAS. Minimal quality control is performed by checking the variance of the data and the data coverage in each grid volume. High variance averages and grid volumes containing sparse relative coverage are discarded. Statistics on the coverage and variance discard rate are reported for each volume scan in standard output.

The ARPS grid used for remapping is established through the regular ARPS input file (e.g., arps.input). The namelist variables dealing with grid spacing, grid

location, and terrain and map projection are used to establish the grid just as if an ARPS forecast were to be run. The remaining namelist variable blocks are not used. Some controls are determined through environment variables; see instructions for running 88d2arps.

A.2 Main Files and Link to Library

The radar re-mapper is contained in several source code files (C and Fortran) that are distributed with the official CAPS source code in the directory:

./src/88d2arps

The main driver source is 88d2arps.c. The directory also contains files needed for building the executable and a short script for setting the necessary environment variables.

The makearps utility will automatically link to certain I/O libraries that have been installed on the CAPS IBM cluster and some Sun workstations in CAPS. One often needs to install the zlib.a library, which is used for uncompressing radar files. If this library is not available, source may be downloaded for free. Information about this can be found on the web at URL http://www.info-zip.org/pub/infozip/zlib/

A.3 Building the Executable

The 88d2arps executables can be built using the makearps command. The executable file is built using the UNIX make utility.

Users outside of CAPS will need to change the directory references for the liba2io.a and libtpio.a libraries in makearps. The source code for the libraries can be obtained by anonymous ftp:

```
ftp ftp.caps.ou.edu
login anonymous
password: your email
binary
cd pub/users/kbrews/archive-2
get a2io.tar
get tpio.tar
get radarinfo.dat
get setREMAPenv
```

Untar and run make in the separate directories to build the a2io and tpio libraries. a2io and tpio are from the National Severe Storms Laboratory. They were written and tested for Sun, IBM and HP Unix workstations. Use on other platforms may require changes that we are not able to support.

After these libraries have been built, one must check the locations for the libraries specified in the makearps csh script to see that they match the actual locations. Also be sure the zlib is specified (-lz) as this was not needed for earlier ARPS releases. The makearps script libarary statements should read something like:

```
case 88d2arps_a2:
set LIBS = '/usr1/local/a2io/liba2tp.a /usr1/local/tpio/libtpio.a -lz'
breaksw
```

The file `radarinfo.dat` contains the location information for each WSR-88D radar. It is a text file, so additional radars can be added via editing, should that be necessary. The file setREMAPenv is a csh script for setting environment variables.

a) To build an executable for reading WSR-88D Archive-II tape or disk file:

1) Edit dims.inc to set the desired nx, ny, nz dimensions (not needed for the ARPS version 5.0 code – in that version nx, ny, nz are set in the input file and memory is dynamically allocated)

2) Make the executable, for example

```
makearps -d 88d2arps_a2
```

b) To build an executable for reading from the RIDDS circular buffer:

1) Edit dims.inc to set the desired nx, ny, nz dimensions

2) Make the executable using makearps and the usual options, for example:

```
makearps -d 88d2arps_rt
```

Users outside of NSSL will need to change the references to the a2rt, nexrad and nssl libraries. The source code for the nexrad and nssl libraries can be obtained from the National Severe Storms Laboratory.

A.4 Running the Program

a) To run 88d2arps to read WSR-88D Archive-II data tape or disk file:

1) Edit an ARPS input file (e.g., `arps40.input`, to specify desired grid parameters, including the terrain file (if desired). A map projection option other than "zero" must be selected.

2) Edit the environment script file, setREMAPenv, to set the proper radar name, and rcp user and destination directory. The setenv commands for rcp are optional and if they are set to a blank value, they will cause the program to skip over this feature.

setREMAPenv lines:

```
setenv RADARNAME KTLX    [4-character name of radar]
setenv REMAP_DIR ./      [destination directory for output files]
setenv REMAP_USER user   [optional user name for rcp command, used
                                to copy output to remote system
                               ..leave blank to disable rcp action]
setenv REMAP_REMOTE stratus
                         [optional: destination machine for rcp command]
setenv REMAP_DEST /scratch/stratus/user
                         [optional: destination directory for rcp]
setenv REMAP_COMPRESS gzip
                         [optional: desired compression utility for output files:
                          gzip, compress or nothing]
```

3) Set the environment variables

```
source setREMAPenv
```

4) Be sure you have the file "radarinfo.dat" in the directory of execution.

5) Insert tape in drive (in the following, drive named /dev/rmt2 is used as an example). The tape drive name used MUST be non-rewinding on close.

6) Advance tape to desired file on tape. Each volume scan (5-10 minutes of data) constitutes a file on the tape. The program processes all files it encounters, so to

save time you need to skip the files you do not wish to process. You may use the mt command.

```
mt -f /dev/rmt2.1 fsf 100
```

7) Run the program

```
88d2arps_a2 -f /dev/rmt2.1 < arps40.input
```

8) Stop the program. The program will run until the end of tape is reached, so use control-C to stop it. The program may also be stopped, and later restarted, if you find you need to reposition the tape to a different file.

```
<ctrl>C
```

b) To run 88d2arps to read from an Archive-II data file on disk

1) Edit ARPS input file to specify desired grid parameters

2) Edit the script, setREMAPenv, to set the proper radar name, and rcp user and destination directory, if desired. See instructions for reading taped data for guidance.

3) Set the environment variables

```
source setREMAPenv
```

4) Run the program

```
88d2arps_a2 -diskf /directory/filename < arps40.input
```

c) To run 88d2arps to read from the RIDDS circular buffer

1) Edit ARPS input file to specify desired grid parameters

2) Edit the script, setREMAPenv, to set the proper radar name, and rcp user and destination directory. See instructions for reading taped data for guidance.

3) Set the environment variables

```
source setREMAPenv
```

4) Run the program

```
88d2arps_rt < arps40.input
```

5) Stop the program. The program will run indefinitely, so use control-C to stop it. The program may also be stopped, and later restarted, if you find you need to reset the environment variables, change the grid, etc.

```
<ctrl>C
```

A.5 Reading and Plotting the Output

The data may be read into an application program using the subroutine RDRADCOL, which is contained in the file rdradcol.f. The data are stored and read-in as columns of non-missing data which are identified by their latitude and longitude. See the RDRADCOL source code for details.

A small program to examine the output of 88d2arps is provided and requires NCAR Graphics libraries. The commands needed to create plots follow.

1) Create the program pltradcol.

```
ncargf77 -o pltradcol pltradcol.f maproj3d.f pltmap.f timelib3d.f
```

2) Run pltradcol, it will prompt for filename.

```
pltradcol
```

3) examine the gmeta file

```
idt gmeta
```

Parameters in the source code in pltradcol.f may be modified to change which data are plotted.

REFERENCES

Albers, S. C., J. A. McGinley, D.A. Birkenhuer, and J. R. Smart, 1996: The Local Analysis and Prediction System (LAPS): Analysis of clouds, precipitation and temperature. *Wea. and Forecasting*, **11**, 273-287.

Anderson, E., J. Haseler, P. Unden, P. Courtier, G. Kelly, D. Vasiljevic, C. Brankovic, C. Cardinali, C. Gaffard, A. Hollingworth, C. Jakob, P. Janssen, E. Klinker, A. Lanzinger, M. Miller, F. Rabier, A. Simmons, B. Strauss, J.-N. Thepaut ,and P. Viterbo, 1998: The ECMWF implementation of three-dimensional variational assimilation (3D-VAR). III: Experimental results. *Quart. J. Roy. Meteor. Soc.*, **124**, 1831-1860.

Anderson, J. L., 2001: An ensemble adjustment Kalman filter for data assimilation. *Mon. Wea. Rev.*, **129**, 2884-2903.

Anthes, R. A., 1977: A cumulus parameterization scheme utilizing a one-dimensional cloud model. *Mon. Wea. Rev.*, **105**, 270-286.

_____, and T. T. Warner, 1978: Development of hydrodynamic models suitable for air pollution and other mesometeorological studies. *Mon. Wea. Rev.*, **106**, 1045-1078.

_____, and D. Keyser, 1979: Tests of a fine-mesh model over Europe and the United States. . *Wea. Rev.*, **107**, 963-984.

Aonashi, K., 1993: An initialization method to incorporate precipitation data into a mesoscale numerical weather prediction model. *J. Meteor. Soc. Japan*, **71**, 393-406.

Barnes, S. L., 1964: A technique for maximizing details in numerical weather map analysis. *J. Appl. Meteor.*, **3**, 396-409.

Belair, S., D.-L. Zhang, and J. Mailhot, 1994: Numerical prediction of the 10-11 June 1985 squall line with the Canadian regional finite-element model. *Wea. Forecasting*, **9**, 157-172.

_____, and J. Mailhot, 2001: Impact of horizontal resolution on the numerical simulation of a midlatitude squall line: Implicit versus explicit condensation. *Mon. Wea. Rev.*, **129**, 2362-2376.

Bengtsson, L., 1975: Four-dimensional data assimilation of meteorological observation. GARP Publ. Ser. No. 15, WMO/ICSU, Geneva.

_____, 1985: Medium range forecasting at the ECMWF. *Adv. Geophys.*, **28B**, 3-56.

_____, M. Kanamitsu, P. Kallberg, and S. Uppala, 1982: FGGE four-dimensional assimilation at ECMWF. *Bull. Amer. Meteor. Soc.*, **63**, 29-43.

Benjamin, S. G., and T. N. Carlson, 1984: Some effects of surface heating and topography on the regional severe storm environment. Part I: Three-dimensional simulations. *Mon. Wea. Rev.*, **114**, 307-329.

Bergman, K. H., 1979: Multivariate analysis of temperatures and winds using optimum interpolation. *Mon. Wea. Rev.*, **107**, 1423-1444.

Birchfield, G. E., 1960: Numerical prediction of hurricane movement with the use of a fine grid. *J. Atmos. Sci.*, **17**, 406-414.

Bloom, S. C., L. L. Takacs, A. M. Da Silva, and D. Ledvina, 1996: Data assimilation using incremental analysis updates. *Mon. Wea. Rev.*, **124**, 1256-1271.

_____, 2003 Private communication.

Bluestein, H. B., 1992: *Synoptic-dynamic meteorology in midlatitudes. Volume I Principles of kinematics and dynamics*, Oxford University Press, 431 pp.

_____, 1993: *Synoptic-dynamic meteorology in midlatitudes. Volume II Observations and theory of weather system*, Oxford University Press, 594 pp.

Bougeault, P., and P. Lacarrere, 1989: Parameterization of orography-induced turbulence in a meso-β scale model. *Mon. Wea. Rev.*, **117**, 1872-1890.

Bourke, W., K. Puri, R. Seaman, B. McAvaney, and J. Le Mashall, 1982: ANMRC data assimilation for the southern hemisphere. *Mon. Wea. Rev.*, **110**, 1749-1771.

_____, and J. L. McGregor, 1983: A nonlinear vertical mode initialization scheme for a limited area prediction model. *Mon. Wea. Rev.*, **111**, 2285-2297.

_____, R. Seaman, and K. Puri, 1985: Data assimilation. *Adv. Geophys.*, **28B**, 124-149.

Bouttier, F., and P. Courtier, 2001: Data assimilation concepts and methods. 'http://www.emwf.int/service/training/rcource_notes/DATA_ASSINILATION/ASSIM_CONCEPTS/Assim_concepts.html'

Brandes, E. A., J. Vivekanandan, and J. W. Wilson, 1999: A comparison of radar reflectivity estimatesof rainfall from collocated radars. *J. Atmos. Oceanic Tech.*, **16**, 1264-1272.

Bratseth, A. M., 1986: Statistical interpolation by means of successive corrections. *Tellus*, **38A**, 439-447.

Brewster, K., 1996: Application of a Bratseth analysis scheme including Doppler radar data. Preprints, *15th Conference on Weather Analysis and Forecasting*. Amer.Meteor. Soc., Norfolk, VA, 92-95.

_____, 1998: ARPS 4.0 Users Guide, Supplement 1, 3-D Analysis with the ARPS Data Assimilation System. CAPS internal documentation, 29 pp.

_____, 1999: Phase-correction data assimilation and application to storm-scale weather prediction. Ph. D. Dissertation, University of Oklahoma, Norman, OK, 175 pp.

_____, 2001a: Simplification of the radar ray path equations. CAPS internal documentation, 5 pp.

_____, 2001b: ADAS-ARPS data assimilation using incremental analysis updating. CAPS internal documentation, 4 pp.

_____, 2002: Recent advances in the diabatic initialization of a non-hydrostatic numerical model. Preprints, *21st Conf. on Severe Local Storms, and Preprints, 15th Conf. Num. Wea. Pred. and 19th Conf. Wea. Anal. Forecasting*, San Antonio, TX, Amer. Meteor. Soc., J6.3.

_____, 2003: Phase-correcting data assimilation and application to storm-scale numerical weather prediction. Part I: Method description and simulation testing. *Mon. Wea. Rev.*, **131**, 480-492.

_____, S. Albers, F. H. Carr, and M. Xue, 1995: Initializing a nonhydrostatic forecast model using WSR-88D data and OLAPS. Preprints, *27th Conference on Radar Meteorology*, Vail, CO, Amer. Meteor. Soc., 252-254.

Brock, F. V., K. C. Crawford, R. L. Elliott, G. W. Cuperus, S. J. Stadler, H. L. Johnson, and M. D. Eilts, 1995: The Oklahoma mesonet: A technical overview. *J. Atmos. Oceanic Tech.*, **12**, 5-19.

Browning, K. A., and G. A. Monk, 1982: A simple model for the synoptic analysis of cold fronts. *Quart. J. Roy. Meteor. Soc.*, **108**, 435-452.

_____, 1986: Conceptual models of precipitation systems. *Wea. Forecasting*, **1**, 23-41.

Bucy, R. S., and P. D. Joseph, 1987: *Filtering for stochastic processes with applications to guidance, second edition*, Chelsea, New York, 217 pp.

Carr, F., 2000: Objective Analysis and data assimilation. COMAP NWP Symposium.

_____, J. Mewes, and K. Brewster, 1996: Quantitative verification of nonhydrostatic model forecasts of convective phenomena. *Preprints, 18th Conf. on Severe Local Storms*, 19-23 February 1996, San Francisco, CA, Amer. Meteor. Soc., 174-177.

Carlson, T. N., 1980: Airflow through midlatitude cyclones and the comma cloud pattern.. *Mon. Wea. Rev.*, **108**, 1498-1509.

Chang, C.-Y., and M. Yoshizaki, 1991: A numerical study of the mesoscale convective system observed over Okinawa Island in June 1987. *Mon. Wea. Rev.*, **119**, 2724-2733.

Changnon, S. A., and J. L. Vogel, 1981: Hydroclimatological characteristics of isolated severe rainstorms. *Water Resour. Res.*, **17**, 1694-1700.

Chao, W. C., and L. P. Chang, 1992: Development of a four-dimensional variational analysis system using the adjoint method at GLA. Part I: Dynamics. *Mon. Wea. Rev.*, **120**, 1661-1673.

Charney, J., M. Halem, and R. Jastrow, 1969: Use of incomplete historical data to infer the present state of the atmosphere. *J. Atmos. Sci.*, **26**, 1160-1163.

Cohn, S. E., 1997: An introduction to estimation theory. *J. Meteor. Soc. Japan.*, **75 1B**, 257-288.

Courtier, P., 1997: Variational methods. *J. Meteor. Soc. Japan.*, **75 1B**, 211-218.

_____, E. Anderson, W. Heckely, J. Pailleux, D. Vasiljevic, M. Hamrud, A. Hollingsworth, F. Rabier, and M. Fisher, 1998: The ECMWF implementation of three-dimensional variational assimilation (3D-Var). Part I: formulation. *Quart. J. Roy. Meteor. Soc.*, **124**, 1783-1807.

Cressman, G. P., 1959: An operational objective analysis system. *Mon. Wea. Rev.*, **87**, 367-374.

Crook, N. A., 1994: Numerical simulations initialized with radar-derived winds. Part I: Simulated data experiments. *Mon. Wea. Rev.*, **122**, 1189-1203.

_____, and J. Sun, 2002: Assimilating radar, surface, and profiler data for the Sydney 2000 forecast demonstration project. *J. Atmos. Oceanic Tech.*, **19**, 888-898.

Daley, R., 1991: *Atmospheric data analysis*. Cambridge University Press, New York, 457 pp.

_____, 1997: Atmospheric data assimilation. *J. Meteor. Soc. Japan*, **75 1B**, 319-329.

Davis, H. C., and R. E. Turner, 1977: Updating prediction models by dynamical relaxation: An examination of the technique. *Quart. J. Roy. Meteor. Soc.*, **103**, 225-245.

Derber, J. 1989: A variational continuous assimilation technique. *Mon. Wea. Rev.*, **117**, 2437-2446.

_____, H.-L. Pan, J. Alpert, P. Caplan, G. White, M. Iredell, Y.-T. Hou, K. Campana, and S. Moorthicoauthors, 1998: Further changes to the 1997 NCEP operational MRF Model Analysis/Forecast System : The use of TOVS level 1-b radiances and increased vertical diffusion. NWS Technical Prodedure Bulletin No. 449, NOAA/AWS, Washington, DC.

Djuric, D., 1994: *Weather Analysis*, Prentice-Hall Inc., 304 pp.

Droegemeier, K. K., 1997: Numerical prediction of thunderstorms: Challenges, potential benefits and results from real-time operational tests. *WMO Bulletin*, **46** (4), 1-13.

_____, J. D. Smith, S. Businger, C. Doswell III, J. Doyle, C. Duffy, E. Foufoula-Georgiou, T. Graziano, L. D. James, V. Krajewski, M. LeMone, D. Lettenmaier, C. Mass, R. Pielke Sr., P. Ray, S. Rutledge, J. Schaake, and E. Zipser, 2000: Hydrological aspects of weather prediction and flood warnings: Report of the Ninth Prospectus Development Team of the U.S. Weather Research Program. *Bull. Amer. Meteor. Soc.*, **81**, 2665-2680.

Dunn, L. B., 1991: Evaluation of vertical motion: Past, present and future. *Wea. Forecasting*, **6**, 65-75.

Durand, Y. 1985: *The use of satellite data in the French high resolution analysis.* Proceedings of the 1985 ECMWF workshop on "High resolution analysis". 24-26 June 1985. (Available from ECMWF, Reading, UK)

Eddy, A., 1967: The statistical objective analysis of scalar data fields. *J. Appl. Meteor.*, **6**, 597-609.

Flattery, T., 1970: Spectral models for global analysis and forecasting. *Proceedings sixth AWS Technical Exchange Conference*, U.S. Naval Academy. Air Weather Service Technical Report 242, 42-54.

Fox-Rabinovitz, M. S., 1996: Diabatic dynamic initialization with an iterative time integration scheme as a filter. *Mon. Wea. Rev.*, **124**, 1544-1557.

Fritsch, J. M., and C. R. Chappell, 1980: Numerical prediction of convectively-driven mesoscale pressure systems. Part I: convective parameterization. *J. Atmos. Sci.*, **37**, 1722-1733.

Gal-Chen, T., 1978: A method for the initialization of the anelastic equations: Implications for matching models with observations. *Mon. Wea. Rev.*, **106**, 587-606.

Gandin, L. S., 1963: Objective analysis of meteorological fields. Leningrad, Gidrometeoizdat, in Russian. (English Translation: Israel Program for Scientific Translations, Jerusalem, 1965, 242 pp.)

_____, 1988: Complex quality control of meteorological observations. *Mon. Wea. Rev.*, **116**, 1137-1156.

Gao, J., M. Xue, A. Shapiro, and K. K. Droegemeier, 1999a: Three dimensional variational wind retrievals from single-Doppler radar. Preprints, *29th International Conference on Radar Meteorology*, Montreal, Quebec, Cananda, Amer. Meteor. Soc., 30-32.

_____, M. Xue, A. Shpiro, and K. K. Droegemeier, 1999b: A variational method for the analysis of three-dimensional wind fields from two Doppler radars. *Mon. Wea Rev.*, **127**, 2128-2142.

_____, M. Xue, A. Shpiro, Q. Xu, and K. K. Droegemeier, 2001: Three-dimensional simple adjoint velocity retrievals from single-Doppler radar. *J. Atmos. Ocean Technol.*, **18**, 26-38.

Ghil, M., 1997: Advances in sequential estimation for atmospheric and oceanic flows. *J. Meteor. Soc. Japan.*, **75 1B**, 289-304.

_____, M. Halem, and R. Atlas, 1979: Time-continuous assimilation of remote sounding data and its effect on weather forecasting. *Mon. Wea. Rev.*, **107**, 140-171.

_____, and P. Malanotte-Rizzoli, 1991: Data assimilation in meteorology and oceanography. *Adv. Geophys.*, **33**, 141-266.

Haltiner, G. J., and R. T. Williams, 1980: *Numerical prediction and dynamic meteorology, second edition*, John Wiley & Sons, New York, 477 pp.

Harms, D. E., S. Raman, and R. V. Madala, 1992: An examination of four-dimensional data-assimilation techniques for numerical weather prediction. *Bull. Amer. Meteor. Soc.*, **73**, 425-440.

Hemler, R. S., F. B. Lipps, and B. B. Ross, 1991: A simulation of a squall line using a nonhydrostatic cloud model with a 5-km horizontal grid. *Mon. Wea. Rev.*, **119**, 3012-3033.

Hilgendorf, E. R., and R. H. Johnson, 1998: A study of the evolution of mesoscale convective system using WSR-88D data. *Wea. Forecasting*, **13**, 437-452.

Hoke, J. E., and R. Anthes, 1976: The initialization of numerical models by a dynamic relaxation technique. *Mon. Wea. Rev.*, **104**, 1551-1556.

_____, N. A. Phillips, G. J. Dimego, J. J. Tuccillo, and J. G. Sela, 1989: The regional analysis and forecast system of the National Meteorological Center. *Wea. Forecasting*, **4**, 323-334.

Holton, J. R., 1992: *An introduction to dynamic meteorology, third edition*, Academic Press, San Diego, 511 pp.

Houtekamer, P. L., and H. L. Mitchell, 1998: Data assimilation using and ensemble Kalman Filter Technique. *Mon. Wea. Rev.*, **126**, 796-811.

Houze, R. A. Jr., S. A. Rutledge, M. I. Biggerstaff, and B. F. Smull, 1989: Interpretation of Doppler weather radar display of midlatitude mesoscale convective systems. *Bull. Amer. Meteor. Soc.*, **70**, 608-619.

Ide, K., P. Courtier, M. Ghil, and A. C. Lorenc: Unified notation for data assimilation: Operational, sequential and variational. *J. Meteor. Soc. Japan.*, **75 1B**, 181-189.

Janish, P. R., and S. J. Weiss, 1996: Evaluation of various mesoscale phenomena associated with severe convection during VORTEX-95 using the Meso Eta model. *Preprints, 15th Conf. on Weather Analysis and Forecasting*, AMS, Norfolk, VA. Aug, 1996.

Jazwinski, A. H., 1970: Stochastic processes and Filtering theory, Academic Press, New-York, 376 pp.

Jones, R., 1965: An experiment in non-linear prediction. *J. Appl. Meteor.*, **4**, 701-705.

Junker, N. W., and J. E. Hoke, 1990: An examination of Nested Grid Model precipitation forecasts in the presence of moderate-to-strong low-level southerly inflow. *Wea. Forecasting*, **5**, 333-344.

Kalman, R. E., 1960: A new approach to linear filtering and prediction problems. *Trans. ASME J. Basic Eng.*, **82D**, 35-45.

_____, and R. S. Bucy, 1961: New results in linear filtering and prediction theory. *Trans. ASME. J. Basic Eng.*, **83D**, 95-108.

Kalnay, E., 1998: Class note of numerical weather prediction, University of Oklahoma.

Kanamitsu, M., K. Tada, T. Kudo, N. Sato, and S. Isa, 1983: Description of the JMA operational spectral model. *J. Meteor. Soc. Japan,* **61**, 812-828.

Kasahara, A., 1972: Simulation experiments for meteorological observing systems for GARP. *Bull. Amer. Meteor. Soc.*, **53**, 252-264.

_____, A. P. Mizzi, and L. J. Donner, 1994: Diabatic initialization for improvement in the tropical analysis of divergence and moisture using satellite radiometric imagery data. *Tellus*, **46A**, 242-264.

Kessler, E. 1969: On the distribution and continuity of water substance in atmospheric circulation. *Meteor. Monogr.*, **10**, No 32, Amer. Meteor. Soc.

Kim, H. W., 2000: Analysis of heavy rainfall Case by mesoscale convective systems using Doppler Radar Data (in Korean). Master's thesis, Seoul National University, Seoul, Korea, 105 pp.

Kistler, R. E., 1974: A study of data assimilation techniques in an autobarotropic, primitive equation, channel model. M.S. thesis, Penn. State. Univ., 84 pp.

_____, and D. Parrish, 1982: Evolution of the NMC data assimilation system: September 1978-January 1982. *Mon. Wea. Rev.*, **110**, 1335-1346.

Klazura, G. E., and D. Imy, 1993: A description of the initial set of analysis products available from the NEXRAD WSR-88D system. *Bull. Amer. Meteor. Soc.*, **74**,1293-1311.

_____, J. M. Thomale, D. S. Kelly, and P. Jendrowski, 1999:A comparison of NEXRAD WSR-88D radar estimates of rain accumulation with gauge measurements for high and low reflectivity horizontal gradient. *J. Atmos. Ocean Technol.*, **16**, 1842-1850.

KMA, 1996: The study of heavy rainfall event which occurred in the middle of Korea ('96. 7. 26~28) (in Korean), Korea Meteorological Administration, 59 pp.

Kreitzberg, C. W., and H. A. Brown, 1970: Mesoscale weather systems within an occlusion. *J. Appl. Meteor.*, **9**, 417-432.

Krishnamutri, T. N., J. Xue, H. S. Bedi, K. Ingles, and D. Oosterhof, 1991: Physical initialization for numerical weather prediction over the tropics. *Tellus*, **43A-B**, 53-81.

Kruger, H. B., 1969: General and special approaches to the problem of objective analysis of meteorological variables. *Quart. J. Roy. Meteor. Soc.*, **95**, 21-39.

Le Dimet, F.-X., H.-E. Ngodock, and B. Luong, 1997: Sensitivity analysis in variational data assimilation. *J. Meteor. Soc. Japan.*, **75 1B**, 245-255.

Lee, D.-K., H.-R. Kim, and S.-Y. Hong, 1998: Heavy rainfall over Korea during 1980-1990. *Korean J. Atmos. Sci.*, **1**, 32-50.

_____, and T.-K. Wee, 1997: Real-time mesoscale prediction at SNU: Preliminary tests. Preprints, *The 2nd Korea-US Joint Workshop on Storm and Mesoscale Weather Analysis and Prediction*, Seoul, Korea, 11-15.

Lewis, J., 1972: An operational upper air analysis using the variational method. *Tellus*, **24**, 514-530.

_____, and J. C. Derber, 1985: The use of adjoint equations to solve a variational adjustment problem with advective constraints. *Tellus*, **37A**, 309-322.

Lin, Y. L., R. D. Farley, and H. D. Orville, 1983: Bulk parameterization of the snow field in a cloud model. *J. Clim. Appl. Meteor.*, **22**, 1065-1092.

Lorenc, A. C., 1976: Results of some experiments assimilating observations from a simulation of the FGGE observing system into a global general circulation model. *In JOC study Conference on Four-Dimensional Data Assimilation*, Paris, 1975. Report II, GARP on Numerical Experimentation. Pub. WMO/ICSU, pp 358-374.

_____, 1981: A global three-dimensional multivariate statistical interpolation scheme. *Mon. Wea. Rev.*, **109**, 701-721.

_____, and O. Hammon, 1988: Objective quality control of observations using Bayesian methods. *Quart. J. Roy. Meteor. Soc.*, **114**, 515-543.

_____, R. S. Bell, and B. MacPherson, 1991: The meteorological office analysis correction data assimilation scheme. *Quart. J. Roy. Meteor. Soc.*, **117**, 59-89.

Lynch, P., 1985: Initialization using Laplace transforms. *Quart. J. Roy. Meteor. Soc.*, **111**, 243-258.

Lyne, W. H., R. Swinbank, and N. T. Birch, 1982: A data assimilation experiment and the global circulation during the FGGE Special Observing Periods. *Quart. J. Roy. Meteor. Soc.*, 108, 575-594.

Maddox, R. A., 1979: A methodology for forecasting heavy convective precipitation and flash flooding. *Nat. Wea. Dig.*, **4**, 30-42.

_____, 1980: Mesoscale convective complexes. *Bull. Amer. Meteor. Soc.*, **61**, 1374-1387.

_____, C. F. Chappell, and L. R. Hoxit, 1979: Synoptic and meso-α scale aspects flash flood events. *Bull. Amer. Meteor. Soc.*, **60**, 115-123.

_____, and C. A. Doswell III, 1983: Forecasting severe thunderstorms: A brief evaluation of accepted techniques. Preprints, *12th Conference on Severe Local Storms*, San Antonio, Amer. Meteor. Soc., 92-95.

Mahrer, Y., and R. A. Pielke, 1977: The effects of topography on the sea and land breezes in a two-dimensional numerical model. *Mon. Wea. Rev.*, **105**, 1151-1162.

Manion, J. D., and G. E. Klazura, 1993: A comparison of data from the WSR-88D storm total precipitation product and a network of gages: Preliminary results. Preprints, *26th Int. Conf. on Radar Meteorology*, Norman, OK, Amer. Meteor. Soc., 151-153.

Marshall, J. S., W. Hitschfeld, and K. L. S. Gunn, 1955: Advances in radar weather. *Adv. Geophys.*, **2**, 1-56.

Mass, C. F., D. Ovens, K. Westrick, B. A. Colle, 2002: Does increasing horizontal resolution produce more skillful forecasts?. *Bull.Amer. Meteor. Soc.*, **80**, 407–430.

McPherson, R. D., 1975: Progress, problems, and prospects in meteorological data assimilation. *Bull. Amer. Meteor. Soc.*, **56**, 1154-1166.

_____, K. H. Bergman, R. E. Kistler, G. E. Rasch, and D. S. Gordon, 1979: The NMC operational global data assimilation system. *Mon. Wea. Rev.*, **107**, 1455-1461.

METRI, 1998: Workshop for severe weather (in Korean). METRI, Seoul, Korea, 33 pp.

Molinari, J., 1993: An overview of cumulus parameterizations in mesoscale models. In The Representation of Cumulus Convection in Numerical Models, *Meteor. Monograph*, **46**, Amer. Meteor. Soc., 155-158.

Morel, P., 1981: An overview of meteorological data assimilation. Dynamic Meteorology: Data Assimilation Methods, L. Bengtsson, M. Ghil, and E. Kallen, Eds., Springer-Verlag, 5-16.

Nascimento, E. D. L., 2002: Dynamic adjustment in an idealized numerically-simulated bow echo. Ph. D. Dissertation, University of Oklahoma, Norman, OK, 289 pp.

NCDC, 2001: Radar Data Inventories homepage:(Available at http://www4.ncdc.noaa.gov/cgi-win/).

NDPCH (National Disaster Prevention and Countermeasures Headquarters in Korea), 2001: (Available at http://www.mogaha.go.kr/ndch/eng-start.htm).

NOAA, 1990: *Doppler radar meteorological observations: Part B Doppler radar theory and meteorology*. Federal Meteorological Handbook No. 11.

National Research Council, 1991: *Four-dimensional model assimilation of data: A strategy for the earth system science*. National Academy Press, Washington, D.C., 78pp.

Olson, D. A., N. W. Junker, and B. Korty, 1995: Evaluation of 33 years of quantitative precipitation forecasting at the NMC. *Wea. Forecasting*, **10**, 498-511.

Parrish, D. F., and J. C. Derber, 1992: The national meteorological center's spectral statistical-interpolation analysis system. *Mon. Wea. Rev.*, **120**, 1747-1763.

Petersen, D., 1973: A comparison of the performance of quasi-optimal and conventional objective analysis schemes. *J. Appl. Meteor.*, **12**, 1093-1101.

Puri, K., and N. E. Davidson, 1992: The use of infrared satellite cloud imagery data as proxy data for moisture and diabatic heating in data assimilation. *Mon. Wea. Rev.*, **120**, 2329-2341.

Ramamurthy, M. K., and F. H. Carr, 1987: Four-dimensional data assimilation in the monsoon region. Part I: Experiments with wind data. *Mon. Wea. Rev.*, **115**, 1678-1706.

_____, and _____, 1988: Four-dimensional data assimilation in the monsoon region. Part II: Role of temperature and moisture data. *Mon. Wea. Rev.*, **116**, 1896-1913.

Rogers, R. F., J. M. Fritsch, and W. C. Lambert, 2000: A simple technique for using radar data in the dynamic initialization of a mesoscale model. *Mon. Wea. Rev.*, **128**, 2560-2574.

Rogers, R. R., and M. K. Yau, 1989: *A short course in cloud physics, third edition*, Butterworth Heinemann, 290 pp.

Romero, R. S., C. Ramis, and S. Alonso, 1997: Numerical simulation of an extreme rainfall event in Catalonia: Role of orography and evaporation from the sea. *Quart. J. Roy. Meteor. Soc.*, **123**, 537-559.

Rosenfeld, D., D. B. Wolff, and D. Atlas, 1993: General probability-matched relations between radar reflectivity and rain rate, *J. Appl. Meteor.*, **32**, 50-72.

Rutherford, I., 1973: Experiments in the updating of P.E. forecasts with real wind and geopotential data. Preprints, *Third Conference on Probability and Statistics in Atmospheric Science*, Boston, Amer. Meteor. Soc., 198-201.

Satomura, I., 1988: Dynamic normal mode initialization of a limited-are model. *J. Meteor. Soc. Japan*, **66,** 261-276.

Shapiro, A., S. Ellis, and J. Shaw, 1995: Single-Doppler velocity retrievals with PhoenixII data: Clear air and microburst retrievals in the planetary boundary layer. *J. Atmos. Sci.*, **52**, 1265-1287.

Sasaki, Y., 1958: An objective analysis based on the variational method. *J. Meteor. Soc. Japan*, **36,** 77-88.

_____, 1969: Proposed inclusion of time variation terms, observational and theoretical, in numerical variational objective analysis. *J. Meteor. Soc. Japan*, **47**, 115-124.

_____, 1970a: Numerical variational analysis formulated under the constraints as determined by longwave equations and a low pass filteralysis. *Mon. Wea. Rev.*, **98**, 884-898.

_____, 1970b: Numerical variational analysis with weak constraint and application to surface analysis of severe storm gust. *Mon. Wea. Rev.*, **98**, 899-910.

Schlatter, T. W., 1975: Some experiments with a multivariate statistical objective analysis scheme. *Mon. Wea. Rev.*, **103**, 246-257.

_____, 1988: Past and present trends in the objective analysis of meteorological data for nowcasting and numerical forecasting. *Preprints, 8th Conference on Numerical Weather Prediction*, Baltimore, Maryland, Amer. Meteor. Soc., J9-J25.

_____, F. H. Carr, R. H. Langland, R. E. Carborne, N. A. Crook, R. W. Daley, J. C. Derber, and S. L. Mullen, 1998: A five-year plan for research related to the assimilation of meteorological data.

Seaman, N. L., 1990: Newtonian nudging: A four-dimesional approach to data assimilation. Mesoscale Data Assimilation, *1990 Summer Colloquium, Advanced Study Program*, National Center for Atmospheric Research, Boulder, Colorado, 263-277.

Short, D., T. Kozu, and K. Nakamura, 1990: Rainfall and raindrop size distribution observations in Darwind Australia. *USRI-F Open Symp. on Regional Factors in Prediction Radiowave Attenuation Due to Rain.* Union of Radio Science International-France, Rio de Janeiro, Brazil, 35-40.

Smith, J. A., and W. F. Krajewski, 1991: Estimation of the mean field bias of radar rainfall estimates. *J. Appl. Meteor.*, **30**, 397-412.

Stensrud, D. J., and J.-W. Bao, 1992: Behaviors of variational and nudging assimilation techniques with a chaotic low-order model. *Mon. Wea. Rev.*, **120**, 3016-3028.

Straka, J. M., E. N. Rasmussen, and S. E. Fredrickson, 1996: A mobile mesonet for finescale meteorological observations. *J. Atmos. Oceanic Tech.*, **13**, 921-936.

Stull, R. B., 1995: *Meteorology Today for Scientists and Engineeres*, West Publishing Company, Minneapolis, 385 pp.

Sun, J., 1994: Fitting a cartesian prediction model to radial velocity data from single-Doppler radar. *J. Atmos. Ocean Technol.*, **11**, 200-204.

_____, 2002: Assimilation of radar data for prediction of convective systems. Preprints, *The 3rd Korea-US Joint Workshop on Storm and Mesoscale Weather Analysis and Prediction*, Boulder, Colorado, 141-146.

_____, D. W., Flicker, and D. K. Lilly, 1991: Recovery of three-dimensional wind and temperature fields from simulated single-Doppler radar data. *J. Atmos. Sci.*, **48**, 876-890.

_____, and N. A. Crook, 1994: Wind and thermodynamic retrieval from single-Doppler radar measurements of a gust front observed during Phoenix II. *Mon. Wea. Rev.*, **122**, 1075-1091.

_____, and _____, 1997: Dynamical and microphysical retrieval from Doppler radar observations using a cloud model and its adjoint. Part I: Model development and simulated data experiments. *J. Atmos. Sci.*, **54**,1642-1661.

_____, and _____, 2001: Real-time low-level wind and temperature analysis using single WSR-88D data. *Wea. Forecasting*, **16**, 117-132.

Takano. I., and A. Segami, 1993: Assimilation and initialization of a mesoscale model for improved spin-up of precipitation. *J. Meteor. Soc. Japan.*, **71**, 377-391.

Talagrand, O., 1997: Assimilation of observations, an introduction. *J. Meteor. Soc. Japan.*, **75 1B**, 191-209.

Tao, W.-K., and J. Simpson, 1993: Goddard Cumulus Ensemble Model. Part I: Model description. *Terrestrial, Atmospheric and Ocean Sciences*, **4**, 35-72.

Thiao, W., R. A. Scofield, and J. Robinson, 1993: The relationship between water vapor plumes and extreme rainfall events during the summer season. NOAA Technical Report NEDIS 67, 50 pp.

Todling, R., and S. E. Cohn, 1994: Suboptimal schemes for atmospheric data assimilation based on the Kalman filter. *Mon. Wea. Rev.*, **122**, 2530-2557.

Tustison, B., E. Foufoula-Georgiou, and D. Harris, 2003: Scale-recursive estimation for multisensor quantitative preciptation forecast verification: A preliminary assessment. *J. Geophysical Res.*, **108**, 8377-8390.

Uccellini, L. W., and P. J. Kocin, 1987: The interaction of Jet streak circulations during heavy snow events along the east coast of the United States. *Wea. Forecasting*, **2**, 289-308.

Vieux, B. E., and P. B. Bedient, 1998: Estimation of rainfall for flood prediction from WSR-88D reflectivity: A case study, 17-18 October 1994. *Wea. Forecasting*, **13**, 126-134.

Vieux, J., 2003: Private communication.

Wang, J., 2001: A nowcast/forecast system for coastal ocean circulation using simple nudging data assimilation. *J. Atmos. Oceanic Technol.*, **18**, 1037-1047.

Wang. W., and T. T. Warner, 1988: Use of four-dimensional data assimilation by Newtonian relaxation and latent-heat forcing to improve a mesoscale-model precipitation forecast: A case study. *Mon. Wea. Rev.*, **116**, 2593-2613.

Warner, T. T.,and H.-M. Hsu, 2000: Nested-model simulation of moist convection: The impact of coarse-grid parameterized convection on fine-grid resolved convection. *Mon. Wea. Rev.*, **128**, 2211-2231.

Weiss, M., and E. A. Smith, 1987: Precipitation discrimination from satellite infrared temperatures over the CCOPE mesonet region. *J. Appl. Meteor.*, **26**, 687-697.

Weygandt, S. S., 1998: The retrieval of initial forecast fields from single Doppler observations of a supercell thunderstorm. Ph. D. Dissertation, University of Oklahoma, Norman, OK, 257 pp.

_____, J. Levit, G. Basset, A. Shapiro, K. Brewster, R. Carpenter., M. Xue, and K. Droegemeier, 1999: Real-time model initialization using single-Doppler retrieved fields obtained from WSR-88D level-II data. Preprints, *29th Int. Conf. on Radar Meteorology*, Montreal, Quebec, Canada, Amer. Meteor. Soc., 150-153.

_____, A. Shapiro, and K. K. Droegemeier, 2002a: Retrieval of model initial fields from single-Doppler observations of a supercell thunderstorm. Part I: Single-Doppler velocity retrieval. *Mon. Wea. Rev.*, **130**, 433-453.

_____, A. Shapiro, and K. K. Droegemeier, 2002b: Retrieval of model initial fields from single-Doppler observations of a supercell thunderstorm. Part II: Thermodynamic retrieval and numerical prediction. *Mon. Wea. Rev.*, **130**, 454-476.

Wilks, D. S., 1995: Statistical Methods in the Atmospheric Sciences. Academic Press, 467 pp.

Wilson, J. W., and E. A. Brandes, 1979: Radar measurements of rainfall. *Bull.Amer. Meteor. Soc.*, **60**, 1048-1058.

Xia, J., and A. Chen, 1999: An objective approach for making heavy rainfall forecasts based on numerical model output and the latest observation. *Wea. Forecasting*, **14**, 49-52.

Xu, M., N. A., Crook, J. Sun, and R. Rasmussen, 2001: Assimilation of radar data for 1-4 hour snowband forecasting using a mesoscale model. Preprints, *14th Conf. on Numerical Weather Prediction*, Fort Lauderdale, Florida, Amer. Meteor. Soc., 283-286.

Xu, Q., 1996: Generalized adjoint for physical processes with parameterized discontinuities. Part I: Basic issues and heuristic examples. *J. Atmos. Sci.*, **53**, 1123-1142.

Xue, M., K. K. Droegemeier, V. Wong, A. Shapiro, and K. Brewster, 1995: *ARPS Version 4.0 User's Guide.* [Available from Center for Analysis and Prediction of Storms, University of Oklahoma, 100E. Boyd St., Norman, OK 73019], 380 pp.

_____, D. Wang, D. Hou, K., Brewster, and K. K. Droegemeier, 1998: Prediction of the 7 May 1995 squall lines over the central U.S. with intermittent data assimilation. Preprints, *12th Conf. On Numerical Weather Prediction*, Phoenix, AZ., Amer. Meteor. Soc., 191-194.

_____, K. K. Droegemeier, and V. Wong, 2000: The Advanced Regional Prediction System (ARPS)- A multiscale nonhydrostatic atmospheric simulation and prediction tool. Part I: Model dynamics and verification. *Meteor. Atmos. Physics*, **75**, 161-193.

_____, K. K. Droegemeier, V. Wong, A. Shapiro, K. Brewster, F. Carr, D. Weber, Y. Liu, and D. Wang, 2001: The Advanced Regional Prediction System (ARPS)- A multiscale nonhydrostatic atmospheric simulation and prediction tool. Part II: Model physics and applications. *Meteor. Atmos. Physics*, **76**, 143-165.

Yoshizaki, M., and Y. Ogura, 1988: Two- and three-dimensional modeling studies of the Big Thompson storm. *J. Atmos. Sci.*, **45**, 3700-3722.

Zhang, D.-L., and J. M. Fritsch, 1986: Numerical simulation of the meso-β scale structure and evolution of the 1977 Johnstown flood. Part I: Model description and verification. *J. Atmos. Sci.*, **43**, 1913-1943.

Zhang, D.-L., and J. M. Fritsch, 1986: Numerical simulation of the meso-β scale structure and evolution of the 1977 Johnstown flood. Part II: Inertially stable warm-core vortex and the mesoscale convective somplex. *J. Atmos. Sci.*, **44**, 2593-2612.

Zhang, J., 1999: Moisture and diabatic initialization based on radar and satellite observations. Ph. D. Dissertation, University of Oklahoma, Norman, OK, 194 pp.

Zhang, J., and T. Gal-Chen, 1996: Single-Doppler wind retrieval in the moving frame of reference. *J. Atmos. Sci.*, **53**, 2609-2623.

_____, F. Carr, and K. Brewster, 1998: ADAS cloud analysis. *Preprints, 12th Conf. on Num. Wea. Prediction*, Phoenix, AZ, AMS, Boston, 185-188.

Zong, J., 1996: Impact of observations on the numerical prediction of the Lahoma, Oklahoma supercell hailstorm. General Examination Paper for the Doctor's Degree, University of Oklahoma, Norman, OK, 83 pp.